

**David Frantz**

vom Fachbereich VI  
Raum- und Umweltwissenschaften  
der Universität Trier  
zur Verleihung des akademischen Grades  
Doktor der Naturwissenschaften  
(Dr. rer. nat.)  
genehmigte Dissertation

**Generation of Higher Level Earth Observation Satellite Products  
for Regional Environmental Monitoring**

Betreuer:

Univ.-Prof. Dr. Joachim Hill

Berichterstattende:

Univ.-Prof. Dr. Joachim Hill

Univ.-Prof. Dr. Günther Heinemann

Univ.-Prof. Dr. Patrick Hostert

Datum der wissenschaftlichen Aussprache:

27.01.2017

Trier, 2017





## Acknowledgements

I have long looked forward to write this section and to eventually thank everybody who has supported me during my work on this thesis. The past 3+ years were a very intense period of time and throughout, I was in the lucky position to be surrounded by amazing people, who have considerably contributed in one way or the other.

I would first like to thank my supervisor Univ.-Prof. Dr. Joachim Hill, head of the Environmental Remote Sensing & Geoinformatics department at Trier University, who cheerfully pushed me into the field of radiative transfer modelling. I am very grateful for the opportunity to work in your team and in the SASSCAL project. I greatly acknowledge your expertise, guidance, support and constructive feedback throughout the past couple of years. I look forward to our new project and to mutually adapt this processing streamline to Sentinel-2.

Thanks to Univ.-Prof. Dr. Thomas Udelhoven, who was always available for statistical advice, as well as for the support of some of the thesis' contributions. I also would like to thank both Joachim Hill and Thomas Udelhoven for providing me with all the equipment necessary to undertake this research, which as outlined in this thesis, one should not take for granted.

To Univ.-Prof. Dr. Günther Heinemann and Univ.-Prof. Dr. Patrick Hostert for agreeing to review the thesis.

The foundation for this dissertation was laid during my time as student assistant in The Future Okavango Project. In this regard, I would express my deepest gratitude to my unofficial supervisors Dr. Achim Röder and Dr. Marion Stellmes. Thank you for all your trust, support and advice, both professionally and privately. You own a large share in this work and basically taught me everything I know about doing science. I greatly appreciate the amount of work and patience you have put into developing this thesis. Marion, I wish you all the best for your new job in Berlin and look forward to have a chat and some beers at MultiTemp or so. I would also like to thank Anne Schneibel, who completes our Africa group. Besides all the productivity, we had a lot of fun in our Africa meetings, which was a very welcome distraction from regular work.

To Michael, Peter, Neil and the rest of the Brisbane team that warmly welcomed me during my visit in the course of my diploma thesis. During this time I made first contact with big data processing, which surely brought me on track to this work. To Patrick Griffiths, whose presentation

in Trier at that time, eventually inspired me to dig deeper into the processing and compositing of Landsat data.

Thanks to Sebastian Mader, who gave me a C crash course and at times brought me back on track when I core-dumped my code. I am also very grateful for all his support in tuning SPLITs to my research needs.

I would also like to thank all my other colleagues for many advices and plenty distractions over one or two cups of coffee. I was lucky to have some great office mates. Thanks to Thomas, Sascha and Erik. To my fellow Ph.D Gilles, who helped to make the past few weeks way more bearable. To Johannes, Christian, Henning, Pyare, Sandra, Barbara, each one of you would have surely deserved an own paragraph, and I certainly forgot to mention some people here, just tell me and we will sort this out over a good old 'Bossung-Brühe'.

Thanks to all my family, danke für all die Unterstützung und den Rückhalt; einfach nur danke dass ihr immer für mich dagewesen seid!

Last, but most importantly, thank you Isabelle and Aaron. It is hard to express all my love and gratitude in only a few sentences, but I want you to know that I certainly couldn't have finished this without you.

## Abstract

Earth's environment sustains a current population of more than seven billion humans, whose well-being are reliant on the provision of ecosystem services jeopardized by environmental change. In this context, space-based earth observation (EO) is a prerequisite for enhanced and sustainable land use management. Only few satellite missions fulfill the basic requirements for operational environmental monitoring on the regional scale; among these the Landsat mission with its open data policy stands out. However, increasing data volumes have led to a 'digital-divide', as the adequate use of this rich EO archive is dependent on high-performing technology. Consequently, it is key to develop methods that account for the most data-intensive processing steps, then used for the generation and provision of analysis-ready, standardized, higher-level (Level 2 and Level 3) baseline products, which in turn enable a wider range of end-users to instate an even wider variety of environmental monitoring systems. Level 2 products are radiometrically normalized image products including atmospheric correction, and represent the first product level for widespread environmental usage. In a complementary sense, Level 3 products are temporal aggregations of lower-level products, and are generally termed 'composites'. Besides other favorable characteristics, Level 3 products have some potential to lessen the 'digital-divide' as a large amount of data can be 'distilled' into a better manageable data volume.

Accordingly, the overarching research task of this dissertation was to develop a framework for generating analysis-ready higher-level EO satellite products that may eventually be linked with operational monitoring systems. Hence, efficient and fully automatic mass data processing streamlines were implemented accounting for the most data-intensive processing steps. In this regard, this thesis attempts to make a significant contribution in the yet under-researched drylands of Southern Africa.

A fully automatic radiometric preprocessing system (Level 2) was implemented, featuring a memory-resident processing streamline. The method was applied to the complete Angolan, Zambian, Zimbabwean, Botswanan, and Namibian Landsat record, amounting 58,731 images with a total data volume of nearly 15 TB. A modified version of the Fmask algorithm was implemented for cloud/shadow detection, wherein dryland-specific improvements were developed to reduce false positives in complexly structured savanna images. Integrated correction of atmospheric, topographic and bidirectional effects was implemented. Atmospheric correction was based on radiative theory and includes corrections for multiple scatterings and the adjacency effect. A multilayered toolset was developed to favorably estimate aerosol optical depth (AOD) over persistent cast shadow and water targets. Therein, a combined image-, database-, and object-based approach was developed with

consideration of the target's view and illumination geometry, altitude, and environmental contribution. In case of dark target absence, a precompiled spatio-temporal AOD climatology was used as reasonable surrogate. A semi-empirical C-correction was implemented for topographic correction, and bidirectional effects were corrected using a global set of bidirectional reflectance distribution function model parameters. Gridding and reprojection to a common reference system were already included at Level 2, hence facilitating easy and efficient processing and analysis.

The selection of phenologically similar observations is a key monitoring requirement for multi-temporal analyses, and hence, the generation of Level 3 products that realize phenological normalization on the pixel-level was pursued. As a prerequisite, Land Surface Phenology (LSP) at appropriate spatial resolution was needed. Therefore, coarse resolution LSP was derived in a first step, then spatially refined by fusing it with a small number of Level 2 images. For this purpose, a novel data fusion technique was developed, wherein a focal filter based approach employs multi-scale and -source prediction proxies. Prediction quality was ensured by simulating artificial landscapes ( $R^2 = 0.84$ ), and by application to a heterogeneous agricultural site. Objects larger than the effective coarse resolution were predicted reliably – and even significantly smaller objects were predicted accurately if there were pure homogeneous coarse resolution pixels within the focal filter.

A phenology-adaptive pixel-based compositing framework (Level 3) was implemented using a parametric weighting-scheme based observation selector, wherein phenological normalization was achieved by coupling the target day (i.e. the main compositing criterion) to the input LSP. Inter-annual variations in the timing of LSP were also accounted for and the inter- to intra-annual contribution was controlled with a single parameter. The approach was demonstrated by generating peak, end and minimum of season composites, and by comparing these with static composites (fixed target day). It was shown that the phenological normalization accounts for terrain- and land cover class-induced LSP differences. However, it needs to be carefully considered which technique is best for a given purpose. In any case, the use of the comprehensively corrected downstream products enables a wide range of monitoring options, among them the detection of within-state processes like forest degradation.

In summary, the developed preprocessing framework is capable of generating several analysis-ready baseline EO satellite products. These include radiometrically normalized and geometrically consistent Landsat time series, as well as phenologically sound and seamless image composites across large areas. These datasets can be used to promote regional case studies like the mapping of agricultural regimes, but may also be directly integrated into more operational monitoring systems – e.g. in support of the Reducing Emissions from Deforestation and Forest Degradation (REDD) incentive.

# Contents

Acknowledgements .....	i
Abstract.....	iii
Contents .....	v
List of Figures .....	vii
List of Tables .....	xii
List of Abbreviations.....	xiii
<b>Chapter I.....</b>	<b>1</b>
Introduction	
1 Regional Environmental Monitoring from Space	2
2 Requirements for Regional Environmental Monitoring	5
2.1 Spectral resolution	5
2.2 Radiometric resolution	6
2.3 Spatial resolution	6
2.4 Temporal resolution	7
3 Capability of current EO Systems for Regional Environmental Monitoring	9
4 Product Specification	12
4.1 Product Level Definitions	12
4.2 Required Product Level	13
4.3 State-of-the-art Product Generation Systems	14
5 Research Question	17
5.1 Gap Analysis	17
5.2 Objectives and Structure	19
<b>Chapter II.....</b>	<b>22</b>
An Operational Radiometric Landsat Preprocessing Framework for Large-Area Time Series Applications	

<b>Chapter III</b> .....	<b>56</b>
Enhancing the Detectability of Clouds and Their Shadows in Multitemporal Dryland Landsat Imagery: Extending Fmask	
<b>Chapter IV</b> .....	<b>69</b>
On the Derivation of a Spatially Distributed Aerosol Climatology for its Incorporation in a Radiometric Landsat Preprocessing Framework	
<b>Chapter V</b> .....	<b>82</b>
Improving the Spatial Resolution of Land Surface Phenology by Fusing Medium- and Coarse-Resolution Inputs	
<b>Chapter VI</b> .....	<b>104</b>
Phenology-Adaptive Pixel-Based Compositing using Optical Earth Observation Imagery	
<b>Chapter VII</b> .....	<b>146</b>
Synthesis	
1 Summary	147
1.1 Objective I: Development of a Level 2 production system	147
1.2 Objective II: Development of a Land Surface Phenology baseline	150
1.3 Objective III: Development of a Level 3 production system	151
2 Conclusions and Outlook	153
References.....	155
Curriculum Vitae.....	176

## List of Figures

Fig. II-1. Location of the study area and number of available L1T images per Landsat frame. ....	26
Fig. II-2. Number of available L1T images per year (top) and month (bottom). ....	27
Fig. II-3. Schematic workflow of the preprocessing framework. B, C and D refer to subchapters 2–4 of the methods section. ....	30
Fig. II-4. Workflow for the radiometric processing. The subsections of this chapter are grouped in boxes. ...	32
Fig. II-5. Visualization of the water vapor database for WRS-2 Path/Row 177/072 (19.71°E, 17.35°S). Top: daily values and 15-day running mean; bottom: average seasonal cycle and standard deviation on monthly basis. ....	34
Fig. II-6. Visualization of a section of the dark object database and two example images (25.06°E, 17.79°S). Top: Dark object persistency; middle: false-color image of a late wet-season image; bottom: false-color image of a dry-season image. The same stretch was applied to both images with R/G/B = NIR/red/green. ....	38
Fig. II-7. Number of processed chips per arbitrary tile, corrected for redundant overlaps. ....	44
Fig. II-8. Histograms of the spectral consistency assessment of overlapping chip pairs. The histogram bin width was set to 0.25% reflectance. The y-axis is drawn logarithmic. Quantiles are drawn in colors. ....	44
Fig. II-9. Linear regression between image-based Landsat and terrestrial AERONET AOD measurements for all stations and all coinciding observations. The colors represent different AERONET sites; blue to purple: Zambia, red/orange: Namibia, green: Botswana. The majority of the data is from the Mongu sites, Zambia. ....	45
Fig. II-10. Potential errors in using climatically derived water vapor estimates instead of daily values. The analysis was performed with two dry/wet season TM images of the Etosha Pan. Both images were corrected with different water vapor values (Table II-3). The figure displays the difference in surface reflectance (in %) between the correction with day-specific values and the correction with climatically derived variants. ....	46
Fig. II-11. Illustration of the topography correction for a mountainous Landsat-8 image in Huila, Angola (13.39°E, 15.86°S; 1000 m elevation range) under low illumination conditions (sun elevation: 41°, azimuth: 37°). Top: no topography correction; middle: topographically corrected; bottom: digital elevation model. The same stretch was applied to both images with R/G/B = NIR/SWIR1/red. ....	48
Fig. II-12. Average aspect-dependent NIR reflectance for the image (full frame) shown in Fig. II-11 for the vegetated (top) and bare (bottom) classes. The image was processed with the implemented C-Correction (green), the Minnaert correction (blue) and with disabled topography correction (red). Flat curves point to a successful topographic normalization. ....	48
Fig. II-13. Topographic correction evaluation. The histogram bin width was set to 0.01 R <sup>2</sup> . The correction was quantitatively evaluated by differencing the R <sup>2</sup> of the relationship between $\cos i$ and $L$ , before and after the radiometric correction. A decrease in R <sup>2</sup> points to a reduction of topographic effects. ....	48

Fig. III-1: Study Area .....	60
Fig. III-2: Workflow of the two-step algorithm. ....	64
Fig. III-3: Illustration of the time series outlier detection for two pixels marked in Fig. III-4. An outlier (blue bars) is detected if its cloud/shadow probability is greater than the pixel median + a standard deviation multiplier (statistics retrieved from the clear-sky observations, black bars), thus being in the grey area. Fmask detections (yellow bars) are used to separate most of the observations before calculating the statistics. NDVI time series of the clear-sky observations are plotted in green. ....	65
Fig. III-4: Landsat RGB-composite (bands 4/5/3, i.e. NIR/SWIR1/RED) for the illustration of the outlier detection method (blue) as compared to the Fmask detections (yellow). The image was captured on 02/03/2007, which corresponds to the date with the blue bars in Fig. III-3; the corresponding pixels are marked with <i>a</i> ) and <i>b</i> ). ....	66
Fig. IV-1. Successful path reflectance retrievals for the six reflective Landsat bands for an illustrative Landsat frame (177/072). The frame is located at the Namibian/Angolan border and includes the perennial Cubango and Cuito rivers. The grey background indicates the dry season. ....	73
Fig. IV-2. Mean path reflectance retrievals (0.483 $\mu\text{m}$ ). Mean values are computed for every Landsat frame for the depicted acquisition months; only the successful retrievals were considered. ‘?’ marks indicate Landsat frames where the dark object identification failed or there were no cloud-free images. ....	74
Fig. IV-3. Initial path reflectance retrievals (0.483 $\mu\text{m}$ ) and prediction (line) for a series of Landsat frames within one orbit (path 170, i.e. in the eastern part of the study area). The path/row is labelled in the bottom right corner. The persistence of the dark objects (DOP) which were used for estimating the path reflectance is indicated by the variable point size. The persistence was used to weight the observations in the prediction. ....	76
Fig. IV-4. Latitude dependence of (a) the timing of peak aerosol loading, (b) the maximum predicted path reflectance and (c) the minimum predicted path reflectance. The data are inferred from the depicted prediction in Fig. IV-3. ....	76
Fig. IV-5. Predicted aerosol optical depth surfaces at 0.483 $\mu\text{m}$ for three dates in the dry season; see the online version of this article for the complete and animated time series. ....	77
Fig. IV-6. Average annual AOD cycle for the AERONET Mongu site and the corresponding AOD prediction. The path reflectance offset was found by inverting the multiple scattering computation such that the RMSE between the AERONET and the predicted AOD is minimized. ....	77
Fig. V-1 ( <i>a</i> ): Study area and coarse resolution LSP. KAZA TFCA: Kavango-Zambezi Transfrontier Conservation Area. The RGB-composite depicts the peak of season (POS, red), end of season (EOS, green) and minimum of season (MOS, blue) for 2005. The “+” indicates the subset in Fig. V-8. ( <i>b</i> ): Histograms of the depicted data. ....	86
Fig. V-2. Temporal density of the available Landsat images per month from 2001–2012. Statistics were calculated per tile and then averaged for the complete study area. ( <i>a</i> ): Temporal density in all tiles; ( <i>b</i> ):	



Temporal density in tiles that do not have orbital overlaps. The alternating bars in the background indicate intervals of 16 days (nominal nadir repeat coverage of a single Landsat system).....	88
Fig. V-3. Workflow of the presented methodology with references to the sections and subsections. ....	90
Fig. V-4. Schematic illustration of the prediction process. In this example, 1 CR pixel equals 9 MR pixels. .	92
Fig. V-5. Simulated random landscape (a) and corresponding true color MR reflectance images (b) in three seasonal windows (left wet, cool dry and hot dry season). The marked regions in (a) are discussed in the text. The same stretch was applied to all images in (b). The size of the simulated landscape is 1024 x 1024 px; the prediction radius $r$ is 100 px. ....	95
Fig. V-6. Algorithm test with simulated data. (a) simulated MR amplitude; (b) simulated CR amplitude; (c) predicted MR amplitude; (d) absolute difference between simulated and predicted MR amplitude. The marked regions in (d) are discussed in the text and are also shown in Fig. V-5a. The monochromatic color bar refers to the amplitude values (a-c) and the right color bar refers to the absolute amplitude difference (d). The size of the simulated landscape is 1024 x 1024 px; the prediction radius $r$ is 100 px. ....	96
Fig. V-7. 2D-histogram of simulated and predicted MR amplitude, bordered by the corresponding 1D-histograms. The letters indicate the simulated land-cover clusters and the legend colors match Fig. V-5a. ....	98
Fig. V-8. Comparison of coarse-resolution LSP (a) and predicted medium-resolution LSP (b). The RGB-composite depicts the peak of season (POS, red), end of season (EOS, green) and minimum of season (MOS, blue) for 2005. Selected areas are enlarged in the right panel (4x zoom). (c) Histograms of the depicted data; the lines refer to MR LSP and the polygons to CR LSP.....	99
Fig. V-9. MR reflectance input data (a-d), MR heterogeneity $T_{ji}$ (e) and CR heterogeneity $U_{ji,p}$ (f) for subset 'A' in Fig. V-8. (a-d): Average reflectance for the four seasonal windows (Table V-1) with RGB = near infrared, shortwave infrared, red. The same stretch is applied to all images. (f): RGB composite of $U_{ji,p}$ for $p = \text{POS, EOS and MOS}$ .....	100
Fig. V-10. MR reflectance input data (a-d), MR heterogeneity $T_{ji}$ (e) and CR heterogeneity $U_{ji,p}$ (f) for subset 'B' in Fig. V-8. (a-d): Average reflectance for the four seasonal windows (Table V-1) with RGB = near infrared, shortwave infrared, red. The same stretch is applied to all images. (f): RGB composite of $U_{ji,p}$ for $p = \text{POS, EOS and MOS}$ .....	100
Fig. VI-1. Overview of the study area (Zambia). (a): Digital Elevation Model (DEM), acquired by the Shuttle Radar Topography Mission (SRTM). The Worldwide Reference System 2 (WRS-2) is superimposed. (b): Monthly rainfall sums for 2005, obtained from the Africa Rainfall Climatology version2 (ARC2; Novella and Thiaw 2013). ....	110
Fig. VI-2. Number of clear-sky observations for the MODIS (a) and Landsat (b) composites for the five-year period 2003–2007. ....	112
Fig. VI-3. Land Surface Phenology (LSP) for 2005; (a): peak of season (POS), (b): end of season (EOS), (c): minimum of season (MOS). (d): normalized histograms of POS, EOS and MOS (standardized by	

histogram maximum), and color bar for (a-c). The POS can be at the end or at the beginning of the calendar year, and as such, the data ranges from December 1, 2004 (DOY 336) to December 31, 2005 (DOY 365). The depicted color-ramp is used for all DOY images throughout the paper. .... 114

Fig. VI-4. Schematic illustration of the LSP-adaptive DOY scoring functions. The Gaussian type is shown in (a-d); the logistic S-curves in (e-h). For illustration purposes, we have either visualized fits to the variable LSP with constant function values (a,b,e,g), or have visualized fits to constant LSP but variable function values (c,d,f,h). The chosen LSP and scoring function values are indicated as  $p_{0-2}$  and  $s_{0-2}$ ; the point signatures indicate the  $p$  and  $s$  values, and ‘var.’ indicates that a parameter was varied; the variation of the  $p$  and  $s$  values can be taken from the x- and y-axis, respectively. For consistency with the following real-life examples, the  $p$ -values were tagged semantically with POS, EOS and MOS. In all cases, the target metric is the phenological parameter with the highest score, i.e. EOS (a-d), POS (e-f) and MOS (g-h)..... 118

Fig. VI-5. Illustration of the Y-factor  $Y_f$  for an arbitrary example. The figure shows isolines of the total score  $S_T$ , drawn with a dependence on  $\Delta Y$  and  $\Delta D$ . The right tail Gaussian type was chosen and two years around the target year are allowed; i.e.  $y = 2$ . The total score was computed as a combination of the Year score  $S_Y$  and the DOY. The higher  $Y_f$ , the higher is  $S_Y$  – and the smaller is the influence of  $\Delta Y$  on  $S_T$ ..... 118

Fig. VI-6. Cloud distance and haze scoring functions;  $d_{req}$  was set to 100 pixels. .... 120

Fig. VI-7. Exemplary illustration of the spectral stability assessment and correlation scoring function. (a): mean absolute correlation derived from the temporal correlation matrix, and Landsat-7 NIR image (Path/Row 172/072) affected by sensor anomalies. (b): correlation scoring function. .... 122

Fig. VI-8. View zenith angle scoring function;  $\theta_{req}$  was set to  $40^\circ$  and  $7.5^\circ$  for MODIS and Landsat, respectively. .... 122

Fig. VI-9. Pixel-based MODIS composites for the target year 2005. The composites were anchored at three different phenological stages; (a-c): peak of season, (d-f): end of season, (g-i): minimum of season. The composites in the first column (a,d,g) were generated with the phenology-adaptive approach; the composites in the second column (b,e,h) were generated using a static target date (mean of the LSP metrics). The depicted band combination is RGB = near infrared, shortwave infrared and red, thus combining complementary information from the three different wavelength domains. The band combination, as well as the same stretch is applied to all reflectance composites throughout the paper. The third column (c,f,i) depicts the difference in the Enhanced Vegetation Index between the phenology-adaptive and static composites; i.e. red colors indicate a higher EVI in the phenology-adaptive composite. The green rectangle in (f) indicates the extent of Fig. VI-11. .... 126

Fig. VI-10. Temporal characteristics of the generated MODIS composites in Fig. VI-9. The three seasons are plotted in the rows; (a-b): peak of season, (c-d): end of season, (e-f): minimum of season. The left half of the figure (a,c,e) refers to the phenology-adaptive composites; the right half (b,d,f) to the static composites. For each composite, the selected DOY, the difference to the target DOY  $\Delta D$  and the

	difference to the target year $\Delta Y$ are shown. The same color ramps are applied throughout the paper where appropriate. ....	127
Fig. VI-11.	EVI of the MODIS EOS composites for a sample area. The subset is indicated in Fig. VI-9 and is characterized by a large terrain elevation gradient ( $> 1000$ m). The phenology-adaptive version is shown in the left column; the static version in the right column. (a–b): EVI maps; the brown–green color ramp is linearly stretched from 0–0.5, (c–d): 2D-histograms between EVI and terrain elevation, (e–f): EVI boxplots for the World Wildlife Fund terrestrial ecoregions (Olson <i>et al.</i> 2001); A–D are Central Zambebian Miombo woodlands, southern Miombo woodlands, Zambebian and Mopane woodlands and Zambebian flooded grasslands, respectively. ....	128
Fig. VI-12.	Effect of different Y-factors on the phenology-adaptive MODIS composites. Histograms of the difference to the target DOY (line signature; top <i>x</i> -axis), and target year (barplot; bottom <i>x</i> -axis) are shown for the peak of season (a), end of season (b) and minimum of season (c) composites. ....	130
Fig. VI-13.	Pixel-based MODIS composites for the target year 2005 across a large latitudinal gradient. The composites are end of season variants, where (b) is a phenology-adaptive composite; (a) and (c) are static composites that were anchored at the average end of season of the northern (a) and southern hemisphere (c). ....	130
Fig. VI-14.	Pixel-based Landsat composites for the target year 2005. The composites were anchored at three different phenological stages; (a): peak of season, (b): end of season, (c): minimum of season. The composites were generated with the proposed phenology-adaptive approach. Temporal characteristics are shown below the corresponding composite. For each composite, the selected DOY, the difference to the target DOY $\Delta D$ and the difference to the target year $\Delta Y$ are shown. ....	131
Fig. VI-15.	EVI cross-comparison of the generated MODIS and Landsat composites. The phenological stages are shown in the rows with peak of season in (a–d), end of season in (e–h) and minimum of season in (i–l). Different statistical measures are shown in the columns with mean error (ME), mean absolute error (MAE), root mean squared error (RMSE) and coefficient of determination ( $R^2$ ) from left to right. The MODIS/Land-sat composites are abbreviated with ‘MOD’/‘LND’ and the phenology adaptive and static versions with ‘LSP’/‘STA’, respectively. The residuals are calculated as $e = x - y$ ; e.g. the lower-left ME value in (a) means that the static MODIS composite features higher EVI values than the phenology adaptive Landsat composite. The color ramps are consistent within each column. ....	132
Fig. VI-16.	CAT Transformation of the annual EOS Landsat composites, mapped to RGB space as Change, Aftereffect, and Trend, respectively. Three exemplary subsets (100 km <sup>2</sup> ) depicting different change processes are shown in (b–d; 13.02°S / 30.76°E), (e–g; 14.78°S / 27.21°E), and (h–j; 16.23°S / 25.79°E) with CAT transformation, 2002 and 2012 composites from left to right. ....	134

## List of Tables

Table I-1. Product level definition. ....	13
Table II-1. Acquired L1T Landsat images.....	27
Table II-2. Mathematical symbols .....	30
Table II-3. Precipitable water values.....	47
Table IV-1. Path reflectance prediction errors for every Landsat band.....	75
Table V-1. Definition of the seasonal windows.....	94
Table VI-1. Mean timing of LSP. ....	114
Table VI-2. Mathematical symbols.....	116
Table VI-3. Parameterization of the MODIS and Landsat composites.....	124
Table VI-4. Temporal basic statistics of MODIS and Landsat composites.....	127

## List of Abbreviations

ACCA	Automated Cloud Cover Assessment	ETM+	Enhanced Thematic Mapper
AERONET	Aerosol Robotic Network	EVI	Enhanced Vegetation Index
AFIS	Advanced Fire Information System	FOV	Field-of-View
AMP	Amplitude	FWHM	Full Width at Half Maximum
AOD	Aerosol Optical Depth	GCOS	Global Climate Observing System
API	Application Programming Interface	GDAL	Geospatial Data Abstraction Library
AVHRR	Advanced Very High Resolution Radiometer	GEO-BON	Group on Earth Observation Biodiversity Observations Network
BLAS	Basic Linear Algebra Subprograms	GMES	Global Monitoring for Environment and Sustainability
BRDF	Bidirectional Reflectance Distribution Function	GSL	GNU Scientific Library
BT	Brightness Temperature	HDF	Hierarchical Data Format
CA	Climatic Average	HITRAN	High-Resolution Transmission Molecular Absorption Database
CAT	Change, Aftereffect, Trend	HOT	Haze Optimized Transformation
CODMAC	Committee on Data Management, Archiving and Computing	HRG	High Resolution Geometric
CR	Coarse Resolution	IFOV	Instantaneous Field-of-View
DDV	Dense Dark Vegetation	ITCZ	Intertropical Convergence Zone
DEM	Digital Elevation Model	KAZA TFCA	Kavango–Zambezi Transfrontier Conservation Area
DN	Digital Number	LAADS	Level 1 and Atmosphere Archive and Distribution System
DO	Dark Object	LAEA	Lambert Azimuthal Equal Area
DOC	Day of Composite	LaSRC	Landsat Surface Reflectance Code
DODB	Dark Object Database	LEDAPS	Landsat Ecosystem Disturbance Adaptive Processing System
DOP	Dark Object Persistency	LGAC	Landsat Global Archive Consolidation
DOS	Dark Object Subtraction	LP DAAC	Land Processes Distributed Active Archive Center
DOY	Day of Year	LPGS	Level 1 Product Generation System
DV	Daily Water Vapor	LSP	Land Surface Phenology
EBV	Essential Biodiversity Variable	MAE	Mean Absolute Error
ECV	Essential Climate Variable	ME	Mean Error
EO	Earth Observation	MERIS	MEdium Resolution Imaging Spectrometer
EOS	End of Season		
EOSDIS	Earth Observing System Data and Information System		
ESA	European Space Agency		
ESS	Ecosystem Services		

MODAPS	MODIS Adaptive Processing System		conservation, sustainable management
MODIS	Moderate Resolution Imaging Spectroradiometer		of forests and enhancement of forest carbon stocks in developing countries]
MOS	Minimum of Season	RMSE	Root Mean Squared Error
MR	Medium Resolution	RSR	Relative Spectral Response
MRV	Monitoring, Reporting and Verification	SAR	Synthetic Aperture Radar
MSI	Multi Spectral Instrument	SASSCAL	Southern African Science Service Centre for Climate Change and Adaptive Land Management
NASA	National Aeronautics and Space Administration		
NBAR	Nadir BRDF-Adjusted Reflectance	SLC	Scan Line Corrector
NDSI	Normalized Difference Snow Index	SNR	Signal to Noise Ratio
NDVI	Normalized Difference Vegetation Index	SOS	Start of Season
NIR	Near Infrared	SPOT	Satellite Pour l'Observation de la Terre
NLCD	National Land Cover Database	SRTM	Shuttle Radar Topography Mission
NOAA	National Oceanic and Atmospheric Administration	STARFM	Spatial and Temporal Adaptive Reflectance Fusion Model
NRT	Near-Real Time	SWIR	Shortwave Infrared
OLCI	Ocean and Land Color Instrument	TIRS	Thermal Infrared Sensor
OLI	Operational Land Imager	TM	Thematic Mapper
OpenMP	Open Multi-Processing	TOA	Top of Atmosphere
PBC	Pixel-Based Composite	TSA	Time Series Analysis
PCA	Principal Component Analysis	TTHG	Two-Term Henyey–Greenstein
PCP	Potential Cloud Pixel	USGS	U.S. Geological Survey
POS	Peak of Season	VI	Vegetation Index
PRODES	Amazon Deforestation Project (approx. translation)	VIS	Visual
RAM	Random Access Memory	WASI	Water Color Simulator
REDD[+]	Reducing Emissions from Deforestation and Forest Degradation [and the role of	WELD	Web-Enabled Landsat Data
		WRMSE	Weighted Root Mean Squared Error
		WRS-2	Worldwide Reference System 2
		WWF	World Wildlife Fund



## **Chapter I**

### **Introduction**



## 1 Regional Environmental Monitoring from Space

Sustaining a current population of more than seven billion humans, planet earth faces many pressures, which makes comprehensive environmental monitoring an indispensable task. Up to date, more than 75% of the terrestrial land surface has already been modified (Ellis and Ramankutty 2008). Humanity is constantly growing and reshapes its surrounding environment at the same time, not necessarily for the good: the world's (semi-) natural ecosystems and biodiversity are diminishing at alarming rates and climate continues to be irreversibly altered (Butchart *et al.* 2010, Hansen *et al.* 2013, IPCC 2013). Human well-being is and will be increasingly influenced by the complex system of interactions and feedbacks between environmental change and the provisioning of ecosystem services (ESS, MEA 2005). As an example, the conflicts between food supply and forest integrity or timber production may result in a self-energizing feedback loop in the long-term: a growing world population tends to transform land at the expense of forest, whose loss is the second largest contributor to global greenhouse gas emission (van der Werf *et al.* 2009). This in turn may change climate towards more frequent extreme weather events (IPCC 2012) that threaten food security and may result in food shortages (McMichael *et al.* 2006), which were traditionally countered by transforming even more land (Godfray *et al.* 2010). At worst, such feedback mechanisms can force components of the Earth system beyond their 'tipping point' with large impacts on human welfare (Lenton *et al.* 2008). In order to break such cycles and to use limited resources sustainably, a key prerequisite for enhanced land use management is to continuously monitor the status and usage of earth's environment, as well as to predict the future impact of current land use (Townshend *et al.* 2008).

This perception is widely accepted, however, the globally most concerning areas are often the most under-researched and under-instrumented areas at the same time. For instance, the Southern African Miombo belt was identified as tipping point of global importance because it supports the transport of summer rainfall and humidity from the Congo rainforest zone towards the southern arid savannas (Leadley *et al.* 2010). Nevertheless, most research takes place (and is tuned to) industrialized countries like the United States of America, Europe, Australia, and to a lesser extent also to emerging countries like China, India and Brazil (Hassan 2008). Brazil as an example has long been in the public eye as deforestation (Myers 1993) and biodiversity loss hotspot (Myers *et al.* 2000), and hence has put significant effort into forest loss combat (Boucher *et al.* 2013) – but at the same time the carbon balance was offset by increased deforestation in Indonesia, Malaysia, Paraguay, Bolivia, Zambia, and Angola (Hansen *et al.* 2013). Space-based earth observation (EO) is certainly the only technology that can account for this imbalance. This becomes apparent when considering that 34 sovereign states launched 197 EO satellite missions during the past couple of decades at an ever increasing rate

(Belward and Skøien 2015), reflecting the fact that this technology was already identified as game-changer half a century ago (DOI 1966):

*‘The time is now right and urgent to  
apply space technology towards the solution of  
many pressing natural resources problems being  
compounded by population and industrial growth.’*

*Stewart Udall, 1966  
U.S. Secretary of the Interior*

Satellite imagery has long been used for EO in general (see e.g. Davis 2007), and increasingly also in an operational sense as most countries or international communities maintain some sort of operational monitoring system like the US National Land Cover Database (NLCD, Homer *et al.* 2015), the Eastern Australian woodland monitoring (Danaher *et al.* 2010), Brazil’s Amazon Deforestation Project (PRODES, Shimabukuro *et al.* 1998), the European Union-led Global Monitoring for Environment and Sustainability services (GMES/Copernicus, Aschbacher and Milagro-Pérez 2012), China’s Earth Observation System (Xingfa and Xudong 2015), or South Africa’s Advanced Fire Information System (AFIS, Frost and Scholes 2007). Yet, many observation programs are nationally grown, and hence are not fully comparable across the globe. Consequently, an ideal, hypothetical EO system would not stop at boundaries but would observe the complete globe. However, due to the scale at which environmental processes occur (see next section), it is at least challenging to do so – and even more important, local processes may be overlooked in a global implementation but may still be globally important. As an example, global studies may underestimate Namibian deforestation because the complete loss of the typically sparse tree cover (< 10%) might be valued as an effect of detection uncertainty in many other parts of the world. At the other end of the spectrum, a rather local monitoring poses the risk of process leakage or displacement (DeFries *et al.* 2007). Hence, a compromise between global and local EO may be beneficial in many circumstances; this compromise is hereby denoted ‘regional’ and is defined as any geographic region large enough to avoid leakage and small enough for environment-specific tuning, which may range from state to (sub-) continental. For instance, such a strategy is pursued in the decentralized but regionally tuned monitoring systems under the REDD[+] incentive (Reducing Emissions from Deforestation and Forest Degradation [and the role of conservation, sustainable management of forests and enhancement of forest carbon stocks in

developing countries]), wherein each participating country needs to formally define ‘forest’ but nonetheless is bound to report land cover status and change within a defined conceptual framework.

Several initiatives exist to define such frameworks with the goal to harmonize and funnel regional EO efforts. On one hand, this is achieved by building consensus about what to monitor (e.g. Pereira *et al.* 2013), and on the other hand by providing good practice guidelines about how to monitor and validate (e.g. Penman *et al.* 2003, Olofsson *et al.* 2014). The Global Climate Observing System (GCOS) accordingly proposed the so-called ‘essential climate variables’ (ECV, GCOS 2003), defined as a ‘physical, chemical or biological variable or a group of linked variables that critically contributes to the characterization of Earth’s Climate’ (Bojinski *et al.* 2014). ECV-qualification includes climate relevancy, observation feasibility and cost-effectiveness (Bojinski *et al.* 2014), hence the ECV concept is dynamic and needs to be understood as the absolute minimal monitoring setup. However, it is also recognized that other variables may be important too, and may become ‘essential’ in the future; in fact GCOS considered 70 variables for land surface characterization, although only a few were formally defined as ECV yet (Bojinski *et al.* 2014). Recently, the Group on Earth Observation Biodiversity Observations Network (GEO-BON) adopted this concept as ‘essential biodiversity variables’ (EBV) in order to measure biodiversity change (Pereira *et al.* 2013). A number of crucial EO-compatible variables have been identified through both consortia, and they are anticipated to form the backbone of future global EO monitoring frameworks. Important terrestrial variables include land cover, fraction of absorbed photosynthetic active radiation, leaf area index, above ground biomass, soil carbon, disturbance regime, phenology, ecosystem structure, extent, fragmentation and composition (Houghton *et al.* 2012, GEO-BON 2016).

In this context, appropriate data streams and processing environments have to be instated. This thesis attempts to make a contribution towards the provision of fundamental satellite baseline datasets, which may be eventually used for the derivation of ECVs, EBVs and similar important environmental variables in a yet under-researched part of the globe, namely Southern Africa. This introduction is structured as follows: section I-2 will give an overview on the requirements of an ideal monitoring system, and section I-3 will review current EO missions in the context of these requirements. Section I-4 will specify the baseline data products needed for regional environmental monitoring and will outline the state-of-the-art. Section I-5 will identify the corresponding research gaps and the thesis’ research objectives will eventually be formulated.

## 2 Requirements for Regional Environmental Monitoring

Considering specifications of a monitoring framework, the immediate question that arises is: what are the technical requirements for monitoring preferably all essential variables and are satellite missions available that fulfill these requirements? The monitoring requirements are closely tied to the main resolutions of remote sensing systems, i.e. the spectral, spatial, temporal and radiometric resolution. These resolutions dictate which processes can be resolved distinctively. In the following, the ideal monitoring requirements are specified for each resolution group, and the subsequent chapter will shortly review current space-borne EO systems with regard to these requirements.

### 2.1 Spectral resolution

The spectral domain and resolution of EO systems potentially have the largest influence regarding the essential variables that can be derived or not. In general, three major domains are suitable: optical reflective, optical thermal and radar systems. They merely provide complementary information and can be utilized under different observation settings. An optimal remote sensing system would have sensitivity for the complete electromagnetic spectrum, but due to engineering constraints, detector arrays or antennas can only be focused on one part of the spectrum, and it is seldom to have all types of sensors onboard a single satellite platform.

The optical reflective domain is most widely used and has been proven effective for many EO tasks. The absolute minimum spectral configuration for environmental monitoring are two optical bands in the red and near infrared as prerequisite for vegetation monitoring due to their sensitivity to chlorophyll absorption and biomass (Tucker 1979, Townshend and Justice 1988). Additional bands in the visible and shortwave infrared are requested for a wider range of purposes like water mapping, soil/vegetation, snow/cloud and deciduous/coniferous differentiation, assessment of healthy vegetation and plant water, and geological applications (Blanchard and Weinstein 1980). Hyperspectral imaging spectrometers represent the maximum spectral configuration and allow to resolve fine biophysical, biochemical, and geochemical details (Kaufmann *et al.* 2006).

Additional capabilities in the optical thermal domain are useful for enhanced cloud detection (Zhu and Woodcock 2012), and enable drought monitoring (Anderson *et al.* 2013), as well as detection of plant heat/water stress (Blanchard and Weinstein 1980). Opposed to reflective systems, thermal sensors also have the capability to sense during night orbits, e.g. for active volcano monitoring (Wulder *et al.* in press).

Synthetic Aperture Radar (SAR) have the ability to penetrate visibly opaque objects, and hence, the backscattered radiation is a function of scattering and attenuation processes within a volume, e.g. a canopy. The intensity is strongly influenced by the dielectric constant of the respective medium, and hence, imaging radars are sensitive to water or moisture variations and can be applied for land cover, biomass, inundation or soil moisture mapping (Kasischke *et al.* 1997). As clouds are transparent in this part of the spectrum, SAR data are a viable addition to optical imagery – especially in parts of the world that are permanently overcast or where vegetation growth coincides with the rainy season (Kasischke *et al.* 1997). However, radar alone cannot overcome this problem: Saatchi *et al.* (1997) demonstrated that wet season SAR images are not suited to map deforestation accurately because of the equalizing effect of moisture in the canopy and on the surface. They recommended to analyze imagery from the dry season – where optical data availability is of less concern likewise.

## 2.2 Radiometric resolution

The radiometric resolution is the ability to resolve differences of received energy, which is directly linked to the sensor's signal-to-noise ratio (SNR). Simply put, the higher the radiometric resolution, the better the discrimination of subtle variations on the earth's surface. Specifically, high SNR decreases the risk of band saturation over bright surfaces like snow, cloud or rock and is very beneficial for approaches that utilize low radiance targets like water or shadows (Roy *et al.* 2014c). The only drawback of increased quantization is an increase in data volume.

## 2.3 Spatial resolution

In terms of geographic scale, environmental processes have to be monitored with imagery that can distinctly resolve them. As an example, forest clearings vary between hundreds of meters (mechanized agriculture) to tens of meters (smaller agricultural or urban clearing) to < 15 m in more heterogeneous landscapes (DeFries *et al.* 2007). Often, a minimum mapping unit of < 1 ha is declared necessary (De Sy *et al.* 2012, Danaher *et al.* 2010). It has to be noted that finer resolution is not necessarily superior for all monitoring purposes, e.g. due to the complicating effect of cast shadow or elevation-dependent object displacement. Methods for estimating the optimal spatial resolution exist and are often based on the analysis of spatial autocorrelation. The optimal resolution can vary greatly for different objectives (e.g. single tree or forest stand monitoring), landscape structures (patch size and heterogeneity) and spectral bands; e.g. Marceau *et al.* (1994) found an optimal resolution of 2.5 m to 21.5 m for discriminating coniferous classes, Menges *et al.* (2001) found that a resolution between 20 m and 27 m was optimal for mapping land cover types. Nested approaches are also possible (Stellmes *et al.* 2010), where coarser resolution data can be used to identify hot spots for further

investigation with finer data (DeFries *et al.* 2007). There is no formal definition on the common spatial resolution domains and their boundaries. This is reflected in inconsistent naming conventions in literature, and as such, high resolution is hereby defined as < 10 m, medium resolution as 10–100 m, and coarse resolution as 100–1000 m, wherein the 100–500 m domain is termed moderate resolution. In general, coarser-than 1 km data are not appropriate for environmental monitoring (Townshend and Justice 1988), unless paired with very high repeat frequency which can partially account for the reduced geometric detail (Stellmes *et al.* 2010).

## 2.4 Temporal resolution

The temporal requirements are even more environment- and process-dependent than the spatial ones. The optimal observation interval, length and timing is dependent on the persistency of the phenomenon as well as on other interfering processes and effects that may mask the process of interest. As an example, carbon stock changes with high uncertainty usually require a measurement frequency of a couple of years to decrease the effect of short-term variability and climate fluctuations (Penman *et al.* 2003). This equally applies to the length of record, as e.g. reliable trend parameters can only be extracted from long time series (Stellmes *et al.* 2010). Other processes should be monitored annually, as e.g. forest clearing may be unobserved with longer intervals due to regrowth of canopy or pasture (Danaher *et al.* 2010). Often, shorter intervals may be beneficial as more frequent observations can often decrease the uncertainty (Penman *et al.* 2003) and are even mandatory in many cases. As an example, savanna burn scars are usually undetectable after about one month due to the predominant fine fuel combustion product that is easily removed by wind; on the contrary burn scars in temperate and boreal forests may be detectable for years or decades (Pereira 2003). The derivation of Land Surface Phenology (LSP) is an example for the need of even denser acquisitions. 16-day temporal resolution is already considered as coarse (Archibald and Scholes 2007) as e.g. spatial and temporal variability can be significantly shorter (Menzel *et al.* 2001). Another aspect is to choose an optimal point in time for monitoring. For instance, barren fields might be falsely classified as fallows if the imagery was acquired in an unfortunate phenological state (Griffiths *et al.* 2013a), seasonal variations in broadleaved canopies might erroneously be classified as deforestation (DeFries *et al.* 2007), or trees and understory grass can be spectrally inseparable in parts of the year (Armston *et al.* 2009). In any case, multi-temporal monitoring requires adequate consistency (Hostert *et al.* 2003), and therefore selected data need to share similar temporal characteristics, i.e. at the same local time, in the same season – or more specifically, in the same phenological state (Röder *et al.* 2008) – and if possible also considering inter-annual fluctuations in vegetation seasonality as these can be larger than the magnitude of the actual change between the years (Lambin 1996). In many cases, the selection of an

optimal observation period has to compete with external constraints, e.g. persistent cloud coverage during a rainy season.

In addition, it is often required to make retrospective assessments, which is e.g. a key requirement and challenge for REDD+ (Herold *et al.* 2011). Accordingly, a satellite data record should extend as far as possible into the past. Equally important is continuity, as it is a prerequisite for consistent operational monitoring (Stellmes *et al.* 2010). A currently emerging new class of monitoring systems is especially interested in timeliness. Early warning management and law enforcement support systems can be developed on top of near-real time (NRT) monitoring systems (Hansen *et al.* 2016) – provided that the satellite data become swiftly available after they were sensed.

### 3 Capability of current EO Systems for Regional Environmental Monitoring

In summary, it was outlined that an ideal EO mission should have high SNR sensitivity in all parts of the spectrum, should be able to capture large regions with a spatial resolution in the order of decameters with high repeat frequency at constant local time, and should provide a data record that extends into the past and future. This chapter will shortly review whether these requirements are fulfilled by existing EO systems and will introduce some of the most widely used satellite missions.

There are or were 197 successfully launched earth-orbiting satellite missions that are designated for non-military land surface observation (as of December 2013, Belward and Skøien 2015), and of these, only sun-synchronous orbiters come into consideration as their near-polar orbit provides the opportunity for global mapping (Belward and Skøien 2015) and to ensure repeat observations at comparable times. High resolution sensors lack swath width and hence are not suitable to cover large areas in a reasonable time frame, although repeat coverage can be significantly increased using satellite constellations with multiple identically equipped spacecrafts. However, the ground segment is equally important to be truly considered: among others, a global acquisition plan must be in place and well calibrated low-level data products must be distributed at no charge (Belward and Skøien 2015). Consequently many commercial satellites are not suitable for operational monitoring per se, but can still be instrumental to support calibration and validation. Belward and Skøien (2015) found evidence that even mild restrictions on data access decrease its usage and discourage the development of monitoring systems around such type of data. As such, free and open data policy is key. The long and the short of it, no single open-access satellite constellation fulfills all requirements yet, and consequently, a compromise between the spatial, temporal, spectral and radiometric monitoring resolutions has to be made.

In practice, the Landsat program currently occupies the leading role for regional environmental monitoring (Roy *et al.* 2014c, Cohen and Goward 2004), and is further consolidating influence as it is evolving into an operational monitoring program (Wulder *et al.* in press) with safeguarded financing over the next couple of decades (Foust 2015). The newest satellites steadily incorporate new technology without sacrificing continuity with the existing long-term data record (1982–today), which represents the most comprehensive and longest uninterrupted cross-calibrated (Markham and Helder 2012) EO data record ever gathered (Wulder *et al.* in press). The radiometric resolution is 8 bit for the Thematic Mapper (TM) type-of sensors onboard Landsat 4, 5 and 7 and was improved to 12 bit for the Operational Land Imager (OLI) onboard Landsat 8 (Roy *et al.* 2014c). The spatial resolution of 30 m is in range of the spatial requirements and is adequate for monitoring landscape processes (Danaher *et al.* 2010). The Field-of-View (FOV) is  $\pm 7.7^\circ$  and one swath is about 185 km wide



(Blanchard and Weinstein 1980), which allows for covering large areas with still relatively low surface reflectance anisotropy effects. The sun-synchronous orbit at 705 km altitude results in near-global coverage at nadir repeat frequency of 16 days at about 09:30 local standard time (Blanchard and Weinstein 1980). The temporal resolution is even higher in overlap areas that increase towards the poles (Kovalskyy and Roy 2013), and for some periods, two satellites were/are operational, which further doubled repeat frequency. However, it also needs to be noted that – with exception of the United States, Australia and eastern China (Wulder *et al.* in press) – the data availability can be of some concern due to a wide variety of reasons like the late instatement of a global acquisition plan (Arvidson *et al.* 2001), changes in program management and budgeting (Goward *et al.* 2006), temporary or permanent sensor outages like the scanline corrector failure of Landsat 7's Enhanced Thematic Mapper (ETM+, Markham *et al.* 2004) or simply adverse climate settings (Asner 2001). Nevertheless, the Landsat Global Archive Consolidation (LGAC) re-migrated internationally held data to U.S. Geological Survey (USGS) holdings, and although some data was irrecoverable, the usable archive has more than doubled thereby (Wulder *et al.* in press), which in combination with the public opening of the Landsat archive in 2008 (Woodcock *et al.* 2008) marked the game changer for environmental monitoring (Wulder *et al.* 2012).

In 2000, the Moderate Resolution Imaging Spectroradiometer (MODIS) onboard Terra was launched into the Landsat 7 orbit to further complement the Landsat monitoring system with multiscale capabilities (Justice *et al.* 1998), while maintaining continuity with the Advanced Very High Resolution Radiometer (AVHRR), too. Outstanding temporal characteristics with one–two day revisit frequency were achieved by wide FOV sensor design (approx.  $\pm 65^\circ$ ), although at the expense of nadir spatial resolution (250–1000 m) and its degradation towards the edges of the swath (Wolfe *et al.* 1998). Hence, MODIS serves the coarse spatial resolution / high frequency segment and is often used for global studies (e.g. Clinton and Gong 2013, Friedl *et al.* 2002) or for analyses that require high temporal or angular resolution like the derivation of LSP (e.g. Zhang *et al.* 2003) or the estimation of the bidirectional reflectance distribution function (BRDF) and albedo (Schaaf *et al.* 2002). Due to the orbital (Justice *et al.* 1998) and spectral congruence, (Barnes *et al.* 1998), MODIS and Landsat are often used in tandem by fusing them into dense synthetic time series (e.g. Gao *et al.* 2006, Zhu *et al.* 2010, Zhu *et al.* 2016) or by applying MODIS-measured variables to Landsat images, e.g. for atmospheric (Ju *et al.* 2012) or BRDF correction (Roy *et al.* 2008).

Currently, these constellations are increasingly backed by the European Space Agency's (ESA) Sentinel fleet. Sentinel-3's Ocean and Land Colour Instrument (OLCI) was designed to provide continuity with the MEdium Resolution Imaging Spectrometer (MERIS, Donlon *et al.* 2012), and thus

has similar capabilities as MODIS. Sentinel-2's Multi Spectral Instrument (MSI) is similar to OLI at better spectral, spatial and temporal resolution. In this thesis, Sentinel data was not yet considered due to the lack of a long data record. This equally applies to SAR data, where an acquisition plan suitable for global operational monitoring was firstly realized with Sentinel-1 (Torres *et al.* 2012). However, it is noted that the synergistic usage of Landsat with the Sentinel-line of satellites – and also similar upcoming optical and SAR missions – possesses a tremendous potential for future regional environmental monitoring systems.

## 4 Product Specification

Although there is currently a lot of enthusiasm regarding the usage of Landsat data, and even more about Sentinel-2, for many researchers and institutions it is challenging – and often impossible – to employ such data for the development of regional monitoring programs. Traditionally, analyses were either based on a few time steps and large areas (Masek *et al.* 2008) or on small areas and shorter time steps (Sonnenschein *et al.* 2011), which often were selected, preprocessed and quality-checked (e.g. cloud masking) with considerable manual effort. Nowadays, state-of-the-art monitoring programs are in demand of integrating a manifold of satellite data at ever-increasing temporal, spatial and spectral resolution that both cover a large area and make use of the full-depth of the existing archive; even global analyses are possible nowadays (e.g. Hansen *et al.* 2013). As of January 2015, there were ~ 5.5 Mio. Landsat images with a total data volume of > 4PB in the USGS holdings (Wulder *et al.* in press), and even for smaller reporting areas like the REDD-qualifying country of Zambia, there are nearly 22K images available for the same period (USGS 2016b). Consequently, with the ever increasing data volume also comes unprecedented data pressure: although data has become available to everyone, the high technical demand in terms of data processing, storage infrastructure (Gibbs *et al.* 2007), and downlink capabilities (Roy *et al.* 2010b) has led to a ‘digital-divide’ (Norris 2001), and hence bars part of the science community from utilizing complete EO archives adequately. Consequently, it is of major importance to develop methods that account for the most data-intensive processing steps, then used for the generation and provision of analysis-ready, standardized baseline products, which in turn enable a wider range of end-users to instate a wide variety of environmental monitoring systems.

### 4.1 Product Level Definitions

As a means of categorizing and standardizing such baseline products, NASA’s Earth Observing System Data and Information System (EOSDIS) hierarchical product level classification scheme is generally used, see Table I-1. Level 0 data, i.e. the raw data downlinked from space, are generally not available to end-users and software developers. Commonly, the space agencies provide Level 1B data, i.e. radiometrically calibrated and georectified data. Level 2 data are derived from Level 1 and most notably include some sort of atmospheric correction. Level 3 data are temporally aggregated Level 2 (or Level 1) data that are provided in a different spatial reference, commonly a grid system with a shared coordinate system. The generation of Level 3 products is commonly termed ‘compositing’. Level 4 products are thematic model output; ECVs and EBVs generally fall under this category.

Table I-1. Product level definition.

Level	Description
Level 0	Reconstructed, unprocessed instrument/payload data at full resolution; any and all communications artifacts, e.g., synchronization frames, communications headers, duplicate data removed.
Level 1A	Reconstructed, unprocessed instrument data at full resolution, time-referenced, and annotated with ancillary information, including radiometric and geometric calibration coefficients and georeferencing parameters, e.g., platform ephemeris, computed and appended but not applied to the Level 0 data.
Level 1B	Level 1A data that have been processed to sensor units.
Level 2	Derived geophysical variables at the same resolution and location as the Level 1 source data.
Level 3	Variables mapped on uniform spacetime grid scales, usually with some completeness and consistency.
Level 4	Model output or results from analyses of lower level data, e.g., variables derived from multiple measurements.

Defined by NASA's Earth Observing System Data and Information System (EOSDIS) in consistency with the Committee on Data Management, Archiving and Computing (CODMAC) definitions (copied from Asrar and Greenstone 1995).

Although the above described level definitions are generally agreed on, several modifications are used by different product generation systems. As an example, Landsat data generated by the Level 1 Product Generation System (LPGS) are distributed as Level 1T, Level 1G or Level 1Gt products, which are essentially Level 1B data with differences in the georectification quality. Among these, only Level 1T data are suitable for Level 3 and Level 4 product generation, as the other categories are not co-registered reliably and hence are not suited for multi-temporal application (Townshend *et al.* 1992). In addition, following the above definitions, Level 3 products are the first that are mapped on a regular grid, whereas the lower level products are still in georectified swath geometry (e.g. the Landsat WRS-2 path/row system). However, there is currently a rising demand for gridded and analysis-ready products (Hansen and Loveland 2012) – regardless of product level. This is e.g. reflected in ESA's production and distribution strategy of Sentinel-2 data as they already include gridding on their Level 1 category C (Drusch *et al.* 2012). Similarly, the attribution of simplistic radiometric corrections like Top-of-Atmosphere (TOA) reflectance is becoming indistinct, as ESA also distributes Level 1C data in TOA reflectance (Drusch *et al.* 2012), which is adopted in this study, too: TOA reflectance is considered Level 1 and surface reflectance is considered Level 2.

## 4.2 Required Product Level

Level 4 products, e.g. ECVs, are eventually needed for reporting environmental resource status and change. According to the EOSDIS definition, these can be derived from any lower-level product and can be based on mono-, bi- or multi-temporal observations, possibly also including products from

different sensors and other data sources. The minimum required product level is strongly dependent on the environmental process of interest. Lower level products might suffice for specific approaches like mono-temporal classification, although Song *et al.* (2001) reported that the accuracy of such analyses was always improved with atmospheric correction. Atmospheric correction is strictly necessary for multi-temporal and/or multi-sensor analyses (Röder *et al.* 2005), and concurrently even enables the derivation of biophysical variables and their use for assessing subtle land degradation processes in sparsely vegetated rangelands (e.g. Hostert *et al.* 2003, Röder *et al.* 2008). As of today, degradation processes are still under-assessed (Mertz *et al.* 2012), which might partially be due to the fact that automatic preprocessing and web-enabled provisioning of atmospherically corrected medium resolution satellite products represents a fairly new development (Loveland and Dwyer 2012). As such, one cannot overemphasize the importance of Level 2 products as fundamental basis of hierarchical product generation streamlines because they represent the first product level for widespread environmental usage. In the context of providing truly analysis-ready products, it becomes increasingly vital to already include gridding and reprojection on Level 2 (opposed to the EOSDIS definition) as this significantly simplifies the application of exhaustive time series algorithms – or facilitates Level 3 composite production – that make use of all available data but are generally invoked on a per-pixel basis (e.g. Zhu and Woodcock 2014b, Griffiths *et al.* 2013b).

In a supplementary sense, Level 3 data can also be suitable for specific research tasks or circumstances. Compositing can be a means to generate spatially consistent datasets at regular repeat frequency, and thus enforces temporal equidistance, which often is a methodological key requirement (e.g. Jönsson and Eklundh 2004, Udelhoven 2011). In addition, the generation of (multi-) annual composites can be sufficient or can even have advantages: 5-year reporting intervals are generally sufficient for operational forest monitoring (Penman *et al.* 2003), and the use of carefully compiled annual time series reduces seasonal variations and hence directly unveils both drastic and long-term landscape changes (e.g. Kennedy *et al.* 2010, Hird *et al.* 2016). Furthermore, temporally aggregated, but spatially complete data enable the use of long-established and effective traditional remote sensing techniques like bi-temporal change detection (Singh 1989). Eventually, Level 3 products have some potential to lessen the ‘digital-divide’ because composites are analysis-ready baseline products that implicitly include the full-depth of the original Level 2 archive – with a fractional amount of the original data volume.

### **4.3 State-of-the-art Product Generation Systems**

As outlined above, Level 2 and Level 3 baseline products are needed in an EO production streamline. There already exist a number of successful Level 2 and 3 product generation systems

tailored for processing large quantities of Landsat data. This sub-chapter will shortly introduce some of the most widely used architectures, as well as it will summarize the key differences that are mainly attributed to the geographic area and thematic objective that has driven their development.

### 1) Level 2 product generation systems

The Landsat Ecosystem Disturbance Adaptive Processing System (LEDAPS, Masek *et al.* 2006) and the Eastern Australian Preprocessing Framework (Flood *et al.* 2013) are of special note as they were successfully applied to a wide range of studies (e.g. Masek *et al.* 2008, Schmidt *et al.* 2015), but are also quite different in design. They differ with respect to supported satellite sensors, and they feature a different set of corrections and processing modules, as well as the specific implementation of these.

LEDAPS initially aimed at providing surface reflectance inputs for the decadal assessment of North American ecosystem disturbance (Masek *et al.* 2006) and was developed on basis of the existing and very successful MODIS preprocessing architecture (Vermote *et al.* 1997, Justice *et al.* 2002, Vermote *et al.* 2002). Aerosol optical depth (AOD) is estimated using an image-based dense dark vegetation approach (DDV, Kaufman and Sendra 1988). Topographic and bidirectional effects are not accounted for. Cloud detection relies on Fmask (Zhu and Woodcock 2012). LEDAPS was developed for TM and ETM+ imagery, but the project was not further developed, and hence, OLI data are processed with a newer suite of methods called Landsat Surface Reflectance Code (LaSRC, Vermote *et al.* in press). To date, global Landsat data are processed with the respective system and made available over the internet (USGS 2016b). As a note of caution, the USGS states that these products should be considered provisional (USGS 2016a), which reflects that the development of Level 2 products is still a running topic that concerns all involved space agencies and international institutions; see e.g. the Atmospheric Correction Inter-comparison Exercise (ESA 2016).

The Eastern Australian Preprocessing Framework (Flood *et al.* 2013) was developed for operational state-wide monitoring of vegetation and land surface change. The framework supports the correction of TM, ETM+ and SPOT High Resolution Geometric (HRG) imagery, and was recently updated to also work with OLI (Flood 2014). Cloud detection is not fully integrated, but is also done using Fmask (Zhu and Woodcock 2012). The framework features an integrated correction of atmospheric, topographic and bidirectional effects – although strongly optimized for Australian settings. AOD is parameterized using a low and fixed constant due to the widespread lack of dark vegetation and the fairly clear Australian atmosphere (Gillingham *et al.* 2011).

## 2) Level 3 product generation systems

There are also significant differences between Level 3 product generation systems as a direct result of the wealth of existing techniques. Often, compositing criteria are based on optimizing band or index statistics (e.g. maximum, minimum or median selection, see Holben 1986, Cabral *et al.* 2003, Dennison *et al.* 2005, Flood 2013), sometimes amended by view angle constraints (e.g. Huete *et al.* 2002). Increasingly, new methods emerge that consider multiple criteria, among them the Web-enabled Landsat Data (WELD, Roy *et al.* 2010a), and the parametric weighting scheme developed by Griffiths *et al.* (2013b).

WELD was initially developed to provide cloud-free composites of the conterminous United States using Level 1 ETM+ imagery. A decision-tree-based compositing technique is employed to generate monthly, seasonal and annual composites. Implemented criteria include tests for cloudiness and the selection tree prefers observations with high brightness temperature and/or Normalized Differenced Vegetation Index (NDVI). Global WELD products are currently generated using additional TM images (Roy *et al.* 2014a), and the approach was also demonstrated with a Level 2 ETM+ baseline (Roy *et al.* 2014b).

Griffiths *et al.* (2013b) developed a compositing approach for monitoring land use change in the Carpathian ecoregion. The approach was also successfully applied to complete Canada (White *et al.* 2014). They utilize multiple years of Level 2 (LEDAPS) TM and ETM+ data to generate seasonal composites and to overcome cloud-induced data shortage in areas where the Landsat archive is less densely populated. The technique employs a parametric weighting scheme, where the suitability of each observation is scored with respect to the intra- and inter-annual difference to a predefined temporal target (e.g. year 2010 / Day-of-Year 180) as well as to the potential cloudiness, which is determined by the spatial proximity to the cloud mask. The observation with the highest total score is selected for the composite. Reprojection and tiling of Level 1 or Level 2 data was performed prior to compositing in both approaches.

## 5 Research Question

In the course of the preceding sections, it was outlined that space-based observation of environmental processes, e.g. in the form of essential climate/biodiversity variables are indispensable for enhanced and sustainable earth resource usage (I-1). The consequential formalization of monitoring requirements (I-2) and capabilities (I-3), as well as product requirements (I-4) leads to the conclusion that a consistent and integrated preprocessing of Level 1 into Level 2 and 3 Landsat products is an integral prerequisite that can facilitate the instatement of regional environmental monitoring systems as it relieves the end-user from any form of preprocessing and hence has great potential to increase operational throughput. The state-of-the-art was shortly reviewed in the last subchapter (I-4.3), and although the currently existing production systems have already proven their effectiveness with regards to environmental monitoring, it also is noted that the current systems still lack functionality in various crucial aspects. These gaps will be outlined in the subsequent subchapter, followed by a specific formalization of the thesis' research objectives and structure.

### 5.1 Gap Analysis

As noted earlier, most research and product development takes place in industrialized countries, whereas less-observed grey spots are present in parts of the globe – among them Southern Africa. Regarding methodology, a gap was identified in such dryland areas, as the presented Level 2 production systems either rely on DDV, or assume that AOD can be approximated by a constant if there is no dark vegetation. Whilst the drawback of the first method is self-explanatory, the latter approach is limited by assuming that AOD is low and does not vary in space and time. Both conditions are violated during the rainless burning season in Southern Africa. To a lesser extent, the cloud detection algorithm Fmask is also error-prone in drylands, as it occasionally produces a high rate of false positives in complexly structured areas with high temperature differences between land covers.

None of the systems corrects for adjacency effects, which denotes the scattering towards the sensor from adjacent surface elements. This effects adds a perturbing component to the target's signal and is especially critical in heterogeneous areas when measuring AOD over dark targets that are embedded in a bright landscape.

Furthermore, the full integration of atmospheric, topographic and bidirectional effects is not sufficiently met by the existing systems – or is strongly optimized for a limited geographic extent. While LEDAPS and LaSRC only feature atmospheric correction, the Australian approach basically includes all three corrections, although the coupled topography-BRDF correction is somewhat limited



as it was derived by an exhaustive sampling of Australian Landsat data under different illumination and viewing conditions in several topography and land cover classes. This approach may not be feasible where Landsat data availability and land cover information are below the Australian standard. The authors of LaSRC reason that additional corrections do not need to be fully integrated during atmospheric correction (Vermote *et al.* in press), as they can also be performed afterwards; however current Level 3 production systems either still use Level 1 data or rely on Level 2 data that lack further corrections for topographic and bidirectional effects. This makes a strong point for the direct integration of these corrections into Level 2 production, as this enables a wider range of applications at Level 3, too.

The harmonized processing of imagery from different sensors is also not fully accomplished, as e.g. the US based LEDAPS and LaSRC algorithms are specialized for TM/ETM+ and OLI data, respectively. Again, the Australian approach fulfills this requirement, although global applicability may not be possible with the current toolset (see last paragraph).

Moreover, the increasing demand for analysis-ready gridded Level 2 products in a single projection is currently not met. Level 3 and Level 4 product developers are still in need to convert the data prior to their analyses, which is not a sophisticated procedure, but still implies an avoidable and computationally costly preprocessing step that – at least temporary – doubles data volume.

In chapter I-2.4, the selection of phenologically similar observations was identified as a key monitoring requirement for multi-temporal analyses, yet, this condition is not exhaustively explored by the existing Level 3 systems. Generally, state-of-the-art techniques are capable of generating ‘seasonal’ composites. However, this is either accomplished by index based selection within a predefined temporal window or by selecting observations that are as close as possible to a predefined day, which both are global approaches that do not consider that spatial and inter-annual variations in phenology may be present across a study area, e.g. in the form of terrain altitude induced shifts in leaf development.

A Level 3 production system that realizes phenological normalization would be the direct consequence, and hence, a Land Surface Phenology baseline at appropriate spatial resolution would be needed for enforcing this criterion on the pixel level. As outlined before, the temporal monitoring requirement for accurately deriving LSP is to employ a time series with a temporal resolution of at least 16 days – a condition that cannot be fulfilled with Landsat data in many parts of the world.

## 5.2 Objectives and Structure

Consequently, the overarching research task of this dissertation was to develop a framework for generating analysis-ready higher-level EO satellite products that may be linked with operational environmental monitoring systems. More specifically, Level 2 and Level 3 products should be produced that fill the specified research gaps within a single production system, using Landsat as an example. This thesis attempts to make a contribution in a yet under-researched part of the globe, namely the drylands of Southern Africa. Hence, efficient and fully automatic mass data processing streamlines needed to be implemented with non-proprietary software components accounting for the most data-intensive processing steps.

In detail, three objectives were formulated, which were addressed in five peer-reviewed publications. The objectives and structure of this thesis are briefly outlined in the following and are summarized and reviewed in Chapter VII.

**Objective I: Development of a Level 2 production system** – Fully automatic radiometric preprocessing of large Level 1 satellite archives with integrated corrections for atmospheric, topographic and bidirectional effects as well as cloud/cloud shadow detection and geometric refurbishment.

**Objective II: Development of a Land Surface Phenology baseline** – Derivation of phenological descriptors for their use in a pixel-based compositing framework.

**Objective III: Development of a Level 3 production system** – Pixel-based compositing on the basis of current state-of-the-art compositing techniques with a special emphasis on developing methods for phenological normalization.

Radiometrically normalized image archives represent the fundamental basis for a broad-ranging set of monitoring demands. This first objective is primarily answered in Chapter II, where the developed Level 2 preprocessing system is presented. Partial aspects are addressed in Chapter III, i.e. a dryland-specific add-on to an existing cloud and cloud shadow detection technique, and Chapter IV, i.e. the derivation of a spatio-temporal aerosol fallback climatology for dryland-specific handling of gaps in image-based AOD estimation.

As a key monitoring requirement for multi-temporal analyses, observations from the same vegetation development stage are needed and it was assessed that this condition is not exhaustively explored by existing compositing techniques. Hence, objective two represents an intermediate – but essential – step towards the third objective, wherein LSP at Landsat’s spatial resolution is needed. As coarse resolution sensors are better suited for the derivation of LSP, Chapter V presents a novel data fusion technique for improving the spatial resolution of coarse continuous fields in general.

Following this, the datasets generated within the first two objectives are used to develop a compositing framework that realizes the selection of phenologically similar observations on the pixel level. This objective is addressed in Chapter VI, which presents a phenology-adaptive version of a parametric weighting based compositing algorithm.

Eventually, Chapter VII will summarize the three objectives and the thesis will conclude with a brief outlook, wherein it will be illustrated how the herein developed methods and datasets may promote regional case studies or be integrated into operational environmental monitoring concepts.



## **Chapter II**

### **An Operational Radiometric Landsat Preprocessing Framework for Large-Area Time Series Applications**

*IEEE Transactions on Geoscience and Remote Sensing* 54 (7),  
July 2016, 3928–3943.

DOI: 10.1109/TGRS.2016.2530856

David Frantz, Achim Röder, Marion Stellmes, and Joachim Hill

© 2016 IEEE.

The following manuscript is a copy of the final version of the accepted manuscript. The paper has been through peer review, but it has not been subject to copy-editing, proofreading and formatting added by the publisher. The version-of-record can be accessed at:

<http://ieeexplore.ieee.org/document/7426833/>

## Abstract

We developed a large area preprocessing framework for multi-sensor Landsat data, capable of processing large data volumes. Cloud and cloud shadow detection is performed by a modified Fmask code. Surface reflectance is inferred from Tanré's formulation of the radiative transfer, including adjacency effect correction. A pre-compiled MODIS water vapor database provides daily or climatological fallback estimates. Aerosol optical depth (AOD) is estimated over dark objects that are identified in a combined database and image-based approach, where information on their temporal persistency is utilized. AOD is inferred with consideration of the actual target reflectance and background contamination effect. In case of absent dark objects in bright scenes, a fallback approach with a modelled AOD climatology is used instead. Topographic normalization is performed by a modified C-correction. The data are projected into a single coordinate system and are organized in a gridded data structure for simplified pixel-based access. We based the assessment of the produced dataset on an exhaustive analysis of overlapping pixels: 98.8% of the redundant overlaps are in the range of the expected  $\pm 2.5\%$  overall radiometric algorithm accuracy. AOD is in very good agreement with AERONET sunphotometer data ( $R^2$ : 0.72 to 0.79, low intercepts and slopes near unity). The uncertainty in using the water vapor fallback climatology is approximately  $\pm 2.8\%$  for the TM SWIR1 band in the wet season. The topographic correction was considered successful by an investigation of the non-relationship between the illumination angle and the corrected radiance.

## 1 Introduction

Landsat data are one of the most valuable resources for earth observation (Cohen and Goward 2004) due to their long term data continuity (Wulder *et al.* 2008) and their optimal resolution to monitor processes at the landscape level (Danaher *et al.* 2010). With the advent of open data policy (Woodcock *et al.* 2008), accompanied by technical progress in terms of processing, storing and transmission infrastructure and the increasing availability of automated processing routines (e.g. Zhu and Woodcock 2012), the usage of Landsat data changed fundamentally (Wulder *et al.* 2012). Historically, analyses were either based on a few images and large areas (Masek *et al.* 2008) or on small areas and shorter time steps (Sonnenschein *et al.* 2011). Now, it has become feasible to make use of the full depth of the Landsat archive, as well as covering very large areas at the same time. Nevertheless, Landsat data are still provided in the traditional Worldwide Reference System 2 (WRS-2) framework (Hansen and Loveland 2012), where the image footprints vary from acquisition to acquisition. This involves several obstacles for the end user, e.g. the integrated usage of data from different paths requires the reprojection to a unique coordinate system, which simplifies the adequate usage of the data-rich orbital overlap area. Even in the case of using only one WRS-2 footprint, all images have to be cropped to the same extent. This is even mandatory if sophisticated follow up applications like time series analyses (TSA) or the derivation of pixel based composites (PBC, Griffiths *et al.* 2013b) are to be addressed. The usage of these dense time-series applications requires the data of a given location to be easily and quickly accessible, regardless of their initial path and row designation, projection, acquisition time or sensor. Therefore, preprocessed imagery in a gridded data structure represents a more suitable structure for TSA or PBC applications (Hansen and Loveland 2012), as demonstrated by the Web-enabled Landsat Data (WELD) project (Roy *et al.* 2010a).

Existing large area production systems (Hansen and Loveland 2012) or similar preprocessing architectures (Roy *et al.* 2010a) most often do not include a full and integrated radiometric treatment, i.e. accounting for atmospheric and topographic effects simultaneously. Topographic variation even has a greater impact on the remotely sensed data than atmospheric effects (Kobayashi and Sanga-Ngoie 2008), thus topography should be accounted for if the area of interest is not merely flat. More sophisticated analyses of large amounts of data like spectral unmixing or the quantitative derivation of biomass indicators (e.g. in support for monitoring systems in a Reducing Emissions from Deforestation and forest Degradation (REDD) in developing countries context) for several or many time steps also requires more sophisticated radiometric corrections, i.e. surface reflectance products. Hansen and Loveland (2012) recently published an overview of several Landsat data processing systems for large area monitoring, whereby the corrections range from Top-of-Atmosphere (TOA)

reflectance to surface reflectance, some of them including topographic and/or directional effects. Most systems only correct the data to TOA reflectance (Hansen and Loveland 2012). The widely-used Landsat Ecosystem Disturbance Adaptive Processing System (LEDAPS, Masek *et al.* 2006) produces surface reflectance by utilizing radiative transfer modelling, though the system does not account for topography. Of note is the Eastern Australia preprocessing framework (Flood *et al.* 2013) that minimizes atmospheric, topographic and bidirectional effects, though their integrated BRDF correction might not allow the direct transfer to areas that suffer from low data availability.

Large area generation systems that apply a terrain normalization and provide gridded surface reflectance products of multi-sensor Landsat data are still scarce or require input data that may not be available in each part of the world. As such, we chose a sufficiently elaborate method set that minimizes the amount of input data, in order to provide a processing framework that may even be applied in areas where the general data availability is still low and where specific environmental settings preclude the usage of specific processing strategies, e.g. in our study area in Southern Africa. We here present an operational approach that processes all available multi-sensor Level 1T (L1T) Landsat Digital Number (DN) data to surface reflectance and stores the processed data in a gridded tile structure as known from the MODIS land products. The generated products are tailored for applications that require rapid and easy data access, make use of a large amount of data across space and time and demand radiometrically normalized data. The processing scheme includes modules for cloud masking, atmospheric and topographic correction, reprojection and gridding.

## 2 Study Area

The method was developed in Southern Africa, entirely including the countries of Angola, Zambia, Zimbabwe, Botswana and Namibia (ca. 3.7 Mio. km<sup>2</sup>). The area was designated because nation-wide and cross-national wall-to-wall mapping of forest and ecosystem related parameters are to be targeted in the future, thus the inclusion of whole countries. For example, any REDD+ assessment should monitor deforestation and forest degradation rates at the national level to avoid leakage to unobserved spots (DeFries *et al.* 2007). In addition, the countries themselves were chosen because their national territory partially falls into the Kavango-Zambezi Transfrontier Conservation Area (KAZA TFCA), which is planned to be centered on the Caprivi-Chobe-Victoria Falls area. Thus, the area is a highly interesting spot for any kind of cross-boundary studies regarding a wide variety of ecological and social questions. The area is climatically diverse, especially owing to the latitudinal precipitation gradient, mainly as a consequence of the Intertropical Convergence Zone (ITCZ, Nicholson 1981). The vegetation cover ranges from dense Miombo forests in Angola to sparse xerilic savanna ecosystems in the Kalahari, and also includes more extreme surface types like swamps, salt



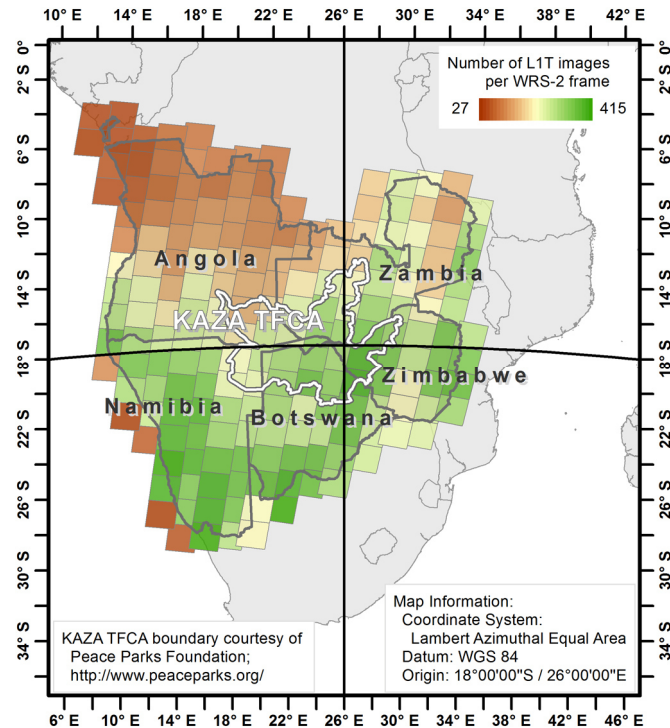


Fig. II-1. Location of the study area and number of available L1T images per Landsat frame.

pans and deserts (Olson *et al.* 2001). The seasonal cycle is closely tied to seasonal changes in large scale air movement and solar configuration, which results in three hygrothermal seasons that spatially and annually differ in timing and length due to the variability in precipitation (Fynn *et al.* 2014): (i) hot wet season (~ November to April), (ii) cool dry season (~ May to August) and (iii) hot dry season (~ September to October). The study area is displayed in Fig. II-1. Nonetheless, the presented preprocessing scheme is not bound to this area and can be ported elsewhere.

### 3 Data

#### 3.1 Landsat data

All available intersecting Landsat images from 194 WRS-2 frames were acquired from the U.S. Geological Survey archive (USGS). We downloaded even very cloudy images of up to 70% cloud coverage because the Automated Cloud Cover Assessment (ACCA) system occasionally fails to estimate the cloud coverage with sufficient precision (Zhu and Woodcock 2012). We discarded images that were not corrected with the Level 1 Product Generation System (LPGS) to L1T precision, as a reliable co-registration among images was considered to be of major importance for TSA and PBC follow-up applications. At the time of writing, we acquired and processed 58,731 L1T images with a total data volume of nearly 15 TB (see Table II-1 for details).

Table II-1. Acquired L1T Landsat images

	Number	Size	Start	End
L4 TM	225	0.03	10/22/1987	03/27/1993
L5 TM	24,204	3.34	04/12/1984	11/17/2011
L7 ETM+ SLC-On	7,166	1.83	06/30/1999	05/28/2003
L7 ETM+ SLC-Off	20,816	4.44	07/22/2003	12/31/2014
L8 OLI	6,332	5.53	04/11/2013	12/31/2014

Number, compressed data volume in TB and time range of the acquired images.

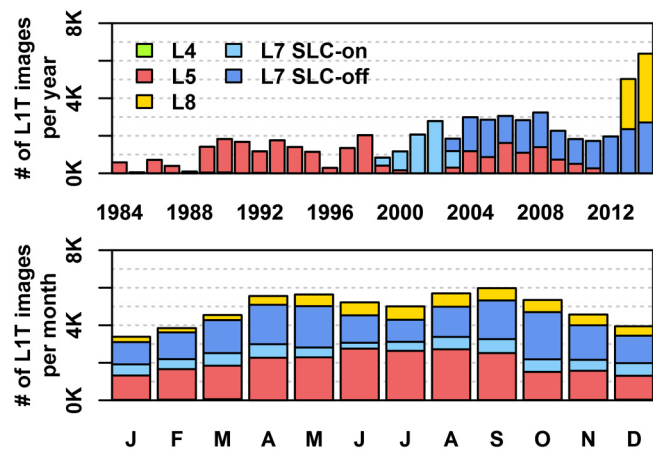


Fig. II-2. Number of available L1T images per year (top) and month (bottom).

Fig. II-1 displays the total number of available images for each WRS-2 frame. The data availability is quite low when compared to other areas such as the United States. There is a pronounced North-South gradient where data availability is extremely low in northern Angola due to the characteristic regional rainfall patterns where the north-western part of the study area is already located in the tropics.

Fig. II-2 displays all available Landsat images for each year (top) and each month (bottom). The data availability is unevenly distributed among the years, e.g. due to satellite (de-) commissioning, changes in acquisition strategies, technical failure, climatic reasons and so forth. There is a seasonality in data availability with more data during the dry season and less data during the wet season.

The Landsat Global Archive Consolidation effort (Loveland and Dwyer 2012) is currently still in progress, and we might expect up to 200 additional Landsat images per frame (Wulder *et al.* in press) which will significantly foster the applicability of subsequent analyses approaches— provided that each image is of sufficient quality to be processed to L1T precision.

### 3.2 Digital Elevation Model

Recently, the USGS publicly released the 1-arc-Second (~30 m) Digital Elevation Model (DEM) derived by the Shuttle Radar Topography Mission (SRTM, USGS 2015). We pre-compiled an elevation mosaic generously covering all of sub-equatorial Africa. DEM data are used for the topographic correction and for applying an elevation correction to the optical depths.

### 3.3 Precipitable Water Vapor

MODIS water vapor data are used for the physically based correction of water vapor absorption in the earth's atmosphere. We use the MOD05 and MYD05 products, as well as the MOD03 and MYD03 geolocation tables, which are automatically downloaded from the Level 1 and Atmosphere Archive and Distribution System (LAADS) at NASA's Goddard Space Flight Center. We use data that were derived from the near infrared water vapor algorithm (Gao and Kaufman 2003), which relies on water vapor attenuation of the near infrared (NIR) radiation. The column water vapor amount is determined from radiative transfer theory on basis of ratios between water vapor absorbing and atmospheric window bands. The product is obtained at 1 km spatial resolution and the temporal resolution is up to one day if considering both Aqua and Terra observations.

## 4 Methods

The presented framework for processing Landsat data from L1 DN values to a gridded surface reflectance product is schematically shown in Fig. II-3. The download of Landsat and SRTM data, as well as the mosaicking of the DEM are performed rather manually in advance. The core functionality of the framework is enclosed in the solid box, where the main modules are the identification of clouds and cloud shadows (4.2), the radiometric processing (4.3) and geometric modules for the finishing of the data (4.4). The radiometric correction combines methods for atmospheric and topographic corrections, which rely on the computation of the angular scene parameters, the derivation of topographic information and an elaborated scheme for retrieving AOD in a joint database-, image- and object-based approach. The gaseous transmission is accounted for by a MODIS derived water vapor database that is scheduled operationally. Table II-2 defines the mathematical symbols used in this paper.

### 4.1 Implementation

The code is able to process Landsat images from the Thematic Mapper (TM), Enhanced Thematic Mapper (ETM+) and Operational Land Imager (OLI) sensors. For the sake of dataset

consistency we opted for processing only the traditional six reflective bands. Thus we omit the ultra blue and cirrus bands of the OLI sensor. We also do not make use of the Landat-8 quality layer for the same reason as well as not using the cirrus band in Fmask, as opposed to Zhu *et al.* (2015).

Detailed processing information of the key modules are appended to the metadata in order to enable the user to gauge the quality of the processed images.

The framework is entirely implemented with Open Source software and is written in C. The Geospatial Data Abstraction Library (GDAL 2013) Application Programming Interface (API) is used for reading data in GeoTiff and Hierarchical Data Format (HDF), as well as for reprojection purposes. The cURL API is used for the automatic download of MODIS data. The GNU Scientific Library is used for optimization procedures. On-node and across-node parallelization is achieved by using GNU parallel (Tange 2011) where one processor is fed with one image at a time. The processing chain is streamlined in Random Access Memory (RAM) such that the data is only read once and only the very final output is written to disc.

Several modules can be disabled or enabled in any possible combination, e.g. the topographic correction, reprojection and/or tiling modules. The atmospheric correction can also be switched off, in which case TOA reflectance is produced. Instead of using the dark object database retrieval options, externally derived AOD values can be passed to the algorithm. More advanced processing options can also be modified, e.g. the environmental correction can be disabled and either the multiple scattering or the simpler single-scattering approximation can be employed.

## 4.2 Cloud and cloud shadow detection

We integrated a modified version of the Fmask algorithm (Zhu and Woodcock 2012) and we implemented the modifications described by Frantz *et al.* (2015b), i.e. the discarding of the termination criterion for shadow matching and the inclusion of an additional darkness filter, as well as most of the Fmask updates (Zhu *et al.* 2015). In addition, we modified the match similarity metric for matching the clouds with their shadows. In the original Fmask code (Zhu and Woodcock 2012), a cloud is shifted along a projected search path and a match between this projected shadow and potential cloud and cloud shadow layers is computed. The original cloud is excluded from the match. Nevertheless, if there is a big cloud in the search path, the match similarity is maxed out, because the projected shadow is completely contained in the bigger cloud. Thus, the shadow matching often “runs” into the next big cloud and the actual shadow is missed. Therefore, we only match the projected shadow with the potential shadow layer, which provides good results when combined with the disabling of the termination criterion (Frantz *et al.* 2015b).

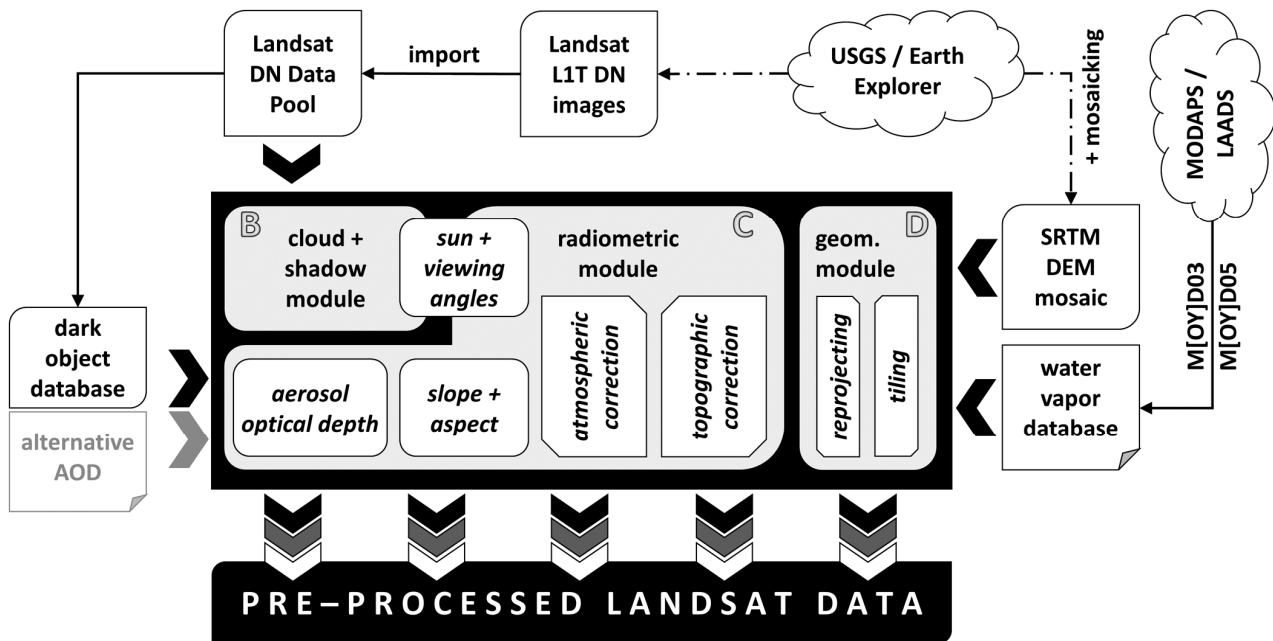


Fig. II-3. Schematic workflow of the preprocessing framework. B, C and D refer to subchapters 2–4 of the methods section.

Table II-2. Mathematical symbols

Symbol	Meaning
$\lambda$	Wavelength
$\rho, \rho^*, \rho_p$	Surface reflectance, at-satellite reflectance, path reflectance
$\langle \rho \rangle$	Background contribution to the apparent target reflectance
$\Theta_s, \Theta_v$	Sun and view zenith angles
$\Phi_s, \Phi_v$	Sun and view azimuth angles
$\mu_s, \mu_v$	Cosine of $\Theta_s$ and $\Theta_v$ , indicating downwelling and upwelling terms, respectively
$T, t_d, t_s$	Total transmittance, direct transmittance, scattered (diffuse) transmittance
$T_g, T_w$	Total gaseous transmittance, water vapor transmittance
$a_w, W, M$	Water vapor absorption coefficient, precipitable water vapor, relative air mass
$L^*, d, ESUN$	At-satellite radiance, Earth-Sun distance, mean solar exo-atmospheric irradiance
$A_{pl}, R, g$	Plane albedo, reflectance functions, asymmetry factor
$\tau, \tau_a, \tau_r$	Total, aerosol and molecular optical depth
$P, P_a, P_r$	Total, aerosol and molecular phase functions
$\Psi_-, s$	Backscattering angle, spherical albedo
$g_1, g_2, \alpha$	Asymmetry parameters of the TTHG function
$\rho_o^*, \rho_e^*, r$	Dark object reflectance, environment reflectance and target radius
$\rho_s, \rho_w, \rho_f$	Reference reflectance, volumic water reflectance, Fresnel reflectance
$a_0, a_1, a_2$	Coefficients of the logarithmic $\tau_a$ vs. $\lambda$ regression
$A, C$	Topographic A- and C-Factors
$i, \cos i$	Incidence angle, illumination angle
$b, m$	Intercept and slope of linear regression between $\cos i$ and $L^*$
$h, h_0$	Portion of the sky dome which contributes to the diffuse illumination ( $h_0$ : $h$ at $\cos i = 0$ )
$\Theta_n, \Phi_n$	Topographic slope and aspect

Definition of the mathematical symbols used in this paper.

Rather than buffering the cloud and cloud objects, we calculate the distance to the next cloud or cloud shadow (Meijster *et al.* 2000) for each pixel. This approach increases the flexibility of this dataset regarding varying demands of different follow-up applications: the user can decide on how large the buffer should be for his specific application or can make use of the full distance information; e.g. Griffiths *et al.* (2013b) used the cloud distance in a PBC application to score the usability of a given observation by using a transfer function. We append the cloud/shadow pixel distance as 7<sup>th</sup> layer to the processed data (spectral information is stored in the first 6 bands).

In order to increase the computational performance, we implemented two full-stop criteria where the processing of an image is terminated after or within (before the costly shadow matching) the cloud detection module if the scene cloud coverage exceeds a given user-defined threshold. We set this threshold to 25% unbuffered cloud and cloud shadow cover.

### 4.3 Radiometric Processing

Following Tanré's formulation for radiative transfer (Tanré *et al.* 1990) and by adding a topographic correction factor  $A$  (Teillet *et al.* 1982, Kobayashi and Sanga-Ngoie 2008), the surface reflectance  $\rho$  can be expressed as (Hill 1993):

$$\rho = A \cdot \frac{\rho^* / T_g(\mu_s, \mu_v) \cdot [1 - \langle \rho \rangle \cdot s] - \rho_p \cdot [1 - \langle \rho \rangle \cdot s] - T(\mu_s) \cdot t_s(\mu_v) \cdot \langle \rho \rangle}{T(\mu_s) \cdot t_d(\mu_v)} \quad (\text{II-1})$$

where  $\rho^*$  is the at-satellite reflectance,  $\rho_p$  is the path reflectance and  $\langle \rho \rangle$  is the background contribution to the apparent target reflectance.  $\mu_s$  and  $\mu_v$  are the cosines of the sun and view zenith angles  $\Theta_s$  and  $\Theta_v$ .  $T(\mu_v)$ ,  $t_d(\mu_v)$  and  $t_s(\mu_v)$  are the total, direct and scattered (i.e. diffuse) upwelling transmittances, respectively; downward transmission terms are indicated by their dependence on  $\mu_s$ .  $T_g(\mu_s, \mu_v)$  is the total gaseous transmission and  $s$  denotes the spherical albedo. Most of the variables in eq. II-1 and the following equations are wavelength-dependent; we omitted the wavelength subscript  $\lambda$  for the sake of simpler equations.

The adjacency effect is accounted for by the background contribution  $\langle \rho \rangle$ , which is derived from the weighted sum of the measured apparent reflectance around the target and from the target itself (for details, see Tanré *et al.* 1981, Hill 1993).

A simplified schematic workflow for the radiometric correction module is shown in Fig. II-4.

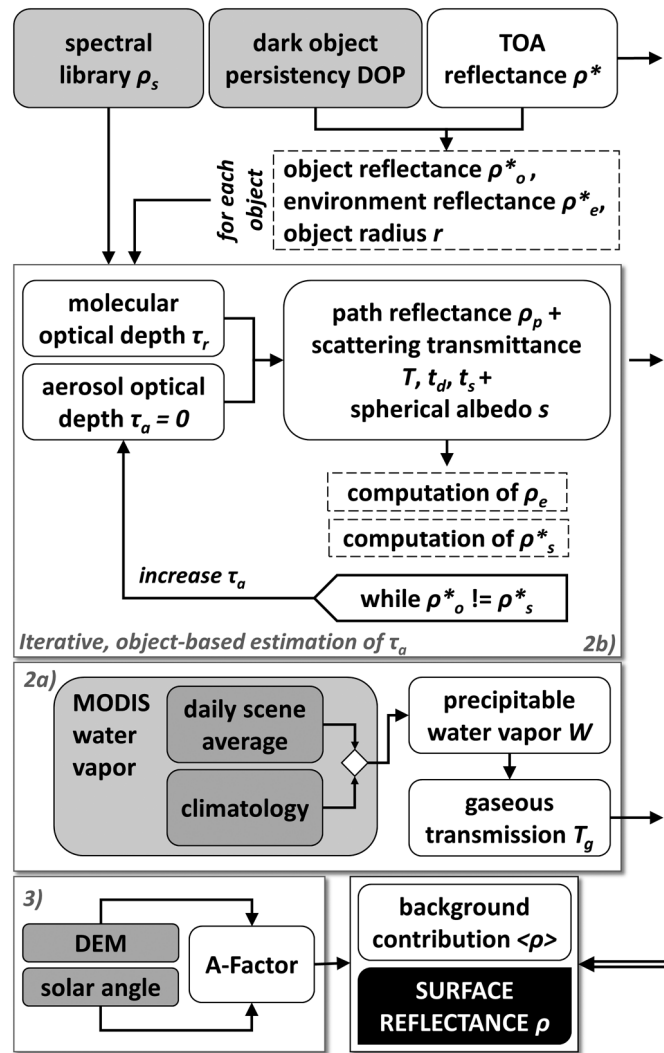


Fig. II-4. Workflow for the radiometric processing. The subsections of this chapter are grouped in boxes.

### 1) DN-to-TOA-reflectance conversion

The TOA reflectance  $\rho^*$  of a tilted surface is computed (Chander *et al.* 2009) by:

$$\rho^* = \pi \cdot d^2 \cdot L^* / (ESUN \cdot \mu_s). \quad (\text{II-2})$$

The at-satellite radiance  $L^*$  is derived from the calibrated DNs by applying the rescaling factors which are included in the metadata (Chander *et al.* 2009). The mean solar exo-atmospheric spectral irradiance  $ESUN$  was derived by applying sensor-specific relative spectral response (RSR) functions to the Thuillier solar spectrum (Chander *et al.* 2009, Thuillier *et al.* 2003).  $\Theta_s$  and the solar azimuth angle  $\Phi_s$ , as well as the Earth-Sun distance  $d$  (Spencer 1971) are computed by using the date and location from the metadata. Though it is generally accepted to only use the sun position at the scene center (Hansen and Loveland 2012), we compute sun positions for square blocks of 333 Landsat pixels,

which results in a roughly 10 km spaced sun position grid; the view zenith  $\Theta_v$  and azimuth angles  $\Phi_v$  are computed likewise.

## 2) Atmospheric correction

### a) Gaseous Transmittance

In our current implementation, we focus on the transmittance of water vapor absorption as first approximation. Amongst the radiance-modifying gases, water vapor is the most variable agent. The gaseous transmittance term in eq. II-1 then simplifies to:

$$T_g(\mu_s, \mu_v) = T_w(\mu_s) \cdot T_w(\mu_v), \quad (\text{II-3})$$

where the down-welling water vapor transmittance function is computed (Bird and Riordan 1986) by:

$$T_w(\mu_s) = \exp\left(-\frac{0.2385 \cdot a_w \cdot W \cdot M(\mu_s)}{[1 + 20.07 \cdot a_w \cdot W \cdot M(\mu_s)]^{0.45}}\right) \quad (\text{II-4})$$

which is dependent on the relative air mass  $M$ , on spectral water vapor absorption coefficients  $a_w$  and on the precipitable water vapor  $W$  (measured in centimeters). The relative air mass  $M$  is defined (Bird and Riordan 1986) as:

$$M(\mu_s) = 1/[\mu_s + 0.15 \cdot (93.885 - \theta_s)^{-1.253}]. \quad (\text{II-5})$$

The up-welling water vapor transmittance is calculated by using  $\Theta_v$  and  $\mu_v$  instead of  $\Theta_s$  and  $\mu_s$ . We derived hyperspectral  $a_w$  values from the high-resolution transmission molecular absorption database (HITRAN, Rothman *et al.* 2013) with the Landsat RSR functions.

Precipitable water estimates  $W$  are provided by a previously generated MODIS water vapor database. Therefore, we implemented an operational module for automatic data acquisition and processing of MODIS data. For each WRS-2 frame in continental sub-equatorial Africa, day-specific water vapor loadings are derived if possible. We determine spatial averages from all cloud- and sun-glint-free pixels within the WRS-2 footprints, separately for the Terra and Aqua granules. If estimates from both sensors are available, we choose the one with the larger number of valid pixels, which in most cases is Terra for Landsat 7 (99.4%) and Aqua for Landsat 5/8 (99.2%) due to orbital characteristics. If there are less than 10% of valid pixels, the average is expected to be unreliable and we fall back on an alternative parameterization, which applies for missing data of any kind, including the pre-MODIS era, coverage gaps between the swaths, sensor outages and the like. Southern African climate is dominated by a stable and pronounced seasonality into a dry and wet season. Therefore,  $W$



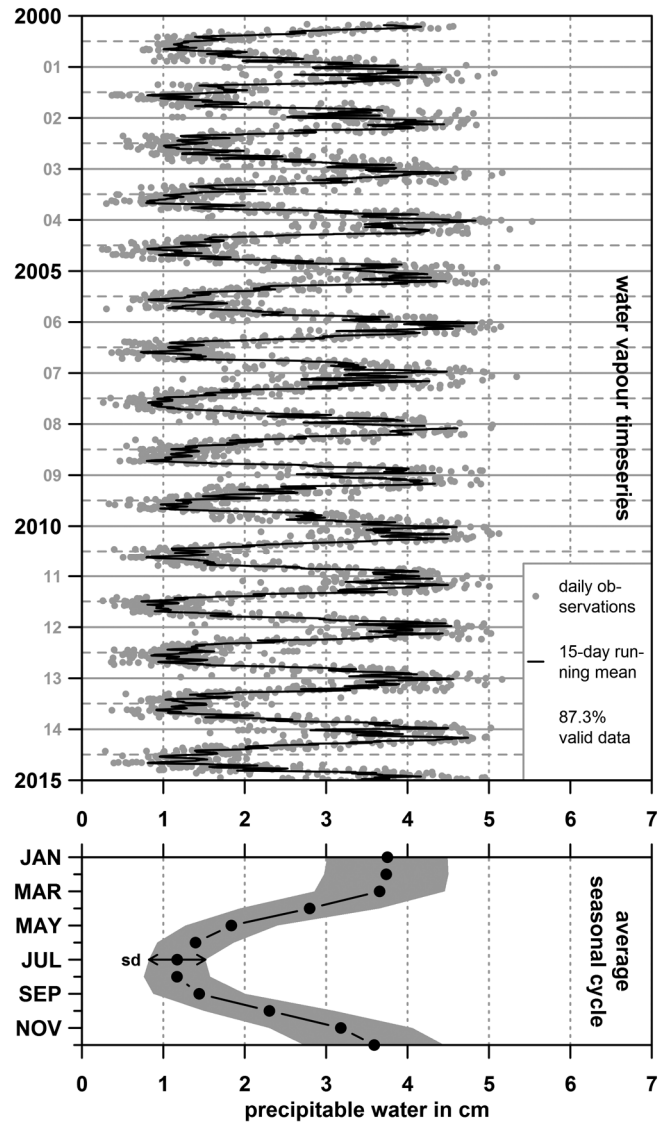


Fig. II-5. Visualization of the water vapor database for WRS-2 Path/Row 177/072 (19.71°E, 17.35°S). Top: daily values and 15-day running mean; bottom: average seasonal cycle and standard deviation on monthly basis.

is replaced by an average seasonal proxy derived from a statistical analysis of the complete MODIS water vapor data sequence – if necessary. This fallback climatology was used in 100% of all cases before 2000, 25.3% in 2000, 2.2% in 2001, 2.8% in 2002 and less than 0.4% thereafter, which reflects the phased commissioning of the Terra and Aqua platforms. Exemplary water vapor data are plotted in Fig. II-5 for WRS-2 Path/Row 177/072 with daily values in the top panel and the fallback climatology below. Water vapor follows a seasonal cycle with low values in the dry season and high values in the wet season. The standard deviation is higher in the wet season, which could indicate that the error in using the fallback values is smaller during the dry season during which Landsat data availability is higher. In order to document the usability of this approach across the study area, we

appended additional examples in the supplemental material section of this article. We chose the Landsat frames with the highest monthly average and standard deviation. The seasonal and annual variability is higher in the latter example (compared to Fig. II-5), but a seasonal pattern is evident nonetheless. In addition, we provide maps of the fallback climatology (as shown in Fig. II-5 bottom for one frame) for complete sub-equatorial Africa in the supplemental material section.

b) Aerosol optical depth

(1) Radiative Transfer Theory

All remaining unknown parameters in eq. II-1 can be derived from aerosol optical depth  $\tau_a$  (Hill and Sturm 1991, Hill 1993), by either using the single scattering approximation (Gordon 1981) or by also considering multiple scattering processes (Sobolev 1975). Equations II-6–II-19 provide the derivation of these atmospheric scattering terms from  $\tau_a$  using the multiple scattering approach (refer to Hill and Sturm (1991) for the simpler single scattering approximation). The practical estimation of  $\tau_a$  is outlined in the next chapters (2–4).

The path reflectance  $\rho_p$  is defined by an exact treatment of first order scattering and an approximate solution for higher order scatterings:

$$\rho_p = A_{pl} + [3(1 + g)\mu_v\mu_s - 2(\mu_v + \mu_s) + P] \cdot [1 - \exp(\tau/\mu_v - \tau/\mu_s)]/[4(\mu_v + \mu_s)]. \quad (\text{II-6})$$

The plane albedo  $A_{pl}$  is given (Irvine 1975) by:

$$A_{pl} = 1 - \frac{R(\mu_v) \cdot R(\mu_s)}{4 + 3(1 - g)\tau} \quad (\text{II-7})$$

where the reflectance functions  $R(\mu_s)$  (replace  $\mu_s$  with  $\mu_v$  to obtain  $R(\mu_v)$ ) are given (Irvine 1975) by:

$$R(\mu_s) = 1 + 3\frac{\mu_s}{2} + \left[1 - 3\frac{\mu_s}{2}\right] \cdot \exp(-\tau/\mu_s) \quad (\text{II-8})$$

with the asymmetry factor (Aranuvachapun 1986)

$$g = [\alpha \cdot (g_1 + g_2) - g_2] \cdot \tau_a/\tau. \quad (\text{II-9})$$

The total optical depth

$$\tau = \tau_a + \tau_r \quad (\text{II-10})$$

is the sum of  $\tau_a$  and the molecular optical depth  $\tau_r$  for a standard Rayleigh atmosphere (Guzzi *et al.* 1987):

$$\tau_r = 0.0088 \cdot \lambda^{-4.15+0.2\lambda}. \quad (\text{II-11})$$

The total phase function

$$P = P_a \cdot \tau_a / \tau + P_r \cdot \tau_r / \tau \quad (\text{II-12})$$

for the backscattering angle

$$\psi_- = \cos^{-1}\{-\mu_v \mu_s - [(1 - \mu_v^2)(1 - \mu_s^2)]^{0.5} \cos(\phi_v - \phi_s)\} \quad (\text{II-13})$$

is obtained from the phase functions for molecular (Bucholtz 1995)

$$P_r = 0.75 \cdot (1 + \cos^2 \psi_-) \quad (\text{II-14})$$

and aerosol scattering  $P_a$ . The aerosol scattering equation is approximated by a two-term Henyey-Greenstein (TTHG) function with  $g_1 = 0.836$ ,  $g_2 = 0.537$  and  $\alpha = 0.968$ , representing a continental aerosol model (Aranuvachapun 1986):

$$P_a = \frac{(1 - g_1^2) \cdot \alpha}{[1 + g_1^2 - 2g_1 \cos \psi_-]^{1.5}} + \frac{(1 - g_2^2) \cdot (1 - \alpha)}{[1 + g_2^2 + 2g_2 \cos \psi_-]^{1.5}} \quad (\text{II-15})$$

The down-welling total scattering transmittance

$$T(\mu_s) = \exp(-(0.52\tau_r + 0.167\tau_a)/\mu_s), \quad (\text{II-16})$$

the direct portion

$$t_d(\mu_s) = \exp(-\tau/\mu_s), \quad (\text{II-17})$$

and the scattered portion

$$t_s(\mu_s) = T(\mu_s) - t_d(\mu_s) \quad (\text{II-18})$$

are readily computed (the up-welling terms are retrieved by replacing  $\mu_s$  with  $\mu_v$ ). The spherical albedo  $s$ , viewed from the ground, is given by:

$$s = \exp(-(\tau_r + \tau_a)) \cdot (0.92\tau_r + 0.333\tau_a). \quad (\text{II-19})$$

Thus, solving eq. II-1 only requires a robust estimation of  $\tau_a$ , which – in the absence of measurements – is commonly derived from the image itself with dark target techniques, assuming that candidate objects exist in every image (e.g. Hill and Sturm 1991).

### (2) Dark Object Database

For the practical implementation of this concept, we utilize a partially image-based approach by using a pre-compiled Dark Object Database (DODB). The DODB is created from the complete data series of each pixel and guarantees that the dark objects (DOs) are estimated from the same pixels for all bands and that preferably the temporally more persistent ones are used for estimating  $\tau_a$ . This prevents that temporary dark objects (like flood water, burned areas or cloud shadows) are used in some images while completely different DOs are used in other images that do not contain such objects.

The generation of the DODB is a prerequisite for our preprocessing algorithm, thus we based the generation of the DODB on an analysis of the DNs of every available image. DOs are identified in each image by using the red and near infrared band histograms (see next paragraph). After all the individual images are analyzed, the dark object persistency DOP (with  $DOP = [0,100]$ , i.e. the percentage of the time a pixel is dark) is derived for each pixel in the study area. In order to account for potential land cover change during the past 30+ years, we compiled 3 decadal databases, i.e. [1984,1995], [1996,2005] and [2006,2015]. The DODB is designed such that newly acquired data can be simply integrated into the database by updating the DOP score. Fig. II-6 displays a subset of the DOP, as well as two examples of Landsat false color images for an area that is characterized by varying water levels (more water during the late wet season, middle) and the presence of burn scars (more likely during the course of the dry season, bottom). The use of the most persistent DOs effectively prevents the usage of the transient dark features, in this case the flood plains and the burned areas, which were also marked as DO in some images (b/w tones in the top panel).

We identify DOs in the red and near infrared bands for each processed image. The NIR band is utilized because of (i) the decreasing scattering effect at longer wavelengths (Luo *et al.* 2008) which increases the darkening effect of shadowed pixels (Zhu and Woodcock 2012) and because (ii) most surface features are bright and thus maximize the contrast to shadowed areas (Zhu and Woodcock 2012). The red band is used to reject highly turbid water bodies. For both bands, the DOs are retrieved from the lower bounds of the band histograms.

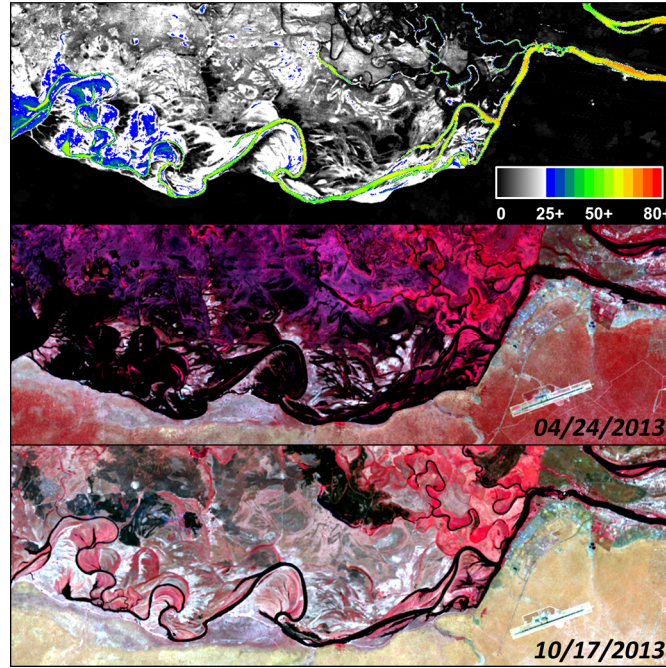


Fig. II-6. Visualization of a section of the dark object database and two example images (25.06°E, 17.79°S). Top: Dark object persistency; middle: false-color image of a late wet-season image; bottom: false-color image of a dry-season image. The same stretch was applied to both images with R/G/B = NIR/red/green.

### (3) Image-based estimation of AOD

Based on the persistent DOs, we employ an object-based approach where it is attempted to derive  $\tau_a$  for each non-transient dark object on a physically sound basis, implicitly including the adjacency effect. During the actual radiometric processing, the DOP is available to the algorithm and is used in combination with the  $\rho^*$  image under consideration. We only use pixels with consecutively decreasing  $\rho^*$  for all bands, which represents an important property of an ideal DO as it should follow a  $\lambda^{-x}$  relation (Chavez 1988). Objects with less than 10 valid pixels or that are in close proximity to clouds (<10 px) are discarded. The object reflectance  $\rho_o^*$ , environment reflection  $\rho_e^*$  and target radius  $r$  are directly inferred from the image, the target altitude is considered by adjusting  $\tau_r$  (Guzzi *et al.* 1987) and the objects are separated into water and topographic shadow targets based on the illumination situation. If  $\rho_e^*$  is smaller than  $\rho_o^*$ , the object is rejected.

Our approach builds on the method of Royer *et al.* (1988), where  $\rho_o^*$  is matched with the spectral reference reflectance  $\rho_s^*$  of a typical dark object. In case of water, the surface reference reflectance is given by:

$$\rho_s = \rho_w + \rho_f t_s(\mu_s)/T(\mu_s), \quad (\text{II-20})$$

with  $\rho_w$  being the volumic water reflectance that is obtained from a spectral reference library (see below). The Fresnel surface specular reflectance  $\rho_f$  is computed as a function of the incidence angle  $i$  (Kay *et al.* 2009), assuming that water surfaces are flat. Aerosol optical depth is determined in a bandwise iterative procedure by gradually adding atmospheric scattering to  $\rho_s$ , thus simulating the reference reflectance  $\rho_s^*$  as it would be sensed at the top of the atmosphere (solve eq. II-1 for  $\rho^*$  with  $A = 1$  while increasing  $\tau_a$ , starting with a pure Rayleigh atmosphere, i.e.  $\tau_a = 0$ ). This process terminates once  $\rho_s^*$  and  $\rho_o^*$  match; see Royer *et al.* (1988) for a detailed description. In the case of cast shadow, we use a modified version of this approach where  $\rho_f$  is ignored but the topographic correction factor  $A$  (see topographic correction) is included in order to model the shaded  $\rho_s^*$ . The procedure is outlined in Fig. II-4 in simplified form.

In order to (i) obtain a more physically coherent set of the wavelength dependent  $\tau_a$ , (ii) reduce measurement dependent variations (Hill 1993) and (iii) to have an instrument for gauging the quality of the estimation, i.e.  $R^2$  (Royer *et al.* 1988), we perform a logarithmic regression between  $\tau_a$  and  $\lambda$ . A second-order polynomial fit is employed:

$$\ln \tau_a = a_0 + a_1 \cdot \ln \lambda + a_2 \cdot (\ln \lambda)^2, \quad (\text{II-21})$$

which enables the modelling of the inherent  $\ln \tau_a$  curvature of biomass burning and desert dust aerosols as a consequence of accumulation mode dominating aerosol size distributions (Eck *et al.* 1999). If unsuccessful (e.g. if the Ångström exponent  $a_1 > 0$ ), the simpler linear Ångström relation (Ångström 1964) is tried in a second step, where the second order term in eq. II-21 is ignored ( $a_2 = 0$ ). If the fit to the Ångström equation is also unsuccessful (e.g. if  $a_1 > 0$ ), the object is rejected.

Due to the profound variability of naturally occurring water bodies / land surfaces, we pre-compiled spectral reference libraries (for a range of possible conditions) using spectral modelling software. The water color simulator WASI (Gege 2004) and the leaf optical properties + canopy bidirectional reflectance model PROSAIL (Jacquemoud *et al.* 2009) are used for the water and cast shadow targets, respectively. For each object, each reference spectrum  $\rho_s$  is tested and the corresponding  $\tau_a$  estimate that yields the best  $R^2$  in the logarithmic regression is retained; if the best  $R^2$  is smaller than 0.1, the object is rejected.

As dark targets are not abundantly available across the images in our study area (Frantz *et al.* 2015a), we compute a  $\tau_a$  scene average from all available targets, weighted by the  $R^2$  of the logarithmic regressions while considering the individual target altitudes (Guzzi *et al.* 1987). Once  $\tau_a$  is retrieved, the governing equation (eq. II-1) can be solved by computing all parameters as described in chapter (1) using eq. II-6–II-19. We introduce some scene fidelity by using coarsely gridded (333 px) sun-

target-view angle dependencies that allow the scattering equations to vary over the scene. In addition,  $\tau_a$  and  $\tau_r$  are adjusted for the pixel's altitude (Guzzi *et al.* 1987) in order to approximate the elevation dependency on the optical depths.

(4) *Fallback strategy*

The African savanna landscape is often bright (Kaufman and Sendra 1988) and a substantial number of Landsat footprints do not contain dark targets (all objects were rejected, see previous section) in which case we cannot retrieve  $\tau_a$  and consequently employ an alternative fallback strategy in a second step.

We implemented a backdoor-interface, where externally generated  $\tau_a$  values can be passed to the algorithm. In this case, the image-based estimation of  $\tau_a$  is skipped and the external values are used instead. We made use of this possibility for the images where we could not identify any valid dark target and re-processed these images with modelled  $\tau_a$  values. This applied to  $\sim 14\%$  of the images and especially occurred in the bright landscapes of southern Namibia and Botswana.

We used the  $\tau_a$  values of all the images where the above presented method worked well and modelled the climatic seasonal course of  $\tau_a$  with a dependence on geolocation: we used a multivariate regression model described by the geolocation and the acquisition day-of-years of the available  $\tau_a$  values to estimate a set of spatio-temporal  $\tau_a$  fallback values with a revisited version of Frantz *et al.* (2015a), i.e. direct modelling of  $\tau_a$  instead of  $\rho_p$ .

c) Topography correction

Topography correction is done by applying a modified C-correction (Kobayashi and Sanga-Ngoie 2008), which is a physically based correction of topography, amended by an empirically derived extra parameter  $C$  (Hantson and Chuvieco 2011). The topographic correction factor in eq. II-1 is determined for every image, band and pixel:

$$A = (\cos \theta_s + C \cdot h_0^{-1}) / (\cos i + C \cdot h_0^{-1} h). \quad (\text{II-22})$$

The illumination angle  $\cos i$  is computed (Smith 1980) by:

$$\cos i = \cos \theta_s \cos \theta_n + \sin \theta_s \sin \theta_n \cos(\phi_s - \phi_n). \quad (\text{II-23})$$

The topographic slope  $\theta_n$  and aspect  $\phi_n$  are computed with the Horn (1981) method from the DEM that was warped to the extent and resolution of the Landsat image under consideration. The

$h$ -factor describes the portion of the sky dome which contributes to the diffuse illumination, where  $h_0$  is the  $h$ -factor at  $\cos i = 0$  (Kobayashi and Sanga-Ngoie 2008). The  $C$ -factor is estimated from a linear regression between  $\cos i$  and the spectral radiance from an inclined surface  $L^*$ . The empirically-derived  $C$ -factor is then the ratio of intercept  $b$  and slope  $m$ :

$$C = b/m. \quad (\text{II-24})$$

The main focus of attention in computing the  $A$ -factor is to derive this  $C$ -factor. Because of the image-based nature of this correction, we were in need to incorporate several stabilizing constraints in order to estimate the  $C$ -factor in a robust manner for preferably all images:

- The results of the  $C$ -correction can be improved if the  $C$ -factor is not derived for the entire Landsat image, but separately for different land cover classes (Kobayashi and Sanga-Ngoie 2008). Thus we split the image pixels into two classes based on an arbitrary Normalized Differenced Vegetation Index (NDVI) threshold of 0.4 (Hantson and Chuvieco 2011).
- If there is no equal abundancy of differently illuminated pixels, the regression-based correction often fails to be representative for all topography classes and results in significant under/overcorrection. Hantson and Chuvieco (2011) used a threshold of  $2^\circ$  slope angle for excluding rather flat pixels. We found that this method worked in many cases, but depending on image-content, this constraint is often not sufficient for Landsat frames with unequally mixed and complex terrain. In our operational setting, we found it very effective to also stratify the image with  $5^\circ$  slope classes. Thus, we estimate the  $C$ -factor for each land cover and slope class separately.
- If the coefficient of determination  $R^2$  is less than 1% in a given class, we assume that the  $C$ -correction did not perform well and we fall back on a simple Minnaert Correction (Teillet *et al.* 1982) with a fixed Minnaert coefficient of 0.8. This simplifies the  $A$ -factor to

$$A = (\cos \theta_s / \cos i)^{0.8}. \quad (\text{II-25})$$

The relationship between  $L^*$  and  $\cos i$  is in general not very high; Kobayashi and Sanga-Ngoie (2008) reported  $R^2$  values between 5% and 30% for the different bands of their testing image. Such high  $R^2$  values are not always given if the image is not entirely mountainous, thus we set the threshold to 1% to test if there is at least any evidence of a relation. The class-dependent topographic correction approach implies that one image may be corrected with different methods, giving precedence to the more advanced  $C$ -correction as it commonly comes off as winner in comparative topographic studies (e.g. Hantson and Chuvieco 2011).



## 4.4 Reprojection and Gridding

Once the Landsat data are radiometrically corrected, they are reprojected into the output coordinate system using bilinear resampling and second order polynomial warping. For our study data, we chose a Lambert Azimuthal Equal Area (LAEA) projection with its origin in the centroid of Southern Africa. After reprojection, the data are organized in smaller arbitrary tiles. Therefore, a grid in the target projection is created. The grid originates at a custom point  $O_{grid}$  and a new tile is created each  $n_{grid}$  pixels. For our study area, we chose the arbitrary grid to origin at  $O_{grid} = 0^{\circ}/0^{\circ}$  in Lat/Lon and  $n_{grid}$  was chosen to be 1000 px in the LAEA projection. In order to avoid confusion about nomenclature, we hereby define the term

- 'grid' as an arbitrary sub-division with square units in the target coordinate system,
- 'tile' as an entity of the grid with a unique tile identifier, e.g. X0003\_Y0002 and
- 'chip' as the individual gridded images that are affiliated with the tile.

The disintegration of the classical Landsat WRS-2 data structure into a new, gridded tile representation has several benefits: (1) easy and rapid pixel based data access, (2) simple co-registration among images – regardless of their initial path and row designation, and thus (3) exploiting the full depth of the Landsat archive, as well as (4) easier ordering of data for study areas that commonly match imperfectly with WRS-2 frames.

## 5 Results

### 5.1 Processing stats

We processed 58,731 Landsat images of 194 WRS-2 frames with the presented method. 41,762 images were fully processed; 16,876 images were terminated in an early stage because the cloud contamination exceeded the maximum allowable cloud cover threshold and 90 images were so far not processed because of a recent failure in the Thermal Infrared Sensor (TIRS) calibration. The processed images were partitioned into 4,524 tiles and 1,912,733 chips, resulting in a total data volume of 27.86 TB. The core processing was finished in less than 4 days on a moderately sized processing cluster (2 nodes à 56 CPUs). Fig. II-7 displays the number of processed chips per tile. The data availability – corrected for redundant data – is highest in the overlap region between two orbits.

## 5.2 Spectral consistency in overlap regions

Our gridded data structure enables us to analyze the spectral consistency within three types of overlapping image regions:

- LPGS generates redundant data in the overlap region of adjacent WRS-2 frames that were captured in the same orbit. Thus, any difference in this redundant overlap should be caused exclusively by the implemented processing chain and enables the exploration of the inherent systematic errors/uncertainties.
- The revisit overlaps between two adjacent orbits, are captured 7 days apart by the same Landsat system. The data might vary somehow due to different atmospheric situations and oppositional viewing directions, which we assume to have the greatest impact. In addition, rapid phenology processes, as well as process-based change like changing water levels, burned areas or active fires might add to the difference.
- The observation frequency reduces to 1 day in the cross-sensor overlaps if data from several sensors are considered, though the viewing aspect angle is still substantially different. A comparison between the 1 day and 7 day differences might be useful to differentiate between the cross-sensor uncertainties and differences that are caused by surface processes.

The assessment is based on an exhaustive analysis of all overlapping chips. The spectral consistency for every chip pair was assessed by the spectral RMSE of the 6 reflective bands  $b$ , averaged over all overlapping pixels  $p$  (eq. II-26). In order to avoid situations with unlike atmospheric conditions, we omitted pixels that are located within a 10 km radius from clouds or cloud shadows.

$$meanRMSE = \frac{1}{n} \sum_{p=1}^n \sqrt{\frac{1}{6} \sum_{b=1}^6 [chip1_{p,b} - chip2_{p,b}]^2}. \quad (II-26)$$

Fig. II-8 displays histograms of this assessment for the three overlap types. Quantiles are drawn in colors. The differences in the redundant overlaps are smallest: the mean of the revisit (cross-sensor) overlaps is 0.70% (0.84%) larger than in the redundant overlaps. The error in the cross-sensor overlaps is usually larger than in the revisit overlaps (0.14% difference in the mean), though the 99% quantile is slightly smaller. The expected accuracy of the full radiometric processing chain is in the order of  $\pm 2.5\%$  reflectance (Röder *et al.* 2005). 98.8% of all redundant chip pairs are within this range. Considering the orbital overlaps, still 92.8% (91.0%) of the revisit (cross-sensor) chip pairs are enclosed.

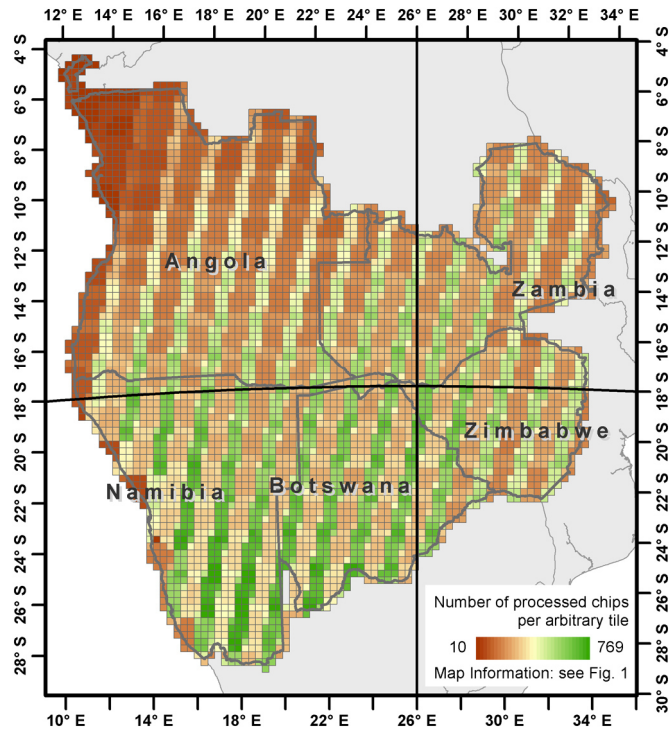


Fig. II-7. Number of processed chips per arbitrary tile, corrected for redundant overlaps.

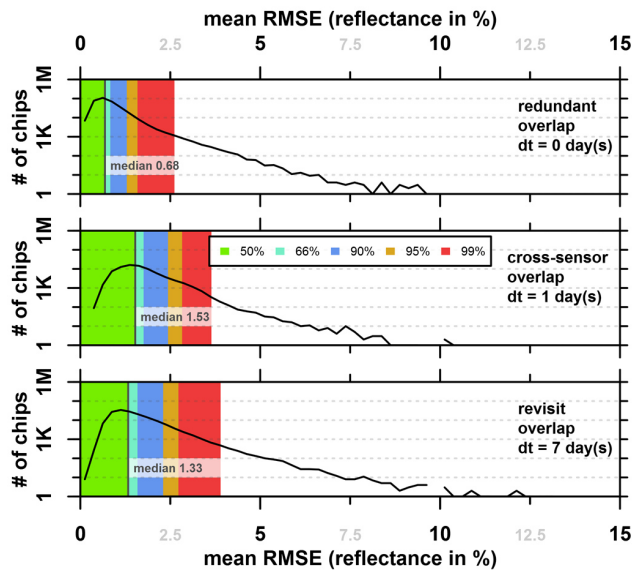


Fig. II-8. Histograms of the spectral consistency assessment of overlapping chip pairs. The histogram bin width was set to 0.25% reflectance. The y-axis is drawn logarithmic. Quantiles are drawn in colors.

### 5.3 Aerosol optical depth

Sunphotometer data from the Aerosol Robotic Network (AERONET, Holben *et al.* 1998) are commonly considered the most accurate terrestrial  $\tau_a$  measurements, and as such, we derived Landsat equivalent  $\tau_a$  from all available AERONET data in our study area with eq. II-21. The relationship ( $R^2$ ) between the satellite-based and the coinciding ground-measured  $\tau_a$  is between 0.72 and 0.79 for all bands (see Fig. II-9), intercepts are in the order of 0.02–0.03 and the relationship is very close to the 1-to-1 line. The colors represent different AERONET sites (blue colors: Zambia, red colors: Namibia, green colors: Botswana, no stations for the remaining countries) and the point sizes indicate the mean DOP of the dark targets. The majority of the observations is from the two Mongu sites (23.15°E, 15.25°S) which are drawn as rectangles.

The fallback surface, i.e. the spatio-temporal aerosol climatology was modelled from all available  $\tau_a$  estimates across the whole study area; see Frantz *et al.* (2015a) for details. Regarding the quality of the aerosol climatology, Frantz *et al.* (2015a) found that the modelled seasonal aerosol cycle matches well with an average seasonal cycle derived from the AERONET Mongu station. An updated assessment of this relationship is included in the supplemental material section of this article with  $R^2$  between 0.81 and 0.84 for all bands.

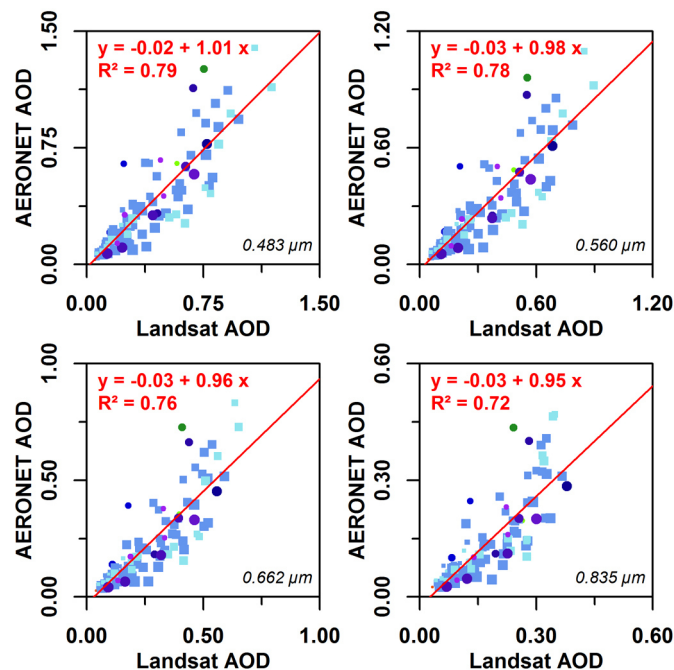


Fig. II-9. Linear regression between image-based Landsat and terrestrial AERONET AOD measurements for all stations and all coinciding observations. The colors represent different AERONET sites; blue to purple: Zambia, red/orange: Namibia, green: Botswana. The majority of the data is from the Mongu sites, Zambia.

## 5.4 Uncertainty in climatic water vapor database

If daily water vapor values are not available, we rely on a fallback climatology. In order to better understand the potential error and document the uncertainty in using this method, we simulated the potential effect of varying water vapor concentrations. The effect of water vapor absorption is albedo-dependent. Therefore, we picked a Landsat frame which includes both bright and dark surface elements. The Etosha pan is a large salt pan without drainage. The pan is normally very bright but it can be partially flooded after heavy rain and the water can be retained during the course of the dry season. The analysis is based on Landsat 5 data since the TM is the most water vapor impacted Landsat sensor because of its spectral configuration. We chose two cloud-free images that captured a partially flooded pan, one in the dry (08/10/2008) and one in the late wet season (03/22/2009).

We corrected each image with the retrieved daily water vapor values (DV) and with the corresponding climatic average (CA) which would be used in case the daily value would not be available. In addition, we also increased and decreased the climatic average by one and two standard

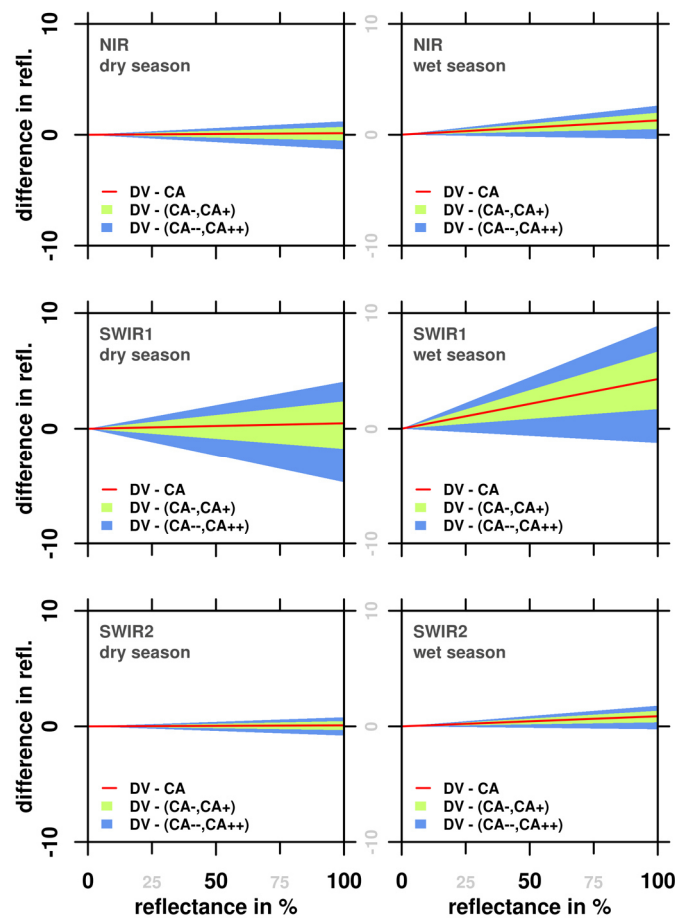


Fig. II-10. Potential errors in using climatically derived water vapor estimates instead of daily values. The analysis was performed with two dry/wet season TM images of the Etosha Pan. Both images were corrected with different water vapor values (Table II-3). The figure displays the difference in surface reflectance (in %) between the correction with day-specific values and the correction with climatically derived variants.

Table II-3. Precipitable water values

<b>Water vapor variant</b>	<b>Abbr.</b>	<b>Dry season 08/10/2008</b>	<b>Wet season 03/22/2009</b>
<i>Daily value</i>	<i>DV</i>	1.02	2.32
Climatic average - 2 sd	CA--	0.29	1.96
Climatic average - 1 sd	CA-	0.70	2.85
Climatic average	CA	1.12	3.74
Climatic average + 1sd	CA+	1.53	4.63
Climatic average + 2sd	CA++	1.95	5.52

Precipitable water value variants (in cm) used for simulating the effect of climatic averages on the corrected reflectance of different land surface types.

deviations (see Table II-3). We base our analysis on the resulting difference in surface reflectance between the DV and the climatic variants, see Fig. II-10. The impact of water vapor is small on the NIR and SWIR2 bands but clearly evident in the SWIR1 band; the VIS bands are hardly affected and thus not displayed here. The effect is more pronounced for very bright surfaces. The daily water vapor estimate of the dry season image is very similar to the climate average, whereas the daily estimate in the wet season is approximately 1.5 standard deviations smaller than the climate average. Thus, the corrected reflectance differs by 0.53% (4.8%) between the DV and CA for the dry (wet) season image for extremely bright features (100% reflectance). The effect is less pronounced for grey objects (50% reflectance): 0.29% (2.6%) difference. For the SWIR1 wet season images, the difference in corrected reflectance between the CA+ (CA++) and the CA- (CA--) variants is approximately 3% (6.2%) for grey objects. In the dry season, the differences are 2.6% and 5.6%, respectively, thus the uncertainty in the wet season is slightly higher.

## 5.5 Topographic correction

Fig. II-11 illustrates the implemented topographic correction for an illustrative sample area. The depicted images were captured over the mountainous Huila province (southern Angola) in the middle of June (winter solstice) under low illumination conditions (sun elevation: 41°). The elevation ranges between 534 m and 1532 m. Topographic effects were substantially reduced and the corrected image appears to be rather flat.

Fig. II-12 demonstrates the effectiveness of the topographic correction by averaging the NIR reflectance (separately for both land cover classes) with dependence on the topographic aspect. The illumination direction (sun azimuth: 37°) is clearly visible in the uncorrected image (red), whereas the effect is substantially reduced in case of the C-correction (green). In order to show the advantage of our method over the simpler fallback option, we also corrected this image with the Minnaert correction (blue), which has a tendency for overcorrection.

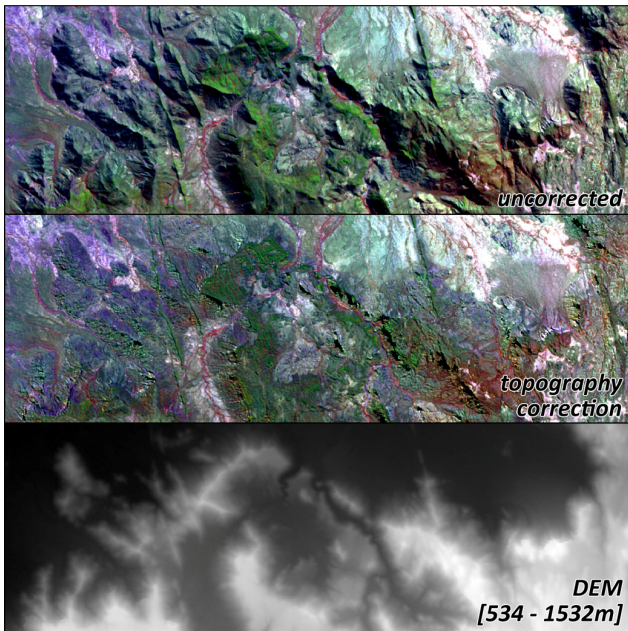


Fig. II-11. Illustration of the topography correction for a mountainous Landsat-8 image in Huila, Angola (13.39°E, 15.86°S; 1000 m elevation range) under low illumination conditions (sun elevation: 41°, azimuth: 37°). Top: no topography correction; middle: topographically corrected; bottom: digital elevation model. The same stretch was applied to both images with R/G/B = NIR/SWIR1/red.

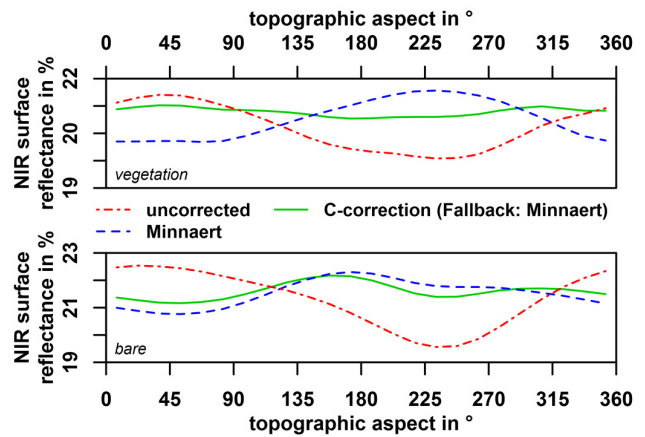


Fig. II-12. Average aspect-dependent NIR reflectance for the image (full frame) shown in Fig. II-11 for the vegetated (top) and bare (bottom) classes. The image was processed with the implemented C-Correction (green), the Minnaert correction (blue) and with disabled topography correction (red). Flat curves point to a successful topographic normalization.

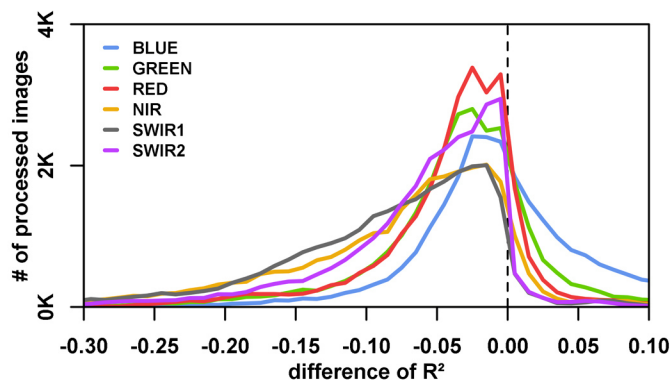


Fig. II-13. Topographic correction evaluation. The histogram bin width was set to 0.01  $R^2$ . The correction was quantitatively evaluated by differencing the  $R^2$  of the relationship between  $\cos i$  and  $L$ , before and after the radiometric correction. A decrease in  $R^2$  points to a reduction of topographic effects.

The topographic correction was quantitatively evaluated by comparing the  $R^2$  of the relationship between  $\cos i$  and  $L$ , before and after the radiometric correction. Fig. II-13 displays histograms of the difference in  $R^2$ . All images with more than 10% of sloped terrain ( $> 5^\circ$ ) were used to derive the histograms. The  $R^2$  usually decreases after the correction. The strength of the decrease is

different for the six spectral bands. The  $R^2$  of the blue band occasionally increases after the correction and the decrease is more apparent in the infrared bands.

## 6 Discussion

### 6.1 Dataset consistency

We mainly based the quantitative assessment of the dataset on an exhaustive analysis of all overlapping chip pairs which enables us to gauge the processing consistency. The differences between processed redundant data are attributed to our processing chain. These differences are usually very small and 98.8% of all overlaps were within the expected 2.5% algorithm accuracy (Röder *et al.* 2005); 99.4% differ by less than 3%. The differences between the chips are likely to be caused by the image based methods, where different image content can cause different AOD retrievals. As such, we conclude that the AOD estimation strategy worked reasonably well (see also next chapter) and we expect our processing chain to be of sufficient quality for any following pixel-based compositing or time series analysis application.

The revisit and cross-sensor overlaps are captured on different dates and inhibit different orbital characteristics, different atmospheric states and potentially also land surface change. We presume that opposite view angles have the greatest impact since we do not correct for BRDF. The differences are indeed greater than in the redundant overlaps. Therefore, we assume that the part of the BRDF, attributed solely to the different viewing geometry (which we partially account for by considering the varying sun-target-view geometry in the atmospheric scattering terms), is in the dimension of this difference, i.e.  $< \sim 1\%$  reflectance. As the sun geometry does not change significantly during this time period, we are not able to assess the actual combined effect of BRDF with the performed overlap analysis, though the impact on our dataset is likely to be significantly larger as recently documented by Nagol *et al.* (2015). Accounting for BRDF effects is complex and not yet a standard correction for Landsat data. An optimal BRDF correction would estimate pixel-based bidirectional parameters by using many observations within a short time period (Schaaf *et al.* 2002) – an approach which is not applicable to Landsat data alone (Flood *et al.* 2013). In addition, the parameter estimation with high temporal and coarse spatial resolution data is also problematic in arid areas during the wet season (Huete *et al.* 2002). Thus, the transfer from MODIS-based bidirectional parameters to Landsat data (e.g. Roy *et al.* 2008) is also restricted in such environments due to the insufficient angular sampling in parts of the year. One notable and promising approach is to infer a globally applicable set of bidirectional parameters by implementing a sampling design, where pixels from a broad range of differently sloped and illuminated pixels in the Landsat orbital overlaps and in



different land cover classes are selected (Flood *et al.* 2013). Nevertheless, a-priori knowledge about the land cover, a confident guess about the spectral stability over time and sufficient input data is needed – demands that are still not met everywhere.

Based on a comparison of the two orbit overlap variants, we might be able to differentiate between the cross-sensor introduced error and changes that are attributed to surface change processes (e.g. green flush events, fire or flooding), because the probability of surface change is higher in the revisit case. In general, the cross-sensor overlap differences were larger than the ones in the revisit overlaps. Thus, we conclude that surface change has less impact than cross-sensor calibration errors on average. As an exception to this, the 99% quantile was larger in the revisit overlaps, which could point to surface change. This implies that surface change happens rarely (within 7 days), but if it does, it has a large impact on the differences of overlapping data. The cross-sensor errors might be amplified by the slightly different spectral configuration of the OLI sensor – compared to the TM and ETM+. Flood (2014) recently found that the error in surface reflectance is around 2%, which also partially conforms to our results. The mean cross-sensor error is 1.64%, though the errors between overlapping Landsat 7 and Landsat 5 (1.67%) / Landsat 8 (1.60%) chips do not differ significantly in our case and the OLI-to-ETM+ error is even slightly smaller than the TM-to-ETM+ error. This might be due to the improved radiometric characterization of the OLI sensor, compared to the TM, or presumably another yet unexplored factor.

## 6.2 Aerosol optical depth

The estimation of AOD in bright landscapes is a difficult task and the absence of dark objects on a large scale might preclude the usage of image based assessments (Gillingham *et al.* 2011). Flood *et al.* (2013) mitigated this problem by using a fixed AOD for eastern Australia. Whilst this is a sound strategy if the AOD is expected to be rather low, errors are inevitably included if the actual aerosol content is high (Gillingham *et al.* 2012). The AOD in Southern Africa is particularly variable (Frantz *et al.* 2015a) due to the accumulation (washout) of aerosols during the dry burning (wet rain) season (Eck *et al.* 2001) and regularly assumes large values (see Fig. II-9). Therefore, we developed a method where the image-based dark object retrievals were amended by temporal information on the persistency of dark objects. This approach supports the use of the temporally more persistent dark objects, which helped to increase the quality of the AOD retrievals in an environment where few dark objects exist. Transient dark objects like burned areas were thus successfully rejected.

We used AERONET data to gauge the quality of our AOD estimation strategy. Unfortunately, few AERONET sites exist in the study area; the majority of the stations is confined to Zambia, there

also exist three (two) stations in Namibia (Botswana) but no station in Angola and Zimbabwe. In addition, most of the stations also have very few high quality Level 2 data. Most of the data is constrained to the two sites in Mongu, Zambia. Fortunately, this location is relatively central in the study area.

It was shown that our physically-based AOD estimation on basis of radiative transfer theory is in very good agreement with available AERONET data (Fig. II-9):  $R^2$  range between 0.72 and 0.79, intercepts are low and slopes are near unity. Despite being mainly driven by the Mongu observations (square signatures), the few observations from the other stations (point signatures) also fit reasonably well (Fig. II-9). We therefore expect that the calibrated AOD retrievals are reasonably accurate in areas with similar climate and landscape composition as the sites with AERONET coverage, which are especially the wooded and forested regions in Angola and Zambia. It cannot be ruled out that the errors in the more arid ecosystems are larger and there is still a considerable amount of images (14%) where this strategy did not work due to the high albedo and dryness of savannas and deserts. We reasonably accounted for this with the fallback strategy by using modelled values (Frantz *et al.* 2015a). We consider these values as an acceptable guess for the actual AOD in a spatially and temporally explicit manner (see (Frantz *et al.* 2015a) and the supplemental material of this article).

Due to the above mentioned difficulties and environmental constraints, we recognize that AOD might still be one of the major uncertainties regarding the quality of our dataset. Nevertheless, we assume the AOD estimations and the AOD climatology to be sufficiently precise to give a reasonable characterization of atmospheric scattering in this highly variable ecosystem.

### 6.3 Water vapor

It was shown that the effect of water vapor is small in all but the SWIR1 bands. The TM is the most impacted sensor regarding water vapor because the SWIR1 band is substantially influenced by water vapor absorption. The OLI sensor in turn is hardly affected by water vapor absorption because the SWIR1 band was substantially reduced and was moved well away from the absorption band. It was shown that the difference in using a climatically derived water vapor value was approximately 2.6% reflectance for grey wet season objects if the daily value is approximately 1.5 standard deviations smaller than the climatology. It was also shown that the uncertainty in using the climatology fallback values is slightly higher in the wet season. The corrected reflectance of grey objects in the dry season differed by approximately 2.6% (5.6%) when considering the 1 (2) standard deviation range from the average. The 2 standard deviation range is only slightly higher than the range of the expected overall algorithm accuracy of  $\pm 2.5\%$  (Röder *et al.* 2005). Therefore we consider it important to derive as

precise as possible water vapor loadings for the current state of the atmosphere; but if not available, the use of a climatologic seasonal cycle is a tolerable fallback strategy with a reasonable uncertainty. It might be worth the effort to improve on the water vapor database, e.g. by filling the pre-MODIS era with NOAA AVHRR derived water vapor estimates (e.g. Sobrino *et al.* 1999), which would e.g. decrease the risk that inappropriate values would be used in significantly wetter, drier, hotter or colder years. Yet, this strategy would necessitate a thorough examination of the different methods and sensors with regards to the continuity of the estimated values and was not yet implemented. In any case, the presence of a clear seasonality in water vapor should be verified for other study areas before using this fallback strategy.

## 6.4 Topographic correction

It was shown that the topographic correction caused a decrease in the correlation strength between  $\cos i$  and  $L$  in most cases, suggesting that topographic effects are substantially reduced (Hill *et al.* 1995). This effect was more pronounced in the NIR and SWIR bands due to the stronger darkening effect of topographic shadow in the longer wavelength bands (Luo *et al.* 2008), where the removal of this effect has a greater impact. Contrary, the blue band was occasionally affected by an increase in the correlation strength. The blue band is not the best estimator of assessing the topographic effect, because thick haze can completely impede a relationship between  $\cos i$  and  $L$ . As such, we tend to not overvalue the  $R^2$  increases in the blue band. Random manual investigation points to a successful topographic normalization, which is also supported by the presented example. In addition, it was shown that the implemented topographic correction performed better than the Minnaert fallback option. Cosine-based corrections tend to overcorrect areas under low illumination conditions (Meyer *et al.* 1993) and the Minnaert factor's purpose is simply to dampen the correction strength. One way to optimize the Minnaert value would be to estimate it via a linear regression (Meyer *et al.* 1993) as it is the case for the C-correction. Nevertheless, as the Minnaert correction is the fallback option in the case that the regression-based C-correction did not work, estimating the Minnaert factor would also not work, and as such, a fixed correction factor is required for this purpose.

## 7 Outlook and Conclusion

In a future version of our algorithm, we consider to expand on the radiometric correction module. Further atmospheric gases like ozone or uniformly mixed gases are to be included and we also consider to provide a more spatially explicit treatment of AOD by interpolating between the dark objects as done by Masek *et al.* (2006). Nevertheless, these strategies will only work if there are plenty of dark objects, which is a severe constraint in Southern Africa (Kaufman and Sendra 1988).

Therefore, the benefit of any further correction should be evaluated with regards (i) to the actual improvement in the corrected reflectance, (ii) to the extra cost in computing time, (iii) to the global applicability and (iv) to the global data availability that any new add-on would require.

The geometric correction of Landsat L1T data is commonly precise; Loveland and Dwyer (2012) report on a global geometric accuracy of ~50 m. Nevertheless, Southern African L1T data are occasionally poorly co-registered. In our current implementation, we do not account for this potential error source but an additional bulk-image registration module could be included in the processing chain.

We also intend to prepare and adapt our framework for new Landsat like systems like any upcoming Landsat 9+ spacecraft or the soon-to-be-available Sentinel-2 data. We consider our approach to be sufficiently transferable to similar medium-resolution data as we are already processing data from all available Landsat systems with the same algorithm, which is e.g. not employed in LEDAPS. The gridded data structure, the sensor-specific water vapor absorption coefficients and exo-atmospheric irradiances will facilitate the incorporation of other data, though specific adaptations will surely be necessary. For Sentinel-2 data, it will be mandatory to include a full BRDF treatment because of the larger swath width. Fortunately, the observing geometry and acquisition frequency of Sentinel-2, combined with Landsat, will also facilitate to obtain BRDF parameters from the data itself, which is very difficult with Landsat data alone.

As already highlighted by Hansen and Loveland (2012), the development of (i) higher level products, (ii) from multi-sensor data, (iii) provided in arbitrarily – but regularly – divided tiles is a key component in enabling end-users to make the best use of medium resolution data, both across space and time. Currently, these demands are not fully met. Landsat standard products lack systematic gridding; higher-level Sentinel-2 products are currently not planned; and Landsat legacy, Landsat 8 and Sentinel-2 data are not processed with the same algorithm. As such, we specifically developed our processing strategy to derive gridded surface reflectance and cloud/shadow products from multi-sensor data – potentially also Sentinel-2 or similar data in the near future. Gridded higher level products will significantly simplify the application of pixel-based algorithms and will also allow a broader range of end-users to perform such analyses. We chose sufficiently elaborate methods with as few as possible input data. As such, we presume that the presented processing framework may even generate consistent and high qualitative data in areas where the general data availability is still low, which we demonstrated for Southern Africa. As such, we preferred image-based solutions where applicable, e.g. for aerosol estimation and topographic correction and opted to not account for BRDF

effects until the general applicability to medium resolution data without any pre-knowledge of the study area has become more feasible.

## **Acknowledgment**

Landsat and SRTM data courtesy of the U.S. Geological Survey. The MODIS data used in this study were acquired as part of the NASA's Earth-Sun System Division and archived and distributed by the MODIS Adaptive Processing System (MODAPS). We thank all PIs and their staff for establishing and maintaining the AERONET sites used in this investigation. KAZA TFCA information and boundary courtesy of Peace Parks Foundation. The authors also thank the two anonymous reviewers whose very constructive comments significantly improved the quality of the final manuscript. This work was funded by the Federal Ministry of Education and Research under contract number FKZ-01LG1201C as part of the Southern African Science Service Centre for Climate Change and Adaptive Land Management project.



## **Chapter III**

### **Enhancing the Detectability of Clouds and Their Shadows in Multitemporal Dryland Landsat Imagery: Extending Fmask**

*IEEE Geoscience and Remote Sensing Letters 12 (6),  
June 2015, 1242–1246.*

DOI: 10.1109/LGRS.2015.2390673

David Frantz, Achim Röder, Thomas Udelhoven, and  
Michael Schmidt

© 2015 IEEE.

The following manuscript is a copy of the final version of the accepted manuscript. The paper has been through peer review, but it has not been subject to copy-editing, proofreading and formatting added by the publisher. The version-of-record can be accessed at:

<http://ieeexplore.ieee.org/document/7035005/>

**Abstract**

We developed a new two-step approach for automated masking of clouds and their shadows in Landsat imagery. The first step is comprised of detecting clouds and cloud shadows in every Landsat image independently by using the Fmask algorithm. We modified two features of the original Fmask: we dropped the termination criterion for shadow matching and we appended a darkness filter to counteract false-positives in bifidly structured dryland areas. The second step utilizes the scene-by-scene detections of the first step and additional time series of cloud and cloud shadow probabilities. All clear-sky observations of a pixel are used to estimate the probabilities' median and standard deviation. Any observation that deviates more than a multiple of the standard deviation from the median is considered an outlier and thus a remaining cloud or cloud shadow. The method was specifically designed for use in water-limited dryland areas, where event-based precipitation is predominant. As an effect, green vegetation peaks are highly variable, both in timing, magnitude and frequency with adverse effects on commonly used Fourier-based outlier detection methods. The method is designed to be robust even if temporally dense data coverage is not available.



## 1 Introduction

Landsat data are one of the most valuable resources for earth observation (Cohen and Goward 2004, Leimgruber *et al.* 2005), because of long term data continuity (Wulder *et al.* 2008), free data access (Woodcock *et al.* 2008) and their optimal resolution to monitor landscape processes (Danaher *et al.* 2010). However, a great proportion of all available Landsat images is obscured by clouds and their shadows, most predominantly in the tropics (Asner 2001).

The detection of clouds and their shadows is an inevitably required early step in any following image analysis application, because clouds adversely influence most analyses, among them atmospheric corrections, biophysical variables like the Normalized Difference Vegetation Index (NDVI, Tucker 1979) values and land cover classifications (Zhu and Woodcock 2012).

Clouds either reduce the amount of usable data if cloud contaminated scenes are simply discarded or they have to be detected and masked. Historically, the overall cloud contamination of a Landsat scene was estimated by the Automated Cloud Cover Assessment (ACCA) system (Irish 2000, Irish *et al.* 2006). In general, ACCA fails to delineate the exact location and boundaries of clouds and their shadows (Zhu and Woodcock 2012) with adverse effects on automated analyses. Therefore, manual cloud detection was often performed, which in turn limited the amount of usable data, because of time and cost limitations.

Fortunately, cloud and cloud shadow detection in Landsat imagery has matured in the previous years with the development of the Fmask algorithm (Zhu and Woodcock 2012). The accuracy of the Fmask results is reported to be good: Zhu and Woodcock (2012) reported an overall accuracy of 96.41%, cloud producer's accuracy of 92.1% and cloud user's accuracy of 89.4%. The producer's accuracy for shadows is more than 70% and the user's accuracy is more than 50%. They used 142 manually screened reference images, globally stratified over 9 latitudinal zones.

The Fmask algorithm applies one scene-specific probability threshold for all pixels in a scene (Zhu and Woodcock 2012). Cloud and cloud shadow masks can be further enhanced by applying time series based detection methods that make use of the scene-by-scene detections of Fmask. Besides other multi-temporal cloud detection approaches (e.g. Hagolle *et al.* 2010), Zhu *et al.* (2012) and Zhu and Woodcock (2014a) presented a subsequent time series analysis of TOA reflectance, developed in a rather humid study area in the northeastern United States. They fit series of sine and cosine functions to the remaining clear-sky observations for each pixel and detect outliers (i.e. missed clouds and cloud shadows) using the model residuals.

Unlike temperate areas, water-limited dryland areas are often comprised of evergreen woodlands, open forests and grasslands that do not follow a strict sinusoidal phenological course. Phenology in arid areas is rather driven by event based precipitation (Tan *et al.* 2011) that is highly variable, both in timing, magnitude and frequency and can trigger a flush of (green) vegetation growth. In these cases, the conditions of equidistantly spaced phenology peaks is not met anymore and thus, fitting a Fourier based model of sine and cosine functions might not be an appropriate choice (Mader 2012). Large data gaps are a general problem where either the acquisition plan or the cloud coverage do not permit a high frequent data coverage, e.g. areas outside the U.S., which were frequently not part of Landsat's acquisition plans. Although the current effort of reallocating data from foreign data providers (Hansen and Loveland 2012) eases this drawback to a certain degree, temporal dense coverage is still an issue in many places. In addition, dryland biomes are often characterized by a pronounced partitioning of seasonality into a dry and wet season. During the wet season, where phenology is most dynamic, cloud-free Landsat data are often not available. Therefore, fitting a sine-based model might not be the best choice under these specific circumstances.

Here we present an approach to identify additional clouds and cloud shadows in Landsat imagery using a two-step cloud screening procedure, especially tailored for dryland ecosystems. The first step is comprised of applying the Fmask algorithm to the individual Landsat images (Zhu and Woodcock 2012). We modified two criteria of the Fmask algorithm to perform better in a dryland environment. The second step is a subsequent time-series based outlier detection method, based on the results of the first step to reduce omission errors. It is designed as an alternative to the method presented by Zhu and Woodcock (2014a) for areas where the middle of the growing period(s) does not occur at the same time every year.

## 2 Study area

The method was developed in an Australian savanna ecosystem in Queensland. The study area is included in WRS-2 Path/Row 093/078 and is centered at approximately 26°00'08''S and 147°25'48''E. The location of the study area (150 x 150 km) is displayed in Fig. III-1 as the white box. The structural formations dominating the area, namely open forests and woodlands, are characteristic for Queensland's savannas, accounting for over 70% of Australian forests in terms of structure and biomass (Lucas *et al.* 2006). The major tree communities in this area are formed by evergreen eucalyptus, acacia or callitris dominated woodlands to open forests (Regional Ecosystem Mapping fo 2006: Neldner *et al.* 2012). The region is characterized by variable rainfall and the ecosystem itself is generally water limited. The average monthly evaporation exceeds the average monthly rainfall throughout the year (Cowie *et al.* 2007) with a pronounced dry and wet season, where

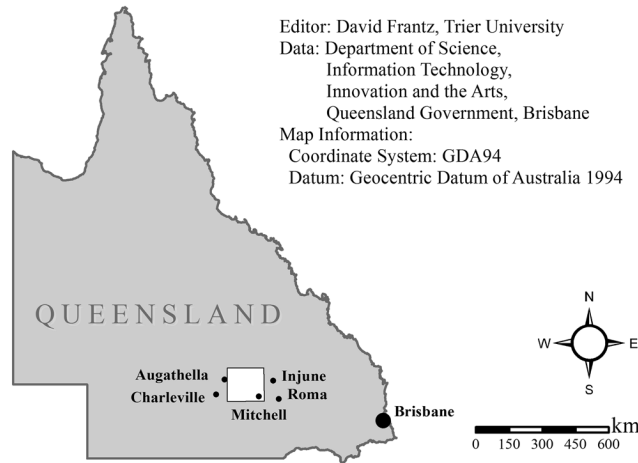


Fig. III-1: Study Area.

the rainfall is precipitated by short duration storms with high temporal and spatial variability (Cowie *et al.* 2007).

### 3 Data

All available Landsat 5 Thematic Mapper (TM) data of WRS-2 path/row 93/78 for the three year period of 2007–2009 were used in this study. Standard terrain corrected (Level 1T) Landsat data were obtained from the U.S. Geological Survey archive (USGS). Images that were not corrected to L1T precision were discarded, as a reliable co-registration among images was considered to be of major importance.

### 4 Methods

The presented method is a two-step cloud screening procedure, where the first step is comprised of scene-by-scene detections with a slightly modified version of the Fmask algorithm (Zhu and Woodcock 2012). The results from the first step are utilized in the second step, where the cloud and cloud shadow probabilities and the final masks are used in a time-series based outlier detection method.

#### 4.1 Step 1: Fmask

Fmask is a fully automated cloud and cloud shadow screening application based on TOA reflectance (Zhu and Woodcock 2012). Fmask is based on physical properties of clouds and their shadows to produce potential layers of clouds and cloud shadows. Cloud shadows are found by combining several existing approaches; i.e. object matching and lapse rate methods. The original

algorithm is described in detail by Zhu and Woodcock (2012). Here we adapted the code in two major points to meet our requirements:

- Termination criterion:

In Fmask (Zhu and Woodcock 2012), shadows are matched by utilizing the geometrical relationship between a cloud and its shadow as well as modeling the three-dimensional shape and its presumed base height by using temperature information. This 3D shape is projected to the ground, while iterating through possible cloud base heights. For every iteration, a match similarity between the calculated shadow and a potential layer of shadows is computed. Iteration proceeds until the match becomes less than 98% of the maximum match similarity. We decided to discard this termination criterion. Shadow matching was found to terminate too early in many cases, which meant that only a fraction of the shadow was captured. In this implementation, the shadow match with the highest match similarity was considered the winner if the score was greater than 0.3. Otherwise no shadow was matched.

- Darkness Filter:

In the dryland ecosystems under investigation, we encountered a special case of land cover composition, where Fmask occasionally produced a high rate of false positives. This applies if the image is composed of two extremely different land cover classes with uneven areal distribution. Drylands are often comprised of very bright and hot surfaces (due to their sparse and dried-out vegetation cover), but in the presence of open water, patches of active vegetation can co-exist in the same image (e.g. river deltas, river basins and the like). These dark vegetation patches might be classified as clouds if the bright surface types are more dominant in terms of area.

During the selection of the PCPs (Potential Cloud Pixel), dark pixels might pass because the implemented Whiteness filter is rather a “Flatness” filter, which excludes pixels that have a high variability in the visible bands. Thus this filter also lets sufficiently black or grey pixels pass. We integrated an additional darkness filter into the PCP selection query (i.e. potentially cloudy only if the mean reflectance of the visible bands  $> 0.15$ ). This filter is based on the observation that clouds are normally rather white.

Furthermore, the cloud probability of these features is usually very high because of the large temperature difference between the bright surrounding area and the vegetated surface. In Fmask, the temperature probability is derived by a quantile based approach that uses all non-PCP pixels. In the savanna systems under investigation, the bright and hot part of the image

often dominates in terms of area, thus the temperature probability gets biased towards the hot surfaces. Water-cooled and transpiring vegetated surfaces are then significantly colder and hence show a very high cloud probability. Therefore, the darkness filter was also added in the selection of the final cloud layer, where the cloud probability is otherwise the dominant driver to identify cloudy pixels.

In addition to the original Fmask implementation, the internal intermediate probability products, namely the cloud and cloud shadow probabilities are stored. Pixel-based time series of these probabilities are used to capture additional clouds and their shadows in the second step. A short description of the probability layers is presented in the following, details can be found in the original Fmask publication (Zhu and Woodcock 2012).

- Cloud probability

In Fmask, the cloud probability is derived by combining land or water specific thematic probabilities. For both land and water, a temperature probability is estimated by rescaling the Brightness Temperature (BT) by percentiles of the land/water clear-sky pixels' BT. Various spectral tests are performed to obtain estimates of clear sky pixels in an early stage of the algorithm. In case of water, a brightness probability is computed. It exploits the property of water to have a very low, but stable reflectance in Band 5 and a significant increase in case of a cloud. Contrary, optical reflectance is very inconsistent for different land cover types, while being quite constant for clouds (Zhu and Woodcock 2012). Thus a variability probability is computed instead of a brightness probability. The Whiteness Index (Gomez-Chova *et al.* 2007) and modified versions of NDVI (Tucker 1979) and Normalized Difference Snow Index (NDSI, Hall *et al.* 1995) are used to capture the earth land surface's spectral variability. Modified versions of NDVI and NDSI are used to counteract inconsistent index behavior in case of saturated VIS but under-saturated NIR and SWIR bands (Dozier 1989).

- Shadow probability

Shadowed areas are mainly illuminated by scattered radiation and the scattering in NIR and SWIR bands is weaker than in VIS (Luo *et al.* 2008). Additionally, NIR and SWIR reflectance is usually higher than the reflectance in VIS. Thus, a stronger darkening effect is evident in the long wavelength bands. Therefore, a morphological flood-fill transformation of bands 4 and 5 is performed in Fmask (Soille *et al.* 2003, Vincent 1993). This filling

procedure causes objects with a local depression in reflectance compared to their surroundings (e.g. cloud shadows, but also lakes or patches of vegetation in a desert) to be filled with the values along their border.

## 4.2 Step 2: Outlier detection

Once all individual images are processed with Fmask and the cloud and cloud probabilities are saved as second output product, we implemented a time series algorithm, which detects additional clouds and shadows on a per-pixel basis. The cloud and shadow masks are used to provide the clear-sky observations, whereas the probabilities are used to separate some remaining clouds and shadows from this data heap. Clear-sky observations are used to estimate basic statistics of the land surface. A deviation from these statistics is considered as cloud remnant. The process is illustrated as workflow in Fig. III-2.

The probabilities of the clear-sky observations are assumed to be stable throughout time – at least for a restricted period of time. Therefore an anomaly in any of the probabilities throughout a three-year-period was considered as being an undetected cloud or cloud shadow. For each pixel  $(x,y)$ , the median and the standard deviation of the clear-sky time series are computed for each probability  $prob_j$ , with  $j = cld$  or  $shd$ . A pixel at time  $t_i$ ,  $i=1, \dots, n$  ( $n =$  number of images) is marked as outlier if any  $prob_j$  is greater than a threshold  $thr_j$ :

$$outlier(x, y, t_i) = prob_{cld}(x, y, t_i) > thr_{cld} \ || \ prob_{shd}(x, y, t_i) > thr_{shd} , \quad (III-1)$$

which is its median plus a multiple  $m$  of its standard deviation:

$$thr_j = med(prob_j(x, y)) + m_j \cdot sd(prob_j(x, y)). \quad (III-2)$$

The multipliers  $m_j$  are the only tweakable input parameters of our algorithm. They allow for balancing the omission and commission errors. Ideally, they can be found by inverting the code with a Look-up-Table approach, where the parameters are chosen that match the best with an independent dataset. In practice, this might not be applicable due to problems in setting up a reference dataset of sufficient quality as outlined by Zhu and Woodcock (2014a). Therefore, the choice of the multipliers  $m_j$  will be in practice based on visual scene analysis. For our presented data, we set  $m_{shd}$  to 3.5,  $m_{cld}$  was set to 3, though we suggest that these parameters should be reconsidered for every study site.

This approach tends to identify many small outlier objects accidentally. Therefore, rigorous spatial filtering is applied to each mask image at times  $t_i$ . An outlier pixel is only accepted if it is completely surrounded by other outliers in an 8-connected neighborhood. If not, the outlier is rejected

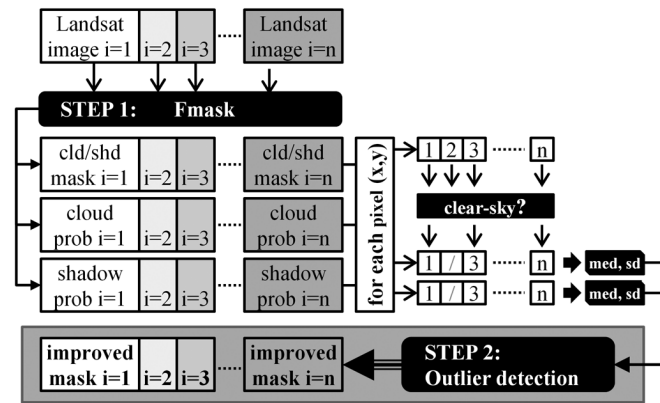


Fig. III-2: Workflow of the two-step algorithm.

and considered to be clear-sky. Finally, all remaining outliers are buffered by 7 pixels and the outlier masks and original Fmask-derived masks are combined for each point in time  $i$ .

## 5 Results and Discussion

Fig. III-3 illustrates the outlier method for two pixels (marked in Fig. III-4) that were missed by Fmask. The outlier detection algorithm was capable of detecting data points within the shadow probability time series ( $a$ ) and the cloud probability time series ( $b$ ). In the case of the cloud probability example ( $b$ ), the importance of the removal of Fmask identifications (yellow) for calculating the statistics is evident, where the inclusion of these data points could bias the standard deviation and the median (the effect on standard deviation might be more severe) in a way that the outlier would not be detected anymore. In addition, apparently the use of cloud and shadow probabilities allows us to use rather simple thresholding techniques compared with Zhu and Woodcock (2014a) as the probability layers are mostly free of phenological fluctuations. We superimposed the clear-sky NDVI time series in Fig. III-3. It can be seen that there is an irregular, rainfall driven phenology, which is clearly visible in the NDVI, but not in the probability time series. The fluctuations in the probability time series are rather erratic and do not seem to inherit from phenological processes.

Furthermore, it can be seen that detecting clouds and shadows in this specialized data space allows even for the detection of thin clouds (example  $b$ ), where the cloud is not even clearly visible in the NDVI transformation.

Fig. III-4 depicts typical results of Fmask and of the extension for an example of a densely packed cumulus formation. Yellow polygons depict the Fmask results and additional outliers are drawn in blue. Especially cloud shadows are subject to omission in Fmask, which was to be expected as the shadow inaccuracy was determined to be higher (Zhu and Woodcock 2012). This is particularly

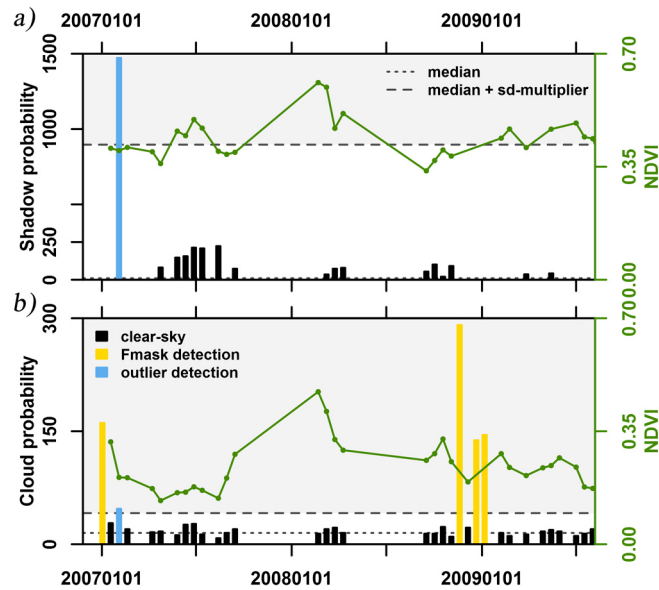


Fig. III-3: Illustration of the time series outlier detection for two pixels marked in Fig. III-4. An outlier (blue bars) is detected if its cloud/shadow probability is greater than the pixel median + a standard deviation multiplier (statistics retrieved from the clear-sky observations, black bars), thus being in the grey area. Fmask detections (yellow bars) are used to separate most of the observations before calculating the statistics. NDVI time series of the clear-sky observations are plotted in green.

true in cases where the cloud was missed or the cloud is extremely cold and high and thus too far away to be linked properly to its shadow. Furthermore, small and almost transparent clouds were sometimes not detected, too (e.g. the cloud marked by *b*). Very thin stratus clouds or plumes of thick haze/high aerosols were also of concern (not depicted here). A high proportion of these objects could be captured with the additional outlier approach. The outlier detection produced reasonable results for most land cover types. As an exception, there were some false positives when dark objects of short duration were present. Fresh burn scars are characterized by a charred and dark surface, thus the shadow probability increases rapidly for a short time. Therefore, some recently burned areas were flagged partially as being shadow. We expect that this is also true for other transient dark features (as temporal flooding), though we did not encounter this in our testing data. In a future version of our algorithm, we might account for this problem by exploiting the cloud/shadow geometry, e.g. by implementing another repeat of the Fmask shadow matching routine after the outlier detection step or by simply rejecting shadow detections that are too far away from the next cloud.

The time series based outlier detection in the probability images was designed to decrease the error of omission. The error of commission might increase to some degree or might remain unaffected. As a suggestion, this method can be used in applications that are very sensitive to remaining cloud contamination, but are robust in case of missing data. For example, the Spatial and Temporal Adaptive



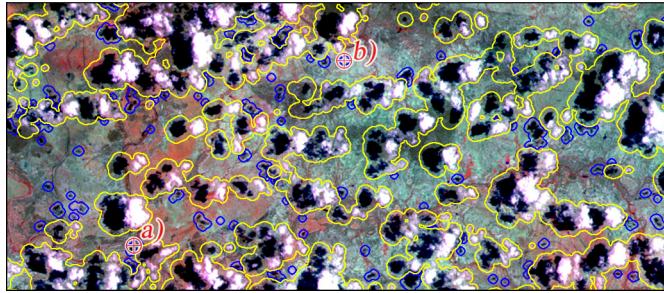


Fig. III-4: Landsat RGB-composite (bands 4/5/3, i.e. NIR/SWIR1/RED) for the illustration of the outlier detection method (blue) as compared to the Fmask detections (yellow). The image was captured on 02/03/2007, which corresponds to the date with the blue bars in Fig. III-3; the corresponding pixels are marked with *a)* and *b)*.

Reflectance Fusion Model (STARFM, Gao *et al.* 2006) predictions are very likely to decrease if transient changes in reflectance are present (e.g. clouds) and are per se designed to bridge temporal data gaps and make use of multiple images and neighborhood information. This means in most cases there will still be an estimated pixel value, even if that specific pixel was masked out in one image.

## 6 Summary

Cloud and cloud shadow detection in Landsat imagery has matured recently with the introduction of Fmask (Zhu and Woodcock 2012). Fmask accuracy is known to be of very high quality, though not perfect. Therefore, a two-step cloud and cloud shadow screening method was introduced to decrease omission errors for applications that are sensitive to remaining cloud contamination. We modified two features of the original Fmask code (first step). Firstly, the termination criterion for shadow matching was dropped. Secondly, we added a darkness filter to improve detections for areas that are characterized by large surface property gradients.

A robust time series based outlier detection method was developed to reduce omission errors. The method utilizes the scene-by-scene detections of the first step. All clear-sky observations of a pixel are used to estimate the median and standard deviation of the cloud and cloud shadow probability time series. The cloud and cloud shadow probabilities are intermediate products of Fmask (Zhu and Woodcock 2012).

Contrary to existing add-ons (Zhu and Woodcock 2014a, Zhu *et al.* 2012), the presented algorithm was specifically developed for dryland areas that are characterized by the absence of phenology peaks at regular intervals. Furthermore, the algorithm is considered to be more robust in case of temporally sparse Landsat data and bad acquisition distributions over the year due to a pronounced dry/wet seasonality because of the conceptual simplicity. In addition, the method's

simplicity and its non-iterative nature might give it an edge compared to Zhu and Woodcock (2014a) if computation speed or access to high-end hardware is a limiting factor.

### **Acknowledgment**

Landsat data courtesy of the U.S. Geological Survey. We like to thank Zhe Zhu & Curtis Woodcock for providing the Fmask code. We are grateful to two anonymous reviewers whose comments helped improve the manuscript.



## **Chapter IV**

### **On the Derivation of a Spatially Distributed Aerosol Climatology for its Incorporation in a Radiometric Landsat Preprocessing Framework**

*Remote Sensing Letters 6 (8),  
August 2015, 647-656.*

DOI: 10.1080/2150704X.2015.1070314

David Frantz, Achim Röder, Marion Stellmes, and Joachim Hill

© 2015 Taylor and Francis.

The following manuscript is a copy of the final version of the accepted manuscript. The paper has been through peer review, but it has not been subject to copy-editing, proofreading and formatting added by the publisher. The version-of-record can be accessed at:

<http://www.tandfonline.com/doi/full/10.1080/2150704X.2015.1070314>

**Abstract**

We developed a spatio-temporal path reflectance climatology for use in atmospheric corrections for a Landsat preprocessing framework. The climatology is intended as a fallback strategy for aerosol estimation in bright Southern African savannah ecosystems where the rarity of dark objects decreases the applicability of common image-based aerosol estimation strategies and the widespread burning prohibits the use of a fixed aerosol loading. We predicted the climatological path reflectance surface by applying a multivariate regression model to all available path reflectance retrievals on basis of the geolocation and the days of the year on which the data were acquired. The resulting predictions are able to successfully model major spatio-temporal gradients of the path reflectance distribution. The prediction error (weighted RMSE at  $0.483 \mu\text{m}$ ) was less than 1% reflectance while the prediction itself varied by 4.6% reflectance. Thus, using the modelled climatology for atmospheric correction is favorable compared to a fixed aerosol content.

## 1 Introduction

Recent advances in open data policies (Woodcock *et al.* 2008) have drastically changed the use of Landsat data and encouraged the development of mass-processing frameworks (Wulder *et al.* 2012). Concurrently, the use of an increasing amount of Landsat images also raised the demands on the radiometric processing quality and on the derivation of ready-to-use standard products (Hansen and Loveland 2012). Currently, radiative transfer modelling (e.g. Tanré *et al.* 1979) is agreed to be the quasi-standard in radiometric corrections and as such the estimation of aerosol optical depth (AOD) becomes a key parameter due to its profound impact on biophysical parameters (Gillingham *et al.* 2012). State-of-the-art large area generation systems like the widely used LEDAPS approach (Landsat Ecosystem Disturbance Adaptive Processing System, Masek *et al.* 2006) estimate the AOD directly from the imagery. It is assumed that a few virtually zero reflectance pixels exist in every image (Hill and Sturm 1991) and the aerosol loading is commonly derived by applying the dark, dense vegetation method (DDV, e.g. Kaufman and Sendra 1988) or the dark object subtraction approach (DOS, e.g. Moran *et al.* 1992, Chavez 1996). Whilst these are generally accepted approaches, the estimation of AOD with dark object methods is not usable if there are no suitable targets. Kaufman and Sendra (1988) already identified regions where the large-scale absence of dark vegetation restricts the operational usage of the DDV approach, which applies for some larger parts of our study area in the bright Southern African savannahs. Gillingham *et al.* (2011) already documented the inability to operationally apply the DDV under the similar Australian conditions which led to the decision of simply fixing the AOD to a reasonable value in the Eastern Australian Landsat preprocessing scheme (Flood *et al.* 2013). Nevertheless, it is more desirable to correct each image with a more appropriate atmospheric parameter set, which is especially mandatory if the assumption of a stable AOD is violated. Southern African savannahs are amongst the most fire-prone and most frequently burnt ecosystems in the world (Bond and Keeley 2005) and as such substantial seasonal and spatial variations in aerosol loadings are prevalent (Eck *et al.* 2001).

We report on the derivation of a spatially explicit path reflectance climatology for its intended use in an operational preprocessing framework as a substitute for occasionally erroneous image-based path reflectance and AOD estimations in the case that meaningful dark objects cannot be identified in a given image. This climatology generates a smooth surface from the surrounding reliable retrieved path reflectance values, thus bridging the gaps where the image-based aerosol characterization failed. The corrected Landsat data are intended to be used in a pixel-based compositing application in the context of wall-to-wall deforestation and forest degradation assessments, as well as being intended for time series applications in general.

## 2 Methods

### 2.1 Background

We implemented an operational large-area preprocessing framework for the generation of multi-sensor surface reflectance Landsat datasets (Frantz *et al.* 2016a). The approach includes methods for the automatic detection of clouds and cloud shadows (Zhu and Woodcock 2012, Zhu *et al.* 2015), functions for reprojecting the data to a shared coordinate system and the partitioning of the data to gridded data structure. The radiometric correction includes a C-correction for terrain normalization (Kobayashi and Sanga-Ngoie 2008, Teillet *et al.* 1982). The atmospheric correction module is based on Tanré’s formulation of the radiative transfer (Tanré *et al.* 1979) and includes adjacency effect correction, the correction of water vapour absorption by a MODIS-derived (Moderate Resolution Imaging Spectroradiometer) water vapour database and a joint database- and image-based estimation of AOD over dark objects. The employed dark object database holds information on the temporal persistence of dark objects and was generated by an exhaustive analysis of all available uncorrected Landsat images. The darkest pixels were identified in each image and the dark object persistency (DOP = [0 ... 100], i.e. the percentage of the time a pixel is dark) is derived for each pixel in the study area. The most permanent objects are then favoured in the actual radiometric processing for the path reflectance estimation. The usage of the DOP substantially increases the quality of retrieved values over the dark objects because transient dark features like temporal flooding or burnt areas are successfully rejected while perennial water bodies or topographic shadows are favoured. A visualization of the DOP for two sample areas is appended as electronic material in the “figshare” section. We processed all available 57,371 Level 1T Landsat images for Angola, Zambia, Zimbabwe, Botswana and Namibia and recorded the estimated path reflectance  $\rho_p$ , on which our prediction model is based. The path reflectance is closely related to AOD (Hill and Sturm 1991), which can be inferred with a scattering model (e.g. the multiple scattering approximation, Sobolev 1975) as demonstrated in (Frantz *et al.* 2016a).

### 2.2 Observations

We successfully characterized the scattering effects for the majority of the Landsat images with this approach. Nevertheless, we encountered serious problems in deriving AOD for a substantial number of Landsat images (~43% of all images), which especially was a problem in southern Namibia and Botswana where the dry season surface is bright and dark objects are rare or not apparent at all. Therefore, we closely investigated the seasonal and spatial patterns of the 57% successful  $\rho_p$  estimates.

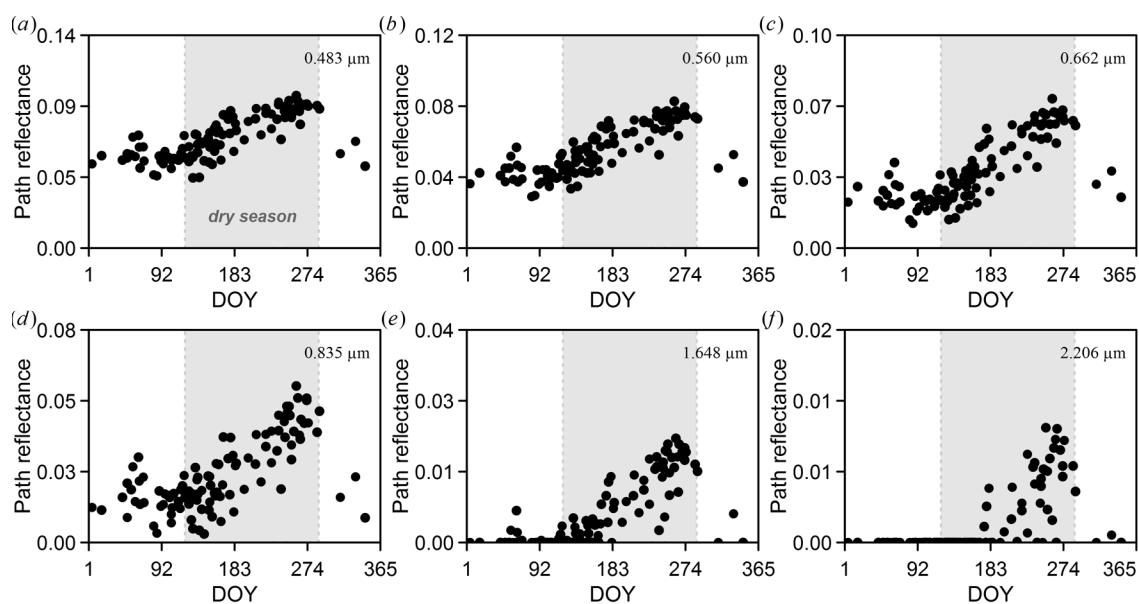


Fig. IV-1. Successful path reflectance retrievals for the six reflective Landsat bands for an illustrative Landsat frame (177/072). The frame is located at the Namibian/Angolan border and includes the perennial Cubango and Cuito rivers. The grey background indicates the dry season.

Fig. IV-1 depicts  $\rho_p$  for an illustrative Landsat frame at the Namibian/Angolan border that includes the perennial Cubango and Cuito rivers. The retrieved  $\rho_p$  values in this frame were of high quality and all depicted points were estimated from permanent dark objects, i.e. objects that are the darkest pixels in the given scene over time. There is a clear seasonal pattern, which is especially pronounced in the visible bands, where the effect of aerosols is most prominent. The depicted region follows the typical Southern African climate with two main seasons, i.e. a wet and a dry season. The dry season begins in May and lasts until September, though the hottest temperatures are not reached until October, when the rainfall sums are also still relatively low (Weber 2013). Path reflectance values are small during the wet season and begin to increase with the onset of the dry season. The increase continues until the approximate end of the dry season in September/October after which the values quickly drop back to the wet season base value.

In addition to the temporal pattern, we also identified spatial dependencies. Fig. IV-2 displays mean  $\rho_p$  values for the blue wavelength band for the dry season acquisition months. The aerosol accumulation apparently starts earlier in north-western Angola and progresses towards Botswana in the south-eastern part of the region. The aerosol depletion also starts earlier in north-Western Angola while the highest loadings are found in the centre of the study area in the late dry season. Overall, the amplitude of the aerosol accumulation is lowest in the South. Fig. IV-2 also indicates the Landsat frames where the identification of dark objects failed, which are especially the southern dry savannah ecotypes, whereas reliable estimates were retrieved in the darker regions, e.g. the Okavango catchment



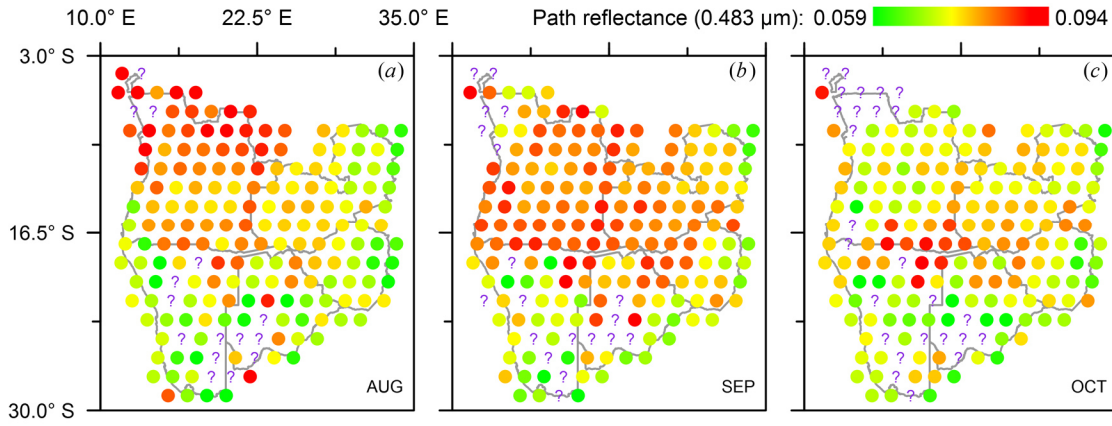


Fig. IV-2. Mean path reflectance retrievals ( $0.483 \mu\text{m}$ ). Mean values are computed for every Landsat frame for the depicted acquisition months; only the successful retrievals were considered. “?” marks indicate Landsat frames where the dark object identification failed or there were no cloud-free images.

area. In addition, some frames in northern Angola are also suspect of missing data, though this is due to a substantial decrease in data availability because of persistent cloud overcast in the tropics.

### 2.3 Modelling

As a consequence of the observed temporal and spatial patterns, we aimed at generating a spatially distributed  $\rho_p$  climatology, modelled from the available data. This climatology is intended to be used as fallback strategy in the implemented Landsat preprocessing framework when actual AOD cannot be retrieved from dark targets.

A multivariate regression model described by the geolocation – coordinates  $(X, Y)$  - and the acquisition day-of-year (DOY) of the 57% successful  $\rho_p$  estimates was employed for every Landsat band  $b$ :

$$\begin{aligned}
 \rho_{p,b} = & c_0 + c_1X + c_2Y + c_3XY + c_4X^2 + c_5Y^2 + c_6(\text{DOY}) + c_7(\text{DOY})^2 + \\
 & c_8X \sin(2\pi(\text{DOY})/365) + c_9X \cos(2\pi(\text{DOY})/365) + \\
 & c_{10}Y \sin(2\pi(\text{DOY})/365) + c_{11}Y \cos(2\pi(\text{DOY})/365) + \\
 & c_{12}X \sin(4\pi(\text{DOY})/365) + c_{13}X \cos(4\pi(\text{DOY})/365) + \\
 & c_{14}Y \sin(4\pi(\text{DOY})/365) + c_{15}Y \cos(4\pi(\text{DOY})/365) + \\
 & c_{16}X \sin(6\pi(\text{DOY})/365) + c_{17}X \cos(6\pi(\text{DOY})/365) + \\
 & c_{18}Y \sin(6\pi(\text{DOY})/365) + c_{19}Y \cos(6\pi(\text{DOY})/365).
 \end{aligned} \tag{IV-1}$$

The DOP (in %, see also Fig. IV-3) was used to weight the observations during the estimation of the regression coefficients  $c_{0-19}$  by the means of weighted least squares fitting. We assumed that

Table IV-1. Path reflectance prediction errors for every Landsat band.

Wavelength ( $\mu\text{m}$ )	Landsat band	ME	MAE	RMSE	WRMSE
		$\sum_{i=1}^n e_i/n$	$\sum_{i=1}^n  e_i /n$	$\sqrt{\sum_{i=1}^n e_i^2/n}$	$\sqrt{\sum_{i=1}^n w_i e_i^2 / \sum_{i=1}^n w_i}$
0.483	Blue	0.00111	0.0080	0.0110	0.0095
0.560	Green	0.00005	0.0080	0.0108	0.0101
0.662	Red	-0.00054	0.0082	0.0109	0.0099
0.835	NIR	-0.00045	0.0080	0.0104	0.0099
1.648	SWIR1	0.00004	0.0020	0.0032	0.0031
2.206	SWIR2	0.00003	0.0006	0.0013	0.0012

Mean Error (ME), Mean Absolute Error (MAE), Root Mean Squared Error (RMSE) and weighted Root Mean Squared Error (WRMSE). All errors are reported in reflectance units.  $e_i$  are the residuals between the model fit and the actual data for every data point  $i$ ,  $w_i$  are the weights used for the prediction.

temporally persistent dark objects are more reliable for characterizing atmospheric scattering effects due to their inherent pseudo-invariant reflectance, which is often exploited for improving atmospheric correction methods (Themistocleous *et al.* 2013). The coefficient  $c_0$  is the path reflectance intercept; the coefficients  $c_{1-5}$  explain purely spatial trends on the path reflectance, whereas the coefficients  $c_{6-7}$  explain the non-interacting temporal trend. The remaining coefficients describe combined spatio-temporal effects by modelling seasonal cycles of varying frequency with geolocation-dependency. As a boundary condition, the prediction is enforced to be cyclic by twofold data repetition yielding three identical annual cycles.

### 3 Results

Table 1 summarizes  $\rho_p$  prediction errors for the employed spatio-temporal model, i.e. the Mean Error (ME) as a measure for the prediction bias, the Mean Absolute Error (MAE), the Root Mean Squared Error (RMSE) and its weighted counterpart (WRMSE).

The ME indicate that the residuals  $e_i$  are close to zero and have a small bias. The bias is largest in the blue wavelength band. The MAE, RMSE and WRMSE all report similar errors and the errors for the first four wavelengths are very similar and in the order of 1% reflectance. The MAE values are smallest and RMSE values are the greatest due to the stronger contribution of outliers. The WRMSE might be the most appropriate measure for quantifying the goodness of the fit since we also employed a weighted prediction.

Fig. IV-3 depicts the blue wavelength  $\rho_p$  retrievals (points) for one path of Landsat data (one orbit in approximate North-South direction), as well as the resulting prediction (line). The prediction successfully modelled the main seasonal and latitudinal variations in  $\rho_p$ . It is also apparent that there are fluctuations and outliers around the modelled fit, which surely affect the prediction errors shown

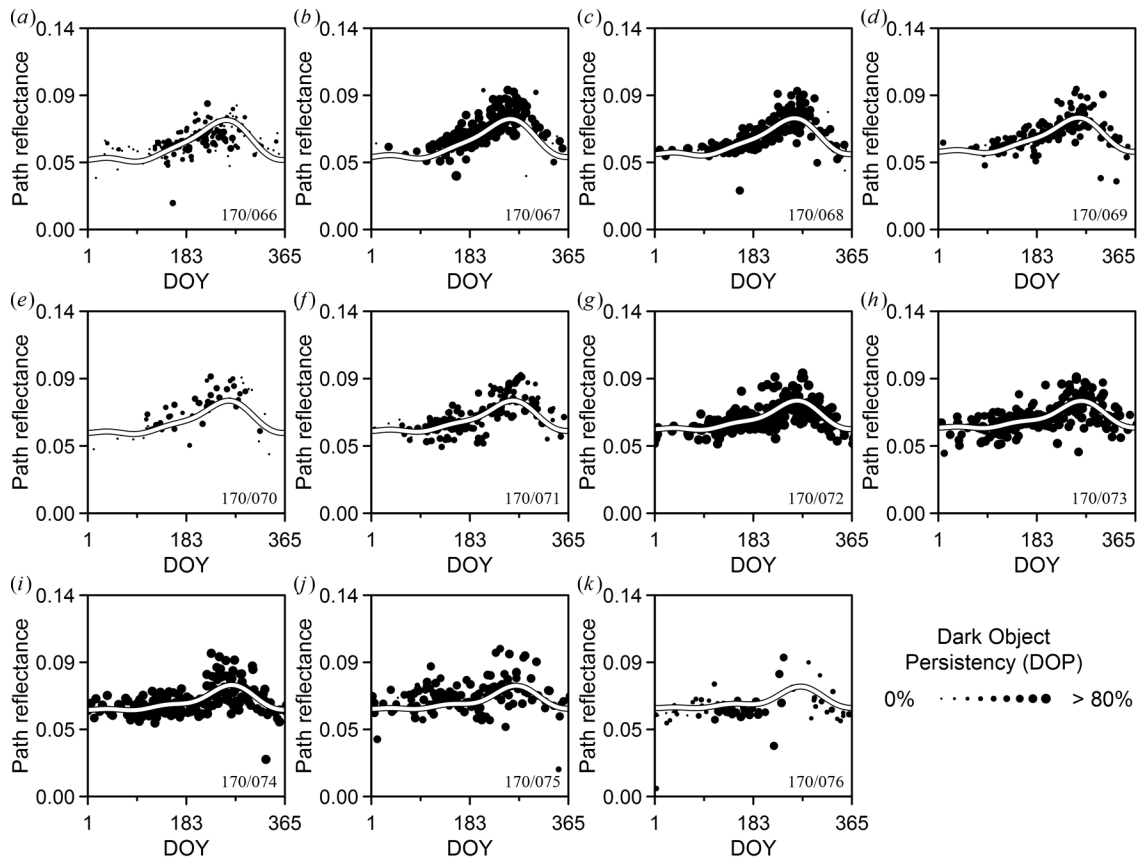


Fig. IV-3. Initial path reflectance retrievals ( $0.483\mu\text{m}$ ) and prediction (line) for a series of Landsat frames within one orbit (path 170, i.e. in the eastern part of the study area). The path/row is labelled in the bottom right corner. The persistence of the dark objects (DOP) which were used for estimating the path reflectance is indicated by the variable point size. The persistence was used to weight the observations in the prediction.

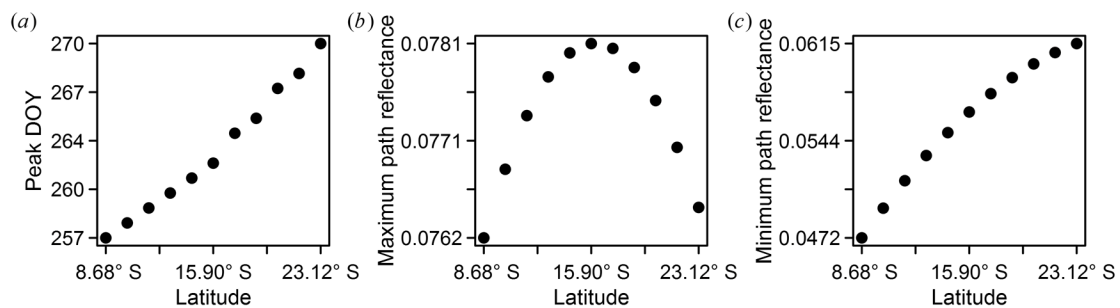


Fig. IV-4. Latitude dependence of (a) the timing of peak aerosol loading, (b) the maximum predicted path reflectance and (c) the minimum predicted path reflectance. The data are inferred from the depicted prediction in Fig. IV-3.

in Table 1. Fig. IV-4 summarizes the latitude dependency of several key parameters of the data show in Fig. IV-3. Fig. IV-4a corroborates the previous finding that the aerosol peaking is delayed in the south. The maximum values (Fig. IV-4b) are found at medium latitudes, though this might be different in other orbital slices in the study area. Concurrently, the minimum predictions (Fig. IV-4c) increase southwards, indicating a higher base level of aerosol loading.

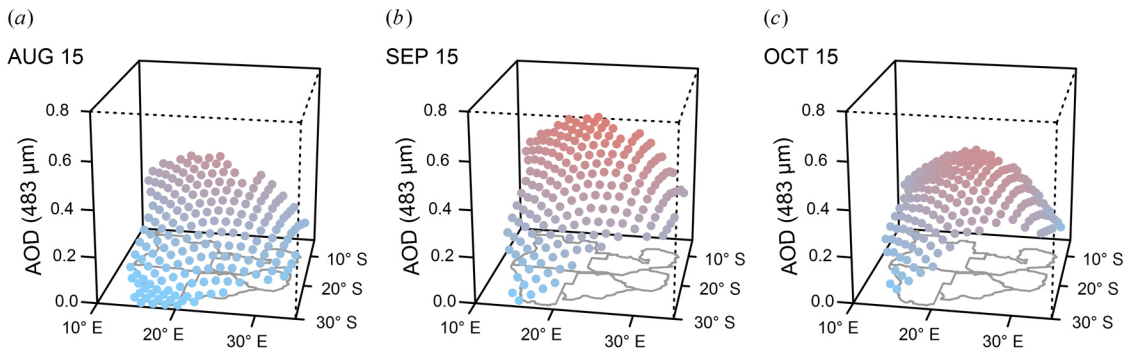


Fig. IV-5. Predicted aerosol optical depth surfaces at  $0.483\mu\text{m}$  for three dates in the dry season; see the online version of this article for the complete and animated time series.

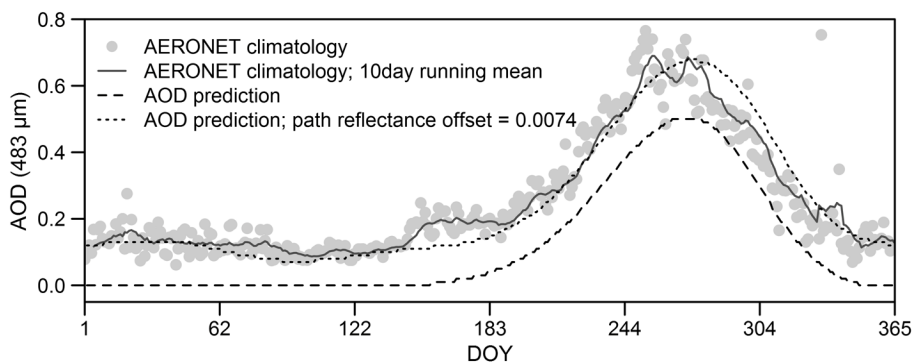


Fig. IV-6. Average annual AOD cycle for the AERONET Mongu site and the corresponding AOD prediction. The path reflectance offset was found by inverting the multiple scattering computation such that the RMSE between the AERONET and the predicted AOD is minimized.

We inferred the aerosol optical depth at  $483\mu\text{m}$  from the modelled  $\rho_p$  climatology by using the multiple scattering approximation (Frantz *et al.* 2016a). Fig. IV-5 illustrates the spatial AOD surfaces for selected dates in the dry season. The prediction resulted in a smooth and seamless AOD surface for the entire study area and corroborates the earlier findings, i.e. (1) an earlier onset in aerosol accumulation in the North, (2) stronger aerosol loadings in the North, (3) earlier aerosol depletion in the North and (4) highest aerosol loadings in the centre of the study area towards the end of the dry season. The complete and animated daily time series of AOD surfaces is appended as electronic material in the “figshare” section of this article.

In order to quantitatively evaluate the goodness of the retrieved  $\rho_p$  and AOD values, we compared our results with data from the Aerosol Robotic Network (AERONET). The site at Mongu, Zambia ( $15.254^\circ\text{S}$ ,  $23.151^\circ\text{E}$ ) is the only station with multiple years of data within our study area. We computed the average seasonal AOD cycle at  $0.483\mu\text{m}$  and used the corresponding Landsat frame

(175/071) for the comparison, see Fig. IV-6. The ME between the AERONET climatology (points) and the inferred AOD climatology (dashed line) is 0.137 which indicates that the path reflectance estimations are systematically too low. We tried to quantitatively assess the underestimation in  $\rho_p$  by inverting the multiple scattering computations such that the RMSE between the AERONET and the predicted AOD is minimized:  $\rho_p$  is then underestimated by 0.0074 reflectance (dotted line in Fig. IV-6). The AERONET climatology and the offset AOD are very similar.

## 4 Discussion

Our prediction model generates seamless and smooth  $\rho_p$  and AOD surfaces for the entire study area and for each DOY. We intended to model the large-scale spatial path reflectance climatology and aimed to reproduce the major aerosol gradients in the study area. The presented model statistics indicated that the prediction model generally adapts to the input data, but there are also deviations from the underlying data. The weighted RMSE indicated that the prediction error is in the order of 0.01 reflectance for the short wavelength bands. The blue-band  $\rho_p$  prediction range (i.e. predicted maximum – minimum) is 0.046 and the input  $\rho_p$  range is even higher: 0.07 (99% of the data). Therefore, the prediction error is 4.6 (7) times smaller than the predicted (observed) data range and thus, we conclude that using such a climatology is preferable over using a constant aerosol loading in the radiometric correction. This observation is also supported by the findings of Gillingham, Flood and Gill (2012), who found that a fixed AOD (at 0.5  $\mu\text{m}$ ) of 0.05 only ensures reliable results if the actual AOD is less than 0.1. The annual AOD variability is significantly higher in our study area (compare with Fig. IV-5) but a quantitative assessment about the effect on generated products when using a constant vs a climatological aerosol characterization would be useful for future work. Nevertheless, these findings should be verified for other study areas where burning might be less influential. In areas where the AOD is rather stable throughout the year, fixing AOD might be the more practical approach.

In general, aerosol tends to accumulate during the course of the dry season but the onset, end, minimum and maximum of the accumulation are variable. The northern part of the study area is more affected by aerosol. The Southern African burning regimes are a major factor in the spatio-temporal distribution of aerosols (Eck *et al.* 2001). In Southern Africa, the seasonality is very strictly partitioned into a wet and a dry season. In the wet season, the aerosol loading is washed out (Eck *et al.* 2001). In the dry season, burning is very widespread (Stellmes *et al.* 2013a) and the absence of precipitation allows for the accumulation of biomass burning aerosol particles. The burning season starts and stops earlier in the North (Stellmes *et al.* 2013a) and so does the aerosol accumulation. The aerosol loading is also higher, which could be partially caused by the early burns because the potential accumulation

time is prolonged. In addition, northern Angola is characterized by the highest fuel loads due to the latitudinal rainfall gradient, which results in a larger amount of burned biomass and emitted aerosols per burned area if the burning efficiency is assumed to be constant (Scholes *et al.* 1996, Barbosa *et al.* 1999). Smaller amounts of fuel, as well as the late start of the main fire season (Stellmes *et al.* 2013a) could be responsible for the delayed aerosol accumulation and the decreased aerosol loadings in the South and centre of the area.

The comparison between the inferred AOD and AERONET data revealed that our method systematically underestimates  $\rho_p$  and AOD. The  $\rho_p$  underestimation was less than 1% reflectance but the effect on AOD was clearly visible. AERONET data availability in our study area is very limited (only one site with sufficient data) and as such, we cannot confirm nor verify that this bias globally applies to our data or if there are regional deviations. The initial estimation of the path reflectance was performed in the employed Landsat preprocessing framework (Frantz *et al.* 2016a) where it was attempted to identify the true reflectance of the dark objects. The iteration step for determining the true reflectance was set to 1% reflectance and thus the underestimation of less than 1% could result from this. Potentially, the increase of the iteration resolution would compensate for the underestimation and will be considered in the next re-processing.

While the approach well represents large scale gradients in the aerosol distribution, the generalized model may not adequately resolve local variations at a spatial extension of approximately two Landsat scenes or less. The observed variations (see e.g. Fig. IV-2) could be caused by distinct local fire regimes, the distribution of urban centers and potentially also locally driven deviations from the climate regime, e.g. the occurrence of orographic rainfalls. In addition, uncertainties in estimating  $\rho_p$  over dark objects could also add to the heterogeneity. Nevertheless, we aimed at reproducing the large-scale variations in order to provide a regionally adapted alternative to using a fixed aerosol characterization in a radiometric preprocessing scheme and as such, we conclude that the local deviations are acceptable in the practical implementation.

## 5 Conclusion

We developed a climatology based alternative strategy for coping with variable aerosol loadings under the environmental constraint of absent dark objects in bright ecoregions. Contrary to fixing the aerosol optical depth to a reasonable value, our approach explicitly models the spatio-temporal aerosol distribution from the available surrounding path reflectance estimations and thus reproduces the major large-scale gradients. The predictions are intended to serve as input to an

---

operational radiometric preprocessing framework for the generation of large area surface reflectance Landsat datasets.

### **Acknowledgement**

Landsat data courtesy of the U.S. Geological Survey. We thank the AERONET PI for its effort in establishing and maintaining the Mongu site. We are grateful to two anonymous reviewers whose comments helped improve the manuscript. The SASSCAL project was funded by the Federal Ministry of Education and Research.





## **Chapter V**

### **Improving the Spatial Resolution of Land Surface Phenology by Fusing Medium- and Coarse-Resolution Inputs**

*IEEE Transactions on Geoscience and Remote Sensing 54 (7),  
July 2016, 4153-4164.*

DOI: 10.1109/TGRS.2016.2537929

David Frantz, Marion Stellmes, Achim Röder, Thomas Udelhoven,  
Sebastian Mader, and Joachim Hill

© 2016 IEEE.

The following manuscript is a copy of the final version of the accepted manuscript. The paper has been through peer review, but it has not been subject to copy-editing, proofreading and formatting added by the publisher. The version-of-record can be accessed at:

<http://ieeexplore.ieee.org/document/7452606/>

**Abstract**

Satellite-derived land surface phenology (LSP) serves as a valuable input source for many environmental applications such as land cover classifications and global change studies. Commonly, LSP is derived from coarse-resolution (CR) sensors due to their well-suited temporal resolution. However, LSP is increasingly demanded at medium-resolution (MR), but inferring LSP directly from medium-resolution imagery remains a challenging task (e.g. due to acquisition frequency). As such, we present a methodology that directly predicts medium-resolution LSP on the basis of the respective CR LSP and MR reflectance imagery. The approach considers information from the local pixel neighborhood at both resolutions by utilizing several prediction proxies, including spectral distance and multi-scale heterogeneity metrics. The prediction performs well with simulated data ( $R^2 = 0.84$ ) and the approach substantially reduces noise. The size of the smallest reliably predicted object coincides with the effective CR pixel size (i.e. instantaneous field-of-view). Nevertheless, even sub-pixel objects can be reliably predicted provided that pure CR pixels are located within the search radius. The application to real MODIS LSP and Landsat reflectance well preserves the phenological landscape composition, and the spatial refinement is especially striking in heterogeneous agricultural areas, where e.g. the circular shape of center pivot irrigation schemes is successfully restored at medium-resolution.

## 1 Introduction

Satellite-derived land surface phenology (LSP) provides important information for land use/cover mapping as well as change detection (Andres *et al.* 1994, Brunsell and Gillies 2003, Stellmes *et al.* 2013b), for determining the vegetation response to climate change and variability (Brown *et al.* 2012, White *et al.* 2005), for usage in large-scale biosphere models (Fisher *et al.* 2006), and is considered to improve pixel-based composites (Griffiths *et al.* 2013b). The use of LSP has proven to improve the accuracy of derived information compared to single date methodologies, especially in areas where inter-annual LSP variability is high (Simonetti *et al.* 2015).

LSP is commonly derived by using data from coarse-resolution (CR) sensors because of their well-suited temporal resolution of less than 16 days (Archibald and Scholes 2007). While LSP derived from these sensors is accepted to be of good quality, its coarse resolution is insufficient to characterize LSP at higher spatial resolution and in heterogeneous areas (Melaas *et al.* 2013), and as such, CR LSP is less useful for applications that rely on the description of LSP at the landscape level or in highly fragmented landscapes.

On the contrary, inferring LSP directly from medium resolution (MR) imagery like Landsat is a challenging task due to the relatively low acquisition frequency (Melaas *et al.* 2013), as well due to the substantially reduced data availability in some parts of the world (see e.g. Kovalskyy and Roy 2013). Whilst the generation of MR LSP is applicable in areas like the United States (Melaas *et al.* 2013), these methods are inappropriate for areas where the Landsat archive is less densely populated, especially in arid areas where the clear-sky data availability during the wet growing season is virtually zero. As a further constraint, Landsat based methods are commonly developed in rather stable north American forests and are based on the long-term LSP average from which small annual deviations are inferred (Fisher *et al.* 2006, Fisher and Mustard 2007, Melaas *et al.* 2013). However, inter-annual variations can be significant (White *et al.* 1997); for instance burning is widespread in Southern Africa (Bond and Keeley 2005) and results in an abrupt end of the green season in one year, whereas the season may extend significantly longer in another year if unburnt. A high inter-annual variability in LSP has also been observed over India (Atkinson *et al.* 2012) and Europe (Atzberger *et al.* 2013). Few approaches exist to infer LSP from actual Landsat time series with methods developed for CR hyper-temporal data (e.g. Kovalskyy *et al.* 2012). Nevertheless, their use is strictly constrained to areas where the Landsat inter- and intra-annual data availability is high and constant; a data density of less than 16 days is needed to describe LSP precisely (Archibald and Scholes 2007).

Another popular approach is to infer MR LSP (e.g. Schmidt *et al.* 2012, Walker *et al.* 2012) in a two-step approach by (i) predicting a time series of synthetic MR surface reflectance images and (ii) applying a CR phenology detection code (e.g. Jonsson and Eklundh 2002) to this synthetic MR time series. The first step is often approached by employing the spatial and temporal adaptive reflectance fusion model (STARFM, Gao *et al.* 2006), one of its modifications (e.g. Zhu *et al.* 2010, Fu *et al.* 2013) or regularized spatial unmixing approaches (e.g. Zhukov *et al.* 1999, Amoros-Lopez *et al.* 2011). Nevertheless, landscape heterogeneity is known to decrease STARFM prediction quality substantially, which results in poor image contrast (Zhu *et al.* 2010), while the enhancement of the modified codes in all environments is as yet inconclusive (Emelyanova *et al.* 2013). Moreover, recent research indicates that a temporal resolution of MR imagery of less than 25 days is eventually needed to ensure high prediction quality (Förster *et al.* 2015). In addition, the technical demand on storage capabilities and processing time is high for large-area projects, since two computationally intensive algorithms are to be applied one after another.

As opposed to existing data fusion techniques, we report on a novel approach that directly predicts LSP at finer resolution on the basis of the respective CR LSP and MR reflectance imagery. The prediction is characterized by great spatial detail and the method avoids the need of predicting a dense time series of MR images in the first step. Southern African (section 2) MODIS LSP (3.1) and Landsat data (3.2) are used in this study, though the method (presented in section 4) is general enough to be also applied to other sensor pairs and similar continuous fields. An indirect validation is performed with a simulation study by applying the method to an artificial landscape in a controlled, yet realistic setting (6). Exemplary results of the application to real data are presented in section 7. Relevant issues are directly discussed in the respective later sections (6, 7) and the key findings are summarized in section 8.

## 2 Study Area

The Southern African study area includes the countries of Angola, Zambia, Zimbabwe, Botswana and Namibia ( $\sim 3.7 \cdot 10^6$  km<sup>2</sup>; see Fig. V-1) and is centered at the upcoming Kavango-Zambezi Transfrontier Conservation Area (KAZA TFCA). The area is phenologically diverse due to differences in large-scale vegetation cover, primarily as a function of climate gradients. The northwestern part of Angola is located in the tropics and the rainfall decreases southwards due to the temporally shorter influence of the Intertropical Convergence Zone (ITCZ, Nicholson 1981): the mean annual rainfall is higher than 1500 mm in northern Angola and less than 200 mm (50 mm) in southern Namibia (Namib Desert) (Hijmans *et al.* 2005). Continentality is also a governing factor, where the Namib Desert is the most arid place due to multiple aridifying effects of climate variables and ocean

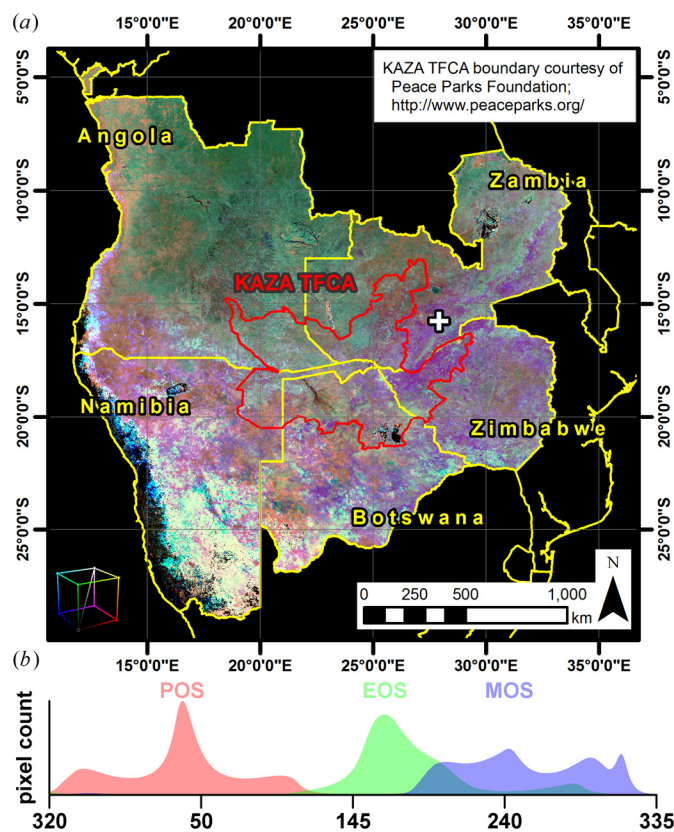


Fig. V-1 (a): Study area and coarse resolution LSP. KAZA TFCA: Kavango-Zambezi Transfrontier Conservation Area. The RGB-composite depicts the peak of season (POS, red), end of season (EOS, green) and minimum of season (MOS, blue) for 2005. The “+” indicates the subset in Fig. V-8. (b): Histograms of the depicted data.

currents (Van Zinderen Bakker 1975). The vegetation cover ranges from dense Miombo forests in Angola to sparse xerilic savanna ecosystems in the Kalahari, and also includes more extreme surface types like swamps, salt pans and deserts (Olson *et al.* 2001). Being in the southern hemisphere, the phenological cycle of a given year  $y$  starts with the peak of season (POS), followed by end of season (EOS), minimum of season (MOS) and ends with the start of season (SOS). Fig. V-1 displays the POS, EOS and MOS for 2005 – derived from CR data (see 3.1). Large-scale differences occur, where especially the Angolan and western Zambian Miombo forests contrast the southern savanna ecotypes and the more arid Namibian landscapes.

### 3 Data

#### 3.1 Coarse resolution LSP: MODIS

We used the 16-day Vegetation Indices (VI) Dataset at 250 m spatial resolution (Huete *et al.* 1999) to capture the CR LSP. The complete time series of the Terra (MOD13Q1) and the Aqua

(MYD13Q1) MODIS sensors was incorporated. We used the Enhanced Vegetation Index (EVI) as a proxy for biomass development and the day-of-composite (DOC) information to recreate the actually sensed time series with a nominal temporal resolution of 8 days. The use of the exact acquisition dates can improve LSP accuracy (Bachoo and Archibald 2007). The DOC was used as the time axis and the VI Usefulness Index (Huete *et al.* 1999) was used to weight the data points during the fitting procedure via a damped exponential transfer function. Observations that were flagged as clouds were assigned a weight of zero.

CR LSP was obtained by applying the Spline analysis of Time Series algorithm (SplITS, Mader 2012). SplITS is a computer code to fit spline models to remotely-sensed time series and to derive LSP. It is a data-driven method that is able to handle non-equidistant time series and to process the exact DOC. A set of 20 LSP parameters is derived for each pixel, including date-specific parameters, integral information about the growing seasons, amplitudes, etc. Our prediction approach can handle any of these parameters and simultaneously processes a number of  $p$  parameters for a given year  $y$ . CR LSP is reprojected on-the-fly with nearest neighbor resampling to match the extent, projection and resolution of the gridded MR data (see 3.2).

### 3.2 Medium resolution reflectance: Landsat

We prepared a comprehensive Landsat surface reflectance dataset, which was specifically developed for its use in applications that demand simplified pixel-based access, higher-level radiometric input data and require as many observations as possible (Frantz *et al.* 2016a). The atmospheric correction module includes radiative transfer code based correction (Tanré *et al.* 1979) of multiple atmospheric scattering processes (Sobolev 1975) with variable illumination/view geometry, a joint database- and image-based estimation of aerosol optical depth (AOD) over dark targets, adjacency effect correction and a spatio-temporally variable water vapor correction using MODIS data. Topographic normalization is achieved by a modified C-correction (Kobayashi and Sanga-Ngoie 2008) with 30 m SRTM data. Cloud and cloud shadow detection is performed with a modified version of the Fmask algorithm (Frantz *et al.* 2016a, Zhu and Woodcock 2012, Zhu *et al.* 2015, Frantz *et al.* 2015b). All available Landsat Level 1T data (Landsat 5, Landsat 7, and Landsat 8) were processed, are stored in a gridded data structure in binary image format, and are readily available as input candidates to our prediction algorithm. We define the term 'tile' as an entity of the processing grid and the term 'chip' as the gridded image datasets that are affiliated with a specific tile (Frantz *et al.* 2016a). 4524 tiles with 1000 x 1000 px (i.e. 194 WRS-2 frames) are needed to cover the study area and 963,563 chips (originating from 20,940 full Landsat images from 2001–2012) were considered to predict MR LSP.

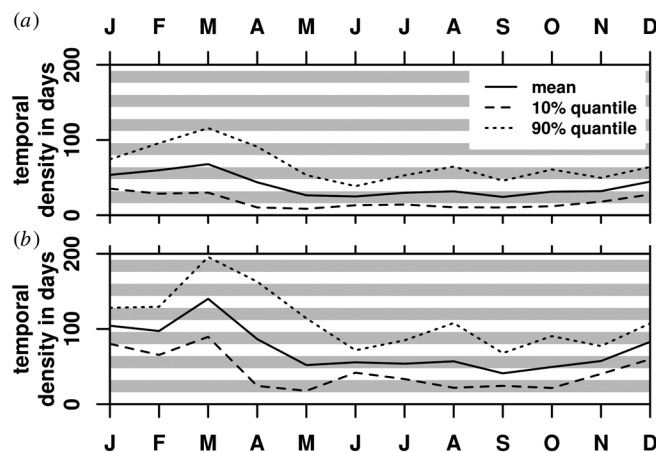


Fig. V-2. Temporal density of the available Landsat images per month from 2001–2012. Statistics were calculated per tile and then averaged for the complete study area. (a): Temporal density in all tiles; (b): Temporal density in tiles that do not have orbital overlaps. The alternating bars in the background indicate intervals of 16 days (nominal nadir repeat coverage of a single Landsat system).

Fig. V-2 displays the temporal density of all processed Landsat images per month from 2001–2012. When considering all tiles (Fig. V-2a), there is usually an observation within four nominal Landsat repeat cycles (i.e. 64 days) throughout the year on average. A large proportion of the data (90% quantile) is characterized by a lower repeat coverage. There is a pronounced seasonality where the repeat coverage in the drier months (May–November) is less than two repeat cycles on average (32 days) and the coverage in the wet season is worse. If only considering tiles that are not part of orbital overlap areas (Fig. V-2b), the temporal density is significantly worse. The repeat coverage in the drier months reduces to around four repeat cycles and the coverage in the wet season is very poor with an average revisit frequency of 90–100 days or more (December to April). A large proportion of the images (90% quantile) has significantly worse repeat coverage. Due to the relative proximity of the study area to the Equator, orbital overlaps are small, and as such Fig. V-2b is more important than Fig. V-2a in assessing if it would be possible to infer LSP reliably from this dataset for the complete area. In addition, the temporal density shown in Fig. V-2 was not corrected for cloud coverage, which is high in the wet season and virtually zero in the dry season, and as such would decrease the repeat coverage even more – of a given pixel – in the wet season. The given data density does not allow us to infer LSP directly, especially when considering that the vegetation period coincides with the wet season (roughly November to April).

## 4 Method

The main assumption of our method is that a few MR observations are sufficient to separate image regions with similar phenology qualitatively, but are not suited to quantify LSP directly with high temporal precision – which in turn is possible using CR data. Therefore, we propose that CR LSP can be related to the evolution of reflectance through time at the medium resolution – provided that the MR images are distributed reasonably well over the year. As such, we aim to link the very accurate CR LSP to the corresponding MR spatial features by exploiting their specific spatio-temporal patterns. This is achieved by using the information from the local pixel neighborhood at both resolutions. This approach is somewhat related to the well-known STARFM code (Gao *et al.* 2006), though we do not remain in reflectance feature space but directly predict LSP from CR LSP and MR reflectance inputs. Based on a few assumptions on the reliability of the CR and MR data under different conditions, we define several proxies at both resolutions (subsections 1–3) that define the final neighboring pixel's weight (4). In order to increase the computational performance, the MR reflectance data are aggregated prior to the prediction (5). The general workflow of the method is outlined in Fig. V-3; the corresponding sections are given in the corners of the boxes.

MR LSP is predicted using a focal filter approach with a circular kernel (kernel diameter  $k = 2 \cdot r + 1$  with radius  $r$ ). All pixels within  $r$  are considered to contribute to the prediction. The kernel size is the main tweakable input parameter and controls the level of detail of the prediction as well as processing time.

In principle, the predicted MR LSP for pixel  $(x,y)$  and LSP parameter  $p$ , i.e.  $M_{xy,p}$  is obtained by computing the weighted mean of the neighboring CR LSP pixels  $(j,i)$ , i.e.  $C_{ji,p}$  with a moving kernel of size  $k$ :

$$M_{xy,p} = \sum_{j=1}^k \sum_{i=1}^k (W'_{ji,p} C_{ji,p}) / \sum_{j=1}^k \sum_{i=1}^k W'_{ji,p}, \quad (\text{V-1})$$

where

- $(x,y), (j,i), k$ : Central pixel, neighbor pixel, kernel size.
- $p$ : Index for LSP parameter.
- $M_{xy,p}$ : Predicted medium-resolution LSP of central pixel.
- $C_{ji,p}$ : Coarse-resolution LSP of neighbor pixels.
- $W'_{ji,p}$ : neighbor pixel weight.



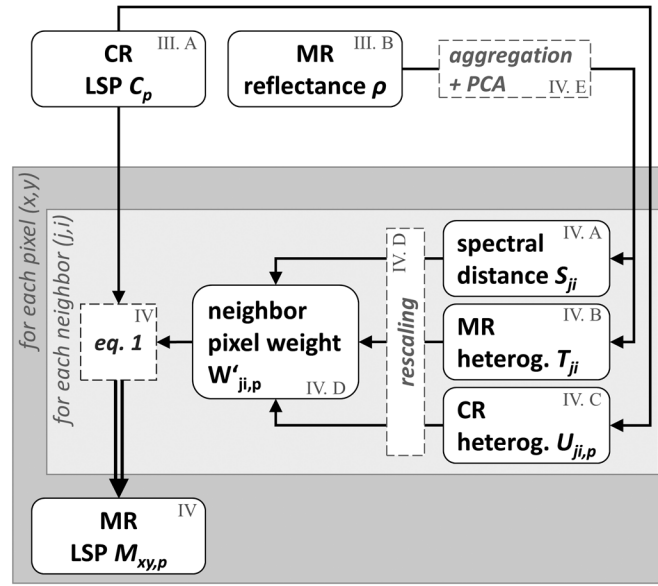


Fig. V-3. Workflow of the presented methodology with references to the sections and subsections.

Note that the rejection criteria are not accounted for in Eq. (V-1) for simplicity, e.g. the use of circular kernels.

In order to solve Eq. (V-1), we need to set up a weight  $W'_{ji,p}$  for each neighboring pixel  $(j,i)$  in order to calculate the MR pixel value at  $(x,y)$ . As outlined before, we weight the neighboring pixels according to several prediction proxies (1–3):

#### 4.1 Spectral distance

As the CR LSP is assumed to be related to the evolution of MR reflectance, a neighboring pixel  $(j,i)$  should contribute more to the weighted mean if it is spectrally similar to  $(x,y)$ . The spectral similarity is a proxy for the probability that the adjacent pixel is characterized by similar surface conditions, which increases the probability of phenological similarity. We measure the spectral distance  $S_{ji}$  by calculating the Mean Absolute Error (MAE) between the spectra at  $(x,y)$  and  $(j,i)$ :

$$S_{ji} = \frac{1}{n_b} \sum_{b=1}^{n_b} |\rho_{xy,b} - \rho_{ji,b}|, \quad (\text{V-2})$$

where  $b$  is the MR spectral band and  $n_b$  is the number of bands (see 4.5 for details).

High values of  $S_{ji}$  indicate a large spectral distance and should not be used, as  $(x,y)$  and  $(j,i)$  do not belong to the same land cover class. Similar to STARFM (Gao *et al.* 2006), the prediction is of higher quality if only within-class pixels are used. Nevertheless, there must also be enough pixels to make a good prediction. We use a dynamic cutoff threshold for  $S_{ji}$ :  $S_{max}$ . We start with an  $S_{max}$  of 0.05

MAE, which is a very strict cutoff threshold. If not enough pixels contribute to the prediction, we iteratively increase  $S_{max}$  by a factor of 2 until more than  $n_{min}$  neighboring pixels are available. Nevertheless, we only allow four iterations to avoid the prediction strength of the weighted mean being weakened too much. We dynamically determine  $n_{min}$  based on  $k$ , where  $n_{min}$  is 0.5% of  $n_k$  (the number of pixels in the kernel):

$$n_k = k^2 \pi / 4 \quad (\text{V-3})$$

$$n_{min} = 0.5 \cdot n_k / 100 \quad (\text{V-4})$$

Fig. V-4 schematically illustrates the prediction process with arbitrary data. The MR reflectance (only one MR band) and the CR LSP are shown in (a–b). The spectral distance proxy is displayed in Fig. V-4c and assumes low values for spectrally similar pixels.

## 4.2 Medium resolution heterogeneity

We propose that CR LSP is more representative at the MR scale if the CR sub-pixel heterogeneity is low. Therefore, we compute the spatial heterogeneity for every band in the MR spectral data. The overall heterogeneity score  $T_{ji}$  is the heterogeneity metric of the band with the greatest heterogeneity. We use a focal standard deviation filter to infer the heterogeneity with a kernel size of 11 px; the full width at half maximum (FWHM) of the line spread function in the scan direction is approximately 10 MR pixels for the red MODIS band (Barnes *et al.* 1998), which we rounded to the next odd number. The kernel size is adjustable in order to permit the usage of other combinations of MR/CR data.

The higher  $T_{ji}$  is, the more heterogeneous is the CR sub-pixel surface. Fig. V-4d displays  $T_{ji}$  for the arbitrary MR data in (a) and  $T_{ji}$  is highest where two cover types in the MR data adjoin.

## 4.3 Coarse resolution heterogeneity

We propose that CR LSP is also more representative at the MR scale if the CR LSP itself is spatially homogeneous. This is because it is more likely that the CR sub-pixel heterogeneity is low when the pixels are also homogeneous at their inherent resolution. Moreover, if the CR LSP is strongly heterogeneous, there are two adjacent CR pixels that have a substantially different phenology. As the real surface elements (as they would be sensed from an MR instrument) most likely do not match the CR pixel boundaries, the CR pixel boundary area cannot be used to estimate MR LSP reliably. Thus, we also compute the textural heterogeneity of the CR LSP for each parameter  $p$ . We use the same

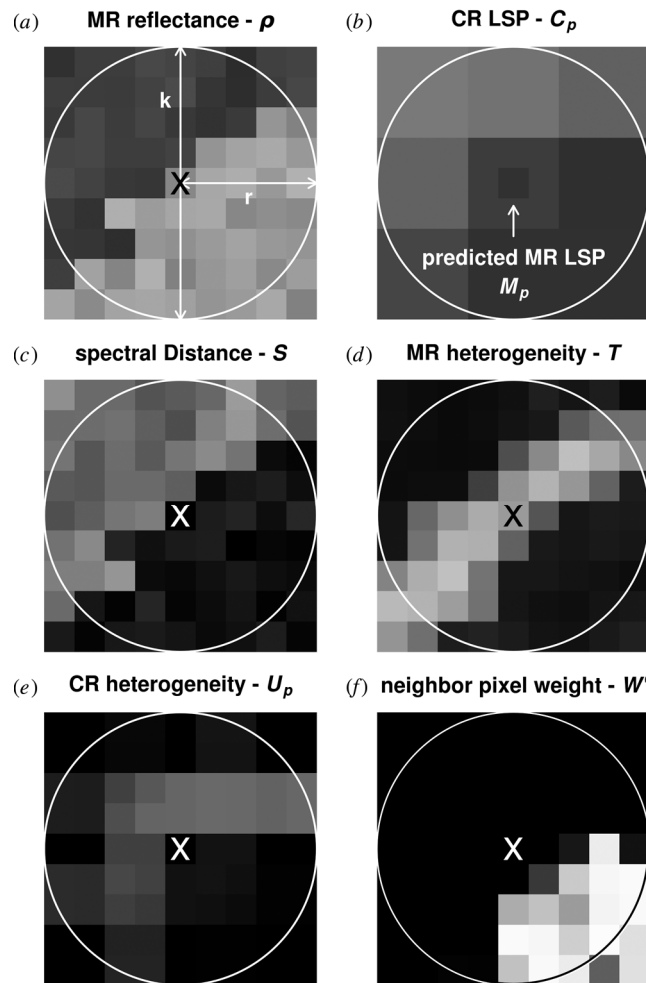


Fig. V-4. Schematic illustration of the prediction process. In this example, 1 CR pixel equals 9 MR pixels.

focal standard deviation filter as in the derivation of the MR texture. This filter accentuates the CR pixel boundaries if they are heterogeneous.

The CR heterogeneity weight  $U_{j,i,p}$  is the estimated CR texture of  $p$  at  $(j,i)$ . The higher  $U_{j,i,p}$  is, the more heterogeneous is CR LSP. Fig. V-4e displays  $U_{ji}$  for the arbitrary CR data in (b) and assumes the highest values in the pixel boundaries where the phenology differs substantially from CR pixel to CR pixel.

#### 4.4 Neighbor weight

In the next step, the retrieved weights  $S_{ji}$ ,  $T_{ji}$  and  $U_{j,i,p}$  are rescaled in order to avoid unit scale factors when calculating the total weight and to increase the flexibility of the presented methods when used with different continuous fields. In addition, rescaling increases the contrast between the best and the worst weights through a sigmoidal transfer function for emphasized usage of the best pixels

in each kernel. Therefore we apply a range adjustment (the fractional term in Eq. (5)) to the individual weights  $R_{ji}$  (i.e.  $S_{ji}$ ,  $T_{ji}$  and  $U_{ji,p}$ ) such that all weights range from 0–1, where 0 is the best pixel in the kernel and 1 is the worst. The logistic S-shaped transfer function with range adjustment of the general form

$$R'_{ji} = 1 / \left[ 1 + \exp \left( 25 \cdot \frac{R_{ji} - R_{min}}{R_{max} - R_{min}} - 7.5 \right) \right] \quad (\text{V-5})$$

is applied to all the weights  $R_{ji}$ , where  $R'_{ji}$  is the rescaled weight, i.e.  $S'_{ji}$ ,  $T'_{ji}$  and  $U'_{ji,p}$ . After transforming the weights,  $R'_{ji} = 1$  indicates a pixel that should contribute greatly to the prediction;  $R'_{ji} = 0$  does not contribute at all.

The final neighbor pixel weight  $W'_{ji,p}$  for the phenology descriptor  $p$  is then simply the product of the rescaled weights  $S'_{ji}$ ,  $T'_{ji}$  and  $U'_{ji,p}$ :

$$W'_{ji,p} = S'_{ji} \cdot T'_{ji} \cdot U'_{ji,p}. \quad (\text{V-6})$$

Fig. V-4f displays  $W'_{ji,p}$ , which assumes the highest values in areas where the three proxies  $S_{ji}$ ,  $T_{ji}$  and  $U_{ji,p}$  are small. The CR LSP  $C_{ji,p}$  in (b) is finally averaged with Eq. (V-6) to predict the LSP of the central pixel, i.e.  $M_{xy,p}$ . The prediction is indicated by the highlighted MR pixel in (b) and is more similar to the pure CR LSP pixels that belong to the same MR land cover class in the bottom-right corner.

## 4.5 Aggregation of MR data

We feed the prediction code with MR reflectance from several seasonal windows within the year under consideration  $y$ . The parameterization of the window lengths and numbers is in control of the user and needs to be adjusted for different study areas. Based on an analysis of the CR LSP and on MR data availability, we defined four windows as they are documented in Table V-1. They approximate the main climatic seasons and their unequal duration compensates for the uneven MR data availability throughout the year.

Each window is filled with the pixel-mean of all available clear-sky MR images. In a first attempt, only Landsat images that were captured with working Scan Line Corrector (SLC-on) are considered. If SLC-on data are insufficient, SLC-off data are also considered. Occasionally, a window is partly or completely unfilled after this procedure, because there was no valid observation at all. Due to the following statistical procedures, we cannot permit no-data observations, and fill those pixels with the pixel mean of the other windows.

Table V-1. Definition of the seasonal windows

seasonal window	window start	window end
left wet season	312 (-1)	130 (0)
cool dry season	131 (0)	218 (0)
hot dry season	219 (0)	330 (0)
right wet season	331 (0)	130 (+1)

Definition of the seasonal windows used for selecting MR input. Values are day-of-year; the values in the brackets represent the year relative to the year under consideration  $y$ , which means that the ‘left wet season’ window starts in the previous year and the ‘right wet season’ extends to the next year.

The MR data volume is reduced with a principal component analysis (PCA) of the windowed MR data. All components that explain at least 97.5% of the overall variance are retained. This step is not strictly necessary to produce good results, but it was merely introduced because of performance considerations. Fewer bands decrease the computational cost of obtaining  $S_{ji}$  and the PCA retains the information that matters most for the discrimination of spectrally similar pixels. Afterwards, the components are normalized in order to avoid that  $S_{ji}$  is merely driven by the first component (i.e. the overall contrast) as key information for the discrimination of phenological types is also inherent in other components.

## 5 Implementation

The code is entirely based on open-source software and is written in C. The application programming interface (API) of the Geospatial Data Abstraction Library (GDAL) is used to reproject the MODIS data to match the Landsat tiles. The PCA was computed using the GNU Scientific Library (GSL) with matrix support provided by the Basic Linear Algebra Subprograms (BLAS) library. Shared memory parallelization was implemented by utilizing the Open Multi-Processing (OpenMP) API. The processing runs on a tile basis. In order to produce a seamless product, we append data of the neighboring 8 tiles to the tile under consideration. The number of appended lines/columns depends on the chosen kernel size  $k$ .

## 6 Algorithm test with simulated data

In order to ensure that the presented approach performs as wanted – within the limits of its assumptions – we performed a simulation study. As such, (i) we generated an artificial simulated landscape that reflects observed landscape characteristics. (ii) We simulated corresponding MR reflectance and (iii) MR LSP based on a statistical analysis of recent Landsat data. CR LSP (iv) was inferred by degrading the MR LSP. We propose our method to be functional if the (v) MR LSP can

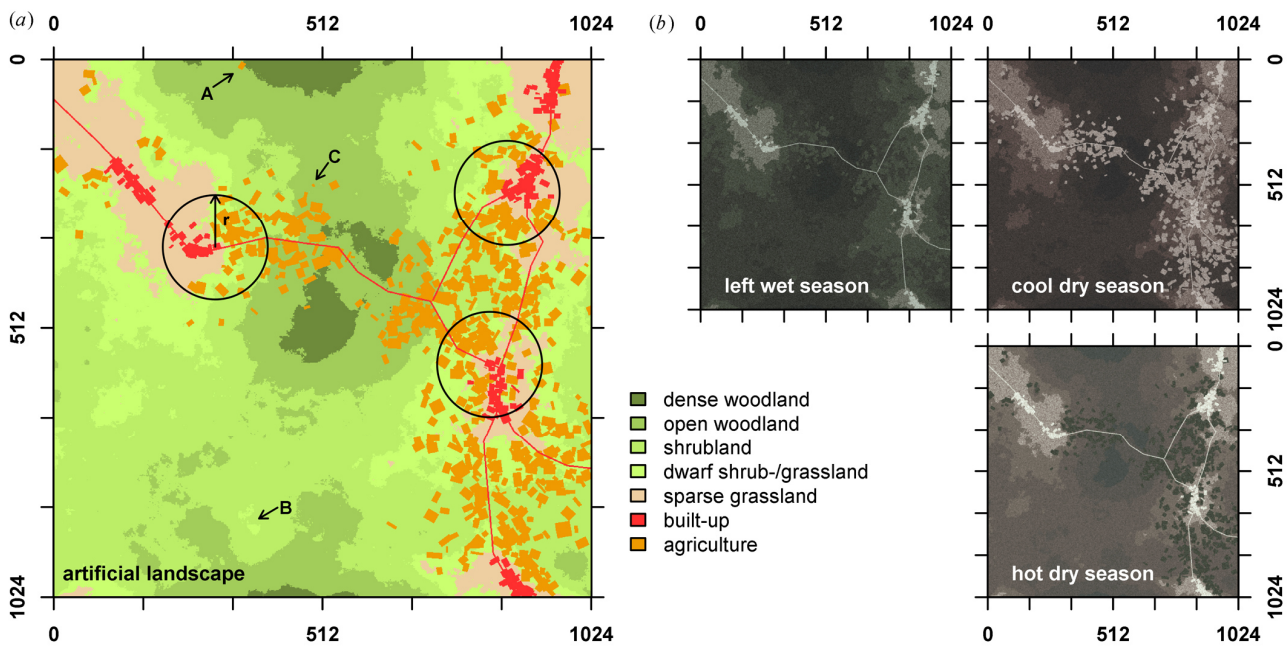


Fig. V-5. Simulated random landscape (a) and corresponding true color MR reflectance images (b) in three seasonal windows (left wet, cool dry and hot dry season). The marked regions in (a) are discussed in the text. The same stretch was applied to all images in (b). The size of the simulated landscape is 1024 x 1024 px; the prediction radius  $r$  is 100 px.

be reasonably well restored by predicting it from degraded CR LSP and simulated MR reflectance inputs.

(i) Southern African environments are generally composed of large wood-, shrub- and grassland patches with smaller agricultural and urban elements. A random multifractal map (Fig. V-5a) was generated with QRULE (Gardner and Urban 2007), and we manually placed streets and defined six urban seeds. Built-up structures were randomly placed around the streets following a lognormal distribution with a penalty on the distance to the next seed. The structure orientation was inferred from street bearing and the width and height were varied by random numbers for the normal distribution. Constrained by knowledge about the occurrence of agriculture in different land covers, and as a function of distance to streets and preferably around settlements (Schneibel *et al.* 2013), fields with random sizes and orientations were also randomly placed in the landscape.

(ii) Based on an existing MR classification (Schneibel *et al.* 2013), we extracted class-wise statistics (mean and standard deviation) within the left green, cool dry and hot dry season windows (Table V-1) from the 2013/14 Landsat 7/8 time series to simulate MR reflectance images (Fig. V-5b). This was achieved by assigning the class-specific reflectance (+ noise) to the simulated landscape (using normally distributed random numbers while ensuring autocorrelation between the bands). The



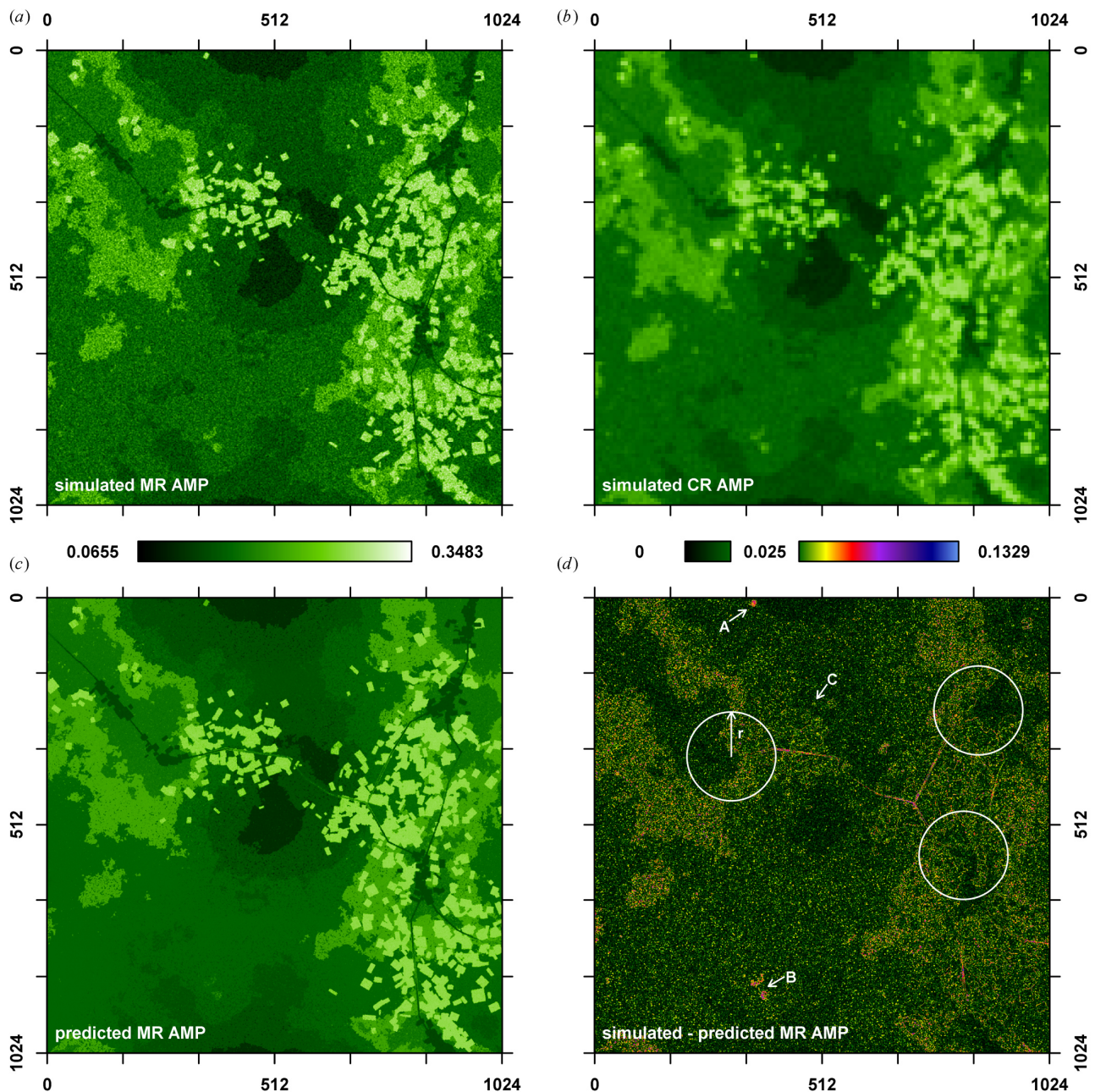


Fig. V-6. Algorithm test with simulated data. (a) simulated MR amplitude; (b) simulated CR amplitude; (c) predicted MR amplitude; (d) absolute difference between simulated and predicted MR amplitude. The marked regions in (d) are discussed in the text and are also shown in Fig. V-5a. The monochromatic color bar refers to the amplitude values (a-c) and the right color bar refers to the absolute amplitude difference (d). The size of the simulated landscape is 1024 x 1024 px; the prediction radius  $r$  is 100 px.

images were filtered (3 x 3 px lowpass) in order to add spatial autocorrelation and to avoid sharp transitions between land covers to approximate real satellite acquisitions better.

(iii) Class-specific MR LSP statistics were inferred from the 2013/14 Landsat time series (mean and standard deviation). Analogous to (ii), normally distributed random numbers were generated and spatial autocorrelation was added. We exemplarily show results for the EVI amplitude

(AMP, Fig. V-6a) - as this parameter can be inferred from the densified Landsat 7/8 time series with sufficient precision.

(iv) The MR AMP was degraded to 250 m (i.e. CR AMP, Fig. V-6b) using a MODIS point spread function (Barnes *et al.* 1998).

(v) Using the degraded CR LSP (iv) and simulated MR reflectance (ii) as input, we predict MR LSP (Fig. V-6c) and assess if the presented approach is able to restore the simulated MR LSP (iii) reasonably well. The kernel size  $k$  was set to 200 px. The difference between simulated and predicted MR LSP is shown in Fig. V-6d, and the statistical correlation as well as histograms are shown in Fig. V-7.

The predicted landscape patches are characterized by clearly defined boundaries (Fig. V-6c) that are even slightly sharper than in the simulated AMP (Fig. V-6a). AMP values were also predicted with high precision (see Fig. V-7,  $R^2 = 0.84$ ). It is very striking that the predicted AMP is less noisy than the inputs (homogeneous appeal in Fig. V-6c) and the distinct LSP of different land cover classes can be better separated than in the simulated dataset (see the 1D-histograms in Fig. V-7). This is caused by the average-based prediction process that strictly uses only the spectrally nearest neighbors. Fig. V-6d depicts the difference between simulated and predicted AMP; 82.7% of all pixels differ by less than 0.025, which is approximately the error that can be expected from a radiometric preprocessing chain (Röder *et al.* 2005). Nevertheless, there are also many pixels with higher differences, mostly as a result of the difference in noise between simulated and predicted AMP. The differences are highest in the dwarf shrub-/grasslands, which is also the land cover with highest variability in AMP and reflectance inputs; whereas the settlements and dense woodlands have low differences due to their low AMP and reflectance variability. There is also some remaining noise in the predicted AMP (Fig. V-6c), which occurs because of the noise-induced inseparability of similar land covers (partially overlapping normal distributions in simulated MR reflectance and AMP; see 1D-histogram in Fig. V-7). In addition, there are also object size- and distance-related effects that clearly demonstrate the strengths and limitations of the presented approach. It is apparent that the prediction strength of the built-up class (street) rapidly decreases once the distance to the outskirts of the settlement exceeds the radius  $r$  (as indicated by the three circles). There were no neighboring pure built-up CR pixels and the street itself was too small (i.e. not even visible in the CR image). Analogously, any object that is smaller than the Field-of-View of the CR instrument (the FWHM of the line spread function in scan direction is approximately 10 MR pixels for the red MODIS band (Barnes *et al.* 1998)) cannot be precisely predicted if there are no pure CR pixels within  $r$ , see e.g. the



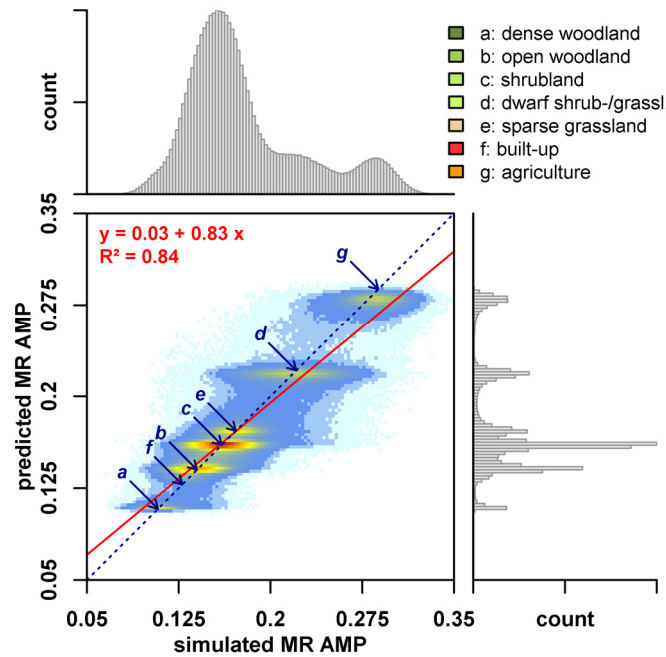


Fig. V-7. 2D-histogram of simulated and predicted MR amplitude, bordered by the corresponding 1D-histograms. The letters indicate the simulated land-cover clusters and the legend colors match Fig. V-5a.

objects marked by ‘A’ and ‘B’ in Fig. V-6. On the contrary, even very small objects can be predicted with sufficient precision if pure pixels exist nearby (see e.g. ‘C’ in Fig. V-6).

## 7 Application to real data

We predicted the POS, EOS, MOS and SOS parameters for the 12 year period from 2001–2012 at Landsat spatial resolution for the entire study area. The kernel size  $k$  was set to 200 pixels.

Fig. V-8 displays prediction results ( $b$ ) as well as the input CR LSP ( $a$ ) for a phenologically diverse area in southern Zambia (15.83°S, 27.93°E; R/G/B: POS/EOS/MOS for 2005). The location of the area is indicated by the “+” in Fig. V-1. The sugar production in Mazabuka is Zambia’s biggest agricultural site and largest freshwater consumer (Richardson 2010). Widespread irrigation causes a broad mix of phenology that contrasts against both the naturally occurring woodlands and the riverine vegetation of the Kafue River. The images reveal that the general composition of LSP is adequately preserved in the predicted image, which is also supported by the nearly identical histograms of CR and MR LSP (Fig. V-8c). The prediction accounts for the mixed pixels in the CR image and has clearly defined object boundaries. This is especially pronounced in the very heterogeneous agricultural areas where e.g. the circular shape of the center pivots or the parcel boundaries were successfully reconstructed (see the enlarged subsets ‘A’ and ‘B’ in the right panel of Fig. V-8).

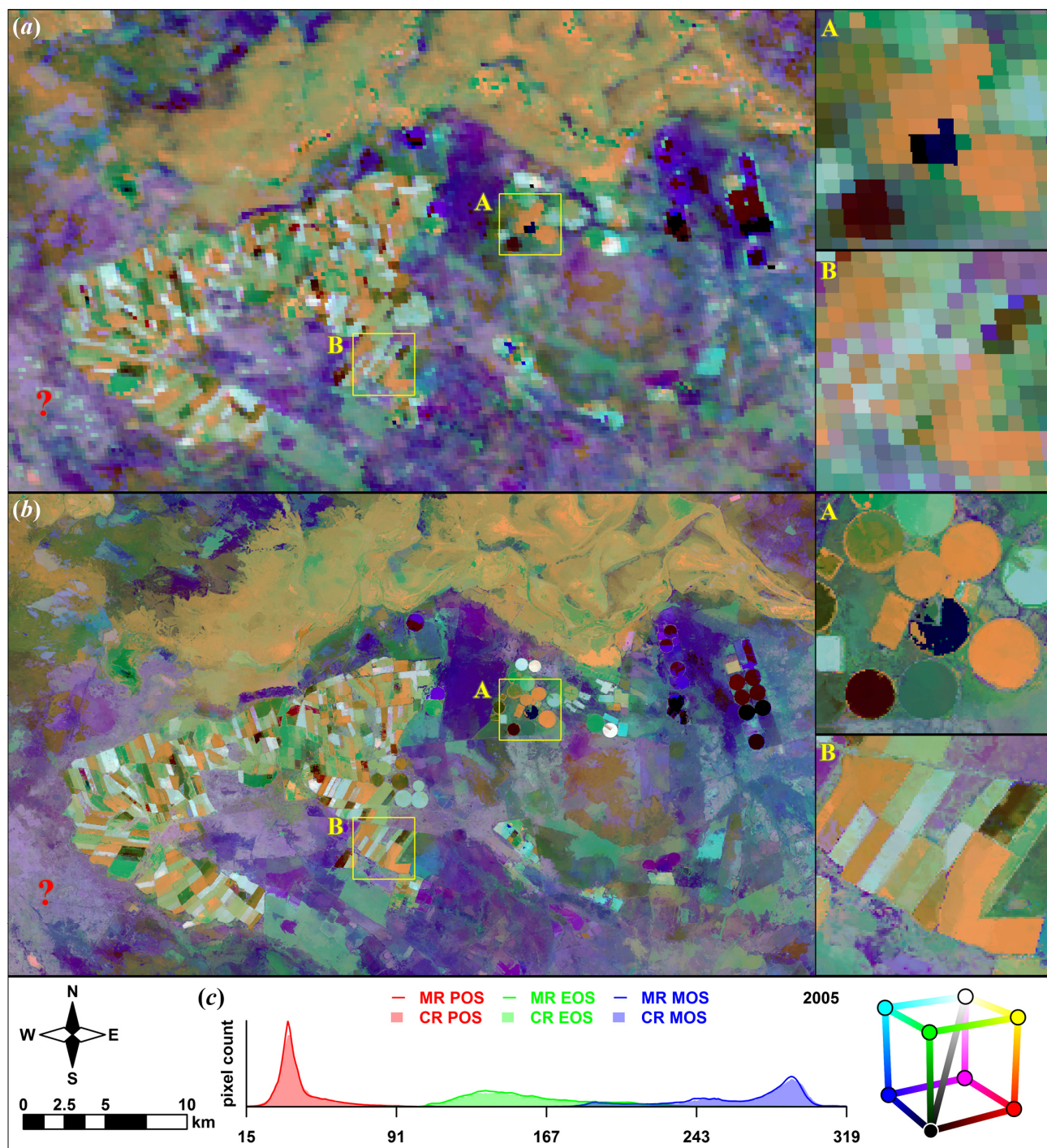


Fig. V-8. Comparison of coarse-resolution LSP (a) and predicted medium-resolution LSP (b). The RGB-composite depicts the peak of season (POS, red), end of season (EOS, green) and minimum of season (MOS, blue) for 2005. Selected areas are enlarged in the right panel (4x zoom). (c) Histograms of the depicted data; the lines refer to MR LSP and the polygons to CR LSP.

Fig. V-9a–d and Fig. V-10a–d depict the MR reflectance input for the four seasonal windows for the subsets ‘A’ and ‘B’, respectively. The data availability was 1-2, 1-2, 4 and 1 SLC-on observations per pixel for the left wet, cool dry, hot dry and right wet season, respectively. The data availability was rather low in most windows, but the approach produces reliable results if at least one high-quality



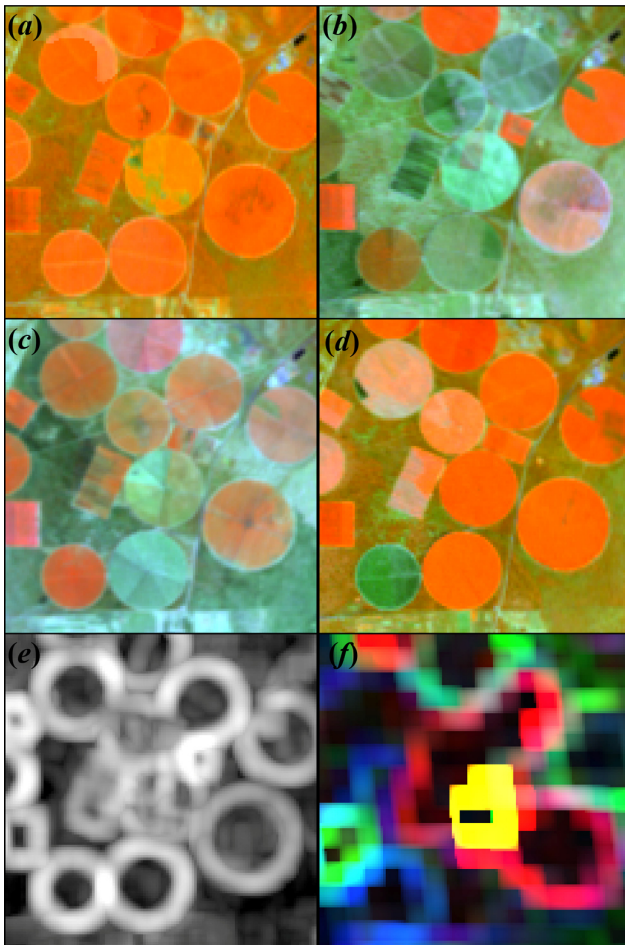


Fig. V-9. MR reflectance input data (*a–d*), MR heterogeneity  $T_{ji}$  (*e*) and CR heterogeneity  $U_{ji,p}$  (*f*) for subset ‘A’ in Fig. V-8. (*a–d*): Average reflectance for the four seasonal windows (Table V-1) with RGB = near infrared, shortwave infrared, red. The same stretch is applied to all images. (*f*): RGB composite of  $U_{ji,p}$  for  $p = \text{POS, EOS and MOS}$ .

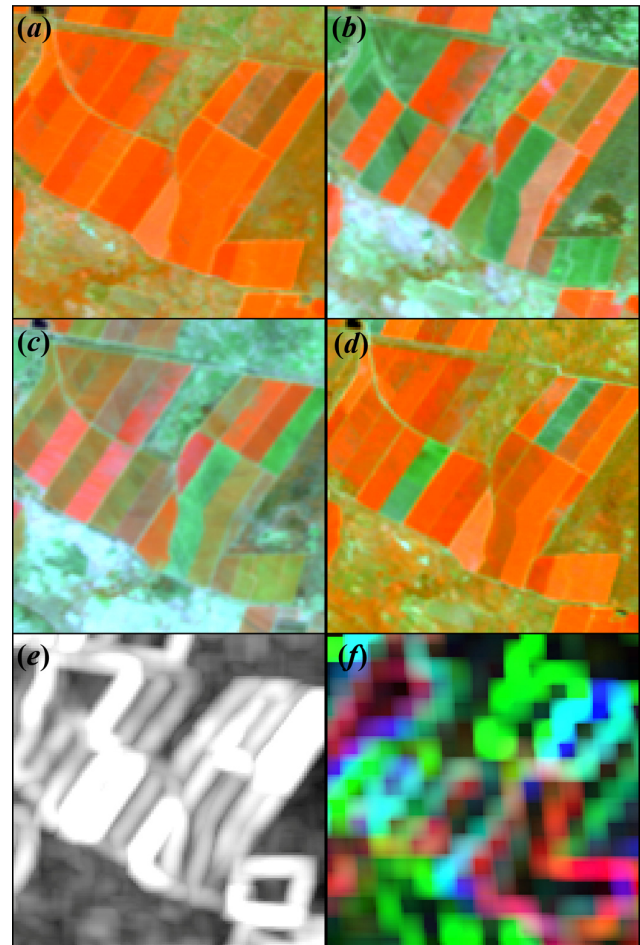


Fig. V-10. MR reflectance input data (*a–d*), MR heterogeneity  $T_{ji}$  (*e*) and CR heterogeneity  $U_{ji,p}$  (*f*) for subset ‘B’ in Fig. V-8. (*a–d*): Average reflectance for the four seasonal windows (Table V-1) with RGB = near infrared, shortwave infrared, red. The same stretch is applied to all images. (*f*): RGB composite of  $U_{ji,p}$  for  $p = \text{POS, EOS and MOS}$ .

image per phenological key stage is available (as approximated by the seasonal windows). The windowed reflectance images allow for a qualitative separation of image regions with similar phenology. In addition, the MR heterogeneity  $T_{ji}$  and the CR heterogeneity  $U_{ji,p}$  of the POS, EOS and MOS parameters are also shown in Fig. V-9*e–f* and Fig. V-10*e–f*, and indicate pixels that are preferred for predicting the MR LSP (dark colors). The successful restoration of clearly defined MR patches like the agricultural parcels in Fig. V-8 supports the validity of the presented procedure and the prediction is characterized by great spatial detail.

Nevertheless, some features that are present in CR LSP are not preserved in the prediction, e.g. the cyan pixels marked by “?” in Fig. V-8. The temporal resolution of the few input windows might be too low, which would imply that this specific phenological process could not be properly

disentangled. The three implemented prediction proxies might also be insufficient in this case, and further inclusion of other proxies might potentially mitigate the mismatch – provided that a further generally valid assumption can be developed. The prediction failed to match the CR LSP with well-defined MR objects that clearly contrast against the surroundings. The mismatch could also be caused by uncertainties in the processing chain of any input data source. The radiometric processing quality of the input Landsat data is generally sound (98.8% of all data was assessed (Frantz *et al.* 2016a) to be within the expected 2.5% algorithm accuracy (Röder *et al.* 2005)) – although it cannot be ruled out that single images are not perfectly corrected, which could e.g. be caused by using modeled AOD fallback values in areas where dark targets do not exist (Frantz *et al.* 2015a). The observed artifacts could also be caused by compositing-related noise in MODIS VI data, which is known to affect the precise determination of LSP (Huete *et al.* 2002). Though the effect of noise is reduced by applying a smoothing spline, remnant artifacts still occur. MODIS VI noise is especially pronounced in arid areas during the rainy season due to the substantially decreased high-quality observation frequency, remaining sensor view angle effects and residual cloud and aerosol contamination (Huete *et al.* 2002). As the simulation (section 6) demonstrated the de-noising capabilities of the presented approach, it is likely that this noise was effectively flattened in the process. Nevertheless, we cannot address the source of this discrepancy with certainty.

## 8 Conclusions

We developed a prediction approach that fuses coarse resolution LSP with medium resolution reflectance imagery. The required medium resolution data density is rather low. Nevertheless, the prediction quality severely decreases if images are not available at several phenological key stages throughout the year. If sufficient temporal sampling is not given any more, the main assumption of the method is violated and areas with similar LSP properties cannot be delineated due to the lack of temporal contrast. This is also the case if the temporal-spectral separability within the pre-defined windows is not sufficient. LSP is directly predicted at the finer scale, and thus the costly need for generating a dense image series at the target resolution is circumvented. The general landscape composition of LSP is well preserved in the prediction, and medium resolution objects are spatially well-defined and have very clear boundaries. LSP values are reliably transferred to the spatial structure at medium resolution. The method implicitly de-noises LSP, yet it preserves sharp edges. The size of the smallest reliably predicted object coincides with the effective size of the coarse resolution pixels (determined by IFOV). Nevertheless, even significantly smaller elements can be successfully predicted if there are pure coarse resolution pixels within the search kernel – if not, the prediction strength decreases. The size of the kernel is the most important determinant regarding prediction

quality, but also with respect to processing time. The results indicate that the generated medium resolution LSP is well-suited for its further usage. The method was presented to be used with Southern African MODIS LSP and Landsat reflectance data, but the method is general enough to be also applied to other study areas, sensor pairs and continuous fields, e.g. SPOT, RapidEye or Sentinel-2 data and above-ground biomass (Saatchi *et al.* 2011).

## **Acknowledgment**

Landsat data courtesy of the U.S. Geological Survey. The MODIS data were retrieved from the online Data Pool, courtesy of the NASA Land Processes Distributed Active Archive Center (LP DAAC), USGS/Earth Resources Observation and Science (EROS) Center, Sioux Falls, South Dakota, [https://lpdaac.usgs.gov/data\\_access/data\\_pool](https://lpdaac.usgs.gov/data_access/data_pool). KAZA TFCA information and boundary courtesy of Peace Parks Foundation. We thank Anne Schneibel for providing the Landsat classification and information on landscape composition used in the simulation study. The authors also thank the three anonymous reviewers whose helpful comments helped to substantially improve the manuscript.



## **Chapter VI**

# **Phenology-Adaptive Pixel-Based Compositing using Optical Earth Observation Imagery**

*In revision for Remote Sensing of Environment.*

David Frantz, Achim Röder, Marion Stellmes, and Joachim Hill

© 2017 Elsevier Inc. All rights reserved.

A shortened version has been accepted by the publisher, thus the version-of-record will differ from the following manuscript. The paper has been through thematic peer review; editorial changes were made before acceptance. It has not been subject to copy-editing, proofreading and formatting added by the publisher. The version-of-record can be accessed at:

*Remote Sensing of Environment 190, March 2017, 331-347.*

DOI: 10.1016/j.rse.2017.01.002

<http://www.sciencedirect.com/science/article/pii/S0034425717300032>

## Abstract

The need for operational monitoring of landscape processes on the national to global scale led to an increased demand for pixel-based composites using moderate- to medium-resolution earth observation (EO) archives. Commonly, composites are generated without explicit consideration of temporal criteria but are rather based on optimizing band indices within a pre-defined temporal window. However, for certain applications phenology-adapted composites that represent the land surface as being in the same phenological stage are required. For instance, tree type or age discrimination for areas with terrain altitude induced shifts in greening up or senescence might greatly benefit from such coherent data sets. We developed a novel pixel-based compositing technique that dynamically adjusts the selection process to the underlying land surface phenology (LSP) of each pixel. By doing so, phenologically sound composites across large areas can be derived for regular intervals and different phenological points in time, e.g. peak, end or minimum of season. Various DOY (day of year) scoring functions were implemented to flexibly define the phenological target. The technique can be applied to any kind of gridded EO archive, which we demonstrated for MODIS and Landsat data. It was also shown that the technique is general enough to be applied globally. Homogeneous and seamless multi-annual composites could be generated across the whole of Zambia (approx.  $750 \cdot 10^3 \text{ km}^2$ ) for most seasons. As an exception, we found even very frequent MODIS observations to be insufficient to generate peak vegetation composites as the green growth in our study area coincides with the rainy season. The phenology-adaptive composites were compared to static ones, i.e. using a single and global target DOY. Results clearly indicated that biomass levels differ significantly if the pixel-based LSP diverges from the static target DOY substantially. The resulting composites were shown to perform a phenological normalization across elevation gradients and land cover classes. However, the implications are non-trivial and the characteristics of both methods need to be considered cautiously before deciding which approach is superior with regards to a specific thematic application. The inter- to intra-annual data contribution was handled with a single parameter, which in combination with different data availabilities between and within the seasons, determines whether an observation from the target year or an observation from an adjacent year closer to the phenological target is selected. The quality of the MODIS and Landsat composites, as well as the performance of the phenology-adaptive and static compositing techniques was assured using a quantitative cross-comparison. The generation of a 12-year annual time series demonstrated the feasibility for land cover change and modification mapping. Several change processes were clearly discriminable. The resulting phenologically coherent composites are important to establish national, regional or even global landscape monitoring, reporting and verification systems.



## 1 Introduction

The need for establishing operational landscape monitoring systems on the national to global scale is more pressing than ever (Hansen and Loveland 2012), e.g. to support the “Reducing Emissions from Deforestation and Forest Degradation and the role of conservation, sustainable management of forests and enhancement of forest carbon stocks in developing countries” (REDD+) mechanism. In this context, it is inevitable to establish national measurement, reporting and verification systems (MRV, Herold and Skutsch 2011), which can only be instated on the basis of non-leaking, wall-to-wall remote sensing products (DeFries *et al.* 2007, Gibbs *et al.* 2007).

The availability of moderate (100–500 m) to medium (10–100 m) resolution optical imagery steadily increased throughout the past decade, starting with the global and operational deliverance of user-friendly standard products (250–500 m) from the Moderate Resolution Imaging Spectroradiometer (MODIS; Justice *et al.* 2002). A change in data policy towards unlimited access to 30 m Landsat data (Woodcock *et al.* 2008) fostered a new era in the field of earth observation (EO) and changed the usage of satellite imagery fundamentally (Wulder *et al.* 2012). The recent commissioning of open access Sentinel-2A imagery (10–20 m) has once again increased the operational monitoring capabilities with optical EO data through increased spatial, temporal and spectral resolution (Drusch *et al.* 2012). The launch of Sentinel-2B, scheduled for early 2017, will further double this revisit frequency, and the continuity of the Landsat mission is also safeguarded; currently Landsat 9 is planned to be launched in 2023.

However, with the ever increasing data volume also comes unprecedented data pressure: although data has become available to everyone, the high technical demand in terms of data processing, storage (Gibbs *et al.* 2007) and also downlink capabilities (Roy *et al.* 2010b) currently bar part of the science community from utilizing complete EO archives adequately. As such, it is of major importance to develop methods for enriching these massive data pools, and to provide ready-to-use, preprocessed baseline data for regular intervals, e.g. for 5 year reporting intervals as required for operational forest monitoring (Penman *et al.* 2003). Pixel-based composites (PBC) are suitable products to accomplish this task, as they substantially reduce the data volume to enable ‘traditional’ analyses (e.g. land cover / change classification as in Griffiths *et al.* 2013a), provide cloud-free and seamless images over large areas (Holben 1986), but nonetheless make use of the full archive depth implicitly.

Numerous compositing techniques were developed for their use with optical EO time series, most notably with the Advanced Very High Resolution Radiometer (AVHRR), MODIS and various

Landsat sensors. Detailed overviews of existing compositing methods and their specific disadvantages can be found in (Dennison *et al.* 2007) or (Lück and van Niekerk 2016). Most commonly, compositing criteria are based on optimizing band or index statistics (e.g. maximum, minimum or median selection, see Holben 1986, Cabral *et al.* 2003, Dennison *et al.* 2005, Flood 2013), sometimes amended by view angle constraints (e.g. Huete *et al.* 2002). It is yet undecided which compositing technique is best (Lück and van Niekerk 2016), as most techniques have certain limitations that decrease the product quality (Dennison *et al.* 2007).

In the past years, the compositing of Landsat data gained enormous popularity (e.g. Griffiths *et al.* 2013b, Roy *et al.* 2010a, Flood 2013), which on the one hand is a result of political, technical and algorithmic progress (Wulder *et al.* 2012), and on the other hand is driven by the demand for seamless (supra-) national “images” at finer spatial resolution. For a range of analyses (Song *et al.* 2001), the generation of composites using top-of-atmosphere (TOA) reflectance inputs, as employed in the Web-enabled Landsat Data project (WELD, Roy *et al.* 2010a) is a straightforward and sufficiently precise procedure. However, other analyses like the quantification of within-state processes – such as forest degradation – require higher level radiometric input data (Hansen and Loveland 2012). For this purpose, a number of large-area production systems exist. The Landsat Ecosystem Disturbance Adaptive Processing System (LEDAPS, Masek *et al.* 2006), which is considered as state of the art standard Landsat product, was e.g. used to generate radiometrically normalized composites across the Carpathians (Griffiths *et al.* 2013b) and Canada (White *et al.* 2014). A full integration of atmospheric correction procedures with further corrections for topographic and bidirectional effects, as well as homogenizing algorithmic for multiple sensors (e.g. Frantz *et al.* 2016a) might additionally pave the way for a number of more advanced analysis procedures like within-state gradual change detection (Vogelmann *et al.* in press).

Although Landsat data receive largest attention in the context of compositing, coarser-resolution data like MODIS or the recently launched Sentinel-3A may be equally valuable for the global assessment of land surface processes, e.g. to identify hot spot areas of forest loss (DeFries *et al.* 2007). As such, flexible compositing techniques that can be applied to any kind of optical EO image archive are required.

Commonly, compositing techniques are designed to provide time series of regularly spaced images (e.g. 8-day global MODIS composites (Justice *et al.* 2002) or monthly to annual Landsat composites (Roy *et al.* 2010a)), though it is not always feasible to generate gap-free products where frequent clear-sky observations cannot be guaranteed. As an example, even annual Landsat composites – of usable quality – cannot be generated in parts of the world (e.g. Griffiths *et al.* 2013b),

due to limited data availability as a consequence of adverse climatic settings and non-systematic acquisition plans outside of the United States. For many operational monitoring tasks, such frequent observations are not necessarily required, e.g. the assessment of carbon stock changes (Penman *et al.* 2003). As such, another class of compositing algorithms was developed that not only use observations from a narrow temporal window, but instead consider all data within a couple of years. Instead of optimizing a single spectral criterion, a parametric weighting scheme is used to combine a multitude of selection criteria, especially introducing temporal characteristics to anchor the composite to a pre-defined Day-of-the-Year (DOY, Griffiths *et al.* 2013b).

Shortcomings of this method mainly occur where phenological differences within target areas result in spectrally ambiguous composites. For instance, barren fields might be falsely classified as fallows if the composited information was acquired in an unfortunate phenological state (Griffiths *et al.* 2013a), or seasonal variations in broadleaved canopies might erroneously be classified as deforestation (DeFries *et al.* 2007). This makes a strong case for the generation of phenologically coherent pixel-based composites. Whilst using a fixed DOY might be a sound strategy if good knowledge on the regional seasonality is available (Griffiths *et al.* 2013b), results may be improved if spatial and temporal variations in LSP are considered explicitly. Large-scale variations in LSP are commonly a result of several abiotic factors, among them topographic factors such as altitude (Jochner *et al.* 2012, Arroyo 1990) and aspect (Arroyo *et al.* 1981), climatic factors such as temperature (Williams-Linera 1997, White *et al.* 1997), rainfall (White *et al.* 1997), continentality (Arroyo 1990), irradiance (Bollen and Donati 2005) and day length (Bollen and Donati 2005). Biotic factors like the degree of urbanization (Jochner *et al.* 2012) also influence LSP. Local variations in LSP can also be significant, and are especially common in water-limited dryland landscapes (or in agricultural areas in general), where one land cover class has unlimited water supply (e.g. riverine or swamp vegetation) whereas other land cover classes quickly dry out after the offset of the rains. In addition, inter-annual variations in LSP can also be substantial (White *et al.* 1997, Atkinson *et al.* 2012, Atzberger *et al.* 2013), e.g. El Niño events decrease the wet season rainfalls and lengthen the dry season in the Amazon forest (Asner *et al.* 2000). Landscape processes like burning can also abruptly end the green season, whereas the season may extend significantly longer in fire-free years (Frantz *et al.* 2016b).

Consequently, a pixel-based LSP dataset as temporal target layer would allow for a more data-driven parameterization and could eliminate the need to manually parameterize the target DOY. Accordingly, we propose a compositing technique that

- employs a parametric weighting scheme with full consideration of annual LSP at the pixel-scale, to generate phenologically coherent composites across large areas,

- allows for a data-driven parameterization of temporal compositing characteristics,
- is flexible with regards of using different compositing criteria,
- is general enough for global application, and
- may be applied to any gridded EO archive.

We introduce our study area with an emphasis on the abiotic factors that shape LSP in section 2. Section 3 provides a brief input data description regarding reflectance and LSP products, including an assessment of data availability. The phenology-adaptive compositing technique is described in section 4, and will be applied to the daily surface reflectance MODIS product and to a nadir bidirectional reflectance distribution function (BRDF) adjusted Landsat reflectance (NBAR) dataset. Compositing statistics in terms of the temporal successfulness of approaching the target DOY and year are presented for both datasets. As a direct result of the outstanding temporal characteristics of MODIS, we demonstrate the effectiveness of our approach by comparing phenology-adaptive MODIS composites to their “fixed-DOY” equivalents using map representations of differences in the Enhanced Vegetation Index (EVI), followed by a quantitative analysis and a demonstration of the phenological normalization across an elevation gradient and between land covers. Global applicability is demonstrated by generating MODIS composites across a latitudinal gradient from boreal Russia to South Africa. The Landsat composite quality is ensured by a quantitative comparison to the MODIS composites, and eventually, a 12-year annual Landsat time series is employed to characterize drastic and decadal-scale landscape dynamics across Zambia. Results are presented in section 5, and are discussed in section 6, including a discussion of the utility of the phenology-adaptive and static techniques with regard to different applications. The paper ends with conclusions in section 7.

## 2 Study Area

Zambia was chosen as study area (approx.  $750 \cdot 10^3$  km<sup>2</sup>) due to its relevance as being qualified for REDD+ financial support because of its considerable forest and woodland cover. Furthermore, the interaction of regional wind currents and terrain supported the development of distinct vegetation patterns with both large-scale gradients and local variations in LSP.

Zambian climate is strongly dependent on elevation, and features tropical-warm climate on the predominant high plateaus (1000 m a.s.l.). Tropical-hot climate characterizes the lower valley plains (325-920 m a.s.l.) in the South, while tropical-cool climate is found on the highest plateaus, e.g. the Nyika Plateau in the North-East (2100-2200 m a.s.l.). The terrain of Zambia is shown in Fig. VI-1a. The seasonality is closely tied to seasonal changes in large scale air movement and solar configuration, which results in three hygrothermal seasons; i.e. (i) the hot wet season (November-April), (ii) cool dry

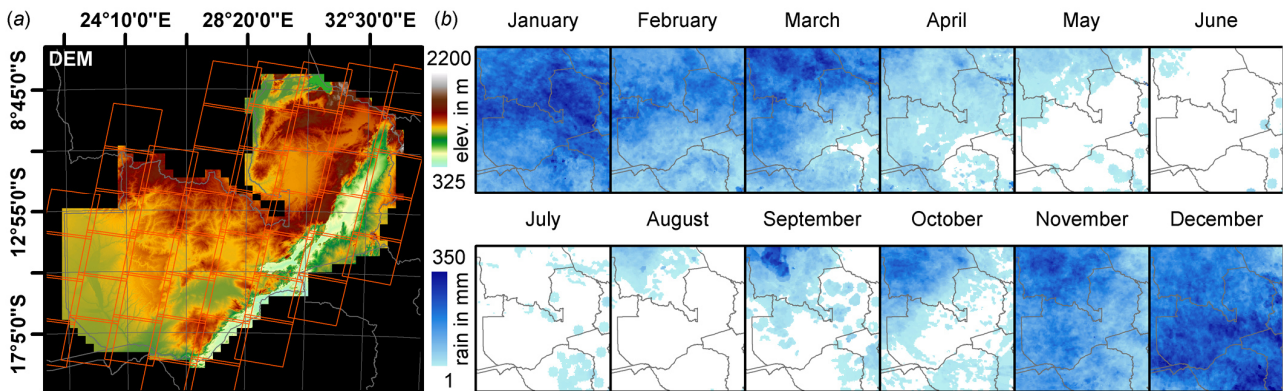


Fig. VI-1. Overview of the study area (Zambia). (a): Digital Elevation Model (DEM), acquired by the Shuttle Radar Topography Mission (SRTM). The Worldwide Reference System 2 (WRS-2) is superimposed. (b): Monthly rainfall sums for 2005, obtained from the Africa Rainfall Climatology version 2 (ARC2; Novella and Thiaw 2013).

season (May-August) and (iii) hot dry season (September-October). The season start, end and lengths, and the precipitation sums are altered both by the local relief and by the geographic location. In general, the season lengths and the precipitation sums decrease from North-West (180-190 days, 1000-1400 mm) to South-East (120-130 days, < 800 mm) due to the temporally shorter influence of the Intertropical Convergence Zone (ITCZ) in the South. The on- and offsets of the rains are also tied to the migration of the ITCZ over Zambia, which is located north of Zambia during the dry season. On average, the rains start in mid-October in the North-West and arrive in the South-East at the end of November. The rains stop in the South at mid-March and last until the end of April in the North-West. The monthly rainfall sums for 2005 are shown in Fig. VI-1b. The timing of the minimum and maximum temperatures also follow this pattern, where the coolest temperatures are found in June/July and the hottest temperatures in October/November immediately before the onset of the rains (Schultz 1983).

The main part of the country is covered by semi-evergreen Miombo woodlands. Evergreen dry forests are found in western Zambia on infertile Kalahari sands and are replaced by grasslands where seasonal waterlogging suppresses tree growth. The drier and hotter southern part of the country is dominated by deciduous woodlands, where Mopane woodlands are found in the lowest and driest regions. Permanent shallow flooding along the rivers and swamps, in combination with the relatively flat terrain support large areas of seasonally flooded grasslands (Olson *et al.* 2001).

### 3 Data

#### 3.1 Surface Reflectance

##### 1) MODIS

We acquired daily MODIS surface reflectance images (using data from the Terra platform, MOD09GA) from the Land Processes Distributed Active Archive Center's (LP DAAC) Data Pool. The product provides surface reflectance images at 500 m resolution and 1–2 day nominal revisit frequency (Vermote and Vermeulen 1999). In order to generate multi-annual composites centered at 2005, each image between 2003 and 2007 for the four tiles covering Zambia (as well as for 11 tiles covering a large latitudinal gradient) was downloaded and processed, resulting in 1814 images per tile. Due to the vicinity of Zambia to the equator, the acquisition orbits do not support daily coverage in most parts of the study area. The number of clear-sky observations is shown in Fig. VI-2a; on average 625 observations were available ( $\sigma = 147$ ,  $\min = 57$ ,  $\max = 1013$ ). The reflectance data (blue:  $0.469\mu\text{m}$ , green:  $0.555\mu\text{m}$ , red:  $0.645\mu\text{m}$ , near infrared:  $0.859\mu\text{m}$ , shortwave infrared:  $1.64\mu\text{m}$  and  $2.13\mu\text{m}$ ) and view zenith angle layers were extracted to binary image format, and the quality layers were parsed to compute the pixel distance to the next cloud or cloud shadow.

##### 2) Landsat

We prepared a ready-to-use multi-sensor Landsat dataset, including reflectance and cloud detection products (Frantz *et al.* 2016a), specifically developed for its use in bulk-data applications like pixel-based compositing. All available Level 1T data from the Thematic Mapper (TM), Enhanced Thematic Mapper plus (ETM+), and the Operational Land Imager (OLI) were processed, and are stored in a gridded data structure in binary image format such that rapid pixel-based access to the full depth of the Landsat archive is instantaneously given. Level 1G data was not processed as a reliable co-registration amongst images was considered of prime importance. All images were available to the compositing algorithm, which was allowed to pick images as needed. Data from different sensors receive equal treatment in the proposed compositing approach. In this study, we focused on the period 2001–2012, where our data pool is populated with 60,800 (TM) and 131,601 (ETM+) gridded image datasets (30 x 30 km) resulting from 1702 (TM) and 3825 (ETM+) original images in Worldwide Reference System 2.

The radiometric processing chain generated NBAR products, featuring an integrated correction of atmospheric, topographic and bidirectional effects. The atmospheric correction module was based on radiative transfer theory (Tanré *et al.* 1979) and accounted for multiple atmospheric

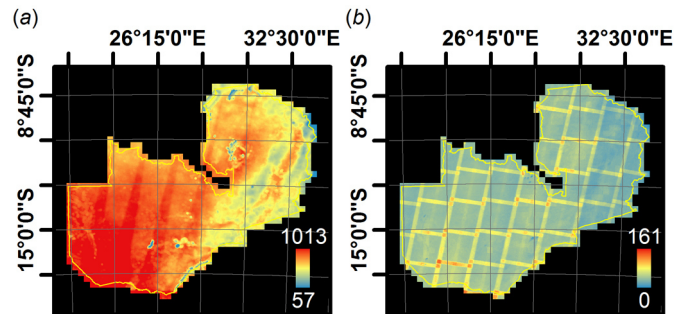


Fig. VI-2. Number of clear-sky observations for the MODIS (a) and Landsat (b) composites for the five-year period 2003–2007.

scatterings with variable illumination/view geometry, and included a combined image-, database- and object-based estimation of aerosol optical depth over temporally persistent dark targets. Adjacency effect correction and a spatio-temporally variable water vapour correction with the MODIS precipitable water product (Gao and Kaufman 2003) are also included. Topographic normalization was achieved with a modified image-based C-correction with 1-arc-Second SRTM data (USGS 2015). The correction of bidirectional effects employs a global set of MODIS-derived BRDF kernel parameters (Roy *et al.* 2016). The pixel distance to the next cloud or cloud shadow was computed with a modified version of the Fmask algorithm (Zhu and Woodcock 2012, Zhu *et al.* 2015, Frantz *et al.* 2015b, Frantz *et al.* 2016a). The haze optimized transformation (HOT; Zhu and Woodcock 2012), and the view zenith angle were also appended to the output stack. All data were prepared in a regular grid, and share a single projection (Lambert Azimuthal Equal Area), such that our proposed algorithm may process tile after tile and pixel after pixel, while utilizing the full archive depth without any need for projection or co-registration considerations.

The intersecting Landsat frames are superimposed in Fig. VI-1a; 49 WRS-2 frames were needed for full coverage. Due to the vicinity to the equator and the small swath of the Landsat sensors, overlaps between adjacent orbits are relatively small, which in combination with the relatively poor data availability poses challenges on generating seamless image products; Frantz *et al.* (2016b) showed that the average clear-sky revisit frequency in non-overlapping areas well exceeds 100 days in the wet season and is about 50 days in the dry season. The clear-sky data availability for the five-year period 2003–2007 is shown in Fig. VI-2b; on average 43.5 observations were available ( $\sigma = 17.5$ ,  $\min = 0$ ,  $\max = 161$ ).

### 3.2 Land Surface Phenology

Land Surface Phenology in Zambia is diverse, primarily as a function of elevation, climate and local variations in water availability. Since phenology on the southern hemisphere is shifted compared

to the northern hemisphere, the vegetation maximum approximately coincides with the turn of the year. In order to facilitate computations, we do not strictly use DOY values, but use a continuous field of values in the algorithm internals, i.e. days since 01/01/0000. The average timing of three phenological key stages used throughout the manuscript is given in Table VI-1.

The peak of season (POS) is the timing of maximum vegetation growth and occurs during the rainy season. The minimum of season (MOS) is the absolute minimum of vegetation development between two peaks and coincides with the hottest temperatures in the dry season. The end of season (EOS) approximately coincides with the annual temperature minimum, where drying already decreased the green stock substantially. The three parameters for 2005 are depicted in Fig. VI-3. The patterns are primarily a function of regional wind currents associated with the rainfall seasonality and terrain altitude (compare to Fig. VI-1).

We prepared two sets of LSP data to guide the compositing process, one at moderate spatial resolution (250 m) and one at medium spatial resolution (30 m). A detailed description of the derivation of these inputs was given by Frantz *et al.* (2016b), and only a brief summary will be given here. Moderate resolution LSP was obtained by applying the Spline analysis of Time Series algorithm (SplITS, Mader 2012) to MODIS EVI time series (MOD13Q1/MYD13Q1). The day of composite information was explicitly used to recreate the actually sensed time series, and the VI usefulness index (a sublayer given in the MODIS products) was used for weighting the data points during the procedure. Data from both MODIS sensors on-board Aqua and Terra were combined to increase the temporal resolution. Spline models were fit to the EVI time series and phenological parameters were extracted thereof: POS and MOS are the timing of annual extremes, and the EOS is defined as the date where the spline crosses 20% of the seasonal amplitude between POS and MOS. Following this, the spatial resolution was further improved by fusing the moderate resolution LSP with the temporally limited Landsat reflectance (Frantz *et al.* 2016b). The fusion intensively uses the information from the local pixel neighborhood at both resolutions, where a few discrete Landsat images are used to disentangle the LSP with textural and spectral homogeneity metrics. The employed methods avoid the need of generating a dense time series of synthetic Landsat like images in a first step as the target layer is directly predicted at increased spatial resolution.

The previously described temporal LSP metrics were derived for the years 2001–2012. As an approximation, the average of the 12 year LSP is computed by the compositing algorithm and is used for missing data, or for pre-2001 and post-2012 periods. The datasets were generated with the same



Table VI-1. Mean timing of LSP.

	Peak of season	End of season	Minimum of season
Abbreviation	POS	EOS	MOS
Mean DOY	25 $\triangleq$ January 25	174 $\triangleq$ June 23	245 $\triangleq$ September 2

Land Surface Phenology (LSP) for three key stages in 2005.

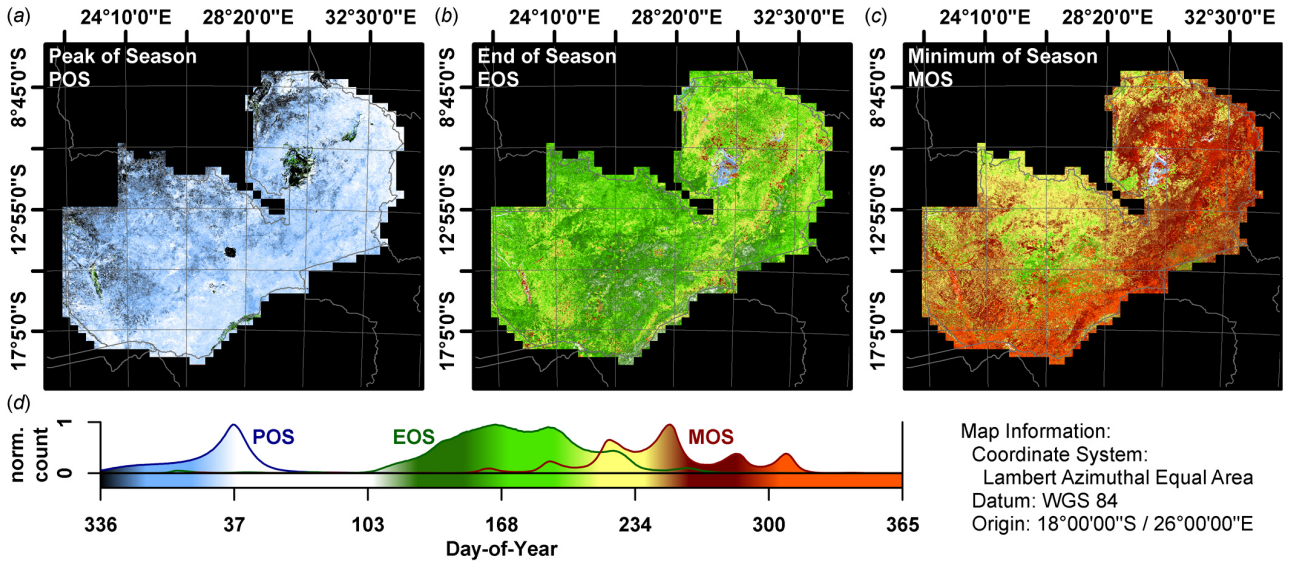


Fig. VI-3. Land Surface Phenology (LSP) for 2005; (a): peak of season (POS), (b): end of season (EOS), (c): minimum of season (MOS). (d): normalized histograms of POS, EOS and MOS (standardized by histogram maximum), and color bar for (a-c). The POS can be at the end or at the beginning of the calendar year, and as such, the data ranges from December 1, 2004 (DOY 336) to December 31, 2005 (DOY 365). The depicted color-ramp is used for all DOY images throughout the paper.

grid system as the MODIS and Landsat data, respectively, such that pixel-based operations can be used during the compositing.

## 4 Methods

### 4.1 Compositing

Image compositing generally identifies the best suited observation in a given period of time on the basis of pre-defined criteria at the pixel-level. Following this definition, we consider each observation from the target year  $Y_t$  and from a number of bracketing years  $y$  (i.e.  $Y_t \pm y$ ), and use a parametric weighting scheme similar to Griffiths *et al.* (2013b) and White *et al.* (2014).

We determine the suitability of any observation by computing the total score  $S_T$  from a weighted linear combination of a number of thematic scores:

$$S_T = \sum WS / \sum W, \quad (\text{VI-1})$$

where the scores  $S$  characterize the phenology-adapted suitability of the acquisition day ( $S_D$ ) and year ( $S_Y$ ), the probability of cloudiness ( $S_C$ ), the potential contamination with haze ( $S_H$ ), the spectral correlation ( $S_R$ ) and the view zenith angle ( $S_V$ ), respectively. The scores are computed on a per-pixel basis and are defined to be within  $[0,1]$ . The employed transfer functions are described in the following sub-sections. The relative importance of the scores may be adjusted with the weighting parameters  $W$ , which are also in the range  $[0,1]$ , where  $W = 0$  disables the usage of the corresponding score. The observation with the highest total score is selected for the composite. The mathematical symbols used throughout the paper are defined in Table VI-2.

### 1) Intra-annual contribution: acquisition day

We use the pixel-based LSP to dynamically adjust scoring functions for each pixel. We use a sequence of three temporal LSP parameters, e.g.

- $p_0$ : POS,
- $p_1$ : EOS and
- $p_2$ : MOS.

Other sequences are also permitted, e.g. start of season (SOS), POS, EOS; which would simply result in composites anchored at a different phenological stage.

Thus, for each pixel and each year in  $[Y_t - y, Y_t + y]$ , there are three temporal parameters:  $p_0$ ,  $p_1$  and  $p_2$ . The correct year of the LSP is selected by choosing the year in which  $p_1$  is closest to the image under consideration, which is necessary if the phenological curve coincides with the turn of the year. Three function values ( $s_0$ ,  $s_1$  and  $s_2$ ) need to be pre-defined, and they are to be evaluated at  $p_0$ ,  $p_1$  and  $p_2$  for each pixel. The choice of  $s_0$ ,  $s_1$  and  $s_2$  triggers the usage of different scoring functions, i.e. either a Gaussian function or ascending/descending sigmoidal ones.

In the case of the Gaussian,  $s_0$ ,  $s_1$  and  $s_2$  must be in  $[0,1]$  and  $s_0 < s_1 > s_2$ . A Gaussian function is then adapted to the LSP by numerically determining the width of the Gaussian bell  $\sigma$ ; the amplitude of the Gaussian is simply  $s_1$  (typically  $s_1 = 1$ ) and  $p_1$  shall represent the target DOY. In order to adapt to asymmetric LSP,  $\sigma$  is determined for both tails separately:

$$\begin{aligned} \sigma_l &= [p_0 - p_1] / \sqrt{-2 \cdot \log(s_0/s_1)} \\ \sigma_r &= [p_2 - p_1] / \sqrt{-2 \cdot \log(s_2/s_1)} \end{aligned} \tag{VI-2}$$

Table VI-2. Mathematical symbols.

Symbol	Meaning
$Y, y$	Target year and allowed number of bracketing years
$D, D$	Target Day-of-the-Year (DOY), DOY of image acquisition
$\Delta Y, \Delta D$	Absolute difference to target year and DOY
$S_T$	Total score
$S_D, S_Y$	Temporal scores for acquisition DOY and year
$S_C, S_H, S_R, S_V$	Auxiliary scores for cloud, haze, correlation and view angle
$W_D, W_Y, W_C,$ $W_H, W_R, W_V$	Weighting parameters for the temporal and auxiliary scores
$p_0, p_1, p_2$	Land Surface Phenology (LSP) metrics
$s_0, s_1, s_2$	Function values for the LSP metrics
$\sigma_l, \sigma_r$	Left- and right-tail width (sigma) for the Gaussian DOY scoring function
$a, b$	Shape parameters for the sigmoidal DOY scoring functions
$Y_f$	Y-factor; i.e. relative inter-/intra-annual contribution
$d, d_{req}$	Cloud and cloud shadow distance, and distance after the sky is assumed to be clear
$\theta, \theta_{req}$	View zenith angle, and angle at which $S_V$ approaches 0

Definition of the mathematical symbols used in this paper.

The DOY score  $S_D$  is computed with

$$S_D = \begin{cases} s_1 \cdot \exp(-0.5 \cdot [D - p_1]^2 / \sigma_l^2), & (D < p_1) \\ s_1 \cdot \exp(-0.5 \cdot [D - p_1]^2 / \sigma_r^2), & (D \geq p_1) \end{cases} \quad (\text{VI-3})$$

where the left-tail function is used if  $D$  is before  $p_1$ . If not, the right-tail function is used.

The procedure of fitting a Gaussian to the LSP ( $p_0 = \text{POS}$ ,  $p_1 = \text{EOS}$ ,  $p_2 = \text{MOS}$ ) is illustrated in Fig. VI-4a–d. In (a–b),  $s_0$ ,  $s_1$  and  $s_2$  are set to 0.01, 1.00 and 0.01;  $p_1$  is assumed constant and  $p_0$  and  $p_2$  converge symmetrically towards  $p_0$  (a) or progress forward asymmetrically (b). The Gaussian functions adapt to the changing LSP accordingly, which in practice would be the LSP of different pixels. In Fig. VI-4c–d, the LSP is held constant and the effect of modifying the function values is demonstrated; the Gaussians also adapt to these variations. The effect of increased  $s_0$  and/or  $s_2$  values on the composite would be that the chance of selecting a broader range of DOYs is increased. On the contrary, a more narrow Gaussian (i.e. low  $s_0$  and/or  $s_2$  values) would increase the selection rate of DOYs that are close to the target DOY.

To account for conditions where the selected DOY should not extend beyond or start before a certain date, we implemented descending and ascending sigmoidal functions, in which case  $p_0$  or  $p_2$  serve as target DOY layer. These functions are particularly useful if e.g., a ‘dry minimum’ composite should be created where only data from within the dry season are to be considered; the onset of the rains typically ends the season, triggers a green flush event, and thus alters the landscape quickly (see also Fig. VI-1 for the monthly rainfall sums).

$$S_D = \begin{cases} s_0/(1 + \exp(a \cdot [D - p_1] + b)), & (s_0 > s_2) \\ s_2/(1 + \exp(a \cdot [D - p_1] + b)), & (s_2 > s_0) \end{cases} \quad (\text{VI-4})$$

Analogous to the Gaussian type, function values  $s_0$ ,  $s_1$  and  $s_2$  at  $p_0$ ,  $p_1$  and  $p_2$  are pre-defined with

- $1 \geq s_0 > s_1 > s_2 \geq 0$  for a descending sigmoid or
- $0 \leq s_0 < s_1 < s_2 \leq 1$  for an ascending sigmoid.

The function parameters  $a$  and  $b$  are retrieved from Nelder-Mead Simplex Optimization (Nelder and Mead 1965) where the RMSE between  $s_0$ ,  $s_1$ ,  $s_2$  and the evaluation of Eq. (VI-4) at  $p_0$ ,  $p_1$  and  $p_2$  is minimized.  $s_0$  or  $s_2$  denote the function maxima and  $b$  causes the midpoint of the function to shift away from  $p_1$  towards  $p_0$  or  $p_2$ . The steepness parameter  $a$  assumes positive (negative) values for the descending (ascending) type. Acquisition dates  $D$  that are before (after)  $D_t$  are scored with the LSP of the previous (next) year with the descending (ascending) sigmoid, such that they assume a very low  $S_D$  – in order to satisfy the need for the generation of within-season only composites.

The procedure of fitting the logistic S-curves is shown in Fig. VI-4e–h for a descending (e–f) and an ascending case (g–h);  $s_0 = 0.99$  (0.01),  $s_1 = 0.10$  and  $s_2 = 0.01$  (0.99). Fig. VI-4e,g demonstrate the capability of the sigmoid to adjust to the dynamic LSP, which in practice would be the LSP of different pixels. Analogous to the Gaussian type, the compositing behavior can be controlled by modifying  $s_0$ ,  $s_1$  and  $s_2$  where an increase generally increases the chance that DOYs further away from  $D_t$  are selected; exemplarily see Fig. VI-4f,h for a sequence of  $s_1$  values.

## 2) Inter-annual contribution: acquisition year

In the case of generating composites from multi-annual observations, it is required to define tradeoff criteria between data from  $Y_t$  and acquisitions from other years that potentially are closer to  $D_t$ . Preferably, observations from  $Y_t$  should be selected to minimize the risk of land cover change between the years while acquisitions close to  $D_t$  are needed to increase the phenological consistency. Observations from bracketing years should not be used until the data availability in  $Y_t$  is too limited. As these are contradicting demands, we introduce the Y-factor  $Y_f$ , which defines the tradeoff between inter- and intra-annual data contribution with a single parameter. To adapt to spatial variations in the steepness of vegetation development or senescence,  $Y_f$  is parameterized with a dynamic adjustment on the basis of pixel-based LSP. Recall that the intra-annual scoring is determined from  $p_0$ ,  $p_1$  and  $p_2$

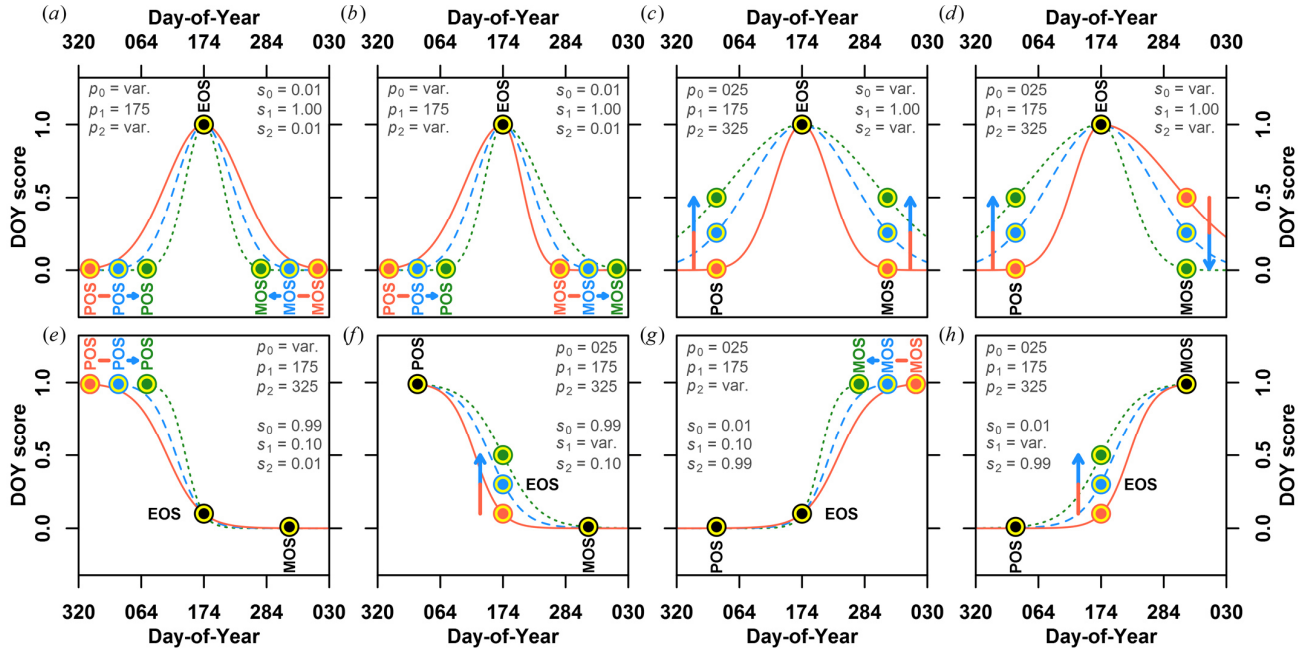


Fig. VI-4. Schematic illustration of the LSP-adaptive DOY scoring functions. The Gaussian type is shown in (a–d); the logistic S-curves in (e–h). For illustration purposes, we have either visualized fits to the variable LSP with constant function values (a, b, e, g), or have visualized fits to constant LSP but variable function values (c, d, f, h). The chosen LSP and scoring function values are indicated as  $p_{0-2}$  and  $s_{0-2}$ ; the point signatures indicate the  $p$  and  $s$  values, and ‘var.’ indicates that a parameter was varied; the variation of the  $p$  and  $s$  values can be taken from the x- and y-axis, respectively. For consistency with the following real-life examples, the  $p$ -values were tagged semantically with POS, EOS and MOS. In all cases, the target metric is the phenological parameter with the highest score, i.e. EOS (a–d), POS (e–f) and MOS (g–h).

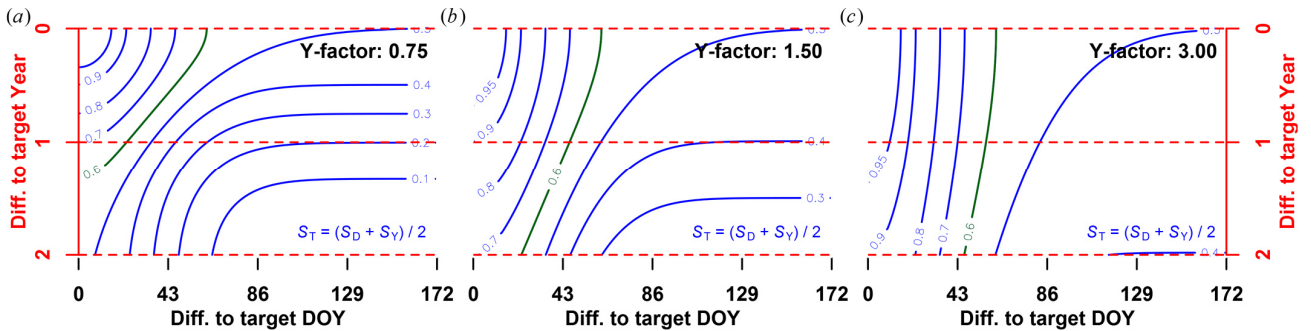


Fig. VI-5. Illustration of the Y-factor  $Y_f$  for an arbitrary example. The figure shows isolines of the total score  $S_T$ , drawn with a dependence on  $\Delta Y$  and  $\Delta D$ . The right tail Gaussian type was chosen and two years around the target year are allowed; i.e.  $y = 2$ . The total score was computed as a combination of the Year score  $S_Y$  and the DOY. The higher  $Y_f$ , the higher is  $S_Y$  – and the smaller is the influence of  $\Delta Y$  on  $S_T$ .

using different scoring functions. We slice the interval of the most dynamic range of  $p_0, p_1, p_2$  into intervals  $p_{\leftrightarrow}$  that are defined by  $Y_f$  and the allowed number of bracketing years  $y$ :

$$p_{\leftrightarrow} = \begin{cases} (p_1 - p_0)/([y + 1] \cdot Y_f), & (D < p_1) | (s_0 > s_2) \\ (p_2 - p_1)/([y + 1] \cdot Y_f), & (D \geq p_1) | (s_2 > s_0) \end{cases} \quad (\text{VI-5})$$

where the first equation is used for the left-tail Gaussian or the descending sigmoid, and the second equation for the right-tail Gaussian or the ascending sigmoid.

The Year score  $S_Y$  is defined to enable a merely DOY-driven selection, but with a penalty on the bracketing years. It is the evaluation of the DOY scoring function relative to the function maximum at  $\Delta Y \cdot p_{\leftrightarrow}$  for the Gaussian type

$$S_Y = \begin{cases} s_1 \cdot \exp(-0.5 \cdot [\Delta Y p_{\leftrightarrow}]^2 / \sigma_1^2), & (D < p_1) \\ s_1 \cdot \exp(-0.5 \cdot [\Delta Y p_{\leftrightarrow}]^2 / \sigma_1^2), & (D \geq p_1) \end{cases} \quad (\text{VI-6})$$

and the sigmoidal types

$$S_Y = \begin{cases} s_0 / (1 + \exp(a[p_0 + \Delta Y p_{\leftrightarrow} - p_1] + b)), & (s_0 > s_2) \\ s_2 / (1 + \exp(a[p_3 - \Delta Y p_{\leftrightarrow} - p_1] + b)), & (s_2 > s_0) \end{cases} \quad (\text{VI-7})$$

Fig. VI-5 illustrates the influence of  $Y_f$  on  $S_T$  for an arbitrary example where  $D$  is after  $p_1$ , and the DOYs are scored with the right-tail Gaussian with  $s_1 = 1$  and  $s_2 = 0.01$ ;  $y = 2$  years. The total score  $S_T$  was computed using  $S_D$  and  $S_Y$  only. Three different  $Y_f$  are shown in (a-c) which alter the curvature of the  $S_T$  isolines. In the case of  $Y_f = 3$ , the isolines are rather vertical, which means that  $S_T$  for a given  $\Delta D$  do not differ substantially between the years, and observations from the bracketing years may be included in the composite. In the case of  $Y_f = 0.75$ , the isolines are curved substantially, which strongly decreases the selecting rate of non- $Y_f$  observations. As an example (green isoline), observations with  $\Delta D \leq 23$  and  $\Delta Y = 1$  can only be selected if there is no observation in  $\Delta Y = 0$  with  $\Delta D \leq 61$ . The chance of selecting a  $\Delta Y = 2$  observation is even worse, as the same  $S_T$  cannot be achieved. The actual effect of varying  $Y_f$  on the composited DOYs and Years is shown in Fig. VI-12.

### 3) Cloud distance score

We score the pixel's distance to the next cloud or cloud shadow  $d$  with a sigmoid in order to devalue pixels that are in close proximity to a cloud or a cloud shadow. Fmask cloud detections are generally of high quality (Zhu and Woodcock 2012) but they are not perfect (Zhu and Woodcock 2014a, Frantz *et al.* 2015b), thus cloud remnants remain in the data and especially shadows might be missed. Nevertheless, clouds are typically clustered and unidentified shadows are also constrained to the proximity of the more reliably detectable clouds. Therefore, the concentric devaluation of pixels around the detected clouds also accounts for the missed objects. Griffiths *et al.* (2013b) defined a

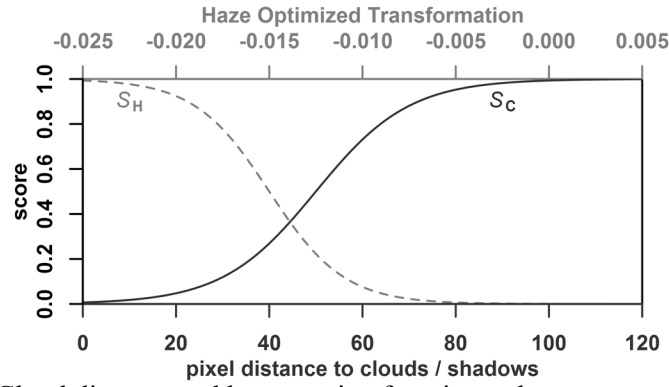


Fig. VI-6. Cloud distance and haze scoring functions;  $d_{\text{req}}$  was set to 100 pixels.

parameter  $d_{\text{req}}$  beyond which the sky is assumed to be clear. We slightly modified the cloud scoring function (Fig. VI-6) to adapt better to different  $d_{\text{req}}$ :

$$S_C = 1 / (1 + \exp(-10/d_{\text{req}} \cdot [d - d_{\text{req}}/2])). \quad (\text{VI-8})$$

#### 4) Haze score

The utilized preprocessing framework included a full radiometric treatment of the data (Frantz *et al.* 2016a). Nevertheless, local plumes of thick haze are still present in the imagery and are also subject of omission in Fmask, e.g. haze caused by biomass burning is not detected reliably due to its transparency and warmth. Therefore, we added the Fmask Haze Optimized Transformation (HOT; Zhu and Woodcock 2012, Zhang *et al.* 2002) to the output stack in the preprocessing framework. The HOT has already proven its usability in compositing techniques (Lück and van Niekerk 2016), and as such, we use this proxy for devaluating hazy observations with a sigmoid (see Fig. VI-6, dashed):

$$S_H = 1 / (1 + \exp(10/0.02 \cdot [HOT + 0.015])). \quad (\text{VI-9})$$

#### 5) Correlation score

EO imagery can contain a variety of errors or undesired effects which are hard to account for with scoring functions tailored for a specific purpose. This especially applies if *a priori* knowledge about potential error sources is not available, and/or specific avoidance strategies cannot be developed. Undesired effects may be data artifacts (e.g. due to impulse noise or any other sensor anomaly see Fig. VI-7a, residual misregistration, or undesired transient phenomena like short-term flooding, active fires or missed clouds/shadows).

As such, we developed a general criterion, which relates a given spectrum to the pixel's spectral stability within the requested period of time, and thus minimizes outlier-induced noise

regardless of the type of noise. Through time, spectra are commonly highly correlated, and as such, we compute the temporal correlation matrix from all spectra of a given pixel. We use the mean absolute correlation  $|r_\mu|$  – i.e. the column average of the correlation matrix; see Fig. VI-7a – as spectral stability proxy in the computation of the correlation score, see Fig. VI-7b:

$$S_R = 1/(1 + \exp(-10/(0.5 \cdot 2/3) \cdot [|r_\mu| - 0.5 \cdot 4/3])). \quad (\text{VI-10})$$

## 6) View angle score

Wide swath sensors like MODIS provide near-daily global coverage, though off-nadir data is of poorer quality due to the “bowtie” effect, where the FOV at the scan edge (approx.  $65^\circ$ ) is approximately 2.0 and 4.8 times larger than at nadir in the track and scan directions, respectively (Wolfe *et al.* 1998). It is well known that the consideration of view angle effects improves composite quality considerably (e.g. Chuvieco *et al.* 2005), therefore we use a sigmoid to devalue off-nadir pixels on the basis of the view zenith angle  $\theta$  of a given observation (see Fig. VI-8):

$$S_V = 1/(1 + \exp(10/\theta_{\text{req}} \cdot [\theta - \theta_{\text{req}}/2])). \quad (\text{VI-11})$$

$\theta_{\text{req}}$  is the angle at which  $S_V$  approaches 0, and can be adapted with respect to the viewing geometry of a specific sensor.

## 4.2 Implementation and user interaction

The code is entirely based on open-source software and is written in C. The GNU Scientific Library is used for optimization procedures. Shared memory parallelization was implemented by utilizing the Open Multi-Processing (OpenMP) API. The compositing algorithm works on a per-tile-basis, though data from the requested tiles are directly written to a single output file, which is basically a mosaic of composites.

If required, the compositing algorithm can be parameterized by setting only a few parameters. The spatial extent, the target Year  $Y_t$ , the number of bracketing years  $y$  and the Y-factor  $Y_f$  must be set. If the phenology-adaptive approach is to be used, the user must input the LSP data ( $p_0$ ,  $p_1$  and  $p_2$ ) and needs to define the corresponding function values  $s_0$ ,  $s_1$  and  $s_2$ . If static composites are to be created, fixed values for  $p_0$ ,  $p_1$  and  $p_2$  need to be defined instead. The function type (Gaussian or sigmoid) is automatically chosen from the given  $s$  values. The weighting parameters  $W$  can also be modified and individual scores  $S$  can be disabled. Several output files can be generated on demand:



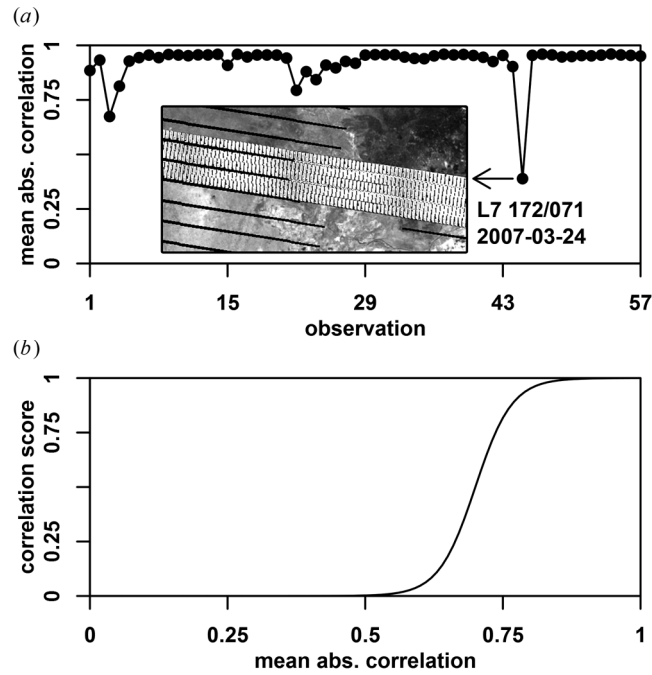


Fig. VI-7. Exemplary illustration of the spectral stability assessment and correlation scoring function. (a): mean absolute correlation derived from the temporal correlation matrix, and Landsat-7 NIR image (Path/Row 172/072) affected by sensor anomalies. (b): correlation scoring function.

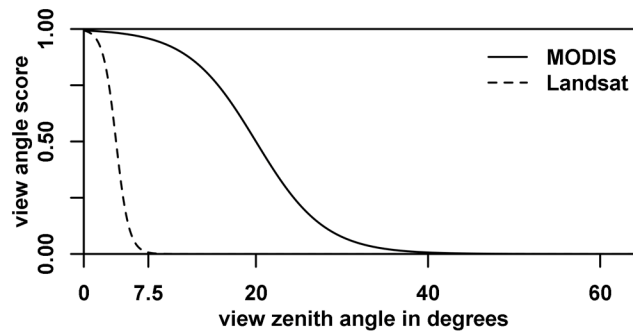


Fig. VI-8. View zenith angle scoring function;  $\theta_{\text{req}}$  was set to  $40^\circ$  and  $7.5^\circ$  for MODIS and Landsat, respectively.

- **pixel-based composites** are written by default,
- **composite information** about (i) the number of considered clear-sky observations (in dependency of  $d_{\text{req}}$  – see Fig. VI-2), (ii) the selected  $D$ , (iii)  $\Delta D$ , (iv)  $\Delta Y$ , (v) sensor ID (4, 5, 7 or 8 in the case of Landsat), (vi) Path/Row of the best observation, and (vii) the 12-year variability of LSP,
- **scores** of the best observation ( $S_T$ ,  $S_D$ ,  $S_Y$ ,  $S_C$ ,  $S_H$ ,  $S_R$ ,  $S_V$ ), and

- **spectral variability metrics** can be produced optionally. The spectral variability is a representation of the stability or variation of the land surface during the  $2y+1$  year compositing period. Spectral variability metrics were shown to be an asset in land cover classifications (Griffiths *et al.* 2013b). Each clear-sky observation which is sufficiently far away from the next cloud (in dependency of  $d_{\text{req}}$ ) contributes to these metrics. Mean (i), standard deviation (ii), minimum (iii), maximum (iv), range (v), skewness (vi) and kurtosis (vii) may be output.

### 4.3 Application to EO archives

We demonstrate our method for application with MODIS and Landsat archives. Very dense MODIS data (temporal resolution  $\sim 2$  days) enable the selection of observations which are as close as possible to the target DOY, and are thus optimal to demonstrate the temporal aspects of the presented approach. In order to demonstrate the effect of using pixel-based LSP, we generated a set of phenology-adaptive composites (using the coarse resolution LSP) and a set using a static target DOY, i.e. the mean value of the LSP (see Table VI-1). For each set, three seasonal composites for  $2005 \pm 2$  were generated: POS, EOS and MOS. The seasonal composites were generated using the same input LSP layers, but with different DOY scoring functions, i.e. the descending sigmoid, two-tailed Gaussian and ascending sigmoid, respectively. The EVI was computed for each composite as benchmark for differences in vegetation development as a result of the two compositing techniques. Differences between the techniques are shown and the composites are compared quantitatively. The mean error (ME) as a measure for bias, the mean absolute error (MAE), the root mean squared error (RMSE) and the coefficient of determination ( $R^2$ ) were computed for each combination. Spatial autocorrelation was reduced with a random selection of  $\sim 17,500$  samples using Poisson Disc sampling (Tulleken 2008). As additional proof of concept, we examine the (non-)relationship between EVI and elevation for a small subset with a large elevation gradient and a number of land cover classes for both the phenology-adaptive and the static composites. We also generated three different phenology-adaptive EOS composites using different Y-factors (0.75, 1.5, 3.0) to demonstrate the effect of the inter- to intra-annual selection process. The full parameterization is summarized in Table VI-3.  $W_D$  and  $W_Y$  were set to 1.  $W_H$  was set to 0, because the HOT was not available as we acquired atmospherically corrected MODIS data.  $W_C$  was set to 0, because we did not encounter severe data artifacts in the resulting composites, and the correlation matrix is computationally expensive for a very large number of input images (1814 images), thus we considered the cost-benefit ratio ineffective for its usage with dense MODIS data.  $W_C$  and  $W_V$  were set to 0.33, in order to guarantee that  $S_D$  cannot be overruled by close-nadir and cloud-free observations in unfavorable seasons. The potential for global applicability is demonstrated by generating MODIS EOS composites for a large latitudinal

Table VI-3. Parameterization of the MODIS and Landsat composites.

	peak of season MODIS	end of season MODIS	min. of season MODIS	peak of season Landsat	end of season Landsat	min. of season Landsat
$Y_t, y$	2005 $\pm$ 2	2005 $\pm$ 2	2005 $\pm$ 2	2005 $\pm$ 2	2005 $\pm$ 2	2005 $\pm$ 2
$Y_f$	0.75 [1.5, 3.0]*	0.75 [1.5, 3.0]*	0.75 [1.5, 3.0]*	0.75	0.75	0.75
$p_{0-2}$ LSP	<b>POS</b> , EOS, MOS	<b>POS</b> , <b>EOS</b> , MOS	<b>POS</b> , EOS, <b>MOS</b>	<b>POS</b> , EOS, MOS	<b>POS</b> , <b>EOS</b> , MOS	<b>POS</b> , EOS, <b>MOS</b>
$p_{0-2}$ static	<b>25</b> , 174, 245	25, <b>174</b> , 245	25, 174, <b>245</b>	<b>25</b> , 174, 245	25, <b>174</b> , 245	25, 174, <b>245</b>
$s_0, s_1, s_2$	<b>0.99</b> , 0.10, 0.01	0.01, <b>1.00</b> , 0.01	0.01, 0.1, <b>0.99</b>	<b>0.99</b> , 0.10, 0.01	0.01, <b>1.00</b> , 0.01	0.01, 0.10, <b>0.99</b>
scoring function	descending sigmoid	two-tailed Gaussian	ascending sigmoid	descending sigmoid	two-tailed Gaussian	ascending sigmoid
$W_D, W_Y$	1.00, 1.00,	1.00, 1.00,	1.00, 1.00,	1.00, 1.00,	1.00, 1.00,	1.00, 1.00,
$W_C, W_H$	0.33, 0.00,	0.33, 0.00,	0.33, 0.00,	0.20, 0.20,	0.20, 0.20,	0.20, 0.20,
$W_R, W_V$	0.00, 0.33	0.00, 0.33	0.00, 0.33	0.20, 0.33	0.20, 0.33	0.20, 0.33
$d_{req}, \theta_{req}$	10, 40	10, 40	10, 40	100, 7.5	100, 7.5	100, 7.5

\* In case of the phenology-adaptive MODIS composites, an experiment with three different Y-factors was performed. For the remaining composites,  $Y_f = 0.75$ .

gradient from boreal Russia to South Africa. We generated a phenology-adaptive version, and static composites that were anchored at the hemispheric mean EOS, which is DOY 256 and 106 for the northern and southern hemisphere, respectively.

In the next step, we applied both the phenology-adaptive and static compositing techniques to the Landsat data, using the medium resolution phenology or the mean LSP values. Analogously to MODIS, we generated three seasonal composites for 2005 $\pm$ 2 years, i.e. POS, EOS and MOS. The Landsat composites were cross-compared with MODIS to ensure data quality. To lessen the effect of differing spatial resolution, the Landsat composites were degraded to 500 m using a MODIS point spread function (Barnes *et al.* 1998). The sampling procedure and statistical measures are the same as described in the last paragraph and are presented together with the cross-comparison between the MODIS composites. The complete parameterization is summarized in Table VI-3. We used all scores, while ensuring that the auxiliary scores cannot outmax the temporal ones. In order to show the potential for land cover change mapping, we generated an annual Landsat EOS time series (2001–2012  $\pm$ 0) with the phenology-adaptive technique. The Change, Aftereffect and Trend (CAT, Hird *et al.* 2016) transform was applied to the EVI representations for visualizing both drastic and gradual landscape dynamics across whole Zambia at medium resolution. Due to the non-optimal data availability of Landsat data, we rigorously rejected all observations that deviate more than  $\pm$ 16 days from  $D_t$ .

## 5 Results

### 5.1 MODIS composites

We generated phenology-adaptive MODIS composites centered at the POS, EOS and MOS metrics, as well as static composites that only use the mean value of the LSP for each pixel. We used the descending sigmoid, two-tailed Gaussian and ascending sigmoid for POS, EOS and MOS, respectively. The same LSP metrics were chosen for each composite while only altering the scoring values  $s_0$ ,  $s_1$  and  $s_2$ . We used a relatively low Y-factor, thus data from  $Y_t$  is preferred – if available. The complete parameterization is summarized in Table VI-3. We uploaded the generated MODIS composites to the Mendeley Data Repository. The data can be accessed with following link: <https://data.mendeley.com/datasets/bj7jn39ds2/draft?a=e0e0a086-f665-40f1-86d2-9f20c292f9a6>.

Fig. VI-9 depicts the composites for the three seasons (rows). The phenology-adaptive composites are shown in the first column; the static composites in the second column. The third column depicts the difference in EVI; red colors indicate a higher EVI in the phenology-adaptive images. The temporal characteristics are shown in Fig. VI-10, i.e. the selected DOY,  $\Delta D$  (either using the phenology-adaptive or static target) and  $\Delta Y$ . Basic statistics are summarized in Table VI-4. The number of observations is identical for all composites because they were generated with the same input data. On average 625 observations were considered ( $\sigma = 147$ ,  $\min = 57$ ,  $\max = 1013$ ). The number of observations is shown in Fig. VI-2a.

Based on visual inspection, the POS composites are of least quality and are characterized by a stained appeal; the phenology-adaptive version is slightly more homogeneous. The EOS and MOS composites are of highest quality. Bidirectional effects are readily visible in the static MOS composite as there is a distinct discontinuity between neighboring orbits, and to a smaller degree also in the static EOS composite. The swaths are not visible in the phenology-adaptive versions, although the composites are generally more grained than the static ones.

The EOS composites differ by less than  $\pm 7$  days from  $D_t$ , and the MOS composites by less than  $\pm 10$  days. On the contrary, the POS composite differs by more than a month (and additionally have a large standard deviation), despite a stronger contribution of the bracketing years. Virtually all data of the EOS composite were acquired in  $Y_t$ , whereas the POS and MOS composites also include data from  $\Delta Y \geq 1$ , which in both cases is more pronounced in the phenology-adaptive version. The selected DOYs resemble the LSP input patterns presented in Fig. VI-3 (with exception of the POS composite), whereas the static versions show little spatial variation besides the acquisition orbits.

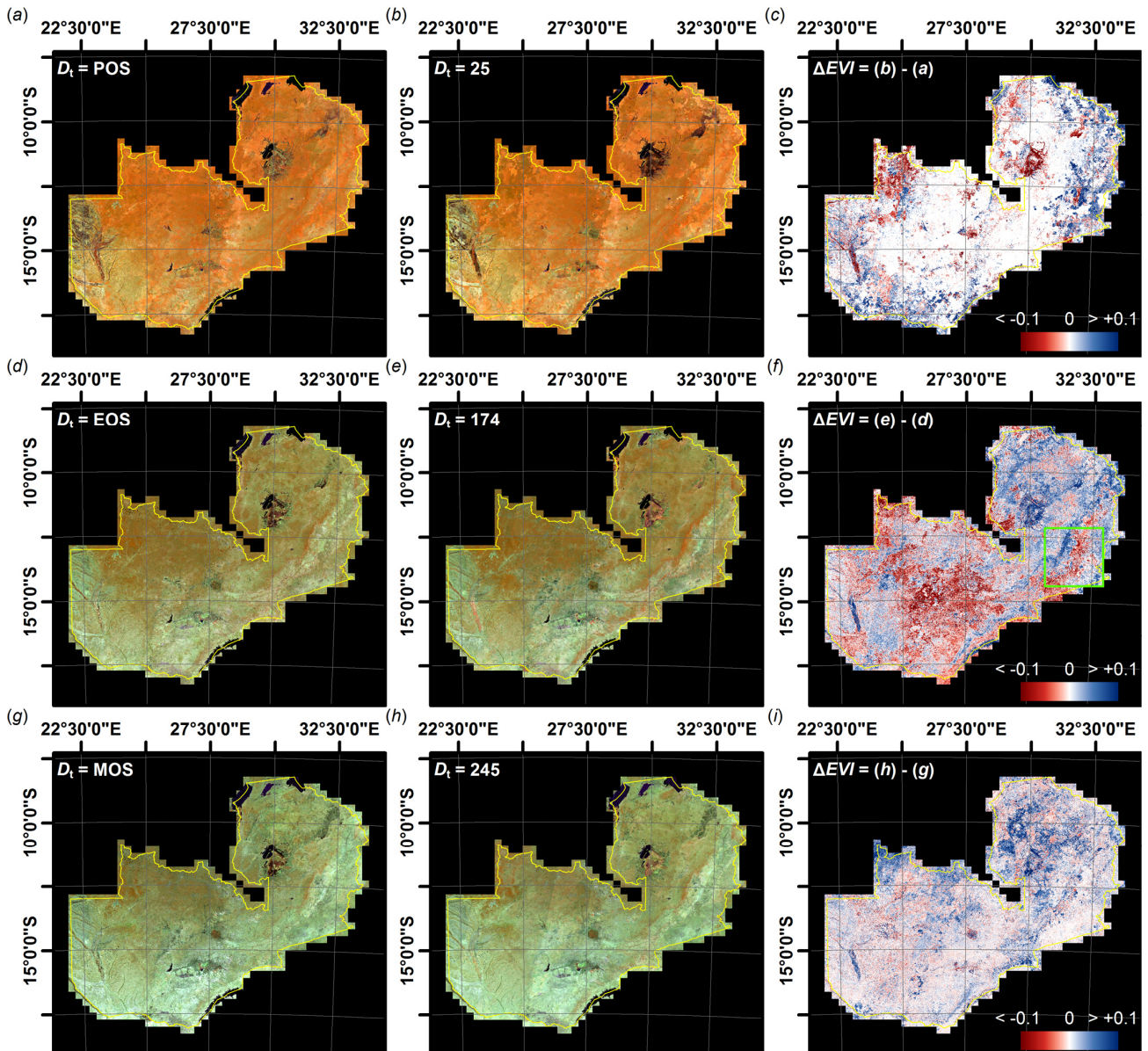


Fig. VI-9. Pixel-based MODIS composites for the target year 2005. The composites were anchored at three different phenological stages; (a-c): peak of season, (d-f): end of season, (g-i): minimum of season. The composites in the first column (a,d,g) were generated with the phenology-adaptive approach; the composites in the second column (b,e,h) were generated using a static target date (mean of the LSP metrics). The depicted band combination is RGB = near infrared, shortwave infrared and red, thus combining complementary information from the three different wavelength domains. The band combination, as well as the same stretch is applied to all reflectance composites throughout the paper. The third column (c,f,i) depicts the difference in the Enhanced Vegetation Index between the phenology-adaptive and static composites; i.e. red colors indicate a higher EVI in the phenology-adaptive composite. The green rectangle in (f) indicates the extent of Fig. VI-11.

Almost all parts of the EOS composites differ substantially with both positive and negative EVI differences. Different ecosystems and topographic units are clearly discriminable in the  $\Delta EVI$  image (static minus phenology-adaptive). Differences in the POS images are rather regionalized. Negative  $\Delta EVI$  values are mainly found in the phenological extremes in the flooded grassland and swamp areas, while other areas in the northwestern part, as well as the positive  $\Delta EVI$  values rather



Table VI-4. Temporal basic statistics of MODIS and Landsat composites.

			$\Delta D$   MODIS		$\Delta Y$   MODIS		$\Delta D$   Landsat		$\Delta Y$   Landsat	
			$\mu$	$\sigma$	$\mu$	$\sigma$	$\mu$	$\sigma$	$\mu$	$\sigma$
$D_t = \text{POS}$	LSP	$Y_f = 0.75$	42.41	27.90	0.24	0.43	50.31	28.68	0.30	0.46
		1.50	39.79	28.05	0.61	0.71				
		3.00	37.59	27.64	0.93	0.83				
$D_t = 25$	static	0.75	34.57	19.26	0.11	0.32	44.48	24.79	0.17	0.38
$D_t = \text{EOS}$	LSP	$Y_f = 0.75$	5.57	5.98	0.00	0.05	16.80	17.21	0.02	0.15
		1.50	5.43	5.20	0.01	0.11				
		3.00	4.84	4.18	0.07	0.27				
$D_t = 174$	static	0.75	6.43	5.19	0.00	0.01	16.28	11.17	0.02	0.14
$D_t = \text{MOS}$	LSP	$Y_f = 0.75$	9.87	10.66	0.21	0.41	16.27	14.13	0.59	0.50
		1.50	9.16	10.72	0.64	0.68				
		3.00	8.54	10.37	0.99	0.77				
$D_t = 245$	static	0.75	8.78	5.62	0.03	0.16	15.57	9.74	0.65	0.47

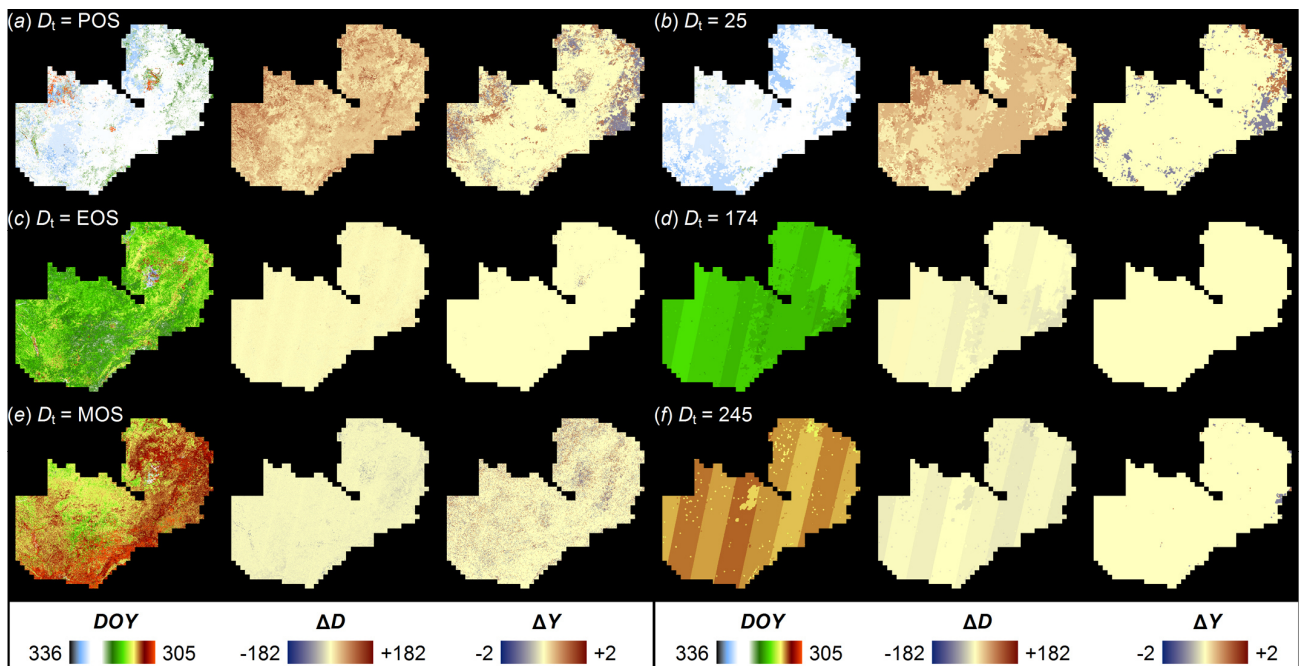


Fig. VI-10. Temporal characteristics of the generated MODIS composites in Fig. VI-9. The three seasons are plotted in the rows; (a-b): peak of season, (c-d): end of season, (e-f): minimum of season. The left half of the figure (a,c,e) refers to the phenology-adaptive composites; the right half (b,d,f) to the static composites. For each composite, the selected DOY, the difference to the target DOY  $\Delta D$  and the difference to the target year  $\Delta Y$  are shown. The same color ramps are applied throughout the paper where appropriate.

coincide with the previously described stained patterns. The MOS composites are characterized by only small negative  $\Delta EVI$  values, while larger parts of Zambia have high positive  $\Delta EVI$  values.

Fig. VI-11 displays the MODIS EOS EVI layer for a subset with a large elevation gradient. The phenology-adaptive version is shown in the left column and the static one in the right column.

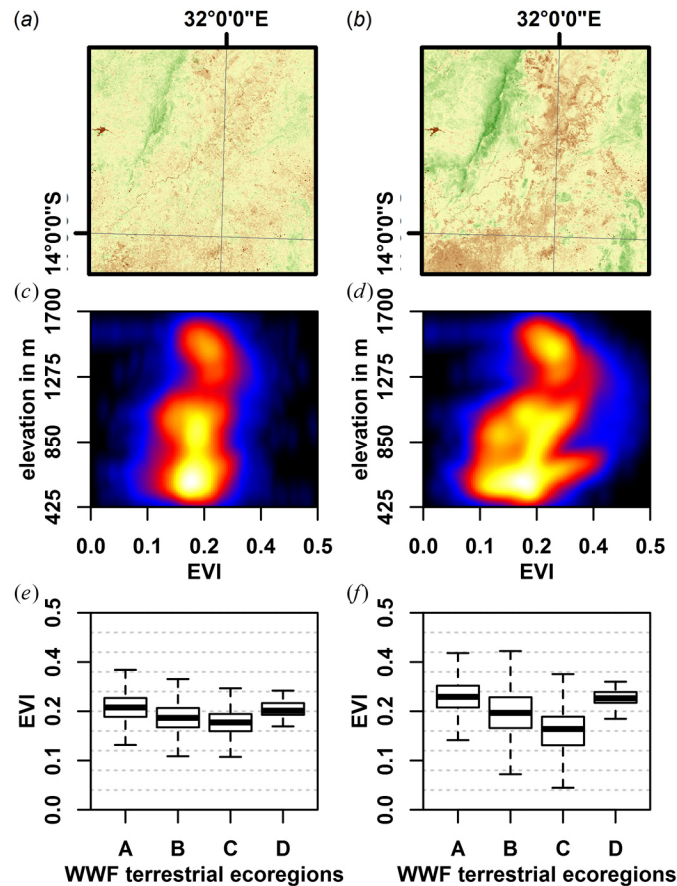


Fig. VI-11. EVI of the MODIS EOS composites for a sample area. The subset is indicated in Fig. VI-9 and is characterized by a large terrain elevation gradient ( $> 1000$  m). The phenology-adaptive version is shown in the left column; the static version in the right column. (a–b): EVI maps; the brown–green color ramp is linearly stretched from 0–0.5, (c–d): 2D-histograms between EVI and terrain elevation, (e–f): EVI boxplots for the World Wildlife Fund terrestrial ecoregions (Olson *et al.* 2001); A–D are Central Zambesian Miombo woodlands, southern Miombo woodlands, Zambesian and Mopane woodlands and Zambesian flooded grasslands, respectively.

The phenology-adaptive composite (a) is spatially homogeneous, whereas larger differences can be seen in the static composite (b). As can be seen in (d), the EVI increases with elevation, whereas this elevation-dependency is largely normalized in (c). There is also land cover dependent variability (f), and as can be seen in (e), the phenological normalization removes large parts of the within and between ecoregion differences.

Fig. VI-12 displays the effect of  $Y_f$  on the relative intra-annual to inter-annual data contribution in the compositing process for the POS, EOS and MOS composites. In case of the EOS, the effect of  $Y_f$  is negligible and virtually all data were acquired in  $Y_t$ , approximately within two weeks before  $D_t$  and one week after. However, the POS and MOS composites also include data from other years,  $\Delta D$  is generally higher (especially in the POS), and the choice of  $Y_f$  clearly affects the compositing process. In any case, most data is from  $Y_t$ . An increase in  $Y_f$  reduces the amount of data from  $Y_t$  and more data from  $\Delta Y \geq \pm 1$  is selected. In case of POS and  $Y_f = 3.00$ , the amount of data from  $\Delta Y = \pm 2$  is even larger

than from  $\Delta Y = \pm 1$ . The choice of  $Y_f$  has the reverse effect on the intra-annual selection. An increase in  $Y_f$  increases the amount of data that was acquired close to  $D_t$ . In case of the POS, data from  $\Delta D < 30$  and  $\Delta Y \geq \pm 1$  is selected at the expense of data with  $\Delta Y = 0$  and  $\Delta D = 40-90$ . In case of the MOS, data from  $\Delta D > -9$  and  $\Delta Y \geq \pm 1$  is selected at the expense of data with  $\Delta Y = 0$  and  $\Delta D = -9--16$ . The mean and standard deviations of  $|\Delta D|$  and  $|\Delta Y|$  are summarized in Table VI-4.

## 5.2 Global application

In order to demonstrate the global applicability of our approach, we generated MODIS EOS composites for 2005 for a large latitudinal gradient from boreal Russia to South Africa (Fig. VI-13). We generated a phenology-adaptive version (*b*), and static composites that were anchored at the hemispheric mean EOS, which is DOY 256 and 106 for the northern (*a*) and southern hemisphere (*c*), respectively. The tropics are similar in all composites. Large differences are visible in the sub-tropical belts ( $\sim 10^\circ\text{N}-10^\circ\text{S}$ ), where the phenology-adaptive version has produced the greatest homogeneity between the North and South. The static northern composite has higher (lower) biomass in the North (South), whereas the static southern composites has lower and approx. equal biomass in the North and South, respectively. Southern Africa also features large differences, where large parts of the sub-continent look barely vegetated in (*a*). Similarly, snow is very abundant at mid- and high northern latitude in (*c*). The phenology-adaptive version is also not free of snow but the northern temperate and boreal forest is spatially more homogeneous in terms of biomass than in the northern static composite.

## 5.3 Landsat composites

Analogously to the MODIS composites, phenology-adaptive and static Landsat composites were generated with a similar setup: POS, EOS and MOS composites using the descending sigmoid, Gaussian and ascending sigmoid functions, respectively. Fig. VI-14 depicts the generated phenology-adaptive composites. The temporal characteristics are shown below the composites, i.e. the selected DOY,  $\Delta D$  and  $\Delta Y$ . Basic statistics are summarized in Table VI-4. The number of observations is identical for all composites because they were generated with the same input data. On average 43.5 observations were considered ( $\sigma = 17.5$ ,  $\text{min} = 0$ ,  $\text{max} = 161$ ). The number of observations is shown in Fig. VI-2*b*.

The Landsat composites look similar to the MODIS ones, and analogously, the POS composite is of least quality, while the EOS and MOS composites are of high visual quality. The EOS and MOS composites differ by less than  $\pm 17$  days from  $D_t$ , while the POS composite differs by more than a  $\pm 50$  days (and additionally by a large standard deviation of about one month). The standard deviation



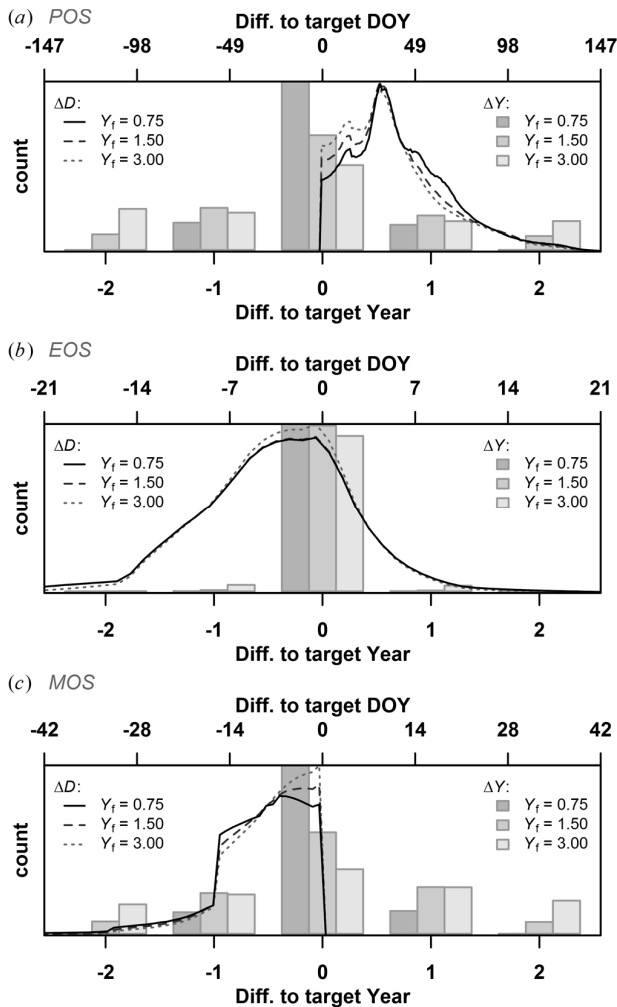


Fig. VI-12. Effect of different Y-factors on the phenology-adaptive MODIS composites. Histograms of the difference to the target DOY (line signature; top x-axis), and target year (barplot; bottom x-axis) are shown for the peak of season (a), end of season (b) and minimum of season (c) composites.

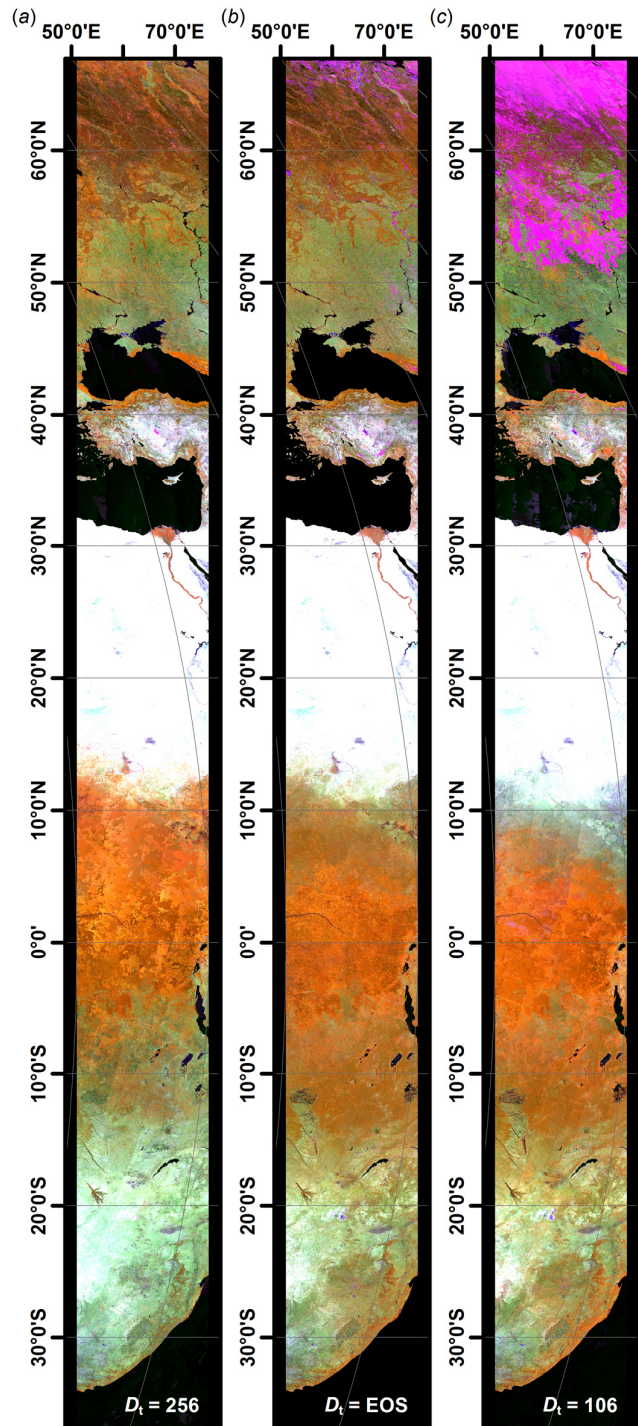


Fig. VI-13. Pixel-based MODIS composites for the target year 2005 across a large latitudinal gradient. The composites are end of season variants, where (b) is a phenology-adaptive composite; (a) and (c) are static composites that were anchored at the average end of season of the northern (a) and southern hemisphere (c).

of the MOS composite is slightly lower than in the EOS composite, which is due to non-optimal data availability in some orbits in the EOS case. The MOS composite is characterized by a higher share of data from the bracketing years, which in this case alleviated the non-optimal data

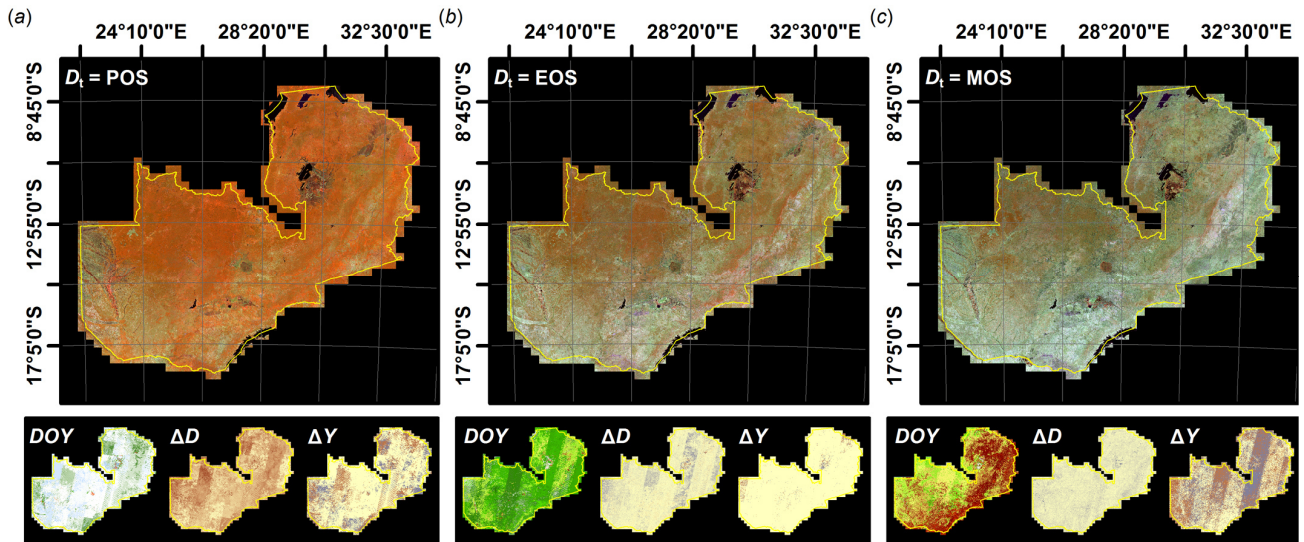


Fig. VI-14. Pixel-based Landsat composites for the target year 2005. The composites were anchored at three different phenological stages; (a): peak of season, (b): end of season, (c): minimum of season. The composites were generated with the proposed phenology-adaptive approach. Temporal characteristics are shown below the corresponding composite. For each composite, the selected DOY, the difference to the target DOY  $\Delta D$  and the difference to the target year  $\Delta Y$  are shown.

availability in  $Y_t$ . Overall, the temporal differences are larger than in the MODIS composites as a result of the different data densities. In case of the EOS and MOS composites, the selected DOYs resemble the LSP input patterns presented in Fig. VI-3, although not as precisely as the MODIS composites.

## 5.4 Cross-comparison

The quantitative cross-comparison of the phenology adaptive and static versions of the MODIS and Landsat composites is shown in Fig. VI-15. The phenological stages are shown in the rows (POS, EOS, and MOS from top to bottom) and the derived statistical measures in the columns. Green colors indicate a good match, red colors indicate differences.

The within-sensor POS composites have low ME, low MAE and RMSE and high  $R^2$ . The within-technique POS composites have high ME, high MAE and RMSE and yet high  $R^2$ . The between-sensor-and-technique composites have similar errors as the within-technique composites, although the sign of ME is not consistent. The  $R^2$  values are high for all combinations.

The within-sensor EOS composites have low ME, relatively high MAE and RMSE and intermediate  $R^2$ . The within-technique EOS composites have high ME, relatively low MAE and RMSE (compared to within-sensor EOS) and relatively high  $R^2$  (compared to within-sensor EOS).

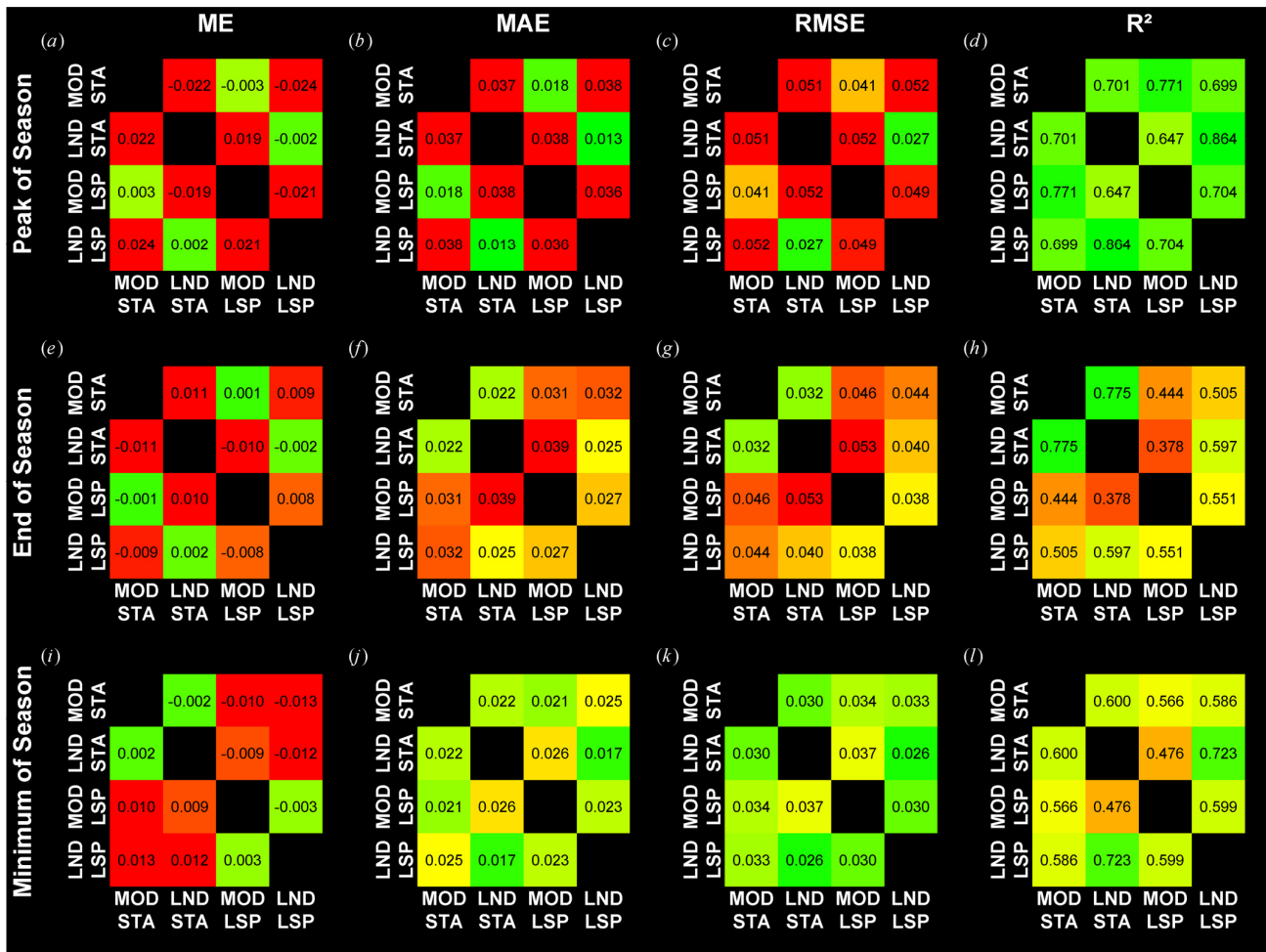


Fig. VI-15. EVI cross-comparison of the generated MODIS and Landsat composites. The phenological stages are shown in the rows with peak of season in (a–d), end of season in (e–h) and minimum of season in (i–l). Different statistical measures are shown in the columns with mean error (ME), mean absolute error (MAE), root mean squared error (RMSE) and coefficient of determination ( $R^2$ ) from left to right. The MODIS/Landsat composites are abbreviated with ‘MOD’/‘LND’ and the phenology adaptive and static versions with ‘LSP’/‘STA’, respectively. The residuals are calculated as  $e = x - y$ ; e.g. the lower-left ME value in (a) means that the static MODIS composite features higher EVI values than the phenology adaptive Landsat composite. The color ramps are consistent within each column.

The static MODIS and Landsat composites have highest  $R^2$ . The between-sensor-and-technique composites have the highest errors.

The within-sensor MOS composites have high ME with higher EVI in the static composites. The within-Landsat composites are characterized by low MAE and RMSE and high  $R^2$ , whereas the within-MODIS composites have good to intermediate MAE, ME and  $R^2$ . The within-technique MOS composites have low ME, RMSE and good  $R^2$  values. The agreement in MAE, RMSE and  $R^2$  is partly better and partly worse in the within-sensor and within-technique composites (except for within-Landsat). The between-sensor-and-technique composites have the highest errors, although the error metrics (apart from ME) are more similar than in the EOS composites.

## 5.5 Time series application

Fig. VI-16 depicts the CAT transformation applied to the annual Landsat EOS composite time series. The CAT transformation was developed to capture change events and gradual decadal-scale landscape dynamics and is effective to ‘distill’ the complete data archive into three variables that describe very different aspects of a changing landscape (Hird *et al.* 2016). The Change (largest difference between years), Aftereffect (mean of post-change) and Trend (slope of regression of the entire time series) components are mapped to RGB space and can be directly interpreted. Deforestation appears in red–orange colors due to the dominance of the Change layer; pure red colors indicate a complete replacement of forest with bare ground or water, whereas orange colors indicate that there remains some biomass after the change which represents a typical agricultural signature (recall that we have produced EOS composites). Stable forests appear in green due to the high biomass and the absence of any change and trend. Forest degradation appears in yellowish tones due to the negative trend; the mixture of red and green is both a function of the standing biomass and the rate of change. Gradual regrowth appears in cyan colors due to the absence of change, and gradual increase of biomass. Pinkish colors denote areas where a change and a positive trend were detected; these are mainly land covers that are characterized by strong inter-annual variations of biomass like the flooding plains and swamps. The CAT transformation is shown for complete Zambia, and for three subsets that depict different change processes. Forest degradation is depicted in Fig. VI-16*b–d*, where the yellowish areas represent areas where trees were selectively removed, while an increase in biomass is evident in the enclosed forest patch. Deforestation is readily visible in (*e–g*), where large forest areas were cleared to establish mechanized agriculture, leaving only isolated pockets of intact forest. A savanna-mosaic landscape is depicted in (*h–j*), where most part of the area was burnt before our analysis period. The area is largely characterized by an increase in biomass (blue areas), whereas the previously unburnt woodlands are stable. In addition, it can be seen that the flood plains are characterized by a high change, which rather is an effect of inter-annual variability within this land cover.

## 6 Discussion

### 6.1 MODIS composites and selected seasons

We developed and implemented a compositing technique based on a parametric weighting scheme as firstly proposed for Landsat data by Griffiths *et al.* (2013b), and in fact, the generated static composites are comparable to the Griffiths method. Besides implementing new selection scores and



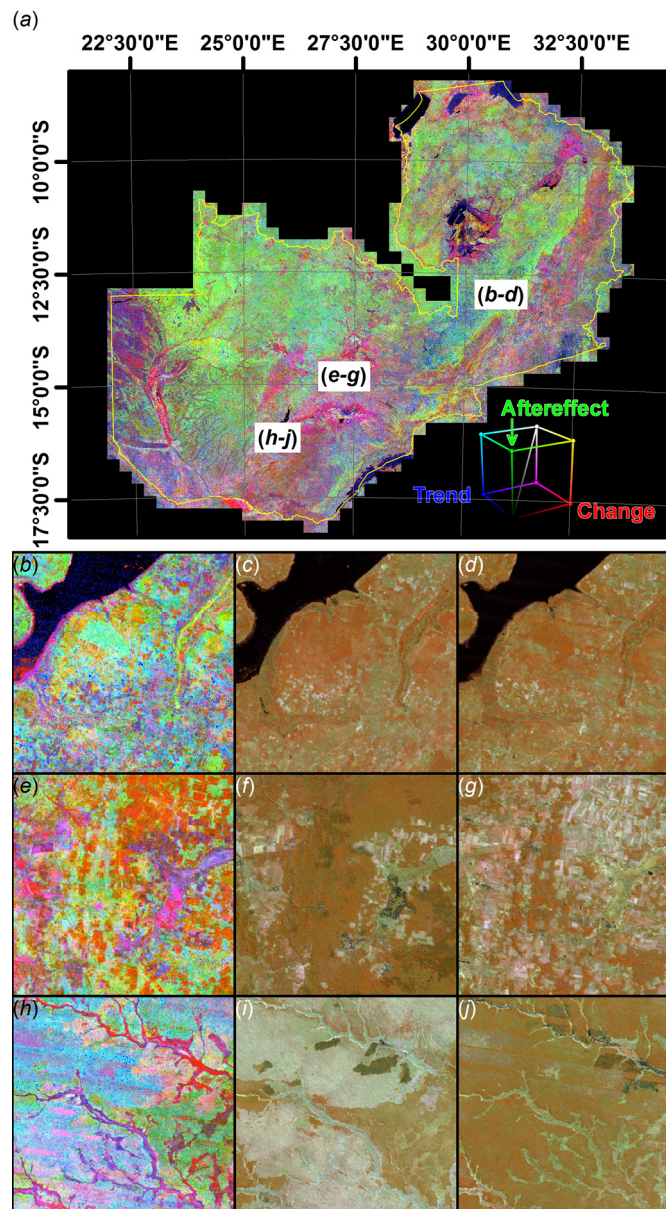


Fig. VI-16. CAT Transformation of the annual EOS Landsat composites, mapped to RGB space as Change, Aftereffect, and Trend, respectively. Three exemplary subsets (100 km<sup>2</sup>) depicting different change processes are shown in (b–d; 13.02°S / 30.76°E), (e–g; 14.78°S / 27.21°E), and (h–j; 16.23°S / 25.79°E) with CAT transformation, 2002 and 2012 composites from left to right.

enabling the code to be applied to optical EO imagery in general, we especially introduced a novel methodology for incorporating phenological information in the compositing process. As the Landsat data availability is relatively poor in this part of the world, the temporal compositing capabilities were tested with the daily MODIS product and were compared to a static equivalent, i.e. fixed DOY representing the mean state of the LSP. Multi-annual composites for three seasons were generated for both variants: peak of season, end of season and minimum of season. We used three different scoring functions (descending sigmoid, two-tailed Gaussian and ascending sigmoid), which resulted in three very different composites, although the same input data were used. The algorithm successfully

generated seasonal composites as close as possible to the phenological/static targets. In case of the phenology-adaptive version, the selected DOYs closely resemble the LSP input, which supports the functionality of the method. The three seasons were chosen as they potentially enable different analyses. Dry season images (e.g. EOS) are often employed for forestry applications in drylands due to the improved separability between trees and grass: drying minimizes photosynthetic herbaceous ground cover while trees might keep up a green foliage throughout the season (Armston *et al.* 2009). The driest point in time (i.e. MOS) is not necessarily suited to accomplish this task as deciduous trees can lose their foliage completely. This time may be appropriate for mapping burned areas. Whereas a single end of season image ( $\cong$  static composite) cannot be used in tropical savannas due to the temporarily limited persistency of the burned signal (Pereira 2003), the pixel-based selection of the minimum vegetation development could be instrumental. This season might also be optimal for soil-related analyses as dead or dry vegetation alter the reflectance shape less than green cover does (Siegal and Goetz 1977). Even though the generation of high-quality POS composites is problematic in areas where the rainy season and vegetation growth coincide, e.g. in dryland areas, POS composites may be highly suitable for certain applications, for instance the derivation of peak biomass maps as needed in the REDD+ context. Often a combination of different seasonal composites might be the best choice to accomplish specific tasks. Thus, for instance in the context of REDD+, EOS composites may be used to differentiate between woody and herbaceous biomass whereas the POS composites would allow for a better quantification of annual biomass. Other DOY-based LSP parameters can easily be integrated to generate other seasonal composites, e.g. start of season or inflection point parameters that might provide further essential information on ecosystems.

## 6.2 Landsat composites

Analogously to MODIS, multi-seasonal Landsat composites were generated. The selected DOYs closely resemble the LSP input, although the different orbits are partly visible (see Fig. VI-14). Similar to MODIS, the POS was of insufficient quality, whereas the EOS and MOS composites are visually homogenous and are characterized by relatively low differences to the target. However, the differences are larger than in the MODIS composites, which we attribute to the lower temporal resolution. The revisit frequency of MODIS was 1–2 days, whereas the nominal Landsat revisit time is 8–16 days in SLC-on and off image areas, respectively. In practice, this frequency cannot be met, see e.g. (Frantz *et al.* 2016b). The visibility of the acquisition orbits in the DOY and composite images is also a result of the worse temporal coverage. However it is noted that this applies to each compositing technique, may it be phenology-adaptive or not. This is the primary reason why we mainly use very dense MODIS to demonstrate the effectiveness of our approach.

### 6.3 Phenology-adaptive vs. static composites

#### 1) Regional application

Despite the visual congruence of the phenology-adaptive and static Zambian composites, there are in fact substantial differences that are illustrated in the  $\Delta EVI$  images (Fig. VI-9). By definition, the phenology-adaptive versions should have higher (lower) EVI values than the static POS (MOS) composites due to the employed one-sided sigmoidal scoring functions. Areas, where the LSP matches the Zambian average should have comparable EVI values. On the contrary, the phenology-adaptive EOS composite should have approximately equal amounts of pixels with higher and lower EVI values as a two-tailed Gaussian function was used. The POS composites are hard to interpret, since the target DOY could not be approached successfully as a consequence of persistent cloud coverage in the rainy season (see also the discussion on the Y-factor). As such, it is not surprising that the phenology-adaptive version does not always feature the highest EVI, as a significant amount of data is from different years with different biomass levels. This also manifests in the composites themselves, which are characterized by a stained appeal and feature severe reflectance discontinuities. This is also reflected in the quantitative cross-comparison: The within-MODIS composites have low ME and MAE values in EVI, thus there is no bias and on average, the composites are very similar. RMSE is intermediate, which means that there are some outliers that deviate from this;  $R^2$  is high nonetheless. This does not imply that the POS composites are of high quality. On the contrary, as already described before, neither the phenology-adaptive nor the static composites could approach the target day successfully, and as such, the composites are simply similar as both versions are rather bound by the end of the rains (in fact, 60% of the composites are the same observations). In principle, this also applies to the Landsat composites, which are even more similar as the temporal resolution is even more problematic, and thus nearly 70% of the composites are the same observations.

On the contrary, The EOS and MOS composites were of high quality and the target DOY could be approached with high precision. The EOS composites feature large connected areas with both negative and positive EVI differences. This supports the correctness of the procedure as in certain biomes and regions the end of the season occurs earlier/later than the Zambian average. The quantitative assessment supports this. The within-sensor composites have low ME, thus there is no bias which is a result of the two-sided Gaussian scoring function that caused both negative and positive EVI differences. MAE, RMSE are high and  $R^2$  are intermediate, which means that there are indeed larger differences pointing to a successful levelling of phenological differences in the phenology-adaptive version.

The MOS composites features large patches of positive differences, which also supports the correctness of the procedure as the phenology-adaptive approach should select observations close to the seasonal minimum. As an exception, there are some negative differences, although the magnitude and abundance is not as large as that of the positive ones. In addition, they do not form large connected areas. Potential error sources may be attributed to minor noise in MOD09GA data or to the derivation of LSP itself, which was inferred from the MODIS EVI products (MOD13Q1, MYD13Q1). The EVI product is derived from constrained-view angle maximum-value compositing, which is not optimal for finding the seasonal minimum with utmost precision. The employed smoothing spline might also have caused some inaccuracies in finding the seasonal minimum as it cannot adapt to breakpoints perfectly, e.g. induced by fire. Nevertheless, the compositing produced the desired results at large, which is also backed by the quantitative cross-comparison as there is a large positive bias (ME) between the within-sensor composites due to the one-sided sigmoid. MAE is relatively low, which is due to the fact that the static composite was parameterized with the mean value of the phenology used in the phenology-adaptive version, and as such, only the land covers that deviate from this mean are different. This explains why the RMSEs are higher than the MAEs due to the stronger effect of outliers.

## 2) Local application

Static and phenology-adaptive EOS versions were further compared for a smaller subset, where elevation gradients ( $> 1000$  m) are a primary source of LSP variability, and as such, the effect of using different compositing techniques can be shown effectively (Fig. VI-11). It was shown that the phenology-adaptive version is spatially homogeneous, whereas larger differences occur in the static composites. The phenology-adaptive technique accounts for the elevation-induced shifts in EOS, and hence, there is more or less one EVI value for the complete elevation range. On the contrary, elevation-induced gradients can be readily seen in the static version, wherein EVI values increase with elevation. Note that this counterintuitive behavior is a result of the temperature distribution as described in chapter 2, where the tropical-warm climate in higher regions provides better conditions for biomass accumulation than the tropical-hot climate in the lower valley plains. In addition, there is also a land-cover class dependent variability in EVI. It needs to be noted that the World Wildlife Fund (WWF) terrestrial ecoregions were used for the stratified boxplots, which are a rather coarse and spatially generalizing description of land cover. Nevertheless, the different classes are clearly separable in the static composite whereas this variability was reduced with phenology-adaptive compositing. This both applies to the between ecoregion and within ecoregion variability, and thus the phenological harmonization was successfully realized.



### 3) Global application

A large latitudinal gradient from boreal Russia to South Africa was chosen to demonstrate the utility of our approach for global scale analysis support. As shown in Fig. VI-13, even cross-hemispheric composites may be generated and the forests in the same geographic zones are similar for both hemispheres. This is especially striking in the sub-tropical belts, whereas large differences occur in the static composites (that were anchored at the hemispheric mean phenology). It is also apparent that a phenology-adaptive composite minimizes the risk to choose an unfortunate target DOY that might cause severe misinterpretations: the complete sub-continent of Southern Africa seems barely vegetated in the static composite tuned to the northern hemisphere, whereas different savanna, grass and woodland biomes can be resolved in the phenology-adaptive version. Northern hemispheric snow contamination is also a good example of this effect, as a less careful selected target DOY can result in severe snow cover (part *c*), whereas the phenology adaptive approach can account for latitudinal variations in the timing of the snowy season and also for inter-annual differences. However, it needs to be noted that the phenology-adaptive version is also not free of snow, although the affected areas are rather unvegetated and are thus of less concern for vegetation-based studies (bare soils and water bodies). It is likely that the phenology detection code might have interpreted the snow signal as a vegetative cycle. Areas that are characterized by a low phenological amplitude (tropics / deserts), are relatively similar in all versions. On the one hand, this is caused by the spectral invariance over the year, but is also a result of the reduced availability of cloud-free observations in tropic regions, which was already discussed in the last chapter in the wet season Zambian example.

### 4) Implications

The question arises whether phenology-adaptive or static composites are superior for large area mapping and monitoring tasks, and we recommend considering the compositing method carefully for any given application. For regions that do not feature large gradients or discontinuities in LSP (this especially might apply to small areas), the overhead in using the more complex phenology-adaptive approach might not be justified, since an LSP dataset at an appropriate spatial scale needs to be derived in the first step. The static approach might also be superior for certain land cover classification tasks, as e.g. the discrimination of crop types partly rely on the phenological phase difference of the growing stages (Van Niel and McVicar 2004) – although this might be equalized by additionally using the selected DOY layer in the classification. On the contrary, the phenology-adaptive technique re-phases the crop development, and thus decreases the spectral variability within the crop classes. This feature might improve the separability against other classes such as grasslands, fallows, abandoned land or

bare grounds (Griffiths *et al.* 2013a). The phenology-adaptive approach might also alleviate problems related to within-class differences in LSP, e.g. as a function of terrain altitude. As an example, the derivation of forest information layers like the classification of tree species (Stoffels *et al.* 2015) would benefit from the disintegration of development stage differences, and would thus account for the altitude-induced delay of foliage growth. In the context of forest clearing, the generation of a homogeneous leaf-on composite could also decrease false detections, as e.g. seasonal variations in broadleaved canopies might erroneously be classified as deforestation if acquired in an unfortunate phenological stage (DeFries *et al.* 2007).

#### 6.4 MODIS vs. Landsat composites

The consistency between the MODIS and Landsat within-technique composites was quantitatively evaluated. It is noted that different spectral response, a different radiometric preprocessing (especially including different types of corrections), different view geometry (although reduced by preferring near-nadir pixels in the compositing) and different spatial resolution (although reduced by degrading the Landsat composites with a MODIS point spread function) will inevitably result in differences. However, we assume that the greatest differences occur due to phenological differences as a result of the different repeat frequencies. This is supported by the ME values that show large positive differences in the POS composites, both for the static and phenology-adaptive version. As can be seen in Table VI-4, the mean  $|\Delta D|$  is “only” 42 (34) days for the phenology-adaptive (static) MODIS composites whereas it is 50 (44) days for Landsat. Thus, the MODIS composites reach farther into the wet season and consequently have higher EVI. The between-sensor MOS composites are very similar and all statistics indicate a good agreement (especially ME), which is also reflected in low mean  $|\Delta D|$  values (Table VI-4). In this comparison, the EOS composite statistics are a bit harder to interpret because of the nature of the two-tailed Gaussian scoring functions, which permits both earlier- and later-than-target observations with higher and lower EVI, respectively. As such, it is possible that an early MODIS observation and a late Landsat observation was chosen, and vice versa, which results in a somewhat larger MAE and RMSE statistics. This is especially driven by the limited data availability of the Landsat system, which might have a bias towards one end: the ME indicates a negative bias which implies that earlier-than-target Landsat observations were preferably chosen (the  $\Delta D$  image in Fig. VI-14 supports this). Nevertheless, the statistics indicate a fairly good agreement – especially if compared to the within-sensor EOS composite statistics. Overall, the quantitative comparison indicates that the between-sensor differences (like radiometry) are indeed within an acceptable range and that differences are mostly a result of temporal characteristics.

## 6.5 Intra- to inter-annual contribution and seasonal suitability

The effect of the  $Y$ -factor on the relative intra- to inter-annual data contribution was shown in Fig. VI-12 for very dense MODIS data. The inter-annual scoring scheme was designed such that data from the target year are always preferred, and it is more likely that a higher share of data from bracketing years are selected if  $Y_f$  is increased.  $Y_f$ , in combination with the inter- and intra-annual data availabilities eventually determines the selection process. If the clear-sky data availability close to the phenological target is high in  $Y_t$ , the effect of  $Y_f$  is negligible – as data from  $Y_t$  is always preferred. This was the case for the EOS composites, where different  $Y$ -factors did not substantially influence the selection process (see Fig. VI-12b) as very low differences to the target DOY could already be achieved with 2005 data only (see Table VI-4). Therefore, the data availability in 2005 was sufficient to generate a homogeneous EOS composite. On the contrary, different  $Y$ -factors substantially influenced the selection in case of the POS and MOS composites (see Fig. VI-12). In case of the POS, the data availability in the wet season was insufficient, and as such, stained composites were generated (see Fig. VI-9). If a higher share of data from the bracketing years are incorporated (increase in  $Y_f$ ), observations closer to the phenological target are selected (see Fig. VI-12a). Nevertheless, the differences to the target DOYs are high with any  $Y_f$  (see Table VI-4). As such, we conclude that the quality of POS composites must be regarded as being of low quality due to the impossibility to approach the phenological target adequately, even when considering 5 years of very frequent MODIS data. While it might be expected that frequent Sentinel-2 acquisitions could alleviate the medium-resolution information retrieval in areas and periods dominated by persistent cloud cover, our results with MODIS clearly indicate the opposite. Hence, we suggest that additional research should be conducted before deciding whether peak season composites in arid areas are of sufficient quality to be incorporated in operational monitoring programs or if the compositing artifacts are of larger magnitude (in terms of spectral contrast) than the effect of the monitored processes. In case of the MOS, the parametrization of  $Y_f$  influenced the compositing process (see Fig. VI-12c), but the differences to the target DOYs were small nonetheless (see Table VI-4). The differences are approximately twice as high as in the EOS composites, which could be due to the employed one-sided sigmoid, whereas a two-tailed Gaussian was used for EOS. However, the differences are still low on average (regardless of  $Y_f$ ) and the resulting composites are visually homogeneous. An increase in  $Y_f$  allowed more data from the bracketing years, which implies that – compared to the EOS – the clear-sky data availability during the driest period of the year is slightly reduced. This might be an effect of the widespread burning plumes (Stellmes *et al.* 2013a) or substantially higher aerosol levels during this period (Frantz *et al.* 2015a).

We cannot provide a general rule on how to choose an optimal Y-factor, but there are a number of environmental and data-related factors that should influence the parameterization. As discussed above, the choice of  $Y_f$  is uncritical if enough data are available in the requested season. If not, following points should be considered. If the study area is dominated by surface types that are rather stable between the years (in terms of reflectance and amount of biomass; however, the timing of the LSP may vary between the years as the phenology-adaptive approach accounts for inter-annual variations), e.g. forests, a higher Y-factor might be feasible in order to decrease  $\Delta D$  and to generate a composite that is as close as possible to the requested phenological target. On the contrary, more unstable cover types might necessitate a low  $Y_f$ . As an example, inter-annual variations in the amount of biomass of grasslands or grass-dominated savannas can be substantial, as biomass is accumulated over multiple years unless burned (Scholes *et al.* 1996), which both alter the spectral characteristics from year to year. Hence, even if a grassland is captured in the same phenological state, the reflectance might differ substantially between the years due to variations in biomass. We also suggest to use a low  $Y_f$  if land cover change is to be expected within the compositing period.

## 6.6 Homogeneity and bidirectional effects

Bidirectional effects were readily visible in the static MODIS composites as a discontinuity of surface reflectance between neighboring orbits. Although the effect is stronger in the MOS, it is also evident in the EOS. On the contrary, this effect is not visible in the phenology-adaptive versions. We presume this being a side effect of the phenology-adaptive approach in that the extensive mixing of acquisition dates on the pixel scale increases the angular variability, and thus masks the visibility of bidirectional effects on the orbital scale. However it needs to be stated that bidirectional effects are still present on the pixel scale. In fact, the phenology-adaptive versions do look more grained in comparison to the static ones, which is likely an effect of the increased angular variability. On the contrary, the static composites only feature a limited angular variability, as continuous orbits were selected (see Fig. VI-10) that are characterized by strictly opposed view geometries. In both cases however, the incorporation of the view zenith score resulted in the avoidance of the worst view geometries. The Landsat data were corrected for bidirectional effects, and the resulting composites are merely free of these effects. There are some discontinuities along the orbits in the EOS composite (Fig. VI-14b), although this is rather induced by phenology as the difference to the target DOY is larger in some orbits than in others. This is also supported by the MOS composite as it has smaller differences to the target DOY and is merely free of such discontinuities (Fig. VI-14c).

In case of Landsat, we produced composites based on higher level radiometric input data, including corrections for atmospheric, topographic and a global part of bidirectional effects. In case

of MODIS, only atmospheric effects were considered, although the MODIS NBAR product may also be input, in which case a phenology-adaptive composite of composites would be generated. However, the very high temporal frequency would be sacrificed by doing so. The compositing algorithm is not in need for a specific input product and may also be parameterized using unelaborate inputs, e.g. TOA reflectance. However, we consider it advantageous to generate the best possible product in order to enable any kind of follow-up analysis, be it qualitative or quantitative.

## 6.7 Implemented scores

Griffiths *et al.* (2013b) determined the suitability of any observation by a combination of acquisition day, acquisition year and the distance of a pixel to the next cloud or shadow. We expanded on this approach by tuning the inter- and intra-annual criteria with pixel-based phenology and by introducing additional scores to devalue hazy observations, spectral outliers and observations acquired with high view angles. Especially the last criterion was instrumental in generating homogeneous MODIS composites; and although the FOV is narrow and orbital overlaps (at least in our study area) are small for the Landsat composites, the inclusion of this scoring function also increased the homogeneity at the very edge of the swaths slightly. However, we expect that this effect would be more pronounced in areas with larger overlaps and with input datasets not featuring a correction for bidirectional effects; as it was the case with MODIS in this study. The implemented correlation score helped to devalue observations with transient land cover change like flooding or active fires, whereas the algorithm behavior is not strictly defined with regards to permanent land cover change. However, the correlation score is expected to favor the land cover that was observed more often, and the use of LSP ensures that the selected observations are at least in same phenological state – although not necessarily in the same land cover class. The year score and the Y-factor further reduce the risk of selecting different land covers as target year observations are generally preferred. We consider our approach flexible with respect to the definition of additional scoring functions, which can be easily integrated into equation VI-1. As an example, spectral scores that devalue burned or flooded areas might be applicable for specific research questions in our study area, or specific sensors may be devaluated as done by White *et al.* (2014). Nevertheless, such criteria should be well-considered since the resulting composites will be harder to interpret as they are no longer dominated by temporal characteristics, and the homogeneity might be decreased.

## 6.8 Time series application

The potential for land cover change mapping was demonstrated by applying the CAT transformation (Hird *et al.* 2016) to an annual Landsat EOS time series (2001–2012 ±0) with the

phenology-adaptive technique. It needs to be noted that biomass differences between a vegetated and an unvegetated surface are lower than in the POS, which decreases the signal-to-noise ratio of this application (therefore, a national stretch was employed instead of the one Hird *et al.* (2016) proposed). However, the EOS is optimal to separate trees and grass, whereas their inseparability can shroud land cover change in the POS. Even more importantly, it was demonstrated that the quality of the EOS composites was high because the target day could be approached successfully with target-year-only data, a requirement that was not met by the POS composites. As such, the EOS is a reasonable compromise to identify land cover change processes.

In order to detect gradual processes, an annual approach was chosen, which has resulted in an increase in  $\Delta D$  compared to the five-year cases shown above, which necessitated the rigorous filtering of the time series before applying the CAT transform; all observations that deviate more than  $\pm 16$  days from  $D_t$  were rejected. This allowed to extract the change, aftereffect and trend information with adequate accuracy. The resulting CAT images are merely free of artifacts, which supports the quality of the approach as inter-annual fluctuations are low. The CAT image clearly indicates different change processes – even gradual ones, and thus provides a comprehensive picture of the land cover transformations and modifications throughout the past decade. The next step would be to quantitatively map the corresponding change classes and to provide nationwide change statistics, which is out of scope of this paper as this is not a straightforward analyses. As can already be seen with the fairly simple CAT transform, the same change process has to be interpreted within a context. As an example, the gradual increase in biomass shown in Fig. VI-16 $h-j$  is due to regrowth after a large savanna fire, which represents a significantly different ecological meaning than e.g. biomass increase in a forest stand or following agricultural abandonment.

## 7 Conclusion

We implemented a parametric pixel-based compositing approach by integrating methods for adapting the compositing process to the underlying land surface phenology of each pixel. The technique can be applied to any kind of gridded EO archive, which we demonstrated for MODIS and Landsat data. In both cases, homogeneous and seamless multi-annual composites could be generated across large areas for most seasons. It was shown that the technique is general enough to be applied globally.

Seasonal composites can be generated by inputting spatially-explicit LSP layers, and the choice of the scoring functions further increases the flexibility in generating composites representing different phenological phases. The resulting composites were shown to perform a phenological

normalization across elevation gradients and land cover classes. As an alternative, fixed DOY composites may also be generated, and the potential application of either method is discussed and should be considered with care. The inter- to intra-annual data contribution can be controlled by a single parameter which handles the tradeoffs between using data from the target year versus using data that is preferably very close to the target day. We implemented a number of auxiliary scores for specific purposes, e.g. to avoid clouds. The scores can be disabled or enabled in any possible combination and the strength of each score may be adjusted freely.

As the Landsat data availability is relatively poor in this part of the world, the temporal improvements of this approach were demonstrated with the daily MODIS product. It was demonstrated that wet season composites could not be generated with sufficient precision, however, dry season composite generation was successful. These composites were found to be coherent and homogeneous in most areas, which also applied to analogously generated Landsat composites. Unsurprisingly, the target dates could not be matched as exactly as in the MODIS composites as a consequence of the lower temporal resolution. The quality of the MODIS and Landsat composites, as well as the performance of the phenology-adaptive and static compositing techniques was assured using a quantitative cross-comparison. The generation of a 12-year annual time series demonstrated the feasibility for land cover change and modification mapping. Several change processes were clearly discriminable.

Potential applications of the method include for instance the generation of decadal, five-year or annual composites representing the land cover in the same phenological stage for the establishment of national, regional or even global landscape monitoring, reporting and verification systems.

## **Acknowledgements**

Landsat and SRTM data courtesy of the USGS. The MODIS data used in this study were retrieved from the online Data Pool, courtesy of the NASA LP DAAC, USGS/EROS Center, Sioux Falls, South Dakota, [https://lpdaac.usgs.gov/data\\_access/data\\_pool](https://lpdaac.usgs.gov/data_access/data_pool). ARC2 data courtesy of the Climate Prediction Center, NOAA, <https://data.noaa.gov/dataset/climate-prediction-center-cpc-africa-rainfall-climatology-version-2-0-arc2>. We thank Dr. Sebastian Mader, Trier University, for providing the SpliTS algorithm used for generating the MODIS LSP dataset. This work was supported by the Federal Ministry of Education and Research under contract number FKZ-01LG1201C as part of the SASSCAL Project. The authors would also like to thank the three anonymous reviewers whose very constructive comments significantly improved the quality of the final paper.





## **Chapter VII**

### **Synthesis**

## 1 Summary

In this thesis, the development of a framework for generating higher-level EO satellite products for potential use in regional environmental monitoring programs was pursued. Special attention was put into the development of processing options for dryland areas, although not explicitly limited to these. This overarching research task was partitioned into three major objectives.

The generation of a radiometrically normalized and geometrically consistent dataset denoted as Level 2 products was pursued with objective I. These baseline data represent the fundamental basis needed for most higher-level environmental analyses. The generation of a Land Surface Phenology baseline was addressed in objective II, and directly leads over to objective III, wherein the datasets generated in I–II are used to frame a Level 3 processing system capable of generating seasonal pixel-based composites with phenological normalization.

In the following, the three objectives are summarized briefly, and the next chapter will eventually illustrate how the herein developed methods and datasets may promote regional case studies or be integrated into operational environmental monitoring concepts.

### 1.1 Objective I: Development of a Level 2 production system

A fully automatic radiometric preprocessing streamline was successfully implemented; see Chapter II. The method was applied to the complete Angolan, Zambian, Zimbabwean, Botswanan and Namibian TM, ETM+ and OLI Level 1T data record held in USGS holdings as of 31.12.2014. The data quality was estimated to be within specification for 98.8% of 41,762 processed images.

Cloud and cloud shadow detection was implemented by integrating a modified version of the Fmask algorithm. The implemented modifications were described in Chapter II - 4.2 and Chapter III - 4.1. Dryland-specific improvements were developed by including an additional darkness filter for reducing false positives in bifidly structured images (cold and hot surface elements); the approach presented in Chapter III can be applied to Southern Africa without modification since Australian and Southern African savannas are similar in structure and landscape composition. In addition, the termination criterion for matching clouds with their shadows was discarded, which in combination with a modification of the match similarity metric increased the shadow detection capabilities. For enhanced computational performance, full-stop criteria were incorporated to skip the costly shadow matching if the image was already assessed to be useless. Note that the time-series based add-on (also presented in Chapter III - 4.2) was not implemented in this product generation system. Although omission errors could have been reduced by incorporating this technique, a per-image processing was

considered most efficient for mass-generation of Level 2 products as it enables the implementation of in-memory processing streamlines.

Atmospheric correction was based on radiative theory and includes corrections for multiple scatterings and the adjacency effect. Significant work was put into the derivation of AOD, and hence a multilayered toolset was developed (and is currently further advanced) where AOD is favorably estimated over persistent cast shadow and water targets. It is based on a combined image-, database-, and object-based approach using the target-specific view and illumination geometry, altitude, and environmental contamination. If there are no persistent targets within an image, AOD may also be estimated from transient targets. If these are also not available, there are two options: for simplicity, a (i) global AERONET-derived constant AOD may be used – or a (ii) variable spatio-temporally AOD surface may be input. The derivation of this surface was described in Chapter IV; note that the method was revisited and the products in Chapter II were based on an AOD surface instead of path reflectance. Both the restriction to persistent dark targets, as well as the fallback to a reasonable AOD climatology (in case of dark target absence) helped to generate a qualitative dataset in an environment where AOD is particularly high and variable, but difficult to determine at the same time. Current work is going on to further advance the AOD module, e.g. by using a spatially explicit AOD map if applicable, and by adding a DDV estimator.

A semi-empirical C-correction was implemented for topographic correction, where a stratified linear regression between the illumination angle and the at-sensor radiance was employed. Topographic effects were substantially reduced after the correction, which was especially successful in the infrared bands, while less reduction was occasionally achieved in the shortwave bands as high aerosol levels with substantial diffuse illumination can impede a linear relation. However, for operational implementation, the correction was deemed sufficiently adequate, especially when compared to readily available alternatives like the Minnaert-correction which was shown to have a tendency for overcorrection.

At the time of writing the article in Chapter II, it was decided to not include a correction for bidirectional effects, until a technique becomes available that could be automatically applied independently of data availability and without *a priori* land cover knowledge. During the course of working on this thesis, researchers have demonstrated that the BRDF shapes of land surfaces are fairly similar over Landsat's FOV, and as such, a global set of MODIS-derived BRDF spectral model parameters may be used to mass-produce NBAR (Roy *et al.* 2016). Consequently, this method was assimilated into the presented Level 2 production system, and the complete dataset was reprocessed to NBAR prior to generating the Level 3 Landsat products presented in Chapter VI.

Gridding and reprojection to a common reference system were fully integrated, such that the resulting Level 2 products are suited for easy and efficient further processing. For the study area, a Lambert Azimuthal Equal Area projection was chosen with its centroid in the middle of Southern Africa, such that adjacent areas could be attached easily if required in the future. The grid size was defined with 30 x 30 km as a reasonable compromise between a sufficiently large geographical extent and modest product volume: the complete time series of one tile should fit into memory for further processing with off-the-shelf hardware, and hence, it was specified that at least 1,000 chips (reflectance + cloud products; compare with Fig. II-7) should be processible with low-tech workstations with 16 GB RAM. Nevertheless, the code was held flexible such that the projection and gridding parameters can be modified or disabled at will, e.g. for global implementation using a sinusoidal projection.

It is noted that two specific processing options deviate from the ideal conception of the per-image analysis, where a given image should be touched once-only. The pre-compilation of the dark object database is a prerequisite for only using the most persistent dark targets for AOD estimation. However, this processing strategy is not mandatory, and although it is conceptually favorable to restrict to invariant and persistent dark targets, sufficiently accurate results may also be produced without (especially in areas where transient dark targets are less dominating). The second deviation is the generation of the AOD climatology: the complete dataset needed to be processed in a first step, the climatology was built on the basis of all successful AOD estimates, and the failed images were finally reprocessed using the external values. Nevertheless, the core processing functionality, i.e. the cloud, radiometric and geometric modules, was streamlined entirely in memory without dumping of temporal data or intermediate products to the hard disk. And thus, the ideal conception of the per-image analysis can be fulfilled if these critical processing strategies are not used, which is expected to be adequate in areas where AOD estimation is less problematic.

The product generation system was developed to process data from all TM-heritage sensors, and it was shown that the radiometric agreement between the OLI and ETM+ was similar as the agreement of the more identically constructed TM and ETM+. Current work is going on to implement Sentinel-2 product generation, and it is expected that the radiometric continuity to OLI will enable a full-fledged synergistic usage.

The radiometrically corrected satellite products are expected to make a contribution towards the simplified integration into data-intensive applications and to promote the development of specific regional case studies. The Level 2 products were already or are currently used for a number of purposes, most obviously for fusing LSP and Level 3 product generation with subsequent delineation

of landscape processes as presented in Chapters V–VI. Other current uses will shortly be presented in the following outlook section.

## 1.2 Objective II: Development of a Land Surface Phenology baseline

As a prerequisite for generating phenology-adaptive Level 3 products, an LSP baseline at appropriate spatial resolution had to be generated. The approach was outlined in Chapter V.

The data availability and the magnitude of inter-annual variations in the study area were identified inadequate for deriving LSP from Landsat data themselves, whereas it is generally accepted to do so with dense but coarse MODIS data. Therefore, a MODIS LSP dataset was generated in a first step using a spline-based phenology extraction algorithm. Afterwards, a novel data fusion technique for improving the spatial resolution of such coarse continuous fields was developed.

A focal filter based approach was implemented where the coarse continuous field is fused with a small number of seasonally distributed medium resolution reflectance images that are insufficient to describe LSP temporally accurate but nonetheless include qualitative information to separate image regions with different phenological patterns. The local pixel neighborhood was intensively used by employing multiscale prediction proxies, including spectral distance and heterogeneity metrics. The quality of the prediction was demonstrated using simulated landscapes, and by application to a heterogeneous agricultural site in Zambia. In general, the prediction was of high quality ( $R^2 = 0.84$ ), and even reduced noise in the input data. Objects larger than the coarse resolution IFOV can be reliably predicted – and even significantly smaller objects can be predicted accurately if there are pure homogeneous coarse resolution pixels within the focal filter window. Spatial patterns, e.g. circular irrigation pivots were successfully restored at medium spatial resolution.

Being a pixel-based method, the approach makes direct use of the gridded Level 2 products generated in Chapter II. Appropriate data are automatically selected; the operator simply needs to define a number of seasonal windows to capture the main phenological patterns. Data from neighboring tiles are appended on-the-fly to the tile under consideration to produce a seamless LSP baseline.

Regarding computational efficiency, comparable existing approaches commonly rely on a two-step procedure where a dense synthetic time series is generated in a first step, and afterwards LSP is inferred thereof. On the contrary, the presented approach infers LSP from coarse resolution and then predicts LSP at finer resolution. This is computationally advantageous in two respects: (i) the derivation of LSP is much faster if done with coarse data (one 250 m MODIS pixel equals ~70 Landsat

pixels) and (ii) the focal-based prediction has to be done once-only – opposed to once per dense time step.

Although this approach was developed and used for phenological normalization of image composites, the derived information also serves as an example of a Level 4 model output as phenology is an EBV itself and may be further used for a wide range of ecological analyses. In a recent study, coarse resolution LSP was shown to be a strong indicator for modelling plant alpha diversity across large areas (Revermann *et al.* 2016). However, the main criticism of this work was the mismatch of MODIS spatial resolution and the employed vegetation plot database. That said, data as presented here have the potential to make a strong contribution in the field of ecology and biodiversity as they match the scale at which many landscape processes are happening.

### 1.3 Objective III: Development of a Level 3 production system

A phenology-adaptive pixel-based compositing framework was successfully implemented using a parametric weighting scheme based observation selector; see Chapter VI. The method was mainly demonstrated with Zambian MODIS and Landsat data, thus showing that any similar EO archive may be input.

The phenological normalization was primarily achieved by allowing the target day to vary from pixel to pixel in dependence of the input LSP. Hence, for each pixel, a function is fit to three phenological parameters – two-tailed Gaussians and ascending/descending sigmoid functions can be used – and the corresponding Landsat data are scored accordingly. This is done separately for each season in order to account for inter-annual differences. The inter-annual contribution was controlled by a single parameter, also in dependence of LSP in order to account for different greenness/senescence rates between the seasons.

Peak, end and minimum of season composites were generated with MODIS and Landsat data. It was shown that similar composites can be generated with both data sources, and the primary source of discrepancy was identified to be the more limited Landsat data availability. Hence, the method makes best use of dense image archives like MODIS and the application to temporally coarser resolved data somehow limits applicability, although it needs to be noted that this applies to any kind of compositing technique and is not a specific drawback of the phenology-adaptive technique. In any case, the enhanced temporal capabilities of the two-satellite Sentinel-2 system will represent a most welcome asset for the presented technique, which is expected to significantly boost medium resolution Level 3 data quality.

The phenology-adaptive composites were compared with static parameterizations that more or less correspond to the original approach of Griffiths *et al.* (2013b). It was demonstrated that large differences between the techniques occur across the study region as a function of large-scale climatic gradients and are locally modified by terrain altitude. It was demonstrated that the phenological normalization can account for such terrain-induced LSP differences. It was also discussed which technique is better; a question that cannot be answered in general because both methods have unique advantages and hence, it needs to be carefully considered which technique is best for a given purpose.

Global applicability was demonstrated by generating composites across a large latitudinal gradient from boreal Russia to South Africa with MODIS data, where the phenological normalization was readily visible across the hemispheres. In addition, it was demonstrated that an unfortunate definition of a static target date can shroud land cover, as e.g. most parts of Southern Africa appeared bare in the composite anchored at the northern hemispheric mean EOS.

The approach makes direct use of the gridded Level 2 and LSP products generated in Chapter II and V. Appropriate data are automatically selected based on a limited number of mandatory criteria. Whilst the approach runs on a per-tile basis, the resulting composites are on the fly mosaicked to a single seamless image. The usage of the comprehensively corrected downstream products enables a wide range of monitoring options, among them the detection of within-state processes like forest degradation. Using the Change, Aftereffect and Trend (CAT) transformation, it was demonstrated that many landscape processes, being abrupt or gradual, can be resolved with the generated data.

## 2 Conclusions and Outlook

The developed preprocessing framework is capable of generating several analysis-ready baseline EO satellite products. These include radiometrically normalized and geometrically consistent Landsat time series, as well as phenologically sound and seamless image composites across large areas. Current work is underway to further develop the methods, to integrate new satellite sensor sources like Sentinel-2 and to further validate the atmospheric correction and aerosol optical depth estimation scheme under a broader range of environmental settings than considered in this thesis. Concurrently, the approach is also transferred, tested and if necessary adapted to other study areas, among them temperate and mountainous forest areas.

Several regional case studies are currently built around the generated Level 2 and Level 3 datasets. As an example, Schneibel *et al.* (2016) used a number of manually selected Level 2 images for mapping agricultural expansion and evaluated the corresponding tradeoffs between food and timber ecosystem services in central Angola. Based on this, they illustrated the utility of annual composites in combination with time series decomposition for characterizing socio-economic induced shifts of agricultural regimes in the context of post-war migration (Schneibel *et al.* upcoming). The potential of multi-seasonal phenology-adaptive composites, in combination with extensive field data is currently explored for vegetation-type mapping. Moreover, phenology-adaptive composites at decadal intervals are currently considered for regional land cover / change mapping, and spectral-unmixing based forest dynamics analysis.

Besides the implementation of these datasets in regional case studies, the generated products also possess the potential for direct integration into more operational monitoring systems. As an example, multiannual composites at regular repeat frequency are a viable basis for the REDD MRV systems, where especially the phenological normalization teamed up with forest structure information could make a contribution towards regional biomass change estimations. More concretely, the developed processing streamline, with ongoing Sentinel-2 adaption, is currently established for statewide tree species mapping in collaboration with state agencies, and is thus potentially transitioning into an operational service. To even go one step further, the full automation of radiometric preprocessing of medium resolution imagery hypothetically enables the implementation of near-real time monitoring systems, e.g. by issuing deforestation alerts (e.g. Hansen *et al.* 2016, Zhu *et al.* 2012). If these are coupled with effective environmental law enforcement (e.g. Nepstad *et al.* 2014), such a system would have great potential to prevent illegal deforestation at an early stage. In general, such systems could make a significant contribution towards a more sustainable resource use,



which is of crucial importance given the dependence of the well-being of the 7+ billion people on the ability of ecosystems to supply services and functions that are vital to mankind.

---

## References

- Amoros-Lopez, J., L. Gomez-Chova, L. Alonso, L. Guanter, J. Moreno, and G. Camps-Valls (2011). Regularized Multiresolution Spatial Unmixing for ENVISAT/MERIS and Landsat/TM Image Fusion. *IEEE Geoscience and Remote Sensing Letters* 8 (5), 844-848. DOI: 10.1109/lgrs.2011.2120591.
- Anderson, M.C., C. Cammalleri, C.R. Hain, J. Otkin, X. Zhan, and W. Kustas (2013). Using a Diagnostic Soil-Plant-Atmosphere Model for Monitoring Drought at Field to Continental Scales. *Procedia Environmental Sciences* 19, 47-56. DOI: 10.1016/j.proenv.2013.06.006.
- Andres, L., W.A. Salas, and D. Skole (1994). Fourier Analysis of Multi-Temporal AVHRR Data Applied to a Land Cover Classification. *International Journal of Remote Sensing* 15 (5), 1115-1121. DOI: 10.1080/01431169408954145.
- Ångström, A. (1964). The Parameters of Atmospheric Turbidity. *Tellus* 16 (1), 64-75. DOI: 10.1111/j.2153-3490.1964.tb00144.x.
- Aranuvachapun, S. (1986). Satellite Remote Sensing of Atmospheric Optical Depth Spectrum. *International Journal of Remote Sensing* 7 (4), 499-514. DOI: 10.1080/01431168608954705.
- Archibald, S., and R.J. Scholes (2007). Leaf Green-Up in a Semi-Arid African Savanna - Separating Tree and Grass Responses to Environmental Cues. *Journal of Vegetation Science* 18 (4), 583-594. DOI: 10.1111/j.1654-1103.2007.tb02572.x.
- Armston, J.D., R.J. Denham, T.J. Danaher, P.F. Scarth, and T.N. Moffiet (2009). Prediction and Validation of Foliage Projective Cover from Landsat-5 TM and Landsat-7 ETM+ Imagery. *Journal of Applied Remote Sensing* 3 (1), 033540-033540-28. DOI: 10.1117/1.3216031.
- Arroyo, J. (1990). Spatial Variation of Flowering Phenology in the Mediterranean Shrublands of Southern Spain. *Israel Journal of Botany* 39 (3), 249-262. DOI: 10.1080/0021213x.1990.10677150.
- Arroyo, M.T.K., J.J. Armesto, and C. Villagran (1981). Plant Phenological Patterns in the High Andean Cordillera of Central Chile. *Journal of Ecology* 69 (1), 205-223. DOI: 10.2307/2259826.
- Arvidson, T., J. Gasch, and S.N. Goward (2001). Landsat 7's Long-Term Acquisition Plan - An Innovative Approach to Building a Global Imagery Archive. *Remote Sensing of Environment* 78 (1-2), 13-26. DOI: 10.1016/S0034-4257(01)00263-2.
- Aschbacher, J., and M.P. Milagro-Pérez (2012). The European Earth Monitoring (GMES) Programme: Status and Perspectives. *Remote Sensing of Environment* 120, 3-8. DOI: 10.1016/j.rse.2011.08.028.
- Asner, G.P., A.R. Townsend, and B.H. Braswell (2000). Satellite Observation of El Niño Effects on Amazon Forest Phenology and Productivity. *Geophysical Research Letters* 27 (7), 981-984. DOI: 10.1029/1999gl011113.
- Asner, G.P. (2001). Cloud Cover in Landsat Observations of the Brazilian Amazon. *International Journal of Remote Sensing* 22 (18), 3855-3862. DOI: 10.1080/01431160010006926.

- Asrar, G., and R. Greenstone, eds (1995). *MTPE EOS Reference Handbook*. Greenbelt, MD, USA. NASA/Goddard Space Flight Center.
- Atkinson, P.M., C. Jeganathan, J. Dash, and C. Atzberger (2012). Inter-Comparison of Four Models for Smoothing Satellite Sensor Time-Series Data to Estimate Vegetation Phenology. *Remote Sensing of Environment* 123, 400-417. DOI: 10.1016/j.rse.2012.04.001.
- Atzberger, C., A. Klisch, M. Mattiuzzi, and F. Vuolo (2013). Phenological Metrics Derived over the European Continent from NDVI3g Data and MODIS Time Series. *Remote Sensing* 6 (1), 257-284. DOI: 10.3390/rs6010257.
- Bachoo, A., and S. Archibald (2007). Influence of Using Date-Specific Values when Extracting Phenological Metrics from 8-Day Composite NDVI Data. *MultiTemp 2007 - International Workshop on the Analysis of Multitemporal Remote Sensing Images*, Leuven, Belgium, 18-20 July 2007. DOI:10.1109/MULTITEMP.2007.4293044.
- Barbosa, P.M., D. Stroppiana, J.-M. Grégoire, and J.M. Cardoso Pereira (1999). An Assessment of Vegetation Fire in Africa (1981–1991): Burned Areas, Burned Biomass, and Atmospheric Emissions. *Global Biogeochemical Cycles* 13 (4), 933-950. DOI: 10.1029/1999gb900042.
- Barnes, W.L., T.S. Pagano, and V.V. Salomonson (1998). Prelaunch Characteristics of the Moderate Resolution Imaging Spectroradiometer (MODIS) on EOS-AM1. *IEEE Transactions on Geoscience and Remote Sensing* 36 (4), 1088-1100. DOI: 10.1109/36.700993.
- Belward, A.S., and J.O. Skøien (2015). Who Launched What, When and Why; Trends in Global Land-Cover Observation Capacity from Civilian Earth Observation Satellites. *ISPRS Journal of Photogrammetry and Remote Sensing* 103, 115-128. DOI: 10.1016/j.isprsjprs.2014.03.009.
- Bird, R.E., and C. Riordan (1986). Simple Solar Spectral Model for Direct and Diffuse Irradiance on Horizontal and Tilted Planes at the Earth's Surface for Cloudless Atmospheres. *Journal of Climate and Applied Meteorology* 25 (1), 87-97. DOI: 10.1175/1520-0450(1986)025<0087:sssmfd>2.0.co;2.
- Blanchard, L.E., and O. Weinstein (1980). Design Challenges of the Thematic Mapper. *IEEE Transactions on Geoscience and Remote Sensing* GE-18 (2), 146-160. DOI: 10.1109/tgrs.1980.350267.
- Bojinski, S., M. Verstraete, T.C. Peterson, C. Richter, A. Simmons, and M. Zemp (2014). The Concept of Essential Climate Variables in Support of Climate Research, Applications, and Policy. *Bulletin of the American Meteorological Society* 95 (9), 1431-1443. DOI: 10.1175/BAMS-D-13-00047.1.
- Bollen, A., and G. Donati (2005). Phenology of the Littoral Forest of Sainte Luce, Southeastern Madagascar. *Biotropica* 37 (1), 32-43. DOI: 10.1111/j.1744-7429.2005.04094.x.
- Bond, W.J., and J.E. Keeley (2005). Fire as a Global 'Herbivore': The Ecology and Evolution of Flammable Ecosystems. *Trends in Ecology & Evolution* 20 (7), 387-394. DOI: 10.1016/j.tree.2005.04.025.
- Boucher, D., S. Roquemore, and E. Fitzhugh (2013). Brazil's Success in Reducing Deforestation. *Tropical Conservation Science* 6 (3), 426-445.

- Brown, M.E., K.M. de Beurs, and M. Marshall (2012). Global Phenological Response to Climate Change in Crop Areas Using Satellite Remote Sensing of Vegetation, Humidity and Temperature over 26 Years. *Remote Sensing of Environment* 126, 174-183. DOI: 10.1016/j.rse.2012.08.009.
- Brunsell, N.A., and R.R. Gillies (2003). Determination of Scaling Characteristics of AVHRR Data with Wavelets: Application to SGP97. *International Journal of Remote Sensing* 24 (14), 2945-2957. DOI: 10.1080/01431160210155983.
- Bucholtz, A. (1995). Rayleigh-Scattering Calculations for the Terrestrial Atmosphere. *Applied Optics* 34 (15), 2765-2773. DOI: 10.1364/ao.34.002765.
- Butchart, S.H.M., M. Walpole, B. Collen, A. van Strien, J.P.W. Scharlemann, R.E.A. Almond, J.E.M. Baillie, B. Bomhard, C. Brown, J. Bruno, K.E. Carpenter, G.M. Carr, J. Chanson, A.M. Chenery, J. Csirke, N.C. Davidson, F. Dentener, M. Foster, A. Galli, J.N. Galloway, P. Genovesi, R.D. Gregory, M. Hockings, V. Kapos, J.-F. Lamarque, F. Leverington, J. Loh, M.A. McGeoch, L. McRae, A. Minasyan, M.H. Morcillo, T.E.E. Oldfield, D. Pauly, S. Quader, C. Revenga, J.R. Sauer, B. Skolnik, D. Spear, D. Stanwell-Smith, S.N. Stuart, A. Symes, M. Tierney, T.D. Tyrrell, J.-C. Vié, and R. Watson (2010). Global Biodiversity: Indicators of Recent Declines. *Science* 328 (5982), 1164-1168. DOI: 10.1126/science.1187512.
- Cabral, A., M.J.P. De Vasconcelos, J.M.C. Pereira, É. Bartholomé, and P. Mayaux (2003). Multi-Temporal Compositing Approaches for SPOT-4 VEGETATION. *International Journal of Remote Sensing* 24 (16), 3343-3350. DOI: 10.1080/0143116031000075936.
- Chander, G., B.L. Markham, and D.L. Helder (2009). Summary of Current Radiometric Calibration Coefficients for Landsat MSS, TM, ETM+, and EO-1 ALI Sensors. *Remote Sensing of Environment* 113 (5), 893-903. DOI: 10.1016/j.rse.2009.01.007.
- Chavez, P.S. (1988). An Improved Dark-Object Subtraction Technique for Atmospheric Scattering Correction of Multispectral Data. *Remote Sensing of Environment* 24 (3), 459-479. DOI: 10.1016/0034-4257(88)90019-3.
- Chavez, P.S. (1996). Image-Based Atmospheric Corrections - Revisited and Improved. *Photogrammetric Engineering and Remote Sensing* 62 (9), 1025-1035.
- Chuvieco, E., G. Ventura, M.P. Martín, and I. Gómez (2005). Assessment of Multitemporal Compositing Techniques of MODIS and AVHRR Images for Burned Land Mapping. *Remote Sensing of Environment* 94 (4), 450-462. DOI: 10.1016/j.rse.2004.11.006.
- Clinton, N., and P. Gong (2013). MODIS Detected Surface Urban Heat Islands and Sinks: Global Locations and Controls. *Remote Sensing of Environment* 134, 294-304. DOI: 10.1016/j.rse.2013.03.008.
- Cohen, W.B., and S.N. Goward (2004). Landsat's Role in Ecological Applications of Remote Sensing. *BioScience* 54 (6), 535-545. DOI: 10.1641/0006-3568(2004)054[0535:lrieao]2.0.co;2.
- Cowie, B.A., C.M. Thornton, and B.J. Radford (2007). The Brigalow Catchment Study: I\*. Overview of a 40-Year Study of the Effects of Land Clearing in the Brigalow Bioregion of Australia. *Soil Research* 45 (7), 479-495. DOI: 10.1071/SR07063.

- Danaher, T., P. Scarth, J. Armston, L. Collett, J. Kitchen, and S. Gillingham (2010). Remote Sensing of Tree-Grass Systems: The Eastern Australian Woodlands. In *Ecosystem Function in Savannas: Measurement and Modeling at Landscape to Global Scales*, edited by M.J. Hill and N.P. Hanan, 175-194. Boca Raton, USA. CRC Press.
- Davis, G. (2007). History of the NOAA Satellite Program. *Journal of Applied Remote Sensing* 1 (1), 012504-012504-18. DOI: 10.1117/1.2642347.
- De Sy, V., M. Herold, F. Achard, G.P. Asner, A. Held, J. Kelldorfer, and J. Verbesselt (2012). Synergies of Multiple Remote Sensing Data Sources for REDD+ Monitoring. *Current Opinion in Environmental Sustainability* 4 (6), 696-706. DOI: 10.1016/j.cosust.2012.09.013.
- DeFries, R., F. Achard, S. Brown, M. Herold, D. Murdiyarso, B. Schlamadinger, and C. de Souza Jr (2007). Earth Observations for Estimating Greenhouse Gas Emissions from Deforestation in Developing Countries. *Environmental Science & Policy* 10 (4), 385-394. DOI: 10.1016/j.envsci.2007.01.010.
- Dennison, P.E., D.A. Roberts, S.H. Peterson, and J. Rechel (2005). Use of Normalized Difference Water Index for Monitoring Live Fuel Moisture. *International Journal of Remote Sensing* 26 (5), 1035-1042. DOI: 10.1080/0143116042000273998.
- Dennison, P.E., D.A. Roberts, and S.H. Peterson (2007). Spectral Shape-Based Temporal Compositing Algorithms for MODIS Surface Reflectance Data. *Remote Sensing of Environment* 109 (4), 510-522. DOI: 10.1016/j.rse.2007.02.009.
- DOI (1966). Earth's Resources to be Studied from Space. U.S. Department of the Interior Press Release.
- Donlon, C., B. Berruti, A. Buongiorno, M.H. Ferreira, P. Féménias, J. Frerick, P. Goryl, U. Klein, H. Laur, C. Mavrocordatos, J. Nieke, H. Rebhan, B. Seitz, J. Stroede, and R. Sciarra (2012). The Global Monitoring for Environment and Security (GMES) Sentinel-3 Mission. *Remote Sensing of Environment* 120 (0), 37-57. DOI: 10.1016/j.rse.2011.07.024.
- Dozier, J. (1989). Spectral Signature of Alpine Snow Cover from the Landsat Thematic Mapper. *Remote Sensing of Environment* 28, 9-22. DOI: 10.1016/0034-4257(89)90101-6.
- Drusch, M., U. Del Bello, S. Carlier, O. Colin, V. Fernandez, F. Gascon, B. Hoersch, C. Isola, P. Laberinti, P. Martimort, A. Meygret, F. Spoto, O. Sy, F. Marchese, and P. Bargellini (2012). Sentinel-2: ESA's Optical High-Resolution Mission for GMES Operational Services. *Remote Sensing of Environment* 120, 25-36. DOI: 10.1016/j.rse.2011.11.026.
- Eck, T.F., B.N. Holben, J.S. Reid, O. Dubovik, A. Smirnov, N.T. O'Neill, I. Slutsker, and S. Kinne (1999). Wavelength Dependence of the Optical Depth of Biomass Burning, Urban, and Desert Dust Aerosols. *Journal of Geophysical Research: Atmospheres* 104 (D24), 31333-31349. DOI: 10.1029/1999jd900923.
- Eck, T.F., B.N. Holben, D. Ward, O. Dubovik, J. Reid, A. Smirnov, M. Mukelabai, N. Hsu, N. O'Neill, and I. Slutsker (2001). Characterization of the Optical Properties of Biomass Burning Aerosols in Zambia during the 1997 ZIBBEE Field Campaign. *Journal of Geophysical Research: Atmospheres* 106 (D4), 3425-3448. DOI: 10.1029/2000JD900555.

- Ellis, E.C., and N. Ramankutty (2008). Putting People in the Map: Anthropogenic Biomes of the World. *Frontiers in Ecology and the Environment* 6 (8), 439-447. DOI: 10.1890/070062.
- Emelyanova, I.V., T.R. McVicar, T.G. Van Niel, L.T. Li, and A.I.J.M. van Dijk (2013). Assessing the Accuracy of Blending Landsat–MODIS Surface Reflectances in Two Landscapes with Contrasting Spatial and Temporal Dynamics: A framework for Algorithm Selection. *Remote Sensing of Environment* 133, 193-209. DOI: 10.1016/j.rse.2013.02.007.
- ESA (2016). ACIX: CEOS-WGCV Atmospheric Correction Inter-Comparison Exercise. *Web Page Accessed* 16.09.2016. <https://earth.esa.int/web/sppa/meetings-workshops/acix>.
- Fisher, J.I., J.F. Mustard, and M.A. Vadeboncoeur (2006). Green Leaf Phenology at Landsat Resolution: Scaling from the Field to the Satellite. *Remote Sensing of Environment* 100 (2), 265-279. DOI: 10.1016/j.rse.2005.10.022.
- Fisher, J.I., and J.F. Mustard (2007). Cross-Scalar Satellite Phenology from Ground, Landsat, and MODIS Data. *Remote Sensing of Environment* 109 (3), 261-273. DOI: 10.1016/j.rse.2007.01.004.
- Flood, N. (2013). Seasonal Composite Landsat TM/ETM+ Images Using the Medoid (a Multi-Dimensional Median). *Remote Sensing* 5 (12), 6481-6500. DOI: 10.3390/rs5126481.
- Flood, N., T. Danaher, T.K. Gill, and S.S. Gillingham (2013). An Operational Scheme for Deriving Standardised Surface Reflectance from Landsat TM/ETM+ and SPOT HRG Imagery for Eastern Australia. *Remote Sensing* 5 (1), 83-109. DOI: 10.3390/rs5010083.
- Flood, N. (2014). Continuity of Reflectance Data between Landsat-7 ETM+ and Landsat-8 OLI, for Both Top-of-Atmosphere and Surface Reflectance: A Study in the Australian Landscape. *Remote Sensing* 6 (9), 7952-7970. DOI: 10.3390/rs6097952.
- Förster, M., T. Schmidt, P. Gartner, B. Kleinschmit, G. Feng, and M. Moller (2015). Evaluating the Temporal Stability of Synthetically Generated Time-Series for Crop Types in Central Germany. *MultiTemp 2015 - International Workshop on the Analysis of Multitemporal Remote Sensing Images*, Annecy, France, 22-24 July 2015. DOI:10.1109/Multi-Temp.2015.7245811.
- Foust, J. (2015). White House Proposes \$18.5 Billion Budget for NASA. *Space News*, 02.09.2015. <http://spacenews.com/white-house-proposes-18-5-billion-budget-for-nasa/>.
- Frantz, D., A. Röder, M. Stellmes, and J. Hill (2015a). On the Derivation of a Spatially Distributed Aerosol Climatology for its Incorporation in a Radiometric Landsat Preprocessing Framework. *Remote Sensing Letters* 6 (8), 647-656. DOI: 10.1080/2150704x.2015.1070314.
- Frantz, D., A. Röder, T. Udelhoven, and M. Schmidt (2015b). Enhancing the Detectability of Clouds and Their Shadows in Multitemporal Dryland Landsat Imagery: Extending Fmask. *IEEE Geoscience and Remote Sensing Letters* 12 (6), 1242-1246. DOI: 10.1109/lgrs.2015.2390673.
- Frantz, D., A. Röder, M. Stellmes, and J. Hill (2016a). An Operational Radiometric Landsat Preprocessing Framework for Large-Area Time Series Applications. *IEEE Transactions on Geoscience and Remote Sensing* 54 (7), 3928-3943. DOI: 10.1109/TGRS.2016.2530856.

- Frantz, D., M. Stellmes, A. Röder, T. Udelhoven, S. Mader, and J. Hill (2016b). Improving the Spatial Resolution of Land Surface Phenology by Fusing Medium- and Coarse-Resolution Inputs. *IEEE Transactions on Geoscience and Remote Sensing* 54 (7), 4153-4164. DOI: 10.1109/TGRS.2016.2537929.
- Friedl, M.A., D.K. McIver, J.C.F. Hodges, X.Y. Zhang, D. Muchoney, A.H. Strahler, C.E. Woodcock, S. Gopal, A. Schneider, A. Cooper, A. Baccini, F. Gao, and C. Schaaf (2002). Global Land Cover Mapping from MODIS: Algorithms and Early Results. *Remote Sensing of Environment* 83 (1–2), 287-302. DOI: 10.1016/S0034-4257(02)00078-0.
- Frost, P., and R. Scholes (2007). Advanced Fire Information System. In *The Full Picture*, edited by G. Secretariat. Geneva. Group on Earth Observations.
- Fu, D., B. Chen, J. Wang, X. Zhu, and T. Hilker (2013). An Improved Image Fusion Approach Based on Enhanced Spatial and Temporal the Adaptive Reflectance Fusion Model. *Remote Sensing* 5 (12), 6346-6360. DOI: 10.3390/rs5126346.
- Fynn, R.W.S., M. Chase, and A. Röder (2014). Functional Habitat Heterogeneity and Large Herbivore Seasonal Habitat Selection in Northern Botswana. *South African Journal of Wildlife Research* 44 (1), 1-15. DOI: 10.3957/056.044.0103.
- Gao, B.-C., and Y.J. Kaufman (2003). Water Vapor Retrievals using Moderate Resolution Imaging Spectroradiometer (MODIS) Near-Infrared Channels. *Journal of Geophysical Research: Atmospheres* 108 (D13). DOI: 10.1029/2002jd003023.
- Gao, F., J. Masek, M. Schwaller, and F. Hall (2006). On the Blending of the Landsat and MODIS Surface Reflectance: Predicting Daily Landsat Surface Reflectance. *IEEE Transactions on Geoscience and Remote Sensing* 44 (8), 2207-2218. DOI: 10.1109/tgrs.2006.872081.
- Gardner, R., and D. Urban (2007). Neutral Models for Testing Landscape Hypotheses. *Landscape Ecology* 22 (1), 15-29. DOI: 10.1007/s10980-006-9011-4.
- GCOS (2003). *The Second Report on the Adequacy of the Global Observing Systems for Climate in Support of the UNFCCC*. Geneva, Switzerland. S.o.t.W.M. Organization.
- GDAL - Geospatial Data Abstraction Library 1.10.0. Open Source Geospatial Foundation. <http://www.gdal.org>.
- Gege, P. (2004). The Water Color Simulator WASI: An Integrating Software Tool for Analysis and Simulation of Optical In Situ Spectra. *Computers & Geosciences* 30 (5), 523-532. DOI: 10.1016/j.cageo.2004.03.005.
- GEO-BON (2016). Essential Biodiversity Variables. *Web Page Accessed 13.09.2016*. <http://geobon.org/essential-biodiversity-variables/ebv-classes-2>.
- Gibbs, H., K., S. Brown, J. Niles, O. , and J. Foley, A. (2007). Monitoring and Estimating Tropical Forest Carbon Stocks: Making REDD a Reality. *Environmental Research Letters* 2 (4). DOI: 10.1088/1748-9326/2/4/045023.

- Gillingham, S.S., N. Flood, T.K. Gill, and R.M. Mitchell (2011). Limitations of the Dense Dark Vegetation Method for Aerosol Retrieval under Australian Conditions. *Remote Sensing Letters* 3 (1), 67-76. DOI: 10.1080/01431161.2010.533298.
- Gillingham, S.S., N. Flood, and T.K. Gill (2012). On Determining Appropriate Aerosol Optical Depth Values for Atmospheric Correction of Satellite Imagery for Biophysical Parameter Retrieval: Requirements and Limitations under Australian Conditions. *International Journal of Remote Sensing* 34 (6), 2089-2100. DOI: 10.1080/01431161.2012.738945.
- Godfray, H.C.J., J.R. Beddington, I.R. Crute, L. Haddad, D. Lawrence, J.F. Muir, J. Pretty, S. Robinson, S.M. Thomas, and C. Toulmin (2010). Food Security: The Challenge of Feeding 9 Billion People. *Science* 327 (5967), 812-818. DOI: 10.1126/science.1185383.
- Gomez-Chova, L., G. Camps-Valls, J. Calpe-Maravilla, L. Guanter, and J. Moreno (2007). Cloud-Screening Algorithm for ENVISAT/MERIS Multispectral Images. *IEEE Transactions on Geoscience and Remote Sensing* 45 (12), 4105-4118. DOI: 10.1109/tgrs.2007.905312.
- Gordon, H. (1981). A Preliminary Assessment of the Nimbus-7 CZCS Atmospheric Correction Algorithm in a Horizontally Inhomogeneous Atmosphere. In *Oceanography from Space*, edited by J.F.R. Gower, 257-265. Boston, MA. Springer US.
- Goward, S., T. Arvidson, D. Williams, J. Faundeen, J. Irons, and S. Franks (2006). Historical Record of Landsat Global Coverage. *Photogrammetric Engineering & Remote Sensing* 72 (10), 1155-1169. DOI: 10.14358/pers.72.10.1155.
- Griffiths, P., D. Müller, T. Kuemmerle, and P. Hostert (2013a). Agricultural Land Change in the Carpathian Ecoregion after the Breakdown of Socialism and Expansion of the European Union. *Environmental Research Letters* 8 (4). DOI: 10.1088/1748-9326/8/4/045024.
- Griffiths, P., S. van der Linden, T. Kuemmerle, and P. Hostert (2013b). A Pixel-Based Landsat Compositing Algorithm for Large Area Land Cover Mapping. *IEEE Journal of Selected Topics in Applied Earth Observations and Remote Sensing* 6 (5), 2088-2101. DOI: 10.1109/jstars.2012.2228167.
- Guzzi, R., R. Rizzi, and G. Zibordi (1987). Atmospheric Correction of Data Measured by a Flying Platform over the Sea: Elements of a Model and its Experimental Validation. *Applied Optics* 26 (15), 3043-3051. DOI: 10.1364/ao.26.003043.
- Hagolle, O., M. Huc, D.V. Pascual, and G. Dedieu (2010). A Multi-Temporal Method for Cloud Detection, Applied to FORMOSAT-2, VEN $\mu$ S, LANDSAT and SENTINEL-2 Images. *Remote Sensing of Environment* 114 (8), 1747-1755. DOI: 10.1016/j.rse.2010.03.002.
- Hall, D.K., G.A. Riggs, and V.V. Salomonson (1995). Development of Methods for Mapping Global Snow Cover using Moderate Resolution Imaging Spectroradiometer Data. *Remote Sensing of Environment* 54 (2), 127-140. DOI: 10.1016/0034-4257(95)00137-P.
- Hansen, M.C., and T.R. Loveland (2012). A Review of Large Area Monitoring of Land Cover Change using Landsat Data. *Remote Sensing of Environment* 122, 66-74. DOI: 10.1016/j.rse.2011.08.024.
- Hansen, M.C., P.V. Potapov, R. Moore, M. Hancher, S.A. Turubanova, A. Tyukavina, D. Thau, S.V. Stehman, S.J. Goetz, T.R. Loveland, A. Kommareddy, A. Egorov, L. Chini, C.O. Justice, and J.R.G.



- Townshend (2013). High-Resolution Global Maps of 21st-Century Forest Cover Change. *Science* 342 (6160), 850-853. DOI: 10.1126/science.1244693.
- Hansen, M.C., A. Krylov, A. Tyukavina, P.V. Potapov, S. Turubanova, B. Zutta, S. Ifo, B. Margono, F. Stolle, and R. Moore (2016). Humid Tropical Forest Disturbance Alerts using Landsat Data. *Environmental Research Letters* 11 (3). DOI: 10.1088/1748-9326/11/3/034008.
- Hantson, S., and E. Chuvieco (2011). Evaluation of Different Topographic Correction Methods for Landsat Imagery. *International Journal of Applied Earth Observation and Geoinformation* 13 (5), 691-700. DOI: 10.1016/j.jag.2011.05.001.
- Hassan, M.H.A. (2008). Global Science Gaps Need Global Action. *Issues in Science and Technology* 24 (2), 57-64.
- Herold, M., R.M. Román-Cuesta, D. Mollicone, Y. Hirata, P. Van Laake, G.P. Asner, C. Souza, M. Skutsch, V. Avitabile, and K. MacDicken (2011). Options for Monitoring and Estimating Historical Carbon Emissions from Forest Degradation in the Context of REDD+. *Carbon Balance and Management* 6 (1), 1-7. DOI: 10.1186/1750-0680-6-13.
- Herold, M., and M. Skutsch (2011). Monitoring, Reporting and Verification for National REDD + Programmes: Two Proposals. *Environmental Research Letters* 6 (1). DOI: 10.1088/1748-9326/6/1/014002.
- Hijmans, R.J., S.E. Cameron, J.L. Parra, P.G. Jones, and A. Jarvis (2005). Very High Resolution Interpolated Climate Surfaces for Global Land Areas. *International Journal of Climatology* 25 (15), 1965-1978. DOI: 10.1002/joc.1276.
- Hill, J., and B. Sturm (1991). Radiometric Correction of Multitemporal Thematic Mapper Data for Use in Agricultural Land-Cover Classification and Vegetation Monitoring. *International Journal of Remote Sensing* 12 (7), 1471-1491. DOI: 10.1080/01431169108955184.
- Hill, J. (1993). High Precision Land Cover Mapping and Inventory with Multi-Temporal Earth Observation Satellite Data: the Ardèche Experiment. *Ph.D. dissertation*, Faculty of Geography/Geosciences, Trier University, Trier, Germany.
- Hill, J., W. Mehl, and V. Radeloff (1995). Improved Forest Mapping by Combining Corrections of Atmospheric and Topographic Effects in Landsat TM Imagery. In *Sensors and environmental applications of remote sensing*, edited by J. Askne, 143-151. Rotterdam, Netherlands. Balkema.
- Hird, J.N., G. Castilla, G.J. McDermid, and I.T. Bueno (2016). A Simple Transformation for Visualizing Non-seasonal Landscape Change From Dense Time Series of Satellite Data. *IEEE Journal of Selected Topics in Applied Earth Observations and Remote Sensing* 9 (8), 3372-3383. DOI: 10.1109/jstars.2015.2419594.
- Holben, B.N. (1986). Characteristics of Maximum-Value Composite Images from Temporal AVHRR Data. *International Journal of Remote Sensing* 7 (11), 1417-1434. DOI: 10.1080/01431168608948945.
- Holben, B.N., T.F. Eck, I. Slutsker, D. Tanré, J.P. Buis, A. Setzer, E. Vermote, J.A. Reagan, Y.J. Kaufman, T. Nakajima, F. Lavenu, I. Jankowiak, and A. Smirnov (1998). AERONET—A Federated Instrument

- Network and Data Archive for Aerosol Characterization. *Remote Sensing of Environment* 66 (1), 1-16. DOI: 10.1016/S0034-4257(98)00031-5.
- Homer, C.G., J.A. Dewitz, L. Yang, S. Jin, P. Danielson, G. Xian, J. Coulston, N.D. Herold, J. Wickham, and K. Megown (2015). Completion of the 2011 National Land Cover Database for the Conterminous United States-Representing a Decade of Land Cover Change Information. *Photogrammetric Engineering and Remote Sensing* 81 (5), 345-354.
- Horn, B.K.P. (1981). Hill Shading and the Reflectance Map. *Proceedings of the IEEE* 69 (1), 14-47. DOI: 10.1109/proc.1981.11918.
- Hostert, P., A. Röder, and J. Hill (2003). Coupling Spectral Unmixing and Trend Analysis for Monitoring of Long-Term Vegetation Dynamics in Mediterranean Rangelands. *Remote Sensing of Environment* 87 (2-3), 183-197. DOI: 10.1016/S0034-4257(03)00145-7.
- Houghton, J., J. Townshend, K. Dawson, P. Mason, J. Zillman, and A. Simmons (2012). The GCOS at 20 Years: The Origin, Achievement and Future Development of the Global Climate Observing System. *Weather* 67 (9), 227-235. DOI: 10.1002/wea.1964.
- Huete, A., C. Justice, and W. Van Leeuwen (1999). *MODIS Vegetation Index (MOD13) - Algorithm Theoretical Basis Document*. [https://modis.gsfc.nasa.gov/data/atbd/atbd\\_mod13.pdf](https://modis.gsfc.nasa.gov/data/atbd/atbd_mod13.pdf).
- Huete, A., K. Didan, T. Miura, E.P. Rodriguez, X. Gao, and L.G. Ferreira (2002). Overview of the Radiometric and Biophysical Performance of the MODIS Vegetation Indices. *Remote Sensing of Environment* 83 (1/2), 195-213. DOI: 10.1016/S0034-4257(02)00096-2.
- IPCC (2012). *Managing the Risks of Extreme Events and Disasters to Advance Climate Change Adaptation - Special Report of the Intergovernmental Panel on Climate Change*. Edited by B. Field, V. Barros, T.F. Stocker, Q. Dahe, D.J. Dokken, K.L. Ebi, M.D. Mastrandrea, K.J. Mach, G.K. Plattner, S.K. Allen, M. Tignor and P.M. Midgley. Cambridge, UK and New York, USA. Cambridge University Press.
- IPCC (2013). *Climate Change 2013: The Physical Science Basis. Contribution of Working Group I to the Fifth Assessment Report of the Intergovernmental Panel on Climate Change*. Edited by T.F. Stocker, D. Qin, G.-K. Plattner, M. Tignor, S.K. Allen, J. Boschung, A. Nauels, Y. Xia, V. Bex and P.M. Midgley. Cambridge, UK and New York, USA. Cambridge University Press. DOI: 10.1017/CBO9781107415324.
- Irish, R.R. (2000). Landsat 7 Automatic Cloud Cover Assessment. *SPIE Proceedings 4049 - Algorithms for Multispectral, Hyperspectral, and Ultraspectral Imagery VI*, Orlando, FL, USA, 24 April 2000. DOI:10.1117/12.410358.
- Irish, R.R., J.L. Barker, S.N. Goward, and T. Arvidson (2006). Characterization of the Landsat-7 ETM+ Automated Cloud-Cover Assessment (ACCA) Algorithm. *Photogrammetric Engineering & Remote Sensing* 72 (10), 1179-1188. DOI: 10.14358/pers.72.10.1179.
- Irvine, W.M. (1975). Multiple Scattering in Planetary Atmospheres. *Icarus* 25 (2), 175-204. DOI: 10.1016/0019-1035(75)90019-6.

- Jacquemoud, S., W. Verhoef, F. Baret, C. Bacour, P.J. Zarco-Tejada, G.P. Asner, C. François, and S.L. Ustin (2009). PROSPECT + SAIL Models: A Review of Use for Vegetation Characterization. *Remote Sensing of Environment* 113, Supplement 1, S56-S66. DOI: 10.1016/j.rse.2008.01.026.
- Jochner, S., T. Sparks, N. Estrella, and A. Menzel (2012). The Influence of Altitude and Urbanisation on Trends and Mean Dates in Phenology (1980–2009). *International Journal of Biometeorology* 56 (2), 387-394. DOI: 10.1007/s00484-011-0444-3.
- Jonsson, P., and L. Eklundh (2002). Seasonality Extraction by Function Fitting to Time-Series of Satellite Sensor Data. *IEEE Transactions on Geoscience and Remote Sensing* 40 (8), 1824-1832. DOI: 10.1109/tgrs.2002.802519.
- Jönsson, P., and L. Eklundh (2004). TIMESAT - A Program for Analyzing Time-Series of Satellite Sensor Data. *Computers & Geosciences* 30 (8), 833-845. DOI: 10.1016/j.cageo.2004.05.006.
- Ju, J., D.P. Roy, E. Vermote, J. Masek, and V. Kovalskyy (2012). Continental-Scale Validation of MODIS-Based and LEDAPS Landsat ETM+ Atmospheric Correction Methods. *Remote Sensing of Environment* 122, 175-184. DOI: 10.1016/j.rse.2011.12.025.
- Justice, C.O., E. Vermote, J.R.G. Townshend, R. DeFries, D.P. Roy, D.K. Hall, V.V. Salomonson, J.L. Privette, G. Riggs, A. Strahler, W. Lucht, R.B. Myneni, Y. Knyazikhin, S.W. Running, R.R. Nemani, W. Zhengming, A.R. Huete, W. Van Leeuwen, R.E. Wolfe, L. Giglio, J.P. Muller, P. Lewis, and M.J. Barnsley (1998). The Moderate Resolution Imaging Spectroradiometer (MODIS): Land Remote Sensing for Global Change Research. *IEEE Transactions on Geoscience and Remote Sensing* 36 (4), 1228-1249. DOI: 10.1109/36.701075.
- Justice, C.O., J.R.G. Townshend, E.F. Vermote, E. Masuoka, R.E. Wolfe, N. Saleous, D.P. Roy, and J.T. Morisette (2002). An Overview of MODIS Land Data Processing and Product Status. *Remote Sensing of Environment* 83 (1–2), 3-15. DOI: 10.1016/S0034-4257(02)00084-6.
- Kasischke, E.S., J.M. Melack, and M. Craig Dobson (1997). The Use of Imaging Radars for Ecological Applications — A Review. *Remote Sensing of Environment* 59 (2), 141-156. DOI: 10.1016/S0034-4257(96)00148-4.
- Kaufman, Y.J., and C. Sendra (1988). Algorithm for Automatic Atmospheric Corrections to Visible and Near-IR Satellite Imagery. *International Journal of Remote Sensing* 9 (8), 1357-1381. DOI: 10.1080/01431168808954942.
- Kaufmann, H., K. Segl, S. Chabrillat, S. Hofer, T. Stuffer, A. Mueller, R. Richter, G. Schreier, R. Haydn, and H. Bach (2006). EnMAP: A Hyperspectral Sensor for Environmental Mapping and Analysis. *IGARSS 2006 - IEEE International Conference on Geoscience and Remote Sensing Symposium*, 31-4 July/August 2006. DOI:10.1109/igarss.2006.417.
- Kay, S., J. Hedley, and S. Lavender (2009). Sun Glint Correction of High and Low Spatial Resolution Images of Aquatic Scenes: a Review of Methods for Visible and Near-Infrared Wavelengths. *Remote Sensing* 1 (4), 697-730. DOI: 10.3390/rs1040697.
- Kennedy, R.E., Z. Yang, and W.B. Cohen (2010). Detecting Trends in Forest Disturbance and Recovery using Yearly Landsat Time Series: 1. LandTrendr — Temporal Segmentation Algorithms. *Remote Sensing of Environment* 114 (12), 2897-2910. DOI: 10.1016/j.rse.2010.07.008.

- Kobayashi, S., and K. Sanga-Ngoie (2008). The Integrated Radiometric Correction of Optical Remote Sensing Imageries. *International Journal of Remote Sensing* 29 (20), 5957-5985. DOI: 10.1080/01431160701881889.
- Kovalskyy, V., D.P. Roy, X.Y. Zhang, and J. Ju (2012). The Suitability of Multi-Temporal Web-Enabled Landsat Data NDVI for Phenological Monitoring – A Comparison with Flux Tower and MODIS NDVI. *Remote Sensing Letters* 3 (4), 325-334. DOI: 10.1080/01431161.2011.593581.
- Kovalskyy, V., and D.P. Roy (2013). The Global Availability of Landsat 5 TM and Landsat 7 ETM+ Land Surface Observations and Implications for Global 30m Landsat Data Product Generation. *Remote Sensing of Environment* 130, 280-293. DOI: 10.1016/j.rse.2012.12.003.
- Lambin, E.F. (1996). Change Detection at Multiple Temporal Scales: Seasonal and Annual Variations in Landscape Variables. *Photogrammetric Engineering and Remote Sensing* 62 (8), 931-938.
- Leadley, P., H.M. Pereira, R. Alkemade, J.F. Fernandez-Manjarrés, V. Proença, J.P.W. Scharlemann, and M.J. Walpole (2010). *Biodiversity Scenarios: Projections of 21st Century Change in Biodiversity and Associated Ecosystem Services - A Technical Report for the Global Biodiversity Outlook 3*. Montreal, Canada. S.o.t.C.o.B. Diversity.
- Leimgruber, P., C. Christen, and A. Laborderie (2005). The Impact of Landsat Satellite Monitoring on Conservation Biology. *Environmental Monitoring and Assessment* 106 (1-3), 81-101. DOI: 10.1007/s10661-005-0763-0.
- Lenton, T., H. Held, E. Kriegler, J. Hall, W. Lucht, S. Rahmstorf, and H. Schellnhuber (2008). Tipping Elements in the Earth's Climate System. *Proceedings of the National Academy of Sciences of the United States of America* 105 (6), 1786-1793. DOI: 10.1073/pnas.0705414105.
- Loveland, T.R., and J.L. Dwyer (2012). Landsat: Building a Strong Future. *Remote Sensing of Environment* 122, 22-29. DOI: 10.1016/j.rse.2011.09.022.
- Lucas, R.M., N. Cronin, A. Lee, M. Moghaddam, C. Witte, and P. Tickle (2006). Empirical Relationships between AIRSAR Backscatter and LiDAR-Derived Forest Biomass, Queensland, Australia. *Remote Sensing of Environment* 100 (3), 407-425. DOI: 10.1016/j.rse.2005.10.019.
- Lück, W., and A. van Niekerk (2016). Evaluation of a Rule-Based Compositing Technique for Landsat-5 TM and Landsat-7 ETM+ Images. *International Journal of Applied Earth Observation and Geoinformation* 47, 1-14. DOI: 10.1016/j.jag.2015.11.019.
- Luo, Y., A.P. Trishchenko, and K.V. Khlopenkov (2008). Developing Clear-Sky, Cloud and Cloud Shadow Mask for Producing Clear-Sky Composites at 250-Meter Spatial Resolution for the Seven MODIS Land Bands over Canada and North America. *Remote Sensing of Environment* 112 (12), 4167-4185. DOI: 10.1016/j.rse.2008.06.010.
- Mader, S. (2012). A Framework for the Phenological Analysis of Hypertemporal Remote Sensing Data Based on Polynomial Spline Models. *Ph.D. dissertation*, Faculty of Geography/Geosciences, Trier University, Trier, Germany.

- Marceau, D.J., D.J. Gratton, R.A. Fournier, and J.-P. Fortin (1994). Remote Sensing and the Measurement of Geographical Entities in a Forested Environment. 2. The Optimal Spatial Resolution. *Remote Sensing of Environment* 49 (2), 105-117. DOI: 10.1016/0034-4257(94)90047-7.
- Markham, B.L., J.C. Storey, D.L. Williams, and J.R. Irons (2004). Landsat Sensor Performance: History and Current Status. *IEEE Transactions on Geoscience and Remote Sensing* 42 (12), 2691-2694. DOI: 10.1109/tgrs.2004.840720.
- Markham, B.L., and D.L. Helder (2012). Forty-Year Calibrated Record of Earth-Reflected Radiance from Landsat: A Review. *Remote Sensing of Environment* 122, 30-40. DOI: 10.1016/j.rse.2011.06.026.
- Masek, J.G., E.F. Vermote, N.E. Saleous, R. Wolfe, F.G. Hall, K.F. Huemmrich, G. Feng, J. Kutler, and L. Teng-Kui (2006). A Landsat Surface Reflectance Dataset for North America, 1990-2000. *IEEE Geoscience and Remote Sensing Letters* 3 (1), 68-72. DOI: 10.1109/lgrs.2005.857030.
- Masek, J.G., C. Huang, R. Wolfe, W. Cohen, F. Hall, J. Kutler, and P. Nelson (2008). North American Forest Disturbance Mapped from a Decadal Landsat Record. *Remote Sensing of Environment* 112 (6), 2914-2926. DOI: 10.1016/j.rse.2008.02.010.
- McMichael, A.J., R.E. Woodruff, and S. Hales (2006). Climate change and Human Health: Present and Future Risks. *The Lancet* 367 (9513), 859-869. DOI: 10.1016/S0140-6736(06)68079-3.
- MEA (2005). *Ecosystems and Human Well-Being: A Framework for Assessment - A Report of the Conceptual Framework Working Group of the Millennium Ecosystem Assessment*. Washington D.C., USA. I. Press.
- Meijster, A., J.B.T.M. Roerdink, and W.H. Hesselink (2000). A General Algorithm for Computing Distance Transforms in Linear Time. In *Mathematical Morphology and its Applications to Image and Signal Processing*, edited by J. Goutsias, L. Vincent and D.S. Bloomberg, 331-340. Springer US.
- Melaas, E.K., M.A. Friedl, and Z. Zhu (2013). Detecting Interannual Variation in Deciduous Broadleaf Forest Phenology using Landsat TM/ETM+ Data. *Remote Sensing of Environment* 132 (0), 176-185. DOI: 10.1016/j.rse.2013.01.011.
- Menges, C.H., G.J.E. Hill, and W. Ahmad (2001). Use of Airborne Video Data for the Characterization of Tropical Savannas in Northern Australia: The Optimal Spatial Resolution for Remote Sensing Applications. *International Journal of Remote Sensing* 22 (5), 727-740. DOI: 10.1080/01431160051060129.
- Menzel, A., N. Estrella, and P. Fabian (2001). Spatial and Temporal Variability of the Phenological Seasons in Germany from 1951 to 1996. *Global Change Biology* 7 (6), 657-666. DOI: 10.1111/j.1365-2486.2001.00430.x.
- Mertz, O., D. Müller, T. Sikor, C. Hett, A. Heinemann, J.-C. Castella, G. Lestrelin, C.M. Ryan, D.S. Reay, D. Schmidt-Vogt, F. Danielsen, I. Theilade, M.v. Noordwijk, L.V. Verchot, N.D. Burgess, N.J. Berry, T.T. Pham, P. Messerli, J. Xu, R. Fensholt, P. Hostert, D. Pflugmacher, T.B. Bruun, A.d. Neergaard, K. Dons, S. Dewi, E. Rutishauser, and Z. Sun (2012). The Forgotten D: Challenges of Addressing Forest Degradation in Complex Mosaic Landscapes under REDD+. *Geografisk Tidsskrift - Danish Journal of Geography* 112 (1), 63-76. DOI: 10.1080/00167223.2012.709678.

- Meyer, P., K.I. Itten, T. Kellenberger, S. Sandmeier, and R. Sandmeier (1993). Radiometric Corrections of Topographically Induced Effects on Landsat TM Data in an Alpine Environment. *ISPRS Journal of Photogrammetry and Remote Sensing* 48 (4), 17-28. DOI: 10.1016/0924-2716(93)90028-L.
- Moran, M.S., R.D. Jackson, P.N. Slater, and P.M. Teillet (1992). Evaluation of Simplified Procedures for Retrieval of Land Surface Reflectance Factors from Satellite Sensor Output. *Remote Sensing of Environment* 41 (2-3), 169-184. DOI: 10.1016/0034-4257(92)90076-V.
- Myers, N. (1993). Tropical Forests: The Main Deforestation Fronts. *Environmental Conservation* 20 (1), 9-16. DOI: 10.1017/s0376892900037176.
- Myers, N., R.A. Mittermeier, C.G. Mittermeier, G.A.B. da Fonseca, and J. Kent (2000). Biodiversity Hotspots for Conservation Priorities. *Nature* 403 (6772), 853-858. DOI: 10.1038/35002501.
- Nagol, J.R., J.O. Sexton, D.-H. Kim, A. Anand, D. Morton, E. Vermote, and J.R. Townshend (2015). Bidirectional Effects in Landsat Reflectance Estimates: Is There a Problem to Solve? *ISPRS Journal of Photogrammetry and Remote Sensing* 103, 129-135. DOI: 10.1016/j.isprsjprs.2014.09.006.
- Nelder, J.A., and R. Mead (1965). A Simplex Method for Function Minimization. *The Computer Journal* 7 (4), 308-313. DOI: 10.1093/comjnl/7.4.308.
- Neldner, V.J., B.A. Wilson, E.J. Thompson, and H.A. Dilleward (2012). *Methodology for Survey and Mapping of Regional Ecosystems and Vegetation Communities in Queensland. Version 3.2*. Brisbane, Australia. Q. Herbarium.
- Nepstad, D., D. McGrath, C. Stickler, A. Alencar, A. Azevedo, B. Swette, T. Bezerra, M. DiGiano, J. Shimada, R. Seroa da Motta, E. Armijo, L. Castello, P. Brando, M.C. Hansen, M. McGrath-Horn, O. Carvalho, and L. Hess (2014). Slowing Amazon Deforestation Through Public Policy and Interventions in Beef and Soy Supply Chains. *Science* 344 (6188), 1118-1123. DOI: 10.1126/science.1248525.
- Nicholson, S.E. (1981). Rainfall and Atmospheric Circulation during Drought Periods and Wetter Years in West Africa. *Monthly Weather Review* 109 (10), 2191-2208. DOI: 10.1175/1520-0493(1981)109<2191:raacdd>2.0.co;2.
- Norris, P. (2001). *Digital Divide: Civic Engagement, Information Poverty, and the Internet Worldwide*. Cambridge, UK. Cambridge University Press.
- Novella, N.S., and W.M. Thiaw (2013). African Rainfall Climatology Version 2 for Famine Early Warning Systems. *Journal of Applied Meteorology and Climatology* 52 (3), 588-606. DOI: 10.1175/jamc-d-11-0238.1.
- Olofsson, P., G.M. Foody, M. Herold, S.V. Stehman, C.E. Woodcock, and M.A. Wulder (2014). Good practices for estimating area and assessing accuracy of land change. *Remote Sensing of Environment* 148 (0), 42-57. DOI: <http://dx.doi.org/10.1016/j.rse.2014.02.015>.
- Olson, D.M., E. Dinerstein, E.D. Wikramanayake, N.D. Burgess, G.V.N. Powell, E.C. Underwood, J.A. D'Amico, I. Itoua, H.E. Strand, J.C. Morrison, C.J. Loucks, T.F. Allnutt, T.H. Ricketts, Y. Kura, J.F. Lamoreux, W.W. Wettengel, P. Hedao, and K.R. Kassem (2001). Terrestrial Ecoregions of the

- World: A New Map of Life on Earth. *BioScience* 51 (11), 933-938. DOI: 10.1641/0006-3568(2001)051[0933:teotwa]2.0.co;2.
- Penman, J., M. Gytarsky, T. Hiraishi, T. Krug, D. Kruger, R. Pipatti, L. Buendia, K. Miwa, T. Ngara, K. Tanabe, and F. Wagner (2003). *Good Practice Guidance for Land Use, Land-Use Change and Forestry*. Kanagawa, Japan. IPCC National Greenhouse Gas Inventories Programme and Institute for Global Environmental Strategies.
- Pereira, H.M., S. Ferrier, M. Walters, G.N. Geller, R.H.G. Jongman, R.J. Scholes, M.W. Bruford, N. Brummitt, S.H.M. Butchart, A.C. Cardoso, N.C. Coops, E. Dullo, D.P. Faith, J. Freyhof, R.D. Gregory, C. Heip, R. Höft, G. Hurtt, W. Jetz, D.S. Karp, M.A. McGeoch, D. Obura, Y. Onoda, N. Pettorelli, B. Reyers, R. Sayre, J.P.W. Scharlemann, S.N. Stuart, E. Turak, M. Walpole, and M. Wegmann (2013). Essential Biodiversity Variables. *Science* 339 (6117), 277-278. DOI: 10.1126/science.1229931.
- Pereira, J.M.C. (2003). Remote Sensing of Burned Areas in Tropical Savannas. *International Journal of Wildland Fire* 12 (4), 259-270. DOI: 10.1071/WF03028.
- Revermann, R., M. Finckh, M. Stellmes, B. Strohbach, D. Frantz, and J. Oldeland (2016). Linking Land Surface Phenology and Vegetation-Plot Databases to Model Terrestrial Plant  $\alpha$ -Diversity of the Okavango Basin. *Remote Sensing* 8 (5), 370. DOI: 10.3390/rs8050370.
- Richardson, B. (2010). Big Sugar in Southern Africa: Rural Development and the Perverted Potential of Sugar/Ethanol Exports. *Journal of Peasant Studies* 37 (4), 917-938. DOI: 10.1080/03066150.2010.512464.
- Röder, A., T. Kuemmerle, and J. Hill (2005). Extension of Retrospective Datasets Using Multiple Sensors. An Approach to Radiometric Intercalibration of Landsat TM and MSS Data. *Remote Sensing of Environment* 95 (2), 195-210. DOI: 10.1016/j.rse.2004.12.008.
- Röder, A., T. Udelhoven, J. Hill, G. del Barrio, and G. Tsiourlis (2008). Trend Analysis of Landsat-TM and -ETM+ Imagery to Monitor Grazing Impact in a Rangeland Ecosystem in Northern Greece. *Remote Sensing of Environment* 112 (6), 2863-2875. DOI: 10.1016/j.rse.2008.01.018.
- Rothman, L., I. Gordon, Y. Babikov, A. Barbe, D. Chris Benner, P. Bernath, M. Birk, L. Bizzocchi, V. Boudon, and L. Brown (2013). The HITRAN2012 Molecular Spectroscopic Database. *Journal of Quantitative Spectroscopy and Radiative Transfer* 130, 4-50. DOI: 10.1016/j.jqsrt.2013.07.002.
- Roy, D.P., J. Ju, P. Lewis, C. Schaaf, F. Gao, M. Hansen, and E. Lindquist (2008). Multi-Temporal MODIS-Landsat Data Fusion for Relative Radiometric Normalization, Gap Filling, and Prediction of Landsat Data. *Remote Sensing of Environment* 112 (6), 3112-3130. DOI: 10.1016/j.rse.2008.03.009.
- Roy, D.P., J. Ju, K. Kline, P.L. Scaramuzza, V. Kovalsky, M. Hansen, T.R. Loveland, E. Vermote, and C. Zhang (2010a). Web-Enabled Landsat Data (WELD): Landsat ETM+ Composited Mosaics of the Conterminous United States. *Remote Sensing of Environment* 114 (1), 35-49. DOI: 10.1016/j.rse.2009.08.011.
- Roy, D.P., J. Ju, C. Mbaw, P. Frost, and T. Loveland (2010b). Accessing Free Landsat Data via the Internet: Africa's Challenge. *Remote Sensing Letters* 1 (2), 111-117. DOI: 10.1080/01431160903486693.

- Roy, D.P., R. Nemani, and M.C. Hansen (2014a). Global Long-Term Multi-Sensor Web-Enabled Landsat Data Record. *Web Page* Accessed 01.10.2016.  
<http://globalmonitoring.sdstate.edu/projects/weldglobal/>.
- Roy, D.P., Y. Qin, V. Kovalskyy, E.F. Vermote, J. Ju, A. Egorov, M.C. Hansen, I. Kommareddy, and L. Yan (2014b). Conterminous United States Demonstration and Characterization of MODIS-Based Landsat ETM+ Atmospheric Correction. *Remote Sensing of Environment* 140, 433-449. DOI: 10.1016/j.rse.2013.09.012.
- Roy, D.P., M.A. Wulder, T.R. Loveland, W. C.E, R.G. Allen, M.C. Anderson, D. Helder, J.R. Irons, D.M. Johnson, R. Kennedy, T.A. Scambos, C.B. Schaaf, J.R. Schott, Y. Sheng, E.F. Vermote, A.S. Belward, R. Bindschadler, W.B. Cohen, F. Gao, J.D. Hipple, P. Hostert, J. Huntington, C.O. Justice, A. Kilic, V. Kovalskyy, Z.P. Lee, L. Lyburner, J.G. Masek, J. McCorkel, Y. Shuai, R. Trezza, J. Vogelmann, R.H. Wynne, and Z. Zhu (2014c). Landsat-8: Science and Product Vision for Terrestrial Global Change Research. *Remote Sensing of Environment* 145, 154-172. DOI: 10.1016/j.rse.2014.02.001.
- Roy, D.P., H.K. Zhang, J. Ju, J.L. Gomez-Dans, P.E. Lewis, C.B. Schaaf, Q. Sun, J. Li, H. Huang, and V. Kovalskyy (2016). A General Method to Normalize Landsat Reflectance Data to Nadir BRDF Adjusted Reflectance. *Remote Sensing of Environment* 176, 255-271. DOI: 10.1016/j.rse.2016.01.023.
- Royer, A., L. Charbonneau, and P.M. Teillet (1988). Interannual Landsat-MSS Reflectance Variation in an Urbanized Temperate Zone. *Remote Sensing of Environment* 24 (3), 423-446. DOI: 10.1016/0034-4257(88)90017-X.
- Saatchi, S.S., J.V. Soares, and D.S. Alves (1997). Mapping Deforestation and Land Use in Amazon Rainforest by using SIR-C Imagery. *Remote Sensing of Environment* 59 (2), 191-202. DOI: 10.1016/S0034-4257(96)00153-8.
- Saatchi, S.S., N.L. Harris, S. Brown, M. Lefsky, E.T. Mitchard, W. Salas, B.R. Zutta, W. Buermann, S.L. Lewis, and S. Hagen (2011). Benchmark Map of Forest Carbon Stocks in Tropical Regions Across Three Continents. *Proceedings of the National Academy of Sciences* 108 (24), 9899-9904. DOI: 10.1073/pnas.1019576108.
- Schaaf, C.B., F. Gao, A.H. Strahler, W. Lucht, X. Li, T. Tsang, N.C. Strugnell, X. Zhang, Y. Jin, J.-P. Muller, P. Lewis, M. Barnsley, P. Hobson, M. Disney, G. Roberts, M. Dunderdale, C. Doll, R.P. d'Entremont, B. Hu, S. Liang, J.L. Privette, and D. Roy (2002). First Operational BRDF, Albedo Nadir Reflectance Products from MODIS. *Remote Sensing of Environment* 83 (1/2), 135-148. DOI: 10.1016/S0034-4257(02)00091-3.
- Schmidt, M., T. Udelhoven, T. Gill, and A. Röder (2012). Long Term Data Fusion for a Dense Time Series Analysis with MODIS and Landsat Imagery in an Australian Savanna. *Journal of Applied Remote Sensing* 6 (1), 063512. DOI: 10.1117/1.jrs.6.063512.
- Schmidt, M., R. Lucas, P. Bunting, J. Verbesselt, and J. Armston (2015). Multi-Resolution Time Series Imagery for Forest Disturbance and Regrowth Monitoring in Queensland, Australia. *Remote Sensing of Environment* 158, 156-168. DOI: 10.1016/j.rse.2014.11.015.
- Schneibel, A., M. Stellmes, R. Revermann, and M. Finckh (2013). Agricultural Expansion during the Post-Civil War Period in Southern Angola based on Bi-Temporal Landsat Data. In *Biodiversity & Ecology*



- 5 - *Special Volume: Environmental Assessments in the Okavango Region*, edited by J. Oldeland, C. Erb, M. Finckh and N. Jürgens. Hamburg, Germany. University of Hamburg.
- Schneibel, A., M. Stellmes, A. Röder, M. Finckh, R. Revermann, D. Frantz, and J. Hill (2016). Evaluating the Trade-Off Between Food and Timber Resulting from the Conversion of Miombo Forests to Agricultural Land in Angola Using Multi-Temporal Landsat Data. *Science of The Total Environment* 548–549, 390-401. DOI: 10.1016/j.scitotenv.2015.12.137.
- Schneibel, A., M. Stellmes, A. Röder, B. Kowalski, D. Frantz, E. Haß, and J. Hill (upcoming). Spatio-Temporal Changes of Smallholder Cultivation Patterns in the Angolan Miombo Belt Assessed by Using Segmentation of Landsat Time Series.
- Scholes, R., J. Kendall, and C. Justice (1996). The Quantity of Biomass Burned in Southern Africa. *Journal of Geophysical Research: Atmospheres* 101 (D19), 23667-23676. DOI: 10.1029/96JD01623.
- Schultz, J. (1983). *Zambia. Wissenschaftliche Länderkunden Bd. 23*. Darmstadt, Germany. Wissenschaftliche Buchgesellschaft.
- Shimabukuro, Y.E., G.T. Batista, E.M.K. Mello, J.C. Moreira, and V. Duarte (1998). Using Shade Fraction Image Segmentation to Evaluate Deforestation in Landsat Thematic Mapper Images of the Amazon Region. *International Journal of Remote Sensing* 19 (3), 535-541. DOI: 10.1080/014311698216152.
- Siegal, B.S., and A.F. Goetz (1977). Effect of Vegetation on Rock and Soil Type Discrimination. *Photogrammetric Engineering and Remote Sensing* 43 (2), 191-196.
- Simonetti, D., E. Simonetti, Z. Szantoi, A. Lupi, and H.D. Eva (2015). First Results From the Phenology-Based Synthesis Classifier Using Landsat 8 Imagery. *IEEE Geoscience and Remote Sensing Letters* 12 (7), 1496-1500. DOI: 10.1109/lgrs.2015.2409982.
- Singh, A. (1989). Digital Change Detection Techniques using Remotely-Sensed Data. *International Journal of Remote Sensing* 10 (6), 989-1003. DOI: 10.1080/01431168908903939.
- Smith, J.A. (1980). The Lambertian Assumption and Landsat Data. *Photogrammetric Engineering & Remote Sensing* 46, 1183-1189.
- Sobolev, V.V. (1975). *Light Scattering in Planetary Atmospheres (translation)*. Oxford, UK and New York, USA. Pergamon Press. Original publication: Rasseianie sveta v atmosferakh planet.
- Sobrino, J.A., N. Raissouni, J. Simarro, F. Nerry, and F. Petitcolin (1999). Atmospheric Water Vapor Content over Land Surfaces Derived from the AVHRR Data: Application to the Iberian Peninsula. *IEEE Transactions on Geoscience and Remote Sensing* 37 (3), 1425-1434. DOI: 10.1109/36.763306.
- Soille, P., J. Vogt, and R. Colombo (2003). Carving and Adaptive Drainage Enforcement of Grid Digital Elevation Models. *Water Resources Research* 39 (12). DOI: 10.1029/2002wr001879.
- Song, C., C.E. Woodcock, K.C. Seto, M.P. Lenney, and S.A. Macomber (2001). Classification and Change Detection Using Landsat TM Data: When and How to Correct Atmospheric Effects? *Remote Sensing of Environment* 75 (2), 230-244. DOI: 10.1016/S0034-4257(00)00169-3.

- Sonnenschein, R., T. Kuemmerle, T. Udelhoven, M. Stellmes, and P. Hostert (2011). Differences in Landsat-Based Trend Analyses in Drylands due to the Choice of Vegetation Estimate. *Remote Sensing of Environment* 115 (6), 1408-1420. DOI: 10.1016/j.rse.2011.01.021.
- Spencer, J. (1971). Fourier Series Representation of the Position of the Sun. *Search* 2 (5), 172-172.
- Stellmes, M., T. Udelhoven, A. Röder, R. Sonnenschein, and J. Hill (2010). Dryland Observation at Local and Regional Scale — Comparison of Landsat TM/ETM+ and NOAA AVHRR Time Series. *Remote Sensing of Environment* 114 (10), 2111-2125. DOI: 10.1016/j.rse.2010.04.016.
- Stellmes, M., D. Frantz, M. Finckh, and R. Revermann (2013a). Fire Frequency, Fire Seasonality and Fire Intensity within the Okavango Region Derived from MODIS Fire Products. In *Biodiversity & Ecology 5 - Special Volume: Environmental Assessments in the Okavango Region*, edited by J. Oldeland, C. Erb, M. Finckh and N. Jürgens, 351-362. Hamburg, Germany. University of Hamburg.
- Stellmes, M., A. Röder, T. Udelhoven, and J. Hill (2013b). Mapping Syndromes of Land Change in Spain with Remote Sensing Time Series, Demographic and Climatic Data. *Land Use Policy* 30 (1), 685-702. DOI: 10.1016/j.landusepol.2012.05.007.
- Stoffels, J., J. Hill, T. Sachtleber, S. Mader, H. Buddenbaum, O. Stern, J. Langshausen, J. Dietz, and G. Ontrup (2015). Satellite-Based Derivation of High-Resolution Forest Information Layers for Operational Forest Management. *Forests* 6 (6), 1982-2013. DOI: 10.3390/f6061982.
- Tan, B., J.T. Morisette, R.E. Wolfe, G. Feng, G.A. Ederer, J. Nightingale, and J.A. Pedelty (2011). An Enhanced TIMESAT Algorithm for Estimating Vegetation Phenology Metrics From MODIS Data. *IEEE Journal of Selected Topics in Applied Earth Observations and Remote Sensing* 4 (2), 361-371. DOI: 10.1109/jstars.2010.2075916.
- Tange, O. (2011). GNU Parallel - The Command-Line Power Tool. *The USENIX Magazine* 36 (1), 42-47.
- Tanré, D., M. Herman, P.Y. Deschamps, and A. de Lefte (1979). Atmospheric Modeling for Space Measurements of Ground Reflectances, Including Bidirectional Properties. *Applied Optics* 18 (21), 3587-3594. DOI: 10.1364/ao.18.003587.
- Tanré, D., M. Herman, and P.Y. Deschamps (1981). Influence of the Background Contribution upon Space Measurements of Ground Reflectance. *Applied Optics* 20 (20), 3676-3684. DOI: 10.1364/ao.20.003676.
- Tanré, D., C. Deroo, P. Duhaut, M. Herman, J.J. Morcrette, J. Perbos, and P.Y. Deschamps (1990). Description of a Computer Code to Simulate the Satellite Signal in the Solar Spectrum: The 5S Code. *International Journal of Remote Sensing* 11 (4), 659-668. DOI: 10.1080/01431169008955048.
- Teillet, P., B. Guindon, and D. Goodenough (1982). On the Slope-Aspect Correction of Multispectral Scanner Data. *Canadian Journal of Remote Sensing* 8 (2), 84-106. DOI: 10.1080/07038992.1982.10855028.
- Themistocleous, K., D.G. Hadjimitsis, A. Retalis, N. Chrysoulakis, and S. Michaelides (2013). Precipitation Effects on the Selection of Suitable Non-Variant Targets Intended for Atmospheric Correction of Satellite Remotely Sensed Imagery. *Atmospheric Research* 131, 73-80. DOI: 10.1016/j.atmosres.2012.02.015.

- Thuillier, G., M. Hersé, D. Labs, T. Foujols, W. Peetermans, D. Gillotay, P.C. Simon, and H. Mandel (2003). The Solar Spectral Irradiance from 200 to 2400 nm as Measured by the SOLSPEC Spectrometer from the Atlas and Eureka Missions. *Solar Physics* 214 (1), 1-22. DOI: 10.1023/a:1024048429145.
- Torres, R., P. Snoeij, D. Geudtner, D. Bibby, M. Davidson, E. Attema, P. Potin, B. Rommen, N. Floury, M. Brown, I.N. Traver, P. Deghaye, B. Duesmann, B. Rosich, N. Miranda, C. Bruno, M. L'Abbate, R. Croci, A. Pietropaolo, M. Huchler, and F. Rostan (2012). GMES Sentinel-1 Mission. *Remote Sensing of Environment* 120, 9-24. DOI: 10.1016/j.rse.2011.05.028.
- Townshend, J., J. Latham, O. Arino, R. Balstad, A. Belward, R. Conant, C. Elvidge, J. Feuquay, D. El Hadani, M. Herold, A. Janetos, C.O. Justice, L. Jiyuan, T. Loveland, F. Nachtergaele, D. Ojima, M. Maiden, F. Palazzo, C. Schmullius, R. Sessa, A. Singh, J. Tschirley, and H. Yamamoto (2008). *Integrated Global Observations of the Land: An IGOS-P Theme*. Food and Agriculture Organization.
- Townshend, J.R.G., and C.O. Justice (1988). Selecting the Spatial Resolution of Satellite Sensors Required For Global Monitoring of Land Transformations. *International Journal of Remote Sensing* 9 (2), 187-236. DOI: 10.1080/01431168808954847.
- Townshend, J.R.G., C.O. Justice, C. Gurney, and J. McManus (1992). The Impact of Misregistration on Change Detection. *IEEE Transactions on Geoscience and Remote Sensing* 30 (5), 1054-1060. DOI: 10.1109/36.175340.
- Tucker, C.J. (1979). Red and Photographic Infrared Linear Combinations for Monitoring Vegetation. *Remote Sensing of Environment* 8 (2), 127-150. DOI: 10.1016/0034-4257(79)90013-0.
- Tulleken, H. (2008). Poisson Disk Sampling. *Dev. Mag* 21, 21-25.
- Udelhoven, T. (2011). TimeStats: A Software Tool for the Retrieval of Temporal Patterns From Global Satellite Archives. *IEEE Journal of Selected Topics in Applied Earth Observations and Remote Sensing* 4 (2), 310-317. DOI: 10.1109/jstars.2010.2051942.
- USGS (2015). SRTM 1 Arc-Second Global. *Web Page* Accessed 01.09.2015. <https://lta.cr.usgs.gov/SRTM1Arc>.
- USGS (2016a). Landsat Surface Reflectance High Level Data Products. *Web Page* Accessed 16.09.2016. [http://landsat.usgs.gov//CDR\\_LSR.php](http://landsat.usgs.gov//CDR_LSR.php).
- USGS (2016b). Earth Explorer. *Web Page* Accessed 06.09.2016. <http://earthexplorer.usgs.gov/>.
- van der Werf, G.R., D.C. Morton, R.S. DeFries, J.G.J. Olivier, P.S. Kasibhatla, R.B. Jackson, G.J. Collatz, and J.T. Randerson (2009). CO2 Emissions from Forest Loss. *Nature Geoscience* 2 (11), 737-738. DOI: 10.1038/ngeo671.
- Van Niel, T.G., and T.R. McVicar (2004). Determining Temporal Windows for Crop Discrimination with Remote Sensing: A Case Study in South-Eastern Australia. *Computers and Electronics in Agriculture* 45 (1-3), 91-108. DOI: 10.1016/j.compag.2004.06.003.
- Van Zinderen Bakker, E. (1975). The Origin and Palaeoenvironment of the Namib Desert Biome. *Journal of Biogeography* 2 (2), 65-73. DOI: 10.2307/3038074.

- Vermote, E., and A. Vermeulen (1999). *Atmospheric Correction Algorithm: Spectral Reflectances (MOD09) - Algorithm Theoretical Basis Document*. [http://dratmos.geog.umd.edu/files/pdf/atbd\\_mod09.pdf](http://dratmos.geog.umd.edu/files/pdf/atbd_mod09.pdf).
- Vermote, E., C. Justice, M. Claverie, and B. Franch (in press). Preliminary Analysis of the Performance of the Landsat 8/OLI Land Surface Reflectance Product. *Remote Sensing of Environment*. DOI: 10.1016/j.rse.2016.04.008.
- Vermote, E.F., D. Tanre, J.L. Deuze, M. Herman, and J.J. Morcette (1997). Second Simulation of the Satellite Signal in the Solar Spectrum, 6S: An Overview. *IEEE Transactions on Geoscience and Remote Sensing* 35 (3), 675-686. DOI: 10.1109/36.581987.
- Vermote, E.F., N.Z. El Saleous, and C.O. Justice (2002). Atmospheric Correction of MODIS Data in the Visible to Middle Infrared: First Results. *Remote Sensing of Environment* 83 (1-2), 97-111. DOI: 10.1016/S0034-4257(02)00089-5.
- Vincent, L. (1993). Morphological Grayscale Reconstruction in Image Analysis: Applications and Efficient Algorithms. *IEEE Transactions on Image Processing* 2 (2), 176-201. DOI: 10.1109/83.217222.
- Vogelmann, J.E., A.L. Gallant, H. Shi, and Z. Zhu (in press). Perspectives on Monitoring Gradual Change across the Continuity of Landsat Sensors using Time-Series Data. *Remote Sensing of Environment*. DOI: 10.1016/j.rse.2016.02.060.
- Walker, J.J., K.M. de Beurs, R.H. Wynne, and F. Gao (2012). Evaluation of Landsat and MODIS Data Fusion Products for Analysis of Dryland Forest Phenology. *Remote Sensing of Environment* 117, 381-393. DOI: 10.1016/j.rse.2011.10.014.
- Weber, T. (2013). Mashare - Climate. In *Biodiversity & Ecology 5 - Special Volume: Environmental Assessments in the Okavango Region*, edited by J. Oldeland, C. Erb, M. Finckh and N. Jürgens. Hamburg, Germany. University of Hamburg.
- White, J.C., M.A. Wulder, G.W. Hobart, J.E. Luther, T. Hermosilla, P. Griffiths, N.C. Coops, R.J. Hall, P. Hostert, A. Dyk, and L. Guindon (2014). Pixel-Based Image Compositing for Large-Area Dense Time Series Applications and Science. *Canadian Journal of Remote Sensing* 40 (3), 192-212. DOI: 10.1080/07038992.2014.945827.
- White, M.A., P.E. Thornton, and S.W. Running (1997). A Continental Phenology Model for Monitoring Vegetation Responses to Interannual Climatic Variability. *Global Biogeochemical Cycles* 11 (2), 217-234. DOI: 10.1029/97gb00330.
- White, M.A., F. Hoffman, W.W. Hargrove, and R.R. Nemani (2005). A Global Framework for Monitoring Phenological Responses to Climate Change. *Geophysical Research Letters* 32 (4), 1-4. DOI: 10.1029/2004gl021961.
- Williams-Linera, G. (1997). Phenology of Deciduous and Broadleaved-Evergreen Tree Species in a Mexican Tropical Lower Montane Forest. *Global Ecology and Biogeography Letters* 6 (2), 115-127.
- Wolfe, R.E., D.P. Roy, and E. Vermote (1998). MODIS Land Data Storage, Gridding, and Compositing Methodology: Level 2 Grid. *IEEE Transactions on Geoscience and Remote Sensing* 36 (4), 1324-1338. DOI: 10.1109/36.701082.

- Woodcock, C.E., R. Allen, M. Anderson, A. Belward, R. Bindschadler, W. Cohen, F. Gao, S.N. Goward, D. Helder, and E. Helmer (2008). Free Access to Landsat Imagery. *Science* 320 (5879), 1011a. DOI: 10.1126/science.320.5879.1011a.
- Wulder, M.A., J.C. White, S.N. Goward, J.G. Masek, J.R. Irons, M. Herold, W.B. Cohen, T.R. Loveland, and C.E. Woodcock (2008). Landsat Continuity: Issues and Opportunities for Land Cover Monitoring. *Remote Sensing of Environment* 112 (3), 955-969. DOI: 10.1016/j.rse.2007.07.004.
- Wulder, M.A., J.G. Masek, W.B. Cohen, T.R. Loveland, and C.E. Woodcock (2012). Opening the Archive: How Free Data has Enabled the Science and Monitoring Promise of Landsat. *Remote Sensing of Environment* 122, 2-10. DOI: 10.1016/j.rse.2012.01.010.
- Wulder, M.A., J.C. White, T.R. Loveland, C.E. Woodcock, A.S. Belward, W.B. Cohen, G. Fosnight, J. Shaw, J.G. Masek, and D.P. Roy (in press). The Global Landsat Archive: Status, Consolidation, and Direction. *Remote Sensing of Environment*.
- Xingfa, G., and T. Xudong (2015). Overview of China Earth Observation Satellite Programs [Space Agencies]. *IEEE Geoscience and Remote Sensing Magazine* 3 (3), 113-129. DOI: 10.1109/mgrs.2015.2467172.
- Zhang, X., M.A. Friedl, C.B. Schaaf, A.H. Strahler, J.C.F. Hodges, F. Gao, B.C. Reed, and A. Huete (2003). Monitoring Vegetation Phenology using MODIS. *Remote Sensing of Environment* 84 (3), 471-475. DOI: 10.1016/S0034-4257(02)00135-9.
- Zhang, Y., B. Guindon, and J. Cihlar (2002). An Image Transform to Characterize and Compensate for Spatial Variations in Thin Cloud Contamination of Landsat Images. *Remote Sensing of Environment* 82 (2-3), 173-187. DOI: 10.1016/S0034-4257(02)00034-2.
- Zhu, X., J. Chen, F. Gao, X. Chen, and J.G. Masek (2010). An Enhanced Spatial and Temporal Adaptive Reflectance Fusion Model for Complex Heterogeneous Regions. *Remote Sensing of Environment* 114 (11), 2610-2623. DOI: 10.1016/j.rse.2010.05.032.
- Zhu, X., E.H. Helmer, F. Gao, D. Liu, J. Chen, and M.A. Lefsky (2016). A Flexible Spatiotemporal Method for Fusing Satellite Images with Different Resolutions. *Remote Sensing of Environment* 172, 165-177. DOI: 10.1016/j.rse.2015.11.016.
- Zhu, Z., and C.E. Woodcock (2012). Object-Based Cloud and Cloud Shadow Detection in Landsat Imagery. *Remote Sensing of Environment* 118, 83-94. DOI: 10.1016/j.rse.2011.10.028.
- Zhu, Z., C.E. Woodcock, and P. Olofsson (2012). Continuous Monitoring of Forest Disturbance Using all Available Landsat Imagery. *Remote Sensing of Environment* 122, 75-91. DOI: 10.1016/j.rse.2011.10.030.
- Zhu, Z., and C.E. Woodcock (2014a). Automated Cloud, Cloud Shadow, and Snow Detection in Multitemporal Landsat Data: An Algorithm Designed Specifically for Monitoring Land Cover Change. *Remote Sensing of Environment* 152, 217-234. DOI: 10.1016/j.rse.2014.06.012.
- Zhu, Z., and C.E. Woodcock (2014b). Continuous Change Detection and Classification of Land Cover using all Available Landsat Data. *Remote Sensing of Environment* 144, 152-171. DOI: 10.1016/j.rse.2014.01.011.

- Zhu, Z., S. Wang, and C.E. Woodcock (2015). Improvement and Expansion of the Fmask Algorithm: Cloud, Cloud Shadow, and Snow Detection for Landsats 4–7, 8, and Sentinel 2 Images. *Remote Sensing of Environment* 159, 269-277. DOI: 10.1016/j.rse.2014.12.014.
- Zhukov, B., D. Oertel, F. Lanzl, and G. Reinhackel (1999). Unmixing-Based Multisensor Multiresolution Image Fusion. *IEEE Transactions on Geoscience and Remote Sensing* 37 (3), 1212-1226. DOI: 10.1109/36.763276.

## Curriculum Vitae

**David Georg Frantz**  
 Address Bergstraße 7  
 54295 Trier, Germany  
 Date of Birth 26.11.1986  
 Place of Birth Heppenheim, Germany

### Professional Experience

06/2013–today **Trier University**, Trier, Germany  
 Department: Environmental Remote Sensing & Geoinformatics  
*Project staff (SASSCAL and Sentinel4GRIPS)*

09/2012–10/2012 **Queensland Government**, Brisbane, Australia  
 Department of Science, Information Technology, Innovation and the Arts  
*Research visit*

04/2011–08/2011 **National Aeronautics and Space Research Centre**, Oberpfaffenhofen, Germany  
**Centre de Recherche Public - Gabriel Lippmann**, Belvaux, Luxemburg  
*Internships*

10/2008–07/2013 **Trier University**, Trier, Germany  
 Departments: Environmental Remote Sensing & Geoinformatics / Cartography /  
 Environmental Meteorology  
*Student assistance, tutor and map library*

### Academic Career

06/2013–today **Trier University**, Trier, Germany  
 Department: Environmental Remote Sensing & Geoinformatics  
*Ph.D candidacy*

10/2006–12/2012 **Trier University**, Trier, Germany  
*Diploma in Applied Environmental Sciences* with main subjects Remote Sensing /  
 Meteorology / Cartography / Geology; overall grade: „with distinction“, i.e. 1.0  
 Diploma thesis entitled ‘Characterization of forest disturbance using data-blending  
 techniques applied to MODIS and Landsat time series in an Australian Savanna’ in  
 collaboration with the Department of Science, Information Technology, Innovation  
 and the Arts, Queensland Government, Brisbane, Australia.  
 Supervisors: Dr. Achim Röder, Prof. Dr. Thomas Udelhoven

08/1997–03/2006 **Secondary School (Herzog-Johann-Gymnasium)**, Simmern, Germany

08/1993–07/1997 **Primary school**, Kirchberg, Germany

## Extra Curricular Activities and Awards

2016	<b>Trier University</b> , Trier, Germany Faculty award for the best Ph.D publication with “An Operational Radiometric Landsat Preprocessing Framework for Large-Area Time Series Applications”.
2013	<b>Trier University</b> , Trier, Germany Award for the best graduation in Applied Environmental Sciences (2012/2013)
11/2010–12/2012	<b>Trier University</b> , Trier, Germany Student member in the diploma board of examiners (Applied Environm. Sciences)

## Publications (peer-reviewed)

upcoming	D. Frantz, M. Stellmes, A. Röder, and J. Hill: Fire spread from MODIS burned area data: obtaining fire dynamics information for every single fire. Accepted for publication in <i>International Journal of Wildland Fire</i> .
2016	R. Revermann, M. Finck, M. Stellmes, B. Strohbach, D. Frantz, and J. Oldeland (2016): Linking Land Surface Phenology and Vegetation-Plot Databases to Model Terrestrial Plant $\alpha$ -Diversity of the Okavango Basin. <i>Remote Sensing</i> 8 (5).  D. Frantz, M. Stellmes, A. Röder, T. Udelhoven, S. Mader, and J. Hill (2016): Improving the Spatial Resolution of Land Surface Phenology by Fusing Medium- and Coarse-Resolution Inputs. <i>IEEE Transactions on Geoscience and Remote Sensing</i> 54 (7).  D. Frantz, A. Röder, T. Udelhoven, and M. Schmidt (2016): Forest Disturbance Mapping Using Dense Synthetic Landsat/MODIS Time-Series and Permutation-Based Disturbance Index Detection. <i>Remote Sensing</i> 8 (4).  D. Frantz, A. Röder, M. Stellmes, and J. Hill (2016): An Operational Radiometric Landsat Preprocessing Framework for Large-Area Time Series Applications. <i>IEEE Transactions on Geoscience and Remote Sensing</i> 54 (7).  A. Schneibel, M. Stellmes, A. Röder, M. Finckh, R. Revermann, D. Frantz and J. Hill (2016): Evaluating the trade-off between food and timber resulting from the conversion of Miombo forests to agricultural land in Angola using multi-temporal Landsat data. <i>Science of The Total Environment</i> 548–549.
2015	D. Frantz, A. Röder, M. Stellmes, and J. Hill (2015): On the derivation of a spatially distributed aerosol climatology for its incorporation in a radiometric Landsat preprocessing framework. <i>Remote Sensing Letters</i> 6 (8).  D. Frantz, A. Röder, T. Udelhoven, and M. Schmidt (2015): Enhancing the Detectability of Clouds and Their Shadows in Multitemporal Dryland Landsat Imagery: Extending Fmask. <i>IEEE Geoscience and Remote Sensing Letters</i> 12 (6).
2014	M. Machwitz, L. Giustarini, C. Bossung, D. Frantz, M. Schlerf, H. Lilienthal, L. Wandera, P. Matgen, L. Hoffmann, and T. Udelhoven (2014): Enhanced biomass prediction by assimilating satellite data into a crop growth model. <i>Environmental Modelling &amp; Software</i> 62.
2013	M. Stellmes, D. Frantz, M. Finckh, R. Revermann, A. Röder, and J. Hill (2013): Fire frequency, fire seasonality and fire intensity within the Okavango region derived from MODIS fire products. <i>Biodiversity &amp; Ecology</i> 5.